UNIVERSITY OF LIVERPOOL

IMPACT RESISTANCE OF PRE-DAMAGED ULTRA-HIGH PERFORMANCE FIBRE REINFORCED CONCRETE (UHPFRC) SLABS

Thesis submitted in accordance with the requirement of the

University of Liverpool for the degree of

Doctor in Philosophy

By

Shaharudin Shah Zaini

February 2015

ACKNOWLEDGEMENTS

I would like to express my utmost gratitude and appreciation to my primary supervisor, Dr. Graham Schleyer for his invaluable guidance, supervision and encouragement throughout these years. I also would like to express my gratitude to my second supervisor, Dr. Steve Jones for providing constructive advice and helpful discussion. A heartfelt appreciation is also dedicated to Dr. Robert Birch, who taught me the techniques to handle the Laser Doppler equipment and processing of the data. Their knowledge, experience and expertise have made a significant contribution in all aspects of my research, and I am tremendously grateful for that.

I would like to extend my thanks to the staff at University of Liverpool, in particular Mr. Stephen Pennington, Mr. David Hunter, Mr. Marc Bratley and Mr. Steven Bode. I'm indebted to them for their assistance during my experimental work. To my colleagues, Dr. Nicholas Underwood, Mr. Goran Mahmud, Dr. Aram Hassan, Mr. Zuhri Yusoff, Miss Alia Aziz, and Mr. Sherif Hassaan, thank you.

I would not have been able to concentrate and accomplish my goals had it not been for the love and support from my understanding wife, Norhayati Yusof, whose patience is limitless throughout the ups and downs in my studies. To my daughter, Nur Aiman Kautsar, and my son Muhammad Al-Amin, God bless both of you for the bits and pieces you have helped me with.

Finally, thank you to Universiti Sains Malaysia and the Government of Malaysia for sponsoring my PhD studies.

LIST OF PUBLICATIONS

1. S. S. Zaini, G. K. Schleyer, S. J. Barnett and N. J. Underwood, “High pressure static test on UHPFRC panels using pulse pressure loading rig,” presented at the Awam International Conference on Civil Engineering, Malaysia, Aug. 28-30, 2012.

2. S. S. Zaini and G. K. Schleyer, “Impact resistance of pre-damaged ultra-high performance fibre-reinforced concrete (UHPFRC) slabs”, presented at the 13th International Conference on Structures under Shock and Impact, Southampton, June 3-5, 2014.

3. S. S. Zaini, G. K. Schleyer, S. J. Barnett and N. J. Underwood, “Performance of UHPFRC panels”, *FABIG Newsletter*, Issue 65, pp. 29-34, 2015

ABSTRACT

This research aims to gain deeper insight and understanding into the behaviour of scaled pre-damaged UHPFRC slabs under the combined loading effect of static pressure followed by low velocity impact loading. The intension is to simulate impact from failed columns onto a damaged UHPFRC slab, as a result of an explosion. The context of these studies is the prevention of progressive collapse of a building through the contribution from using UHPFRC slabs.

A static pressure device was used to create the initial damage with low velocity drop tests carried out subsequently. The interest is focused on ability of the pre-damaged UHPFRC slabs to withstand cumulative impact energy, manifested via the measurement of the impact resistance, deformations and stiffness degradation compared to the undamaged slabs. The sensitivity of the impact locations were also investigated by setting the impact locations to be at the centre, edge and corner of the slab. Impact at an oblique angle of 10° was also included. The results showed that the impact resistance of the pre-damaged slabs were substantially high, approximately 50 - 85% of the undamaged slab. Similarly, the high residual strength of the pre-damaged slabs was also reflected in the pattern of the deformations and stiffness degradation where in most cases, the patterns were found to be relatively similar to the undamaged slabs. Their high strength reserves after initial damage make them appealing as a construction material to withstand abnormal loading and mitigate progressive collapse of a structure. On the other hand, the slabs subjected to the asymmetrical impact showed lower impact resistance and therefore possessed higher risk towards initiating a progressive collapse failure. On the contrary, tilting the slabs to 10° only exhibited higher impact resistance.

To predict the response of slabs, FE models were developed using ANSYS Explicit Dynamics Release 13.0 software. RHT concrete formulation was used to represent the dynamic properties of UHPFRC materials. A new technique was also introduced to model the pre-damaged slabs. Although showing scattered results, the FE models were able to predict the response with reasonable accuracy ranging from 3%-52% in the majority of the cases.

Finally, the results from the analytical simulations using an SDOF model were also able to produce a reasonably close agreement with the experimental data and particularly true when the resistance functions were derived from the static tests. Therefore, SDOF modelling can be considered as a credible method to predict the deformation of UHPFRC slabs.

TABLE OF CONTENTS

LIST OF FIGURES

LIST OF TABLES

NOTATION

c_1 & c_2	damping coefficients
d	diameter of the impactor
k	elastic stiffness
m	mass
n	number of strikes
l	effective span of slab
h	thickness of slab
E_{cie}	cumulative impact energy
$F(t)$	force with respect to time
V_f	fibre volume.
V_0	standard impact velocity
$a(t)$	acceleration with respect to time
f_n	natural frequency
$s(t)$	deformation with respect to time
v_i	velocity before contact
α, β, θ	angle, support rotation
σ_n	normal stress
σ_c	cracking stress
σ_t	maximum tensile stress

Notation for finite element model

G	shear modulus
K	bulk modulus
P	pressure
m	residual strength exponent
n	failure surface parameter
E_c	modulus of elasticity
$D1$	damage constant
$D2$	damage exponent
F_{CAP}	pressure dependent elastic cap function,
F_{fail}	generalised failure surface
F_{RATE}	strain rate dependency
P^*	pressure normalised by the uniaxial compressive strength
P^*_s	normalised hydrodynamic tensile limit
R_3	third invariant dependency
Y^*	pre-peak yield surface on the compressive meridian
Y^*_{TXC}	pressure and rate dependent peak surface on the compressive meridian
f_c	uniaxial compressive strength
y_{res}	residual surface strength
α	compressive strain rate exponent
δ	tensile strain rate exponent
ε_p	plastic strain
$\dot{\varepsilon}$	strain rate
$\dot{\varepsilon}_p$	plastic strain rate
$\dot{\varepsilon}_0$	quasi-static strain rate
θ	lode angle,

υ	poisson ratio
σ_{eq}	equivalent stress

Notation for analytical model

E	modulus of elasticity
F	force
I	second moment of area
L	effective span
M	distributed mass of the specimen
U	bending strain energy
X	half span of slab in x-axis
Y	half span of slab in y-axis
k	elastic stiffness
t	thickness of slab
w	shape function
x	distance along half span of slab in x-axis
y	distance along half span of slab in y-axis
z	half thickness of slab
$F(t)$	force with respect to time
$F_e(t)$	equivalent force with time
K_L	load factor
K_M	mass factor
M_e	equivalent single lumped mass
M_{ult}	ultimate moment of resistant
P_{ult}	ultimate load at collapse

R_e	equivalent resistance
R_M	maximum resistance force
k_e	equivalent spring stiffness
m_1	mass of slab
m_2	mass of the impactor
m_u & m_u'	positive and negative moment of resistance
v_e	equivalent velocity
v_i	velocity of impactor
v_s	theoretical velocity of slab
$\dot{w}$	velocity of the slab by differentiating *w*
ÿ	acceleration
y_{el}	elastic deformation
y_{max}	maximum deformation
y_{per}	permanent deformation
ϵ	strain
δ	deflection
δ_m	maximum deflection
$\varepsilon_{f_{ct}}$	maximum tensile strain at the end of the pseudo-plastic tensile plateau
υ	poisson ratio
ρ	density of slab

ABBREVIATIONS

ACI	American Concrete Institute
ANFO	Aluminium Nitrate Fuel Oil
ASCE	American Society of Civil Engineers
BCA	Building and Construction Authority (Singapore)
BS	British Standard
BSA	Burst Spectrum Analyzer
CEB	Comité Européen du Béton (European Committee for Concrete)
CEN	Centre
CIE	Cumulative Impact Energy
CMOD	Crack Mouth Opening Displacement
COR	Corner
DIF	Dynamic Increase Factor
EC	Euro Code
ECC	Engineered Cementitious Composite
EDG	Edge
FE	Finite Element
FRC	Fibre Reinforced Concrete
GGBS	Ground Granulated Blast-Furnace Slag
GSA	General Services Administration
HPFRC	High Performance Fibre Reinforced Concrete
HSC	High Strength Concrete
LDV	Laser Doppler Velocimeter
LVDT	Linear Variable Differential Transducer
NSC	Normal Strength Concrete
OBL	Oblique
PD	Pre-damaged
PPLR	Pulse Pressure Loading Rig

RC	Reinforced Concrete
RHSC	Reinforced High Strength Concrete
RPC	Reactive Powder Concrete
SDOF	Single-Degree-of-Freedom
SFRC	Steel Fibre Reinforced Concrete
SHS	Square Hollow Section
SIFCON	Slurry Infiltrated Fibre Concrete
TDOF	Two-Degree-of-Freedom
TNT	Trinitrotoluene
UD	Undamaged
UFC	United Facilities Criteria
UHPFRC	Ultra-high Performance Fibre Reinforced Concrete
UHPCC	Ultra-high Performance Cement Based Composite
UHSC	Ultra-high Strength Concrete

CHAPTER 1
INTRODUCTION

1.1 Background

A number of incidents resulting in progressive collapse of structures have been reported to be caused by an accidental explosion, a construction error or a deliberate act of terrorism [1]. Out of these three sources of causes, the collapse of structures due to a deliberate act of terrorism has been shown to cause the most damage and loss of life, the worst being a total collapse of the World Trade Centre twin towers on September 11th 2001 with around 3,000 fatalities [2]. The deliberate act that can be associated with the current global warfare, armed conflict, and the frustration or indignation of citizens towards the ruling government has increased terrorist activities significantly [3].

When a building is subjected to a blast load either due to an accidental explosion or deliberate act, that building will be exposed to a highly impulsive and large dynamic pressure load greater than the normal design loading. As a result, a blast load that is situated within or nearby a building is able to cause severe damage to that building and possibly lead to progressive collapse. The blast effect, building collapse, debris impact, fire and smoke can cause the loss of life [4].

The current design approach in mitigating progressive collapse of a structure is grouped into three categories which are generally common to different codes and guidelines around the world namely, the tie-force design, the alternate path method and key element design [5]. Over the years, much attention has been given to study the behaviour of structures following the loss of a key structural element particularly in the event of a sudden column loss [6-7]. However, due to the complexity of progressive collapse that depends on many factors such as the magnitude of the abnormal load, the structural form and the structural material, this area has set a challenge to researchers and design engineers.

To date, a number of new ideas and innovations using cables [8-9] to enhance the catenary action of the slabs, collapse barriers using energy absorbing column [10] and the concept of designing a reinforced concrete twin structure [11] have been reported. On the other hand, several researchers have demonstrated that ultra-high performance fibre reinforced concrete

(UHPFRC) slab/panel was able to absorb high energy resulting from blast and impact loading [12-14]. UHPFRC is highly regarded as a promising material to be used under extreme events where the hypothesis is that UHPFRC, when designed as a structural element, is able to develop sufficient resistance to mitigate progressive collapse.

1.2 Overview of Blast-Induced Progressive Collapse Events

There are several well-known cases involving blast-induced progressive collapse namely the collapse of the Ronan Point apartments in the United Kingdom and the Alfred P. Murrah building in the United States. These progressive collapses have cost millions of dollars in damages and repairs, as well as the loss of hundreds of lives.

On May 16, 1968, Ronan Point, a 22-storey residential apartment tower in Newham, East London became the major turning point and set to be the historical benchmark on progressive collapse. The high rise apartment was constructed using the Larsen-Nielsen precast concrete system comprising load bearing wall, slab and staircase. A leakage from the gas stove on the 18th floor created an explosion and blew out the internal non-load bearing wall of the kitchen and living room as well as the exterior south-west load bearing wall supporting four storeys above. The illustration showing the floor plan of the 18th floor and the anticipated blast location is shown in Figure 1.1.

Figure 1.1: Typical floor layout [15].

The investigation ruled that the collapse was initiated by the cumulative impact on floor 18 due to the progressive collapse of the several floors above [16-17]. The overloaded floor 18 then created a chain reaction and the corner apartments progressively collapsed all the way to ground level as shown in Figure 1.2 [17]. The investigation also revealed several flaws in the design and construction of the apartment, from the substandard connection used in the gas piping system to the lack of robustness where no redundancy or alternate load path mechanism was provided.

Figure 1.2: Disproportionate collapse of Ronan Point Apartment [17].

On April 19, 1995, a large part of the Alfred P. Murrah Federal Building in Oklahoma City collapsed to the ground during peak working hours. The building was a nine-storey reinforced concrete frame structure with mainly one way slab spanning over wide beams as shown in Figure 1.3 [18]. The corner columns along line G were constructed from roof to the ground floor level. However the alternate columns were terminated at the 3rd floor level and supported by transfer girders.

A truck filled with 1,800 kg TNT equivalent explosive [18] was parked about 4 m in front of the building. At the instance of detonation, column G/20 was shattered by the process of brisance and immediately led to the loss of four bays over the full height of the building.

Figure 1.3: Typical floor plan for Murrah Federal Building [18].

The blast wave expanded into the building and created an upward force on the floor slab resulting in reversed bending. The uplift movement of the slabs transferred the reaction to the floor beams where the reversed flexural and shear action cracked the beam-column joint. It is worth mentioning that the slabs and beams were not designed for reversed loading.

Once the blast pressure decayed, the structure was governed by the gravity load again. The slabs moved downward and the weak beam-column connection created the catenary action that in turn rotated and pulled the top of the transfer girder inwards as shown in Figure 1.4 [18]. This action resulted in a large torsion force that detached the transfer girder from the supporting column and the loss of four additional bays over the full height.

Figure1.4: Illustration showing catenary action of floor slabs and beams prior to the collapse of Murrah Federal Building [18].

The punching shear failure at the beam-column connection along line F also caused the columns along the line to be laterally unsupported over three storeys high. Some columns remained standing due to the lateral support from the falling debris but column F/24 buckled and collapsed taking out two more bays. Deliberately targeted, the explosion resulted in 168 fatalities, including 19 children. The sketch showing the final extent of the damage is shown in Figure 1.5 [19].

Figure 1.5: Illustration showing Murrah Federal Building after the blast-induced progressive collapse [19].

On August 7, 1998, the four-storey Ufundi Cooperative Building in Kenya suffered collateral damage as a result of the deliberate attack aimed at the United States Embassy. The U.S.A. Embassy building suffered heavy damage at its facade but the structure remained intact while the Ufundi building was completely flattened as shown in Figure 1.5 [20]. However, no extensive technical data was available in the open literature that discussed in detail the collapse mechanism of the building. A total of 213 people were killed due to this fateful event.

Figure 1.6: Collapse of Ufundi Cooperative Building [20].

Based on the examples given, it can be seen that a building can suffer from progressive or total collapse when subjected to blast loading. The structural failure can be triggered by failure or damage from a small part of the building and spread towards a larger area. As such, design guidelines for mitigating progressive collapse should also consider the use of construction materials that are able to absorb high impact energy. A material that is able to withstand abnormal loading despite being damaged can be an important factor in preventing progressive collapse.

1.3 Ultra-high Performance Fibre Reinforced Concrete (UHPFRC)

One of the breakthroughs in concrete technology is the ultrahigh performance fibre reinforced concrete (UHPFRC) that is achieved by integrating high strength concrete with fibres. The design mix of UHPFRC is characterized by the high-binder/low-water cement ratio, elimination of coarse aggregates, significant amount of cement replacement materials and inclusion of fibres. The basic fibre categories are metallic, mineral, synthetic or natural and in a variety of sizes and shapes. Figure 1.7 shows the examples of the metallic fibres commonly used in concrete mix [21].

Figure 1.7: Examples of metallic fibres [21].

UHPFRC is a highly specialized material with compressive and flexural strength in the range of 150-200 MPa and 25-50MPa, respectively while the direct tensile strength is within the range of 8-30 MPa [22]. It also exhibits high energy absorbing capacity, reported to be around 20,000-40,000 J/m^2 which is generally 130 times more than normal concrete [23].

The high compressive strength is the result of the dense particle packing of the matrix and the high tensile strength is associated with the fibre bridging and multiple cracking capabilities. This outstanding property allows UHPFRC to withstand significant mechanical stresses at crack zones as shown in Figure 1.8 (a) and multiple cracking as shown in Figure 1.8 (b) [24].

This text box is where the unabridged thesis included the following third party copyrighted material:

Graybeal BA, Baby F. Development of direct tension test method for ultra-high-performance fiber-reinforced concrete. ACI Material Journal, 2003;110(2):177-186.

http://doi.org/10.14359/51685532

(a) (b)

Figure 1.8: Features of UHPFRC showing (a) fibre bridging at cracked location; (b) multiple cracking under tensile loading [24].

A number of experimental studies and numerical simulations have been carried out and confirmed the high energy absorbing capability of UHPFRC materials [25-27]. The toughness of UHPFRC materials due to the high matrix strength and enhanced ductility via fibre bridging makes UHPFRC a potential candidate to be used in a building where extreme loading can be expected. Among the notable potential to be explored is UHPFRC's ability in the form of a slab to withstand abnormal loading conditions such as blast and impact.

1.4 Research Aim

This research aims to gain deeper insight and understanding into the behaviour of scaled pre-damaged UHPFRC slabs under the combined loading effect of static pressure followed by low velocity impact loading. The intention is to simulate impact from failed columns onto a damaged UHPFRC slab, as a result from a blast loading. The interest is focused on ability of the pre-damaged UHPFRC slabs to sustain low velocity impact compared to the undamaged UHPFRC slabs via the measurement of the impact resistance, deformations, stiffness recovery and local degradation of the materials. Various impact scenarios will be covered for this purpose in order to represent more realistic impact loading conditions.

1.5 Objectives

This research is focused on four objectives in studying the potential usage of UHPFRC as a structural slab capable of withstanding abnormal loading and mitigating progressive collapse, namely:-

i) To experimentally evaluate the impact resistance of the pre-damaged UHPFRC slabs subjected to various loading conditions.

ii) To develop an understanding on the sensitivity of the impact angle and impact location.

iii) To develop the finite element models and predict the mechanical response of the UHPFRC slabs subjected to low velocity impact and validate with the experimental results.

iv) To predict the mechanical response of the UHPFRC slabs subjected to central impact using single-degree-of-freedom (SDOF) analysis and validate with the experimental results.

1.6 Scope of Work

This research will use small slabs with the size 660 mm × 660 mm × 25 mm thickness containing 2% short steel fibre content only. The distance between supports is 500 mm centre to centre. With the *l*/*h* ratio of 20, this particular panel size could resemble the typical ratio of a slab panel in a real application. However, as this panel is not exactly scaled down in terms of its material components, the results from this study cannot be directly scaled up to the response of an actual slab panel due to the 'size effect' phenomena.

A typical UHPFRC mix design and curing procedure which has been proven to achieve the characteristics of UHPFRC used by previous researchers at the University of Liverpool will be used. Since the same mix will be used in this research, some parts of the previous tests carried out by other researchers involving the mechanical properties of UHPFRC will be applied, especially for the numerical models.

Because the exact nature of progressive collapse that might impair a structural system is complex, a multitude of angles can be explored. For this particular research, pre-damaged slabs are created by applying quasi-static pressure load using an air pressure device. This method will simulate panels having initial damage caused by abnormal pressure load. Impact load will then be applied using a modified impactor, resembling the front of a circular UHPFRC column impacting on the slab. Ideally, all loads from the above failed floor must be taken into consideration to simulate the real impact event, however due to the complexity of such arrangement, only impact from a column will be considered.

Research scope is further expanded by using the numerical simulation approach with the aid of ANSYS Explicit Dynamics Release 13.0 software. This software has the ability to analyse the dynamic response of concrete material subjected to the drop weight impact. In terms of analytical modelling, where possible, a suitable spring-mass system will be identified to determine the deformation of the UHPFRC panels. The output from this numerical simulation and analytical model will be validated and discussed with respect to the experimental work.

1.7 Thesis Outline

This thesis consists of further six chapters and organised as follows:

Chapter 2: Literature Review. This chapter briefly introduces the three major approaches in designing a building against progressive collapse and the associated comments on the reliability of each method. The contribution of a slab in mitigating progressive collapse of a building is also highlighted. In addition, the response of slab or panel under dynamic loading, the numerical analysis and finite element modelling especially involving fibre concrete based on previous research is reviewed.

Chapter 3: Materials and Experimental Arrangements. This chapter describes the materials, design mix, equipment and experimental set-up for both static as well as impact tests used in the research. Methods and concepts of processing the signal from Laser Doppler Velocimeter raw data are also described.

Chapter 4: Numerical Procedures. This chapter presents the development of the three-dimensional finite element and single-degree-of-freedom (SDOF) models. Calibration of selected RHT input parameters for the finite element models and procedure to derive the parameters for SDOF models are discussed.

Chapter 5: Experimental Results and Discussions. This chapter presents the individual results from pre-damaging exercise and the low velocity drop tests. The ability of the pre-damaged UHPFRC slabs to withstand impact loading and the responses are compared to the undamaged slabs. The effects of varying the impact location and angle are discussed in detail.

Chapter 6: Numerical Results and Discussions. This chapter presents and discusses the results of the numerical simulations comprising the finite element and the SDOF models. Validation between the numerical models and the experimental work are shown.

Chapter 7: Conclusions and Future Work. This chapter summarizes the main findings and reviews the objectives of the research before conclusions are drawn. Recommendations for future work and research opportunities are also presented.

1.8 References

[1] D. E. Grierson, L. Xu and Y. Liu, "Progressive-failure analysis of buildings subjected to abnormal loading," *Computer-Aided Civil and Infrastructure Engineering*, vol. 20, no. 3, pp. 155-171, 2005.

[2] B. Monahan, "World trade center collapse-Civil engineering considerations," *Practice Periodical on Structural Design and Construction*, vol. 7, no. 3, pp. 134-135, 2002.

[3] A. H. Garrison, "Defining terrorism: philosophy of the bomb, propaganda by deed and change through fear and violence," *Criminal Justice Studies: A Critical Journal of Crime, Law and Society*, vol. 17, no. 3, pp. 259-279, 2004.

[4] T. Ngo, P. Mendis, A. Gupta and J. Ramsay, "Blast loading and blast effects on structures-an overview," *Electronic Journal of Structural Engineering*, vol. 7, pp. 76-91, 2007.

[5] M. Byfield, W. Mudalige, C. Morison and E. Stoddart, "A review of progressive collapse research and regulations," in *Proceedings of the Institution of Civil Engineers – Structures and Buildings*, vol. 167, no. 8, ICE, 2014, pp. 447-456.

[6] H. Li, and S. El-Tawil, "Three-dimensional effects and collapse resistance mechanisms in steel frame buildings," *Journal of Structural Engineering-ASCE Special Issue: Computational Simulation in Structural Engineering*, vol. 140, no. 8, pp. A4014017, 2013.

[7] K. Qian, B. Li and J. X. Ma, "Load-carrying mechanism to resist progressive collapse of RC buildings," *Journal of Structural Engineering*, vol. 141, no, 2, pp. 04014017, 2014.

[8] S. Tan and A. Astaneh-Asl, "Use of steel cables to prevent progressive collapse of existing buildings," presented at the 6th Conference on Tall Buildings in Seismic Regions, Los Angeles, California, June 4, 2003, pp 1-20.

[9] J. Kim and & W. S. Shin, "Retrofit of RC frames against progressive collapse using pre-stressing tendons," *The Structural Design of Tall and Special Buildings*, vol. 22, no. 4, pp. 349-361, 2013.

[10] D. E. Newland and D. Cebon, "Could the World Trade Center have been modified to prevent its collapse?," *Journal of Engineering Mechanics*, vol. 128, no. 7, pp. 795-800, 2002.

[11] H. H. Jia and D. M. Wei, "Basic principal and design methodology of progressive storey collapse resistance in a new type RC twin-frame structure," *Advanced Materials Research*, vol. 368, pp. 946-952, 2012.

[12] M. Rebentrost and G. Wight, "Investigation of UHPFRC slabs under blast loads," in *Designing and Building with UHPFRC: State of the Art and Development*, F. Toutlemonde and J. Resplendino, Eds. New York: John Wiley & Sons, 2013, pp. 363-376.

[13] P. Maca, R. Sovjak and P. Konvalinka, "Mix design of UHPFRC and its response to projectile impact," *International Journal of Impact Engineering*, vol. 63, pp. 158-163, 2014.

[14] S. Astarlioglu and T. Krauthammer, "Response of normal-strength and ultra-high-performance fiber-reinforced concrete columns to idealized blast loads," *Engineering Structures*, vol. 61, pp. 1-12, 2014.

[15] M. Levy and M. G. Salvadori, *Why buildings fall down: How structures fail*. New York: WW Norton & Company, 2002.

[16] H. Griffiths, A. Pugsley and O. Saunders, "Report of the inquiry into the collapse of flats at Ronan Point, Canning Town," Her Majesty's Stationary Office, London, 1968.

[17] C. Pearson and N. Delatte, "Ronan point apartment tower collapse and its effect on building codes," *Journal of Performance of Constructed Facilities*, vol. 19, no. 2, pp. 172-177, 2005.

[18] J. D. Osteraas, "Murrah Building bombing revisited: A qualitative assessment of blast damage and collapse patterns," *Journal of Performance of Constructed Facilities*, vol. 20, no. 4, pp. 330-335, 2006.

[19] H. Tagel-Din and N. Rahman, "Simulation of the Alfred P. Murrah Federal Building collapse due to blast loads," in *Proceedings of the 2006 AEI Conference, Nebraska*, vol. 190, ASCE, 2006, pp. 32-47.

[20] Anne Mawathe. "Kenya's terror scars yet to heal". Internet: http://news.bbc.co.uk/1/hi/world/africa/7545613.stm, Feb. 4, 2015.

[21] A.E. Naaman, "Engineered steel fibres with optimal properties for reinforcement of cement composites," *Journal of Advanced Concrete Technology*, vol. 1, no. 3, pp 241-252, 2003.

[22] P. Acker and M. Behloul, "Ductal® Technology: A large spectrum of properties, a wide range of applications," in *Proceeding of the International Symposium on Ultra High Performance Concrete*, Kassel University Press, 2004, pp. 11-23.

[23] S. G. Millard, T. C. K. Molyneaux, S. J. Barnett and X. Gao, "Dynamic enhancement of blast-resistant ultra high performance fibre-reinforced concrete under flexural and shear loading," *International Journal of Impact Engineering, vol. 37, no*. 4, pp. 405-413, 2010.

[24] B. A. Graybeal and F. Baby, "Development of direct tension test method for ultra-high-performance fiber-reinforced concrete," *ACI Materials Journal*, vol. 110, no. 2, pp. 177-186, 2013.

[25] S. J. Barnett, S. G. Millard, G. K. Schleyer and A. Tyas, "Briefing: Blast tests of fibre-reinforced concrete panels" in *Proceedings of the ICE-Construction Materials*, vol. 163, no. 3, ICE, 2010, pp. 127-129.

[26] B. D. Ellis, B. P. DiPaolo, D. L. McDowell, and M. Zhou, "Experimental investigation and multiscale modeling of ultra-high-performance concrete panels subject to blast loading," *International Journal of Impact Engineering*, vol. 69, pp. 95-103, 2014.

[27] K. Wille, A. E. Naaman, and S. El-Tawll, "Optimizing ultra-high-performance fiber-reinforced concrete," *Concrete International*, vol. 33, no. 9, pp. 35-41, 2011.

CHAPTER 2
LITERATURE REVIEW

2.1 Introduction

All buildings are susceptible to progressive collapse in varying degrees [1]. The response of structures during a progressive collapse event is a very complex problem, mainly because it is dynamic in nature [2] and there are many ways in which a local collapse may propagate from initial damage to its final state. As such, designing a structure that can arrest progressive collapse under abnormal loading conditions has become one of the challenges in the professional civil engineering community. Apart from updating the current design practices, the selection of suitable material either selectively or for the entire structural members is no less important. Currently, state-of-the-art UHPFRC has been widely reported as one of the materials that shows promising performance under blast or impact loading [3-7]. In this chapter, a concise overview of the approaches of preventing progressive collapse is discussed. Relevant studies underlining the importance of slab structure in arresting progressive collapse are also presented. The properties of UHPFRC, its mechanical behaviour under high strain rate and the numerical simulations on low velocity impact test based on work of other researchers are also highlighted.

2.2 Progressive Collapse

There are many interpretations for the term progressive collapse as indicated in Table 2.1. However, there is no unique definition of what constitutes a progressive or disproportionate collapse [8]. Whether a progressive collapse event falls under 'proportionate' or 'disproportionate' category is still debatable among researchers [9-11] but generally all the definitions agree that progressive collapse is initiated by a local failure or damage. Eventually, this local failure sets a chain reaction that leads to a bigger scale of damage or a total collapse of the structure [12-14].

Table 2.1: Progressive collapse definitions.

Definition	Source
Progressive collapse is defined as the spread of an initial local failure from element to element resulting, eventually, in the collapse of an entire structure or disproportionate large part of it.	ASCE [15]
Progressive collapse is defined as an extent of damage or collapse that is disproportionate to the magnitude of the initiating event.	GSA [16]
The spread of local damage, from an initiating event, from element to element, resulting, eventually, in the collapse of an entire structure or a disproportionately large part of it.	Ellingwood *et al.* [17]
Progressive collapse can be defined as collapse of all or large part of a structure precipitated by failure or damage of a relatively small part of it.	Nair [11]
Progressive collapse can be defined as a widespread propagation of structural member failures in which the resulting damage is disproportionate to the original cause.	Kaewkulchai and Williamson [2]

2.2.1 Design Procedures on Preventing Progressive Collapse

Currently, there are three design methods with the aim of reducing the potential for progressive collapse [18], namely

1. Provision of ties between the structural members. This provision falls under *Indirect Design* method. The requirement of this prescriptive approach is achieved by designing the recommended minimum tying force in the slabs (horizontal, transverse and peripheral) and columns (vertical) as shown in Figure 2.1 [19]. The calculation related to the minimum tie forces can be referred to in Clause 9.10 of Eurocode 2 [19].

Figure 2.1: Ties requirement for mitigating progressive collapse [17].

2. The alternate load path method. This *Direct Design* method is attained by the bridging capability of the structural components over the removal of the load-bearing member. The alternate path is adopted to ensure that the excess load is transferred and supported by immediate members typically via membrane or catenary actions. Numerical analyses are performed where one or more primary load-bearing members are notionally removed (one member at a time) and the extent of the collapse progression is checked against the limits. The UK Building Regulation [20] limits the collapse progression following the removal of such element to 15% of the floor area of the storey at risk or 70 m^2, whichever is lesser. On the other hand, EC 1 [21] maintains the same percentage but increases the area to a maximum of 100 m^2 in each of two adjacent storeys.

3. The specific local resistance design method. This direct design method is aimed at enhancing the local resistance of the identified key elements in the structure (column, load-bearing wall and transfer girder) by designing them to withstand a specific abnormal design load. This requirement is employed when tying the whole structure or bridging over the removed key member is not possible and serves as a rational approach when retrofitting certain important elements is required. The complete process involves the structural design (including reversed load) and detailing of the key element together with the connections associated with that element. The UK Building Regulation [20] and EC 1 [21] specifies that such key elements must be able to resist a pressure of 34 kN/m^2 applied in any direction (one direction at a time). However, it is worth mentioning that this design pressure can significantly underestimate a real blast pressure. In the case of the Murrah bombing, the pressure that directly hit the column was estimated to be 10,000 psi [22] or approximately 70,000 kN/m^2.

Apart from these methods, several studies adopting the seismic detailing to mitigate progressive collapse of a building have also been reported [23-25].

2.2.2 Comments on the Effectiveness of the Current Design Codes

History has demonstrated that buildings designed to conventional codes were lacking in the robustness that is necessary to withstand localized damage, partial or even total collapse [26]. However, the reliability of the current design codes and procedures for mitigating progressive collapse of a building has raised arguments among scholars and professionals. Some of the comments are listed in Table 2.2. These comments were highlighted due to the complexity of the progressive collapse mechanism, difficulty in simulating the real dynamic event and the difference in the construction materials.

Table 2.2: Comments on the current progressive collapse mitigation approach.

Comments	Source
The current Tie Force approach in EC 1 is inadequate in increasing the progressive collapse resistance. The basic tie strength requirement is not a reliable theoretical value and underestimates the reinforcement demand. The computational results for a 8-storey frame structure showed that the Tie Force approach was not able to provide adequate progressive collapse prevention when the column at the upper level is removed.	Li *et al.* [27]
Minimum requirements on the resistance to progressive collapse need to be established for different types of construction. The commonly used finite element codes are unable to simulate dynamic collapse problems which contain strong non-linearity and discontinuity that can lead to unrealistic results.	Krauthammer *et al.* [28]
The level of the details in the design codes and standards varies considerably and to literally incorporate every code, standards and guidelines into the structural design process can be difficult.	Baldridge and Humay [29]
Analytical approach would not be able to accurately represent the actual event simply by simulating the sudden removal of a single column or beam. In reality, the sudden removal of the load-bearing element causes a rapid geometric change, resulting in the release of the potential energy, and variation of internal forces that leads to immediate damage to other structural members within the vicinity of that element.	Marjanishvili and Agnew [30]
The codified procedures in the tying method using static calculation for steel-frame building may provide the lower bound estimate of the tying force required to arrest the downwards movement of a damaged bay. The dynamic amplification of the tying force as a result from the additional kinetic energy produced due to the downward movement is not taken into consideration. No specific requirements were provided in order to achieve the sufficient rotational capacity of the joints due to the possible beam rotation under catenary action.	Byfield and Paramasivam [31]

2.2.3 Slab Contribution in the Progressive Collapse Study

A slab is a horizontal member with significantly large and exposed surface area. In a typical building, a slab will only support its own self weight, floor finishes and live load while a beam typically will support a few slabs and a column will support a few beams. From this point, a slab would be the structure bearing the least amount of load compared to the beam or column. As such, the column or any vertical load bearing members are considered to be the key element and the removal of such members is the most common procedure recommended for progressive collapse mitigation [32]. However, the structural robustness is still directly connected to the capability of the structure to redistribute the additional loads and at the same time remain stable making all structural elements to have their unique importance in mitigating progressive collapse.

Mitchell and Cook [33] stated that one of the key measures in preventing the progressive collapse of flat slab structures is to design and detail the slabs in such a way that they are able to develop a secondary load carrying mechanism. This catenary action must be developed after an initial failure occurs at the slab-column joint and the slab is experiencing extremely large deflection. They also noted that factors contributing to the potential punching shear failure at this joint can be due to overload, a design error, a construction error or the loss of a supporting member. Later, they demonstrated the role of a properly anchored continuous bottom reinforcement to withstand the punching shear failure. Finally, they proposed a simple design equation for the provision of the minimum area of an effective continuous bottom bar as well as the detailing procedure of such reinforcement. Similar work concentrating on the need to strengthen the flat slab connection as a means to mitigate progressive collapse can be found in Mullers and Vogel [34], Mirzaei and Sasani [35] and Ruiz *et al.* [36].

Zineddin and Krauthammer [37] raised a concern on the lack of appreciation pertaining to the detailed behaviour of slabs under impact. Their argument is based on the fact that slabs subjected to blast or to a fallen object are exposed to large transient load that is able to induce two possible modes of failure, namely the shear localized failure and the global failure. The global failure, which relates the softening of the moment resisting capacity of the slab, diminishes the slab's ability to transfer forces hence causing the building to lose some degree of lateral stability. Nevertheless, both types of failure could develop into a progressive collapse condition. An example of this type of failure can be seen in the case of the Alfred P. Murrah bombing where the column F/24 (see Figure 1.3) buckled due to the loss of the lateral support and resulted in the collapse of an additional two bays over the full height of the building [38]. An illustration showing the buckling of a column due to the loss of lateral support system is shown in Figure 2.2 [39].

Figure 2.2: Loss of column lateral support system due to blast load [39].

.

Zineddin and Krauthammer [37] investigated the dynamic response of slab specimens with different types of reinforcement details and impact energies under low velocity drop test. The results showed that as the drop height is increased, the local response dominated the behaviour of the slab and increased the probability of punching shear. Less steel reinforcement in the slab induced a brittle failure. They concluded that both the reinforcement details of the slab and the magnitude of the impact energies have to be considered as influential parameters for a possible mode of failure.

Qian and Li [40] raised a concern on the lack of experimental work that incorporates a slab as part of the test specimen when assessing the progressive collapse resistance of a structure due to the sudden removal of a column. Such tests that only consider beam-column sub-assemblages conducted on planar specimens without the presence of monolithic floor slabs and transverse beams will most likely ignore the effect of the slab on the strength of the beams. As a result, a significant underestimation of the vertical force resistance capacity can be expected. In their study, they compared the ultimate load carrying capacity of a floor system with and without a monolithically casted RC slab after simulating the removal of a corner column. The experimental results revealed that by incorporating the slab into the beam-column substructures, the ultimate resistance capacity of the floor system is 40% - 60% higher compared to the frame. They attribute the higher load carrying capacity of the floor system to the function of the slab interacting with the flange of the beam. Finally, they concluded that an extremely conservative result may be achieved by ignoring the contribution of the RC slab in resisting progressive collapse, especially if the construction of the structure involves in-situ casting.

Dat and Hai [41] studied the membrane action of reinforced concrete slabs in mitigating progressive collapse. They raised concern on the dependency of the reserve capacity of catenary action in beams. This argument is based on the fact that the catenary action of the beam is only effective if lateral restraint from adjacent boundary members is adequate. However, when a penultimate-external or penultimate-internal column is removed, the catenary tension forces may pull inwards the perimeter columns. Such condition will only aggravate the progressive collapse. They performed a quasi-static numerical analysis to investigate the membrane behaviour of a beam-slab substructure subjected to a penultimate-internal column loss and compared the results with simply supported slabs with different reinforcement detailing. The numerical results showed that the slab capacity was enhanced by the membrane action in the slab and can achieve twice its flexural capacity. As such, they concluded that the membrane action can be a feasible solution for preventing progressive collapse of building structures under column loss scenarios.

McCann and Smith [42] distinguished the difference between progressive collapse-resistant design and blast-resistant design. The first design concept is system-focused where the whole or a combination of structural members are involved and divided into direct and indirect design method. The latter design concept is element-focused and enhances the toughness, ductility, strength and dynamic characteristics of individual structural elements to air-blast induced loading. Such elements can be slabs, beams or columns that can be made from various construction materials. The direct design method embedded in the collapse-resistant design is similar to the blast-resistant design concept.

They also highlighted the importance of selecting the appropriate member size and material so as to possess some degree of inelastic response and efficient mechanism for energy dissipation due to the extreme nature of the blast loading. The author also presented the maximum response limits for SDOF analysis of a slab developed by the U.S. Army Corps of Engineers Protective Design Centre as shown in Table 2.3 [42]. It is worth mentioning that the maximum support rotation (θ_{max}) showed in Table 2.3 is derived from the plastic deformation of the slab and only to be used in conjunction with SDOF analysis.

Table 2.3: Limit for ductility and support rotation of slab using SDOF model [42].

On the other hand, the guideline for designing a building to resist progressive collapse UFC 4-023-03 [32] provides the modelling parameters and acceptance criteria for two-way slab. The acceptance criteria are also based on the plastic rotation angle. However, the modelling parameters that control the analysis can only be carried out using gravity load.

2.2.4 Studies on the Impact from a Failed Floor System

Vlassis *et al.* [43] reported that the impact from a failed floor is one of the most prevailing progressive collapse initiation mechanisms and can be considered as the limit state requirement in the progressive collapse analysis. In the event where a building is subjected to an internal explosion either accidentally or intentionally, all structural members within the vicinity of the explosion become vulnerable to severe damage, including the slabs.

The authors admitted that it would be a great challenge to design a floor system capable of arresting progressive collapse due to a failed floor impact in view of the significant kinetic energy acquired by one or more floors following failure. However, under specific circumstances (number of failed floors, energy loss upon impact and the strength of the lower floor) it is still possible for the lower structure to contribute in preventing progressive collapse. In arresting the progressive collapse, the ability of an impacted floor is directly linked to its energy absorption characteristic. The authors then proposed a new design-oriented methodology for the progressive collapse assessment of floor systems within multi-storey buildings subject to impact from an above failed floor.

Using a seven-storey steel frame grillage model and the impact of a failed floor as an independent event, they established the pseudo-static response of the floor based on the estimated energy transfer associated with the specific characteristic of the impact event. The analytical procedure started with calculating the anticipated range of kinetic energy transferred from an impacting floor to the floor below based on the nonlinear static response approach. Static load-deformation curves and dynamic demand for the impacted floor was established at this stage. The least demanding impact scenario was taken as the impact from a falling floor that carried half of the impacted floor gravity load and only 20% kinetic energy being transferred. Later, the linear static load-deformation response was modified using the pseudo-static response to account for the effect of the initial deformations of the lower floor under the gravity load. The capacity of the impacted floor based on the calculated kinetic energy transfer was then established. The results from the analytical simulation showed that within all the impact scenarios being considered, the ratio of the impacted floor capacity/demand never exceeded one. They concluded that a floor system within a steel-framed composite building has limited opportunity to arrest the impact from an upper floor even in the least demanding impact scenario where the capacity only marginally exceeds half its dynamic demand.

Kaewkulchai and Williamson [2] used a computational planar framework that accounts for the change of structural properties and configurations of a damaged structure to investigate the potential of progressive collapse initiated by an impact of a failed member. They highlighted that when a building is subjected to an abnormal loading condition such as blast, other structural members such as beams could fail and move independently from the main structure. This beam can fall down and impact another beam below with a large dynamic force and likely to be one of the key reasons causing the collapse of the building as shown in Figure 2.3 [2].

Figure 2.3: Impact of a failed member on a structure due to blast load [2].

They used a five storey 2-D frame model as shown in Figure 2.4 (a). In the simulation, a non-impact, impact with load only and impact with load as well as velocity were considered. The two possible impact scenarios are shown in Figure 2.4 (b) and (c). The beams and columns were assigned with the appropriate sizes and respective yield moments as well as maximum force capacities. The failure was set when the response exceeded these maximum values.

(a) (b) (c)

Figure 2.4: Computational planar framework for assessing progressive collapse showing (a) five-storey 2-D model under consideration; (b) one end of a failed beam impacting on another beam; (c) a beam member failed at both ends impacting on another beam [2].

By plotting the moment histories for the impacted beam, they showed that the internal moment for Beam A was magnified eleven times higher than the yield moment when both the load and velocity were taken into account resulting in progressive collapse. A non-impact or impact with load only showed insignificant increase in the internal moment. However, the effect of impact considering the load and velocity did not affect the internal force of Column B significantly as the impact energy was reported to have dissipated through the plastic deformation of the failing beams. They concluded that the velocity of a failed member impacted onto an intact member played the most important role in the collapse process.

Strassosek [44] proposed the methods to avoid disproportionate collapse of tall buildings with tube structure based on five general approaches namely non-structural protective measures, specific local resistance, alternative paths, isolation of collapsing sections and prescriptive design rules. In the specific local resistance approach, the author considered the tube structure as the primary load transfer system and provided several recommendations on the detailing of the tube structure with regards to the minimum thickness, reinforcement type, opening, location and operational safety. The floors cantilevering from the tube were considered as the secondary load transfer system and the failure of these floors can lead to a pancake-type progressive collapse. As shown in Figure 2.5 [44], in the case where a local failure of a floor occurred, the impacted floor must be able to arrest a progressive failure by transferring the impact energy as little as possible to another floor below. According to the author, this mechanism can be achieved by designing the plastic hinge of the impacted floor with sufficient rotational capacity. As such, the impacted floor will deform until it touches the tip of the floor below and reduce the impact energy.

Figure 2.5: Assumed damaged and admissible deformation in secondary load transfer of one floor to another floor below [44].

2.2.5 Summary

Current design methods mainly focus on the performance of the key elements such as columns and load bearing walls to arrest progressive collapse. However interest has also been shown by other researchers in investigating the contribution and performance from slab structures for the same purposes. This concern was raised due to the fact that an impact from a failed floor member onto another floor system is able to cause a devastating effect and has been highlighted in a number of studies in the open literature.

2.3 UHPFRC as a High Energy Absorption Material

The design philosophy for a structure to withstand an abnormal loading condition such as blast load is to increase the energy absorption capacity of its structural element [45]. Cavill *et al.* [46] performed blast tests using conventional explosive on seven *Ductal* panels, a patented material and proprietary name for UHPFRC. This material is reported to exhibit compressive strength of 160-200 MPa and flexural strength of 30-40 MPa. The dimensions of the panels were 2 m by 1 m with varying thickness. Pre-stressing strands were also incorporated in five of the panels. In the blast test that involved detonation of 5 tonnes of bare charge (equivalent to six tonnes of TNT), the panels were placed at a stand-off distance of 30 m, 40 m and 50 m accordingly. All *Ductal* panels showed remarkable results showing significant deflection (high ductility) up to span/28 and no significant damage or fracture compared to the conventional reinforced concrete (RC) panel. The *Ductal* panel without pre-stressing strands was reported to have fractured but without any sign of fragmentation. Some of the photographic results are shown in Figure 2.6.

(a) (b)

Figure 2.6: UHPFRC protective panel test results for (a) 100 mm thick panel at 30 m stand-off distance showing no damage; (b) 50 mm thick panel at 50 m stand-off distance with shallow crack and no fragmentation or spalling [46].

Barnett *et al.* [47] tested four one-way UHPFRC panels measuring 3.5 m by 1.3 m width by 100 mm thick using an explosive charge equivalent to 100 kg TNT. The variables of the test are shown in Table 2.4. A shorter stand-off distance between 7-12 m was selected in order to ensure failure of the panels.

Table 2.4: Variables of the blast test [47].

The results showed that all UHPFRC panels deflected and cracked when exposed to such load, panel C being the weakest of the four panels. They highlighted that despite the severe cracking, panel C remained standing and no spalling was observed on the rear face as shown in Figure 2.7 [47]. Spalling and the creation of shrapnel can cause serious injury and these features are among the primary concern in blast resistant structure. They concluded that UHPFRC panels exhibited the properties which make it suitable for resisting explosions and potentially be used to protect people and buildings from blast.

(a) (b)

Figure 2.7: UHPFRC panels subjected to blast loading showing (a) minor crack in panel A; (b) severe crack in panel C [47].

Kim *et al.* [48] performed blast tests on 1 m by 1 m by 150 mm thick Reactive Powder Concrete (RPC) slabs containing only 2% short fibres and Ultra-high Strength Concrete (UHSC) containing equivalent steel reinforcement ratio. The control specimen was the ordinary RC slab, also containing 2% steel reinforcement ratio. The explosive charge used in the main test and stand-off distance was 35 lbs ANFO (28.7 lbs TNT equivalent) and 1.5 m, respectively. All specimens were placed at the same ground level and the edges were clamped. The RPC showed the least amount of deflection. The crack pattern of the loaded specimens is shown in Figure 2.8 [48]. In this test, they noted the failure mode of the RPC slab where the resistance capacity of RPC and UHSC showed an increase of 35.9% and 30.9% over the NSC, respectively and concluded that both UHSC and RPC possessed more resistance to blast loading than RC slabs.

(a) (b) (c)

Figure 2.8: Surface examination of the specimen showing (a) well dispersed turtle back type crack pattern for NSC (b) macrocracks concentrated near or on the yield lines for UHSC; (c) predominantly one directional centre bisecting type macrocracks for RPC [48].

2.3.1 Behaviour of UHPFRC under High Strain Rate

Millard *et al.* [49] investigated the dynamic increase factor (DIF) of plain concrete and UHPFRC under both flexural and shear high speed loading test. The results for the flexural test conducted at the University of Liverpool were combined with the results obtained at the Royal Melbourne Institute of Technology for comparison purposes. The strain rate range for the dynamic flexural tests was between 1×10^{-2} and 1×10^{1} s^{-1}.

They reported that the UHPFRC showed DIF of about 1.5 and 2.5 for 2% and 1.5% fibre content, respectively. However, the DIF was not significantly influenced at 6% fibre content. The relationship between the DIF and strain rate from the test was plotted together with the modified CEB formulation proposed by Malvar and Ross [50] and Tedesco and Ross [51] as shown in Figure 2.9 [49]. They concluded that the modified CEB formulation can be used to predict the DIF enhancement for UHPFRC at strain rates above 1 s^{-1}.

Figure 2.9: Dynamic increase factor for UHPFRC in flexure [49].

In the dynamic shear testing, they reported that there was no significant DIF that can be attained with the increase in the peak stress as shown in Figure 2.10 [49] and as such, no DIF should be used to increase the shear strength at high loading rate.

Figure 2.10: Dynamic increase factor for UHPFRC in shear [49].

Habel and Gauvreau [52] presented the experimental and analytical study on UHPFRC subjected to static and low velocity drop test. In addition to the four-point static bending test and three-point dynamic bending test, they also performed direct tensile tests at varying strain rate to investigate the strain rate sensitivity of UHPFRC under tensile loading. The results showed that at higher strain rate, the UHPFRC specimen exhibited higher maximum tensile strength, approximately 25% compared to the static test as shown in Figure 2.11 (a) [52]. In addition, the fracture energy, taken as the area under the graph during softening stage was also increased at higher strain rate as shown in Figure 2.11 (b) [52].

(a) (b)

Figure 2.11: UHPFRC under tensile behaviour showing (a) linear-elastic and strain hardening part; (b) strain softening part [52].

Rong *et al.* [53] investigated the dynamic compression behaviour of plain and ultra-high performance cement based composites (UHPCC). The dynamic compression tests were carried out using a Spilt Hopkinson Pressure Bar (SHPB) set-up on cylinder specimens measuring 70 mm in diameter and 35 mm thickness. Based on the test results, they reported that the peak stress and ultimate strain of the UHPFCC increased with the increase in the strain rate as shown in Figure 2.12 [53]. Furthermore, increase in the strain rate also showed a beneficial effect on the toughness of UHPCC as it increases the area under the curve for the descending branch. As such, this material has a great prospect to be used for explosion and penetration resistant structures.

(a) (b) (c)

Figure 2.12: Dynamic compression stress-strain curves for UHPCC with (a) 0%; (b) 3%; (c) 4% fibre volume [53].

2.3.2 Tensile Stress-Strain Response of UHPFRC

The tensile stress-strain response of UHPFRC is a basic constitutive property [54] and reliable knowledge of the response is necessary when performing numerical analysis. Several researchers have used a 3-phase tensile stress-strain relationship to describe the behaviour of UHPFRC under tensile loading [55]. On the other hand, Graybeal *et al.* [56] used an idealized 4-phases tensile stress-strain relationship as shown in Figure 2.13. The 4-phases of the tensile behaviour of UHPFRC are detailed as follows:

Phase I (Elastic Phase) – initiation of the tensile behaviour up to the cracking stress (σ_c);

Phase II (Multiple Cracking Phase) – continuous cracking of the cementitious matrix and distributed within the specimen but without significant widening of individual cracks and characterized by a nearly constant stress level. Fibres can carry large tensile force compared to the matrix hence developing a large number of distributed microcracks. As such, the activation and effectiveness of this stage requires adequate amount of fibre content to be incorporated into the mix;

Phase III (Crack Straining Phase) – accumulation of strain within the existing set of microcracks but unlikely to generate additional cracks. This pseudo-plastic phase increases the stress up to the maximum tensile strength (f_t) as a result of the increase of the elastic strain in the fibres. The end of this phase marks the maximum tensile strength of the specimen; and

Phase IV (Localisation) – conversion of microcracks to macrocracks takes place where the fibres effectively bridge the widening of individual macrocracks until the fibres reach interface debonding and fibre pull-out. This phase reflects the primary reinforcement mechanism of the fibres that significantly improve energy absorption capacity while ensuring the ductility of the UHPFRC.

Figure 2.13: Idealised tensile mechanical response of UHPFRC divided into 4 phases, namely (a) elastic; (b) first cracking; (c) crack saturation; (d) localisation [56].

2.3.3 Influence of Fibres on the Impact Resistance of Concrete

Reinforced concrete is said to be the second best stand-alone material to steel in its ability to withstand blast overpressures, mostly due to its mass [57]. This statement is particularly true if the reinforced concrete element is relatively thick and the reinforcement ratio is relatively high. However, thicker structural elements used in a building that need to be designed under abnormal load can increase the self-weight significantly leading to an increase in the overall construction cost. As failure of slabs can also trigger a progressive collapse under blast effect it would be impractical to thicken the reinforced concrete slab due to the fact that the concrete volume for the slab is the highest compared to a beam or a column. The example given by BCA Singapore [58] showed that for a 24-storey building, slab construction can be as high as 77% of the total concrete volume. Adding fibres to the concrete is one of the possible ways to overcome this problem.

Sukontasukkul *et al.* [59] tested plain and fibre concrete circular plates under concentric flexural drop test. Three types of fibres namely steel, polypropylene and carbon fibres were used. For the fibre reinforced concrete (FRC) specimens, the fibre content was kept at 1% by volume either using a single fibre type, combination between steel and polypropylene or combination between steel and carbon fibres. The results showed that all FRC specimens, excluding the carbon fibre mix, exhibited 6-8 times higher energy absorption capacity compared to the plain concrete. They also reported that the hybrid FRC system did not show any significant improvement in the energy absorption capacity compared to using only steel fibres. Similar results were also reported by Swamy and Jojagha [60] and Nataraja *et al.* [61]. Mindes and Yan [62] concluded that the superiority of the steel fibre reinforced concrete over the polypropylene fibre reinforced concrete was attributed to its significantly higher elastic modulus (by a factor of about 20).

An investigation of the individual effect of silica fume or steel fibre and the combined effect of adding both materials on the impact performance of high strength concrete (HSC) under dynamic loading was carried out by Yan *et al.* [63]. They reported that the dynamic performance of HSC under repeated impact improved significantly under the influence of fibre rather than the silica fume. Under the repeated impact test, the number of blows to rupture increased from 235 for HSC to 400 for HSC/Silica Fume and 3,896 for HSC/Steel Fibre. Nevertheless, the combined effect of HSC/Silica-Fume/Steel Fibre showed the highest resistance where the number of blows to rupture was recorded to be 6,779. Similar trends were also reported for fatigue testing. The combining effect started with the ability of the silica fume to improve the interface structure of HSC and enhancing the interfacial bond strength thus greatly increasing the present ability of the fibres to restrain cracking.

From an experimental study on the penetration resistance of high strength fibre concrete subjected to projectile impact, Zhang *et al.* [64] found that the effectiveness of incorporating fibres arises from the bridging effect of the fibres at the crack zones. The presence of fibres was able to reduce the crater diameter by 40-80% than that of the plain concrete specimens, restraining the crack propagation beyond the crater region and preventing the specimens from splitting. Similar work conducted by Luo *et al.* [65] also showed that the penetration resistance of reinforced high strength concrete (RHSC) was increased significantly by the inclusion of fibres into the matrix. Their experimental results showed that the RHPC targets were broken thoroughly into several pieces although being impacted with projectiles at low velocity, while the RHPC with fibres remained intact and only radial cracks were present on the impacted face. The inclusion of fibres restrained the crack propagation by the bridging effect and thus changing the failure mode from brittle to pseudo-plastic. Further information on the effect of adding fibres to plain or reinforced concrete subjected to projectile impact can be found in Maalej *et al.* [66] and Dancygier *et al.* [67].

Masuya *et al.* [68] performed low velocity drop tests on plain and steel fibre reinforced concrete (SFRC) slabs. The variables were the slab thickness (40-60 mm) and the fibre content (0-1%). The slabs were impacted at the centroid using 10.77 kg mass and the drop height was maintained at 1.5 m for all cases. They evaluated the performance of the slabs and reported that the SFRC slabs were not showing any sign of scabbing (only shear plug) compared to the plain concrete that shattered into pieces upon failure. The energy required to perforate the SFRC was found to be 3-8 times higher than plain concrete. Furthermore, they also modified the available semi-analytical formula developed by Chang [69] to suit the incorporation of fibres into the slab and proposed a relationship between the thickness of the slab and the energy to complete the perforation under a single impact as

$$e = \left(\frac{V_0}{v_i}\right)^{0.25} \left(\frac{m{v_i}^2}{df_c}\right)^{0.5} \left(1 + 5.39V_f\right)^{0.38} \tag{2.1}$$

where

V_0 = standard impact velocity (60.96 m/s),

v_i = measured impact velocity (m/s),

m = mass of the impactor (kg),

d = diameter of the impactor (m),

f_c = compressive strength of the slab (N/m^2), and

V_f = fibre volume (%).

Ong *et al.* [70] also reported that concrete slabs reinforced with steel fibres exhibited higher fracture energy, superior performance against cracking characteristic and resistance to shear plugging followed by concrete with polyvinyl alcohol (PVA) and polyolefin fibres, respectively. The important factor that controlled the performance of these fibre reinforced concrete specimens was associated with the mechanism of the fibre failure mode where steel and PVA fibres failed by pull-out alone and polyolefin fibres failed by both pull-out and rupture. Wang *et al.* [71] experimental work on the fibre mode of failure also reported that fibres have a greater tendency to rupture under impact load unless the fibre volume is high enough to resist all the tensile force transferred from the concrete at the crack. Although higher fibre volume can improve the fracture energy, no significant increase can be expected in the compressive strength. Finally, Bindiganavile and Banthia [72] in their study on the fibre-matrix bond showed that the preservation of pull-out failure mode resulted in a vast improvement in its dynamic performance compared to fibres that fractured. They also concluded that concrete with higher strength matrix increased the bond energy and favours those fibres which pull out completely under impact loading.

Lok and Pei [73] performed an experimental investigation to study the impact resistance and ductility of simply supported reinforced steel fibre concrete square slabs under repeated concentric impact. The variables for the test were the slab thickness (50 mm and 70 mm), the reinforcement (plain, welded mesh or steel fibre) and the characteristic of the fibre (aspect ratio and end condition). They reported that the slabs with fibres were able to resist higher number of blows compared to plain concrete and concrete reinforced with welded mesh. However, the aspect ratio and end condition of the fibres (e.g. hooked ends) showed less influence on the impact resistance where insignificant increase in the number of blows was observed. The ductility of the fibre reinforced concrete also was calculated to be as high as 23-33 times higher compared to the plain concrete and 0.94-9 times higher than the concrete reinforced with welded mesh. The authors also suggested using only 50% of the maximum displacement of each panel in order to calculate the ductility ratio for repeated impact condition although they acknowledged that such an approach could lead to conservative values.

Zhang *et al.* [74] presented an experimental study to evaluate the damage and failure mode of full scale blast shelter hybrid-fibre engineered cementitious composite (ECC) panel under repeated concentric low velocity projectile impact test. The results were compared to the FRC (1% fibre volume) and commercially available reinforced concrete RC blast shelter. The hybrid ECC material was prepared using reinforcing bars, 0.5% steel and 1.5% polyethylene fibre and the concrete grade was maintained at 40 MPa for all specimens. They reported that the ECC panels exhibited smaller indentation depth and crater size compared to FRC and RC. Furthermore, the ECC panels also showed higher residual strength and impact resistance under multiple impacts where the ECC panels suffered less damage per impact as indicated in the trend line of the peak impact force in Figure 2.14 [74]. The authors viewed that the dramatic drop in the gradient shown by the FRC100 and RC100 panels was the result of the greater internal damage leading to earlier reduction in the stiffness for every impact number. In a study on the residual strength of a carbon composite under repeated impact, Wyrick and Adams [75] also expressed the same view and explained that the previously damaged material in the specimen cushioned the impactor during the next impact. However, it is worth mentioning that the magnitude of the peak force is also governed by the amount of impact energy absorbed by the specimen. Obviously, lower impact energy will result in lower peak force.

Figure 2.14: Peak load against number of impacts for various types of concrete [74].

2.3.4 Summary

UHPFRC, shown through several experimental studies involving blast loading, exhibits high energy absorbing capacity compared to other types of concrete. The failure pattern of UHPFRC material due to blast loading not showing spalling or fragmentation adds to the value of this material for the protection of people and buildings. The remarkable performance of UHPFRC material is through the fibre bridging capacity. Similarly, under multiple low velocity impact tests, UHPFRC shows high impact resistance and residual strength.

2.4 Numerical Simulations

Analytical and finite element modelling of UHPFRC structures under dynamic loading involves complex analysis, assumptions and in-depth investigation of the UHPFRC material properties itself. Nevertheless, to overcome the cost of conducting experimental work related to impact or blast that are often expensive and difficult, numerical simulations using finite element analysis have increasingly become important and relevant in engineering.

2.4.1 Spring-mass Model

Spring mass models are generally used to simplify the analysis of the dynamic response event either under high or low velocity impact. The basic spring-mass system comprises a force, a mass and a spring, commonly known as the single-degree-of-freedom (SDOF) system. Hrynyk and Vecchio [76] commented that SDOF models are often unsuitable for impact simulation. The argument was based on the experimental results showing non-uniform distribution of the specimen acceleration both in terms of magnitude and shape over the duration of impact. As such, the slab inertia forces that contributed to the loading distribution differ significantly from those developed under static loading. They also noted that the unsuitability of the SDOF model is obvious when punching shear dominates the failure mode.

On the other hand, Habel [77] used the SDOF model to predict the dynamic response of a slab strip with UHPFRC overlay subjected to low velocity impact. The spring-mass model is shown in Figure 2.15 [77].

Figure 2.15: Single-degree-of freedom (SDOF) model [77].

The governing equation of motion is given by

$$m_b \frac{d^2 u_B}{dt^2} + R_B(u_B, t) - F_{DW}(t) = 0 \quad (2.2)$$

The mass m_b corresponds to the equivalent slab strip mass based on the deflected shape function while the drop weight force F_{DW} was directly obtained from the test result. In addition, the non-linear spring constant R_B was obtained from the static test by adjusting the force values with a scalar but keeping the deformation values unchanged. The parameters for the SDOF model such as the stiffness, and the maximum resistance were obtained directly from Biggs [78]. As the SDOF model did not consider damping effects, only the first deflection rise (the maximum deformation) can be simulated. This approach is suitable to be used in order to avoid a more complex SDOF model. Damping effects can be ignored in the case of impact loading because the response of the structural member will occur almost immediately and no damping can be invoked [79]. The SDOF model adopted by Habel [77] was able to produce good correlation with the experimental work at predicting the deformation-time and acceleration-time relationship at mid-span. Successful usage of SDOF model for simulating the response of test specimens subjected to impact loading were reported by Zhang *et al.* [74], El-Dakhani *et al.* [80], Fisher and Haring [81], Hussein [82] and Schleyer *et al.* [83].

Fujikake [84] proposed a two-degree-of-freedom (TDOF) spring-mass-damper system for low velocity drop test on reinforced RPC beams as shown in Figure 2.16 [84].This model is reported to be able to predict the global response of the beam and the local response at the contact point and the drop hammer although not showing good agreement for predicting the peak force. In order to use this model, several assumptions were highlighted such as:

i) the deformation rate of the RPC beam at midspan is equal to the initial velocity of the drop hammer;
ii) the contact force-local deformation relationship was taken as linear as opposed to the Hertz contact theory

$$P = k\delta^{3/2}; \quad (2.3)$$

iii) shear effect is ignored; and

iv) the damping coefficients c_1 and c_2 were taken as proportional to stiffness following the Rayleigh Damping equation.

Figure 2.16: Two-degree-of-freedom (TDOF) spring-mass model [84].

2.4.2 Finite Element Model

Finite element modelling is one of the several numerical methods that can be used to solve the response of solids under dynamic loading conditions. In this approach, any complex structure is discretized into a finite number of small elements (mesh) with fixed number of nodes and defined boundaries to which loads and boundary conditions can be applied. The discretization of the structure and the fields associated with the structure is performed using computational points in space, connected to each other through the computational elements. In general, there are three basic types of element or mesh [85] namely:

i) 1-D elements (line or beam) – assigned to line features and generally suitable for structural members where the cross section dimensions are smaller than the length. The parameters involved are axial forces (line element only), bending moment, shear force and torsion (beam element).

ii) 2-D elements (plate and shell) – assigned to surface features and generally suitable for flat or curved structures where the thickness of such structures is relatively much smaller than the length or width. The analysis covers out of plane forces and moments (plate) and in-plane forces (shell). 2-D continuum meshes (plane stress and plane strain) are assigned to 2-D surface features that represent a section through a 3-D structure. 2-D elements can have triangular, rectangular or quadrilateral shape.

iii) 3-D continuum elements or solid elements (tetrahedral and hexahedral) – used when it is necessary to model the actual geometry of the structure where detailed analysis is required and cannot be represented by other types of mesh. Each node in the 3-D element has three translational degrees of freedom and can deform in all three directions in space.

The continuum mechanics in FEM adheres to two basic types of formulation of motion namely Lagrangian and Eulerian [86]. In the Lagrangian formulation, individual nodes in the mesh move and deform with the material during motion. This formulation is ideal for analysing the motion and deformation of material where relatively low distortion and possibly large displacement can be expected. However, the disadvantage of this formulation is its inability to follow large distortions where the mesh can be tangled in an extremely deformed region which can significantly affect the accuracy of the results. On the other hand, Eulerian formulation fixes the computational nodes and meshes while the material flows through the grid. As such, this formulation is generally suited for material behaviour exhibiting severe deformation such as fluids and gases. Although Eulerian formulation can be used to describe solid behaviour, additional computational work is required to transport the solid stress tensor and the history of the material through the grid.

The numerical simulation of a dynamic system requires efficient algorithm of time-dependent integration. Generally, there are two basic types of step-by-step integration method namely, implicit and explicit [87]. Implicit time integration requires updating and reconstructing of an effective stiffness matrix causing a much larger and intensive computational effort. However, the solution from this approach is stable even at large time steps. As such, implicit integration is more suitable for handling quasi-static and cyclic loading where larger time steps can be utilized without affecting the accuracy of the results. On the other hand, explicit method solves the acceleration vector hence bypasses the inversion of the complex stiffness matrix. This approach is conditionally stable only if the time-step size is smaller than the critical time step for the structure being simulated. The small time-step size requirement in explicit integration for stability purposes makes the method useful for handling very short-duration events or dynamic forces such as blast and impact.

In FEM involving impact, the two bodies that came into contact during impact can also lose contact upon impact. As a result, there will be some changes of contact status and loading that is applied on the boundary of the element [88]. Consequently, a suitable contact algorithm that is able to track the contact locations and accounts for the change in the boundary location is required. In general, there are two basic formulations to handle the contact problems namely, the penalty method and Lagrange multipliers method. The penalty method allows small interpenetration at the target surface and introduces a force with the purpose of eliminating the penetration [89]. This method is suitable for use in dynamic problems where the velocity field is time-continuous. This method also maintains the number of unknowns in the algorithm by enforcing the contact constraints. As such, the arrangement of equations remains positive definite, making the penalty method fit well into an explicit time integration of an impact analysis. The Lagrange multiplier fulfills the contact constraint almost perfectly but it involves the introduction of additional variables that will increase the matrix size and can lead to an ill-converging solution.

A number of studies involving finite element modelling of UHPFRC material under static loading can be found in the open literature. Mahmud *et al.* [89] performed finite element analysis (FEA) using plane stress elements to study the size effect on UHPFRC beams subjected to static bending load. The non-linear FE simulations were carried out using the

Concrete Damage Plasticity (CDP) model in ABAQUS software. They reported that both the numerical and experimental studies showed insignificant size effect on the nominal flexural strength of those beams and the CDP model can be used to represent the material properties of UHPFRC under static loading. Fairbain *et al.* [90] performed experimental and numerical work on UHPFRC plates and shells. The FE analysis was performed using TNO-Delft DIANA commercial code utilising a Drucker-Prager Plasticity model and reported to give good correlation with the experimental results in terms of the load-deflection and crack pattern. Similar work on the numerical modelling of UHPFRC under static loading can be found in Le [91], Azzawi *et al.* [92] and Chen and Graybeal [93].

Mao *et al.* [94] simulated the performance of four UHPFRC panels subjected to blast load using the explicit non-linear finite element program LS-DYNA. In the simulation work, the effect of steel fibre orientation was not considered and the steel fibre was not modelled explicitly. They adopted the Karagozian & Case (K&C) concrete model and 20 mm × 20 mm × 5 mm solid elements to analyse the UHPFRC response to blast load. As the automatic parameter generation in the K&C model is based on test data from normal strength concrete with uniaxial compressive strength of 45 MPa, they calibrated and modified several parameters to reflect the material behaviour of UHPFRC. The stress-strain relationship in the K&C model was modified by calibrating the parameter b_2 that controlled the softening of the material in tension. The default value for parameter b_1 that controlled the softening for compression was used directly without modification.

Using a single element analysis, they compared the stress-strain relationship developed using modified b_2 parameter and the idealized stress-strain relationship of UHPFRC from tensile test. They reported that the modified curve matched the idealized curve although not able to simulate the hardening behaviour clearly. They also mentioned that the parameter b_2 should be changed accordingly for different element sizes in order to obtain the same stress-strain relationship, otherwise the computed energy release will be incorrect. In their study, the fracture energy of UHPFRC was adjusted to match the idealized stress-strain curve. The finite element model was able to predict the peak blast pressure and the blast impulse with good accuracy. The maximum and permanent deformations as well as the damage of the UHPFRC panels were predicted with good accuracy in most of the cases. However in one of

the simulations, the predicted damage produced a larger difference from the actual experimental data.

Gopinath *et al.* [95] performed finite element analysis on ultra-high strength concrete (UHSC) panels containing hooked-end fibres subjected to low velocity drop test. The numerical simulation utilised the non-linear dynamic finite element code ABAQUS. The UHSC was modelled as plain concrete while the fibres were incorporated explicitly and randomly orientated as shown in Figure 2.17 [95]. However, the details of the concept and technique to randomly disperse the fibres in the 3-D concrete model were not discussed. A brittle cracking model incorporating the elasto-plastic behaviour of the material was used to define the failure where the brittle cracking strain was set as the input parameter. This approach enabled the peak acceleration of the panel to be predicted with good agreement although it was not able to predict the whole acceleration-time history of the panel. No other comparison was made with the experimental results such as the deformation or the peak force. As such, the credibility of this approach is difficult to justify.

Figure 2.17: 3-D finite element model for the UHSC containing distributed fibres [95].

Sovjak *et al.* [96] simulated the response and damage of HSC, FRC, UHPC and UHPFRC slab damage due to high velocity small projectile impact. The numerical analysis was carried out using AUTODYN software employing RHT (Riedel, Hiermaier and Thoma) concrete model that was reported suitable to simulate the behaviour of brittle materials under short time loading. The RHT concrete model consists of three different pressure dependant surface; elastic, failure and residual strength that takes into account the material strength increase with an increasing hydrostatic pressure. The model also incorporated the effects of strain rate and strain rate hardening. Default parameters for grade 35 and grade 140 concrete were provided in the model.

Sovjak et al. [96] followed Tu and Lu [97] on the recommendations to calibrate the RHT input parameters as shown in Table 2.5 [96]. The results obtained by the numerical simulations predicted the experimental residual velocity of the non-deformable projectile and the damage patterns on the slabs with good agreement. Finite element simulations and validation employing modified RHT concrete model to predict the response of concrete under high velocity or blast loading can be found in Tu and Lu [97], Tham [98], Leppanen [99], Nystrom and Gylltoft [100], Reidel [101], Berg and Preece [102] and Hasson and Skoglund [103].

Table 2.5: RHT input parameters for UHPFRC subjected to high velocity impact load [96].

2.4.3 Summary

It was noted that both SDOF and TDOF models can be used to predict the response of slabs subjected to dynamic loading including the low velocity impact test. While the SDOF model is only able to predict the deformation values, the approach is simplified and has been used for predicting the response of fibre reinforced concrete with reasonable agreement. Several works involving FEA to simulate the response of UHPFRC under static and dynamic loading were reported. Under dynamic loading conditions, the RHT concrete model and the K&C model were reported to be able to represent the material behaviour of plain and fibre-concrete subjected to blast loading. Both material models represent the advancement from the plasticity damage model and developed based on the behaviour of plain concrete under high strain rate loading. Although the input parameters in the K&C model can be automatically generated from a single compressive strength value, the material model was developed based on grade 45 concrete. As such, the representation of high strength concrete including UHPFRC materials may require extensive calibrations. Modifying only the input parameter b_2 together with the fracture energy in order to match the stress-strain relationship in tension may be inadequate to express the overall behaviour of UHPFRC material. RHT concrete model provided two sets of default parameters to show a clear distinction between the behaviour of normal and high strength concrete under high strain rates. A number of successful simulations and recommendations on the approach to modify the input parameters have been reported in the open literature. Nevertheless, the RHT concrete model, similar to other material models, also requires modification before it can be used to represent UHPFRC material.

2.5 Summary of Chapter 2

The review of previous work strongly suggests the need to explore new ideas and innovations focusing on the resistance of a structure subjected to abnormal loading as a result of the complexity of the progressive collapse event that can be on a case by case basis. Significant interest has been raised to explore the contribution of the slab or floor system in its ability to arrest progressive collapse. However, the experimental work was limited to a single type of impact and only performed on undamaged specimens. In the event of an internal blast in a building, the slab will be damaged but may still be able to withstand impacts from failed members. Consequently, this work will address the contribution of the slab to arrest progressive collapse under this condition by investigating the performance of pre-damaged UHPFRC slabs subjected to low velocity impact. UHPFRC material is selected due to its superior mechanical performance and ability to absorb high impact energy compared to other types of concrete.

In reality, the impact from a failed member onto another member can take place at any location and at various contact angles. These conditions may set different types of risks for triggering a progressive collapse and need to be better understood. Currently, impact studies on slabs or panels have only focused on concentric impact. As such, this work will investigate the sensitivity of the impact location and angle by setting the impact at various locations as well as introducing an oblique contact condition.

The reviews also noted the limited information on the concrete model to represent UHPFRC material under low velocity impact. Although RHT concrete model has been used to represent the UHPFRC materials, the simulations were carried out under high velocity projectile impact and blast loading. Moreover, the method to calibrate the input parameters for RHT is not extensively described. Therefore, the finite element simulation in this work will use RHT concrete model where several of the input parameters will be calibrated from available test data.

2.6 References

[1] D. A. Taylor, "Progressive collapse," *Canadian Journal of Civil Engineering*, vol. 2, no. 4, pp. 517-529, 1975.

[2] G. Kaewkulchai and E. B. Williamson, "Modeling the impact of failed members for progressive collapse analysis of frame structures," *Journal of Performance of Constructed Facilities*, vol. 20, no. 4, pp. 375-383, 2006.

[3] M. Rebentrost and G. Wight, "UHPC perspective from a specialist construction company*,"* presented at the International Workshop on UHPFRC, Marseille, France, Nov. 17-18, 2009, pp. 1-9.

[4] E. Bruhwiler, "Improving safety and durability of civil structures," in *Damage Assessment and Reconstruction after War or Natural Disaster, A. Ibrahimbegovic* and M. Zlatar, Eds, Dordrecht: Springer, 2008, pp. 63-93.

[5] N. H. Yi, J. H. J. Kim, T. S. Han, Y. G. Cho and J. H. Lee, "Blast-resistant characteristics of ultra-high strength concrete and reactive powder concrete," *Construction and Building Materials*, vol. 28, no. 1, pp. 694-707, 2012.

[6] A. E. Naaman and K. Wille, "The path to ultra-high performance fiber reinforced concrete (UHP-FRC): five decades of progress," in *International Symposium on UHPC and Nanotechnology for High Performance Construction Materials: Proceedings of 3rd Hipermat*, Kassel, Germany, M. Schmidt, E. Fehling, C. Clotzbach, S, Frohlich and S. Piotrowski, Eds. Kassel University Press, 2012, pp. 3-16.

[7] M. Alhadid, A. M. Soliman, M. L. Nehdi and M. A. Youssef, "Critical overview of blast resistance of different concrete types," *Magazine of Concrete Research*, vol. 66, no. 1-2, pp. 72-81, 2014.

[8] M. Haberland and U. Starossek, "Progressive collapse nomenclature," presented at the ASCE SEI Structures Congress, Austin, Texas, Apr. 30- May 2, 2009, pp. 1888-1895.

[9] D. V. Val and E. G. Val, "Robustness of frame structures," *Structural Engineering International*, vol. 16, no. 2, pp. 108-112, 2006.

[10] O. A. Mohamed, "Progressive collapse of structures: Annotated bibliography and comparison of codes and standards," *Journal of Performance of Constructed Facilities*, vol. 20, no. 4, pp. 418-425, 2006.

[11] R. S. Nair, "Preventing disproportionate collapse," *Journal of Performance of Constructed Facilities*, vol. 20, no. 4, pp. 309-314, 2006.

[12] T. D. G. Canisius, J. D. Sorensen and J. W. Baker, "Robustness of structural systems– a new focus for the joint committee on structural safety (JCSS)," presented at the 10th International Conference on Application of Statistic and Probability in Civil Engineering, Tokyo, July 31-Aug. 3, 2007, pp. 1-8.

[13] J. Agarwal and J. England, "Recent developments in robustness and relation with risk," in *Proceedings of the ICE-Structures and Buildings*, 2008, vol. 161, no. 4, pp. 183-188.

[14] U. Starossek and M. Haberland, "Disproportionate collapse: Terminology and procedures," *Journal of Performance of Constructed Facilities*, vol. 24, no. 6, pp. 519-528, 2010.

[15] American Society of Civil Engineers, *Minimum design loads for buildings and other structures*, SEI/ASCE 7-95, New York, 2005.

[16] General Service Administration, *Progressive collapse analysis and design guidelines for new federal office buildings and major modernization projects*, GSA, Washington, 2003.

[17] B. R. Ellingwood, R. Smilowitz, D. O. Dusenberry, D. Duthinh, H. S. Lew and N. J. Carino, *Best practices for reducing the potential for progressive collapse in buildings*, National Institute of Standards and Technology, NISTIR 7396, USA, 2007

[18] S. M. Marjanishvili, "Progressive analysis procedure for progressive collapse," *Journal of Performance of Constructed Facilities*, vol. 18, no. 2, pp. 79-85, 2004.

[19] British Standards Institution, *Design of Concrete Structures: Part 1-1: General Rules and Rules for Buildings*, BS EN 1992-1-1, BSI, 2004.

[20] Office of the Deputy Prime Minister, *The Building Regulations, Part A3: Disproportionate Collapse*, ODPM, London, 2010.

[21] British Standards Institution, *Actions on Structures: Part 1-7: Accidental actions*, BS EN 1991-1-7, BSI, 2006.

[22] P. F. Mlakar Sr, W. G. Corley, M. A. Sozen, and C. H. Thornton, "The Oklahoma City bombing: Analysis of blast damage to the Murrah Building," *Journal of Performance of Constructed Facilities*, vol. 12, no. 3, pp. 113-119, 1998.

[23] J. R. Hayes, S. C. Woodson, R. G. Pekelnicky, C. D. Poland, W. G. Corley and M. A. Sozen, "Can strengthening for earthquake improve blast and progressive collapse resistance?," *Journal of Structural Engineering*, vol. 131, no. 8, pp. 1157-1177, 2005.

[24] M. Saatcioglu, T. Ozbakkaloglu, N. Naumoski, and A. Lloyd, "Response of earthquake-resistant reinforced-concrete buildings to blast loading," *Canadian Journal of Civil Engineering*, vol. 36, no. 8, pp. 1378-1390, 2009.

[25] K. Khandelwal, S. El-Tawil and F. Sadek, "Progressive collapse analysis of seismically designed steel braced frames," *Journal of Constructional Steel Research*, vol. 65, no. 3, pp. 699-708, 2009.

[26] M. Byfield, W. Mudalige, C. Morison and E. Stoddart, "A review of progressive collapse research and regulations," in *Proceedings of the Institution of Civil Engineers – Structures and Buildings*, vol. 167, no. 8, ICE, 2014, pp. 447-456.

[27] Y. Li, X. Lu, H. Guan, H and L. Ye, "An improved tie force method for progressive collapse resistance design of reinforced concrete frame structures," *Engineering Structures*, vol. 33, no. 10, pp. 2931-2942, 2011.

[28] T. Krauthammer, R. L. Hall, S. C. Woodson, J. T. Baylot, J. R. Hayes and Y. Sohn, Y. "Development of progressive collapse analysis procedure and condition assessment for structures," presented at the National Workshop on Prevention of Progressive Collapse, Rosemont, Illinois, July 10-12, 2002.

[29] S.M. Baldridge and F.K. Humay, "Preventing progressive collapse in concrete buildings," *Concrete International*, vol. 25 ,no. 11, pp. 73-79, 2003.

[30] S. Marjanishvili and E. Agnew, "Comparison of various procedures for progressive collapse analysis," *Journal of Performance of Constructed Facilities*, vol. 20, no. 4, pp. 365-374, 2006.

[31] M. Byfield and S. Paramasivam, "Catenary action in steel-framed buildings," in *Proceedings of the ICE-Structures and Buildings*, vol. 160, no. 5, ICE, 2007, pp. 247-257.

[32] Department of Defence, *Unified Facilities Criteria, Design of buildings to resist progressive collapse*, UFC 4-023-023, USA, 2005.

[33] D. Mitchell and W. D. Cook, "Preventing progressive collapse of slab structures," *Journal of Structural Engineering*, vol. 110, no. 7, pp. 1513-1532, 1984.

[34] I. Mullers and T. Vogel, "Vulnerability of flat slab structures," in *Proceeding of the 2005 Structures Congress: Metropolis & Beyond*, New York, Apr. 20-24, 2005, ASCE, pp. 1-8.

[35] Y. Mirzaei and M. Sasani, "Punching shear failure in progressive collapse analysis," in *Proceeding of Structures Congress 2011*, Las Vegas, Nevada, Apr. 14-16, 2011, ASCE, pp. 2941-2950.

[36] M. F. Ruiz, Y, Mirzaei and A. Muttoni, "Post-punching behavior of flat slabs," *ACI Structural Journal*, vol. 110, no. 5, pp. 801-811, 2013.

[37] M. Zineddin and T. Krauthammer, "Dynamic response and behavior of reinforced concrete slabs under impact loading," *International Journal of Impact Engineering*, vol. *34, no.* 9, pp. 1517-1534, 2007.

[38] J. D. Osteraas, "Murrah Building bombing revisited: A qualitative assessment of blast damage and collapse patterns," *Journal of Performance of Constructed Facilities*, vol. *20, no.* 4, pp. 330-335, 2006.

[39] M. Ettouney, R. Smilowitz and T. Rittenhouse, "Blast resistant design of commercial buildings," *Practice Periodical on Structural Design and Construction*, vol. 1 no. 1, pp. 31-39. 1996.

[40] K. Qian and B. Li, "Slab effects on response of reinforced concrete substructures after loss of corner column," *ACI Structural Journal*, vol. 109, no. 6, pp. 845-856, 2012.

[41] P. X. Dat and T. K. Hai, "Membrane actions of RC slabs in mitigating progressive collapse of building structures," *Engineering Structures*, vol. 55, pp. 107-115, 2013.

[42] D. M. McCann and S. J. Smith, "Resistant design of reinforced concrete structures", *STRUCTURE Magazine*, pp. 22-26, 2007.

[43] A.G. Vlassis, B. A. Izzuddin, A. Y. Elghazouli and D. A. Nethercot, "Progressive collapse of multi-storey buildings due to failed floor impact," *Engineering Structures*, vol. 31, no. 7, pp. 1522-1534, 2009.

[44] U. Starossek, "Avoiding disproportionate collapse of tall buildings," *Structural Engineering International*, vol. 18, no. 3, pp. 238-246, 2008.

[45] R. F. Zollo, "Fiber-reinforced concrete: an overview after 30 years of development," *Cement and Concrete Composites*, vol. 19, no. 2, pp. 107-122, 1997.

[46] B. Cavill, M. Rebentrost and V. Perry, "Ductal®-An ultra-high performance material for resistance to blasts and impacts," presented at the 1st Specialty Conference on Disaster Mitigation, Calgary, Canada, May 23-26, 2006.

[47] S. J. Barnett, S. G. Millard, G. K. Schleyer and A. Tyas, "Briefing: Blast tests of fibre-reinforced concrete panels" in *Proceedings of the ICE-Construction Materials*, vol. 163, no. 3, ICE, 2010, pp. 127-129.

[48] J. H. J. Kim, N. H. Yi, I. S. Oh, H. S. Lee, J. K. Choi and Y. G. Cho, "Blast loading response of ultra high performance concrete and reactive powder concrete slabs," *in Proceedings of the Fracture Mechanics of Concrete and Concrete Structures,* Jeju, South Korea, B. H. Oh, O. C. Choi and L. Chung, Eds. Korea Concrete Institute, 2010, pp. 1715-1722.

[49] S. G. Millard, T. C. K. Molyneaux, S. J. Barnett and X. Gao, "Dynamic enhancement of blast-resistant ultra high performance fibre-reinforced concrete under flexural and shear loading," *International Journal of Impact Engineering*, *37*(4), pp. 405-413, 2010.

[50] L. J. Malvar and C. A. Ross, "Review of strain rate effects for concrete in tension," *ACI Materials Journal*, vol. 95, no. 6, pp. 735-739, 1998.

[51] J. W. Tedesco and C. A. Ross, "Strain-rate-dependent constitutive equations for concrete," *Journal of Pressure Vessel Technology*, vol. 120, no. 4, pp. 398-405, 1998.

[52] K. Habel and P. Gauvreau, "Response of ultra-high performance fiber reinforced concrete (UHPFRC) to impact and static loading," *Cement and Concrete Composites*, vol 30, no. 10, pp. 938-946, 2008.

[53] Z. Rong, W. Sun and Y. Zhang, "Dynamic compression behavior of ultra-high performance cement based composites," *International Journal of Impact Engineering*, vol. *37, no.* 5, pp. 515-520, 2010.

[54] F. Baby, B. Graybeal, P. Marchand and F. Toutlemonde, "UHPFRC tensile behavior characterization: inverse analysis of four-point bending test results," *Materials and Structures*, vol. *46, no.* 8, pp. 1337-1354, 2013.

[55] K. Wille, S. El-Tawil and A. E. Naaman, A. E. "Properties of strain hardening ultra high performance fiber reinforced concrete (UHP-FRC) under direct tensile loading," *Cement and Concrete Composites*, vol. 48, pp. 53-66, 2014.

[56] B. A. Graybeal, F. Baby, P. Marchand and F. Toutlemonde, "Direct and flexural tension test methods for determination of the tensile stress–strain response of UHPFRC," in *International Symposium on UHPC and Nanotechnology for High Performance Construction Materials: Proceedings of 3rd Hipermat* , Kassel, Germany, M. Schmidt, E. Fehling, C. Clotzbach, S, Frohlich and S. Piotrowski, Eds. Kassel University Press, 2012, pp. 395-418.

[57] R. Lane, B. Craig and W. Babcock, "Materials for blast and penetration resistance," *AMPTIAC Quarterly*, vol. 6, no. 4, pp. 39-45, 2002.

[58] Building and Construction Authority, Sustainable construction: A guide on concrete usage index, *Building and Construction Authority*, BA Singapore, 2012.

[59] P. Sukontasukkul, S. Mindess and N. Banthia, "Penetration resistance of hybrid fibre reinforced concrete under low velocity impact loading," presented at the 2nd Material Specialty Conference of the *Canadian Society for Civil Engineering*, Montreal, Canada, June 5-8, 2002.

[60] R. N. Swamy and A. H. Jojagha, "Impact resistance of steel fibre reinforced lightweight concrete," *International Journal of Cement Composites and Lightweight Concrete*, vol. 4, no. 4, pp. 209-220, 1982.

[61] M. C. Nataraja, T. S. Nagaraj and S. B. Basavaraja, "Reproportioning of steel fibre reinforced concrete mixes and their impact resistance," *Cement and Concrete Research*, vol. *35*, no. 12, pp. 2350-2359, 2005.

[62] S. Mindess and C. Yan, "Perforation of plain and fibre reinforced concretes subjected to low-velocity impact loading," *Cement and Concrete Research*, vol. 23, no. 1, pp. 83-92, 1993.

[63] H. Yan, W. Sun, and H. Chen, "The effect of silica fume and steel fiber on the dynamic mechanical performance of high-strength concrete," *Cement and Concrete Research*, vol. *29, no.* 3, pp. 423-426, 1999.

[64] M. H. Zhang, V. P. W. Shim, G. Lu and C. W. Chew, "Resistance of high-strength concrete to projectile impact," *International Journal of Impact Engineering*, vol. 31, no. 7, pp. 825-841, 2005.

[65] X. Luo, W. Sun and S. Y. N. Chan, "Steel fiber reinforced high-performance concrete: A study on the mechanical properties and resistance against impact," *Materials and Structures*, vol. 34, no. 3, pp. 144-149, 2001.

[66] M. Maalej, S. T. Quek and J. Zhang, "Behavior of hybrid-fiber engineered cementitious composites subjected to dynamic tensile loading and projectile impact," *Journal of Materials in Civil Engineering*, vol. 17, no. 2, pp. 143-152, 2005.

[67] A. N. Dancygier, D. Z. Yankelevsky and C. Jaegermann, "Response of high performance concrete plates to impact of non-deforming projectiles," *International Journal of Impact Engineering*, vol. *34, no.* 11, pp. 1768-1779, 2007.

[68] H. Masuya, M. Yamamoto, M. Toyama and Y. Kajikawa, "Experimental study on the perforation of steel fiber reinforced concrete slab by impact," *Structures and Materials*, vol. 8, pp. 205-214, 2000.

[69] W. S. Chang, "Impact of solid missiles on concrete barriers," *Journal of the Structural Division*, vol. 107, no. 2, pp. 257-271, 1981.

[70] K. C. G. Ong, M. Basheerkhan and P. Paramasivam, "Resistance of fibre concrete slabs to low velocity projectile impact," *Cement and Concrete Composites*, vol. 21, no. 5, pp. 391-401, 1999.

[71] N. Wang, S. Mindess and K. Ko, "Fibre reinforced concrete beams under impact loading," *Cement and Concrete Research*, vol. 26, no. 3, pp. 363-376, 1996.

[72] V. Bindiganavile and N. Banthia, "Impact response of the fiber-matrix bond in concrete," *Canadian Journal of Civil Engineering*, vol. 32, no. 5, pp. 924-933, 2005.

[73] T. S. Lok and J. S. Pei, "Impact resistance and ductility of steel fibre reinforced concrete panels," *HKIE Transactions*, vol. 3, no. 3, pp. 7-16, 1996.

[74] J. Zhang, M. Maalej and S.T. Quek "Performance of hybrid-fiber ECC blast/shelter panels subjected to drop weight impact," *Journal of Materials in Civil Engineering*, vol. 19, no. 10, pp. 855-863, 2007.

[75] D. A. Wyrick and D. F. Adams, "Residual strength of a carbon/epoxy composite material subjected to repeated impact," *Journal of Composite Materials*, vol. 22, no. 8, pp. 749-765, 1988,

[76] T. D. Hrynyk and F. J. Vecchio, "Behavior of steel fiber-reinforced concrete slabs under impact load," *ACI Structural Journal*, vol. *111, no.* 5, pp. 1213-1224, 2014.

[77] K. Habel, "Impact response of post-tensioned and reinforced concrete members with an UHPFRC overlay," *in Proceedings of the Fracture Mechanics of Concrete and Concrete Structures*, Jeju, South Korea, B. H. Oh, O. C. Choi and L. Chung, Eds. Korea Concrete Institute, 2010, pp. 437-444.

[78] J. M. Biggs, *Introduction to Structural Dynamics*. New York: McGraw-Hill Book Company, 1964.

[79] H. Y. Low and H. Hao, "Reliability analysis of reinforced concrete slabs under explosive loading," Structural Safety, vol. 23, no. 2, pp. 157-178, 2001.

[80] W. W. El-Dakhakhni, W. F. Mekky and S. C. Rezaei, "Validity of SDOF models for analyzing two-way reinforced concrete panels under blast loading," *Journal of Performance of Constructed Facilities*, vol. 24, no. 4, pp. 311-325, 2009.

[81] K. Fischer and I. Haring, "SDOF response model parameters from dynamic blast loading experiments," *Engineering Structures*, vol. 31, no. 8, pp. 1677-1686, 2009.

[82] A. T. Hussein, "Nonlinear analysis of SDOF system under blast load," *European Journal of Scientific Research*, vol. 45, no. 3, pp. 430-437, 2010.

[83] G. K. Schleyer, S. J. Barnett, S. G. Millard and G. Wight, "Modelling the response of UHPFRC panels to explosive loading," in *International Conference on Structures under Shock and Impact XI*, Tallinn, Estonia, N. Jones, C. A. Brebbia and U. Mander, Eds. Southampton: WIT Press, 2010, pp. 173-184.

[84] K. Fujikake, T. Senga, N. Ueda, T. Ohno and M. Katagiri, "Study on impact response of reactive powder concrete beam and its analytical model," *Journal of Advanced Concrete Technology*, vol. 4, no. 1, pp. 99-108, 2006.

[85] R. D. Cook, D. S. Malkus, M. E. Plesha and R. J. Witt, *Concepts and applications of finite element analysis* (Volume 4). New York: John Wiley & Sons Inc. 2002.

[86] D. V. Hutton and J. Wu, *Fundamentals of finite element analysis* (Vol. 1). New York: McGraw-Hill. 2004.

[87] S. Ham and K. J. Bathe, "A finite element method enriched for wave propagation problems," *Computers and Structures*, vol. 94-95, pp. 1-12, 2012.

[88] S. Lamarche, F. Voldoire, H. B. Dhia and C. Zammali, "Validation of contact-impact approaches for FEM software," presented at the *6th European Conference on Structural Dynamics*, Paris, Sept. 4-7, 2005.

[89] G. H. Mahmud, Z. Yang and A. M. Hassan, "Experimental and numerical studies of size effects of Ultra High Performance Steel Fibre Reinforced Concrete (UHPFRC) beams," *Construction and Building Materials*, vol. 48, pp. 1027-1034, 2013.

[90] E. M. R. Fairbairn, R. D. Toledo, R. C. Battista, R. C., J. H. Brandao and J. I. Rosa, "Experimental and numerical analysis of UHPFRC plates and shells," in *Measuring, Monitoring and Modeling Concrete Properties*, M. S. Konsta-Gdoutos, Ed. Dordrecht: Springer, 2006, pp. 49-58.

[91] T. T. Le, *Ultra high performance fibre reinforced concrete paving flags*, PhD Thesis, University of Liverpool), 2008.

[92] A. A. A. Azzawi, A. S. Ali and H. K. Risan, "Behavior of ultra high performance concrete structures," *ARPN Journal of Engineering and Applied Sciences*, vol. 6, no. 5, pp. 95-109, 2011.

[93] L. Chen and B. A. Graybeal, "Modeling structural performance of ultrahigh performance concrete I-girders," *Journal of Bridge Engineering*, vol. 17, no. 5, pp. 754-764, 2011.

[94] L. Mao, S. Barnett, D. Begg, G. Schleyer and G. Wight, "Numerical simulation of ultra high performance fibre reinforced concrete panel subjected to blast loading," *International Journal of Impact Engineering*, vol. 64, pp. 91-100, 2014.

[95] S. Gopinath, R. Ayashwarya, V. R. Kumar, P. R. Prem, A. R. C. Murthy, C. Madheswaran and R. N. Iyer, "Low velocity impact behaviour of ultra high strength concrete panels," *Sadhana*, vol. 39, no. 6, pp. 1497-1507, 2014.

[96] R. Sovjak, T. Vavrinik, J. Zatloukal, P. Maca, T. Micunek and M. Frydryn, "Resistance of slim UHPFRC targets to projectile impact using in-service bullets," *International Journal of Impact Engineering*, vol. 76, pp. 166-177, 2014.

[97] Z. Tu and Y. Lu, "Modifications of RHT material model for improved numerical simulation of dynamic response of concrete," *International Journal of Impact Engineering*, vol. 37, no. 10, pp. 1072-1082, 2010.

[98] C. Y. Tham, "Reinforced concrete perforation and penetration simulation using AUTODYN-3D," *Finite Elements in Analysis and Design*, vol. 41, no. 14, pp. 1401-1410, 2005.

[99] J. Leppanen, "Concrete subjected to projectile and fragment impacts: Modelling of crack softening and strain rate dependency in tension," *International Journal of Impact Engineering*, vol. 32, no. 11, pp. 1828-1841, 2006.

[100] U. Nystrom and K. Gylltoft, "Comparative numerical studies of projectile impacts on plain and steel-fibre reinforced concrete," *International Journal of Impact Engineering*, vol. *38, no.* 2, pp. 95-105, 2011.

[101] W. Riedel, "10 years RHT: A review of concrete modelling and hydrocode application," in Predictive modelling of dynamic processes – a tribute," K. Thoma and S. Hiermaier, Eds, London: Springer, pp. 143-165, 2009.

[102] V. Berg and D. Preece, "Shape charge induced concrete damage predictions using RHT constitutive modelling" *in Proceedings of the Annual Conference on Explosives and Blasting Technique*, vol.2, ISEE, 2004, pp. 261-272.

[103] H. Hasson and P. Skoglund, *Simulation of concrete penetration in 2D and 3D with RHT material model*, Swedish Defence Research Agency, FOI-R-0720-SE, Sweden, 2002.

CHAPTER 3
EXPERIMENTAL PROCEDURES

3.1 Introduction

This chapter focuses on the experimental procedures used in the study to investigate the response of undamaged and pre-damaged UHPFRC slabs under low velocity impact. An overview of the preparation of the UHPFRC slabs including the pre-damaged specimens is provided. Following this, the details on the procedure of the impact test with various impact scenarios together with the method to process the raw data until achieving the anticipated results are also presented. All the experimental works were conducted at the University of Liverpool utilising the existing facilities.

3.2 Materials and Mix Design

All the materials used in this study, except for the steel fibres, were locally produced. The UHPFRC mix design used for this research utilised the same materials, mix design and curing regime as previously used in the University of Liverpool for the purpose of studying the response of UHPFRC under blast and impact load [1]. Similar mix design was also used by other researchers [2-3] and has proven to produce concrete with ultra-high performance properties.

3.2.1 Portland Cement

Ordinary Portland cement type CEM 1 52.5N conforming to BS EN 197-1 [4] supplied by Hanson Heidelberg Cement Group was used. The number '52.5' refers to the class strength of 52.5 MPa at 28 days and letter 'N' refers to cement with ordinary early strength development. This type of cement is used to ensure the production of high strength concrete which is one of the characteristics of UHPFRC.

3.2.2 Ground Granulated Blast-Furnace Slag (GGBS)

The Ground Granulated Blast Furnace Slag (GGBS) is a by-product from the steel industry and is also supplied by Hanson Heidelberg Cement Group. The material is very fine, typically off-white and non-metallic consisting essentially of calcium silicates. GGBS is known as the cement replacement material, a good binder and has the ability to reduce thermal cracking. The specification of GGBS for construction practice is covered under BS EN 15167-1 [5].

3.2.3 Silica Fume

Silica fume or microsilica is a by-product from ferrosilicon alloys production in smelting furnace at a temperature of 2000°Celcius. The main composition of silica fume is silica oxide with a typical content of more than 90%. The reaction of silica fume with calcium hydroxide that refines the microstructure of the concrete is able to improve the compressive strength, and the abrasion resistance [6]. Moreover, the silica fume also refines the interfacial transition zones between the binder and aggregates and the binder and steel fibres hence improving the bond strength [7]. The specification for silica fume is covered under BS EN 13263-1 [8]. This mix design used Grade 920 Silica Fume supplied by Elkem Materials Ltd.

3.2.4 Silica Sand

Silica sand used in the mix is a high quality fine sand mainly containing silica oxide. This type of sand is produced from loosely consolidated sand deposits and crushing weakly cemented stones. The silica sand used in the design mix has a particle size in the range of 150-300 μm, supplied by WBB Minerals UK. The chemical composition of the silica sand is covered under BS EN 12620 [9].

3.2.5 Superplasticiser

The high range water reducer used previously in the design mix was Structuro 1180, manufactured by Fosroc Ltd UK. This superplasticiser is a water based polycarboxylate that allows significant reduction of the water-binder ratio in the production of self-compacting, high strength and high performance concretes. However, the production of Structuro 1180 was stopped and replaced with Auracast 200, a similar superplasticiser designed for producing self-compacting concrete.

3.2.6 Steel Fibres

The steel fibres are straight, brass coated high carbon steel with 0.2 mm diameter and 13 mm length produced by N.V Bekaert S.A as shown in Figure 3.1. The tensile strength and Young's Modulus of the fibres is 2000 MPa and 210 GPa, respectively.

Figure 3.1: Straight, brass coated steel fibres (13 mm long).

3.3 Preparation of UHPFRC Slabs and Cubes

Figure 3.2 shows the schematic of the UHPFRC slab. The overall size is 660 mm × 660 mm × 25 mm thick. At every corner, 40 mm × 40 mm fillet was provided to accommodate the set-up in the static test device. Along each edge, four 25 mm diameter holes at 130 mm spacing were provided to cater for the studs. It is expected that the presence of these studs creates some degree of fixity along the edges of the slab although it is well understood that a fully fixed condition cannot be achieved. The overall plan dimensions of the UHPFRC slab are basically the standard dimensions to be used with the Pulse Pressure Loading Rig (PPLR) for performing static pressure load test (refer section 3.4).

Cubes of 100 mm and 50 mm in size were also produced for checking the consistency of the UHPFRC batches.

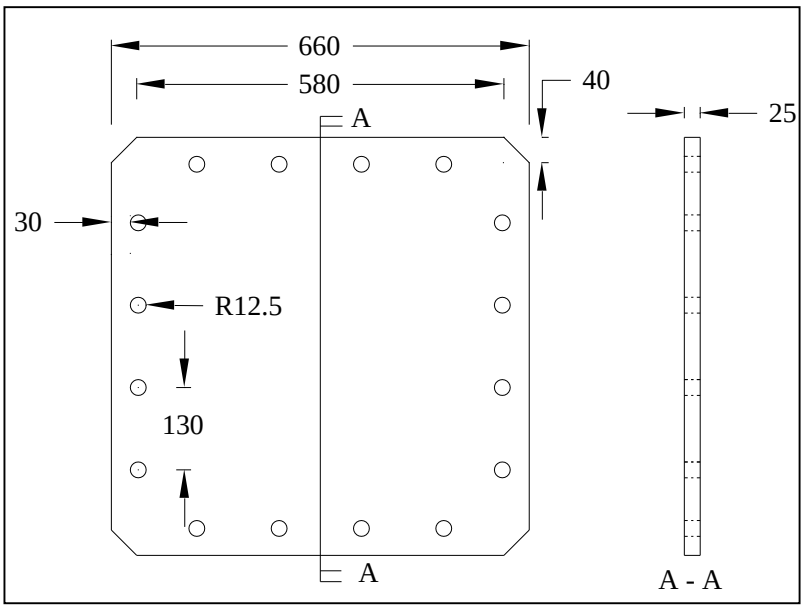

Figure 3.2: Schematic drawing of the UHPFRC slab (all dimensions in mm).

3.3.1 Design Mix

The design mix was calculated based on the weight of each material to produce 1 m^3 of UHPFRC and is shown in Table 3.1.

Table 3.1: UHPFRC design mix.

Item	Unit	Quantity
CEM1 52.5N Cement	kg	657
Ground Granulated Blast-Furnace Slag	kg	418
Undensified Microsilica	kg	119
Silica Sand	kg	1051
Auracast 200 Superplasticiser	kg	40
Steel Wire Fibres OL 13/.20	kg	157
Water	kg	185

3.3.2 Mixing Procedure

Mixing was carried out using a rotating drum pan mixer as shown in Figure 3.3. Each material was weighted proportionately according to the required volume. All the dry materials which have been weighted were added systematically into the pan mixer, starting with the cement, followed by the silica fume, GGBS and silica sand. The materials were then dry-mixed for one minute to ensure a thoroughly blended mixture. Following this, the superplasticiser together with the clean water was added into the mixture and the mixing continued for another 10-12 minutes. Finally, steel fibres were carefully spread into the pan and mixed for another 2-3 minutes. This technique ensured a proper dispersion of the steel fibres in the cement paste.

Figure 3.3: UHPFRC mix in a rotating pan mixer.

3.3.3 Casting and Compaction

The UPHFRC wet mix was poured immediately into the lightly oiled mould starting from the centre as recommended by Barnett *et al.* [10]. Although this technique was reported to be suitable for the preparation of circular specimens, it is also useful for thin square slabs as it allows the fibres to line up in a plane orientation hence increasing the number of fibres bridging the cracks. Each batch of the UHPFRC casting exercise produces three panels, six 100 mm cubes and six 50 mm cubes. All specimens were compacted using a vibrating table for about 1-2 minutes. Even though UHPFRC is claimed to be a type of 'self-compacting concrete', the compaction process was still carried out to ensure the elimination of any trapped air. Figure 3.4 shows the UHPFRC slab specimens after the pouring and compaction process.

Figure 3.4: UHPFRC specimens (after compaction).

3.3.4 Curing

The compacted UHPFRC specimens were covered with a layer of damp hessian sheet and polythene sheet for 24 hours. Following that, the specimens were de-moulded and treated in the in-house hot curing tank at a constant temperature of 90° Celsius for 48 hours. Curing of concrete at elevated temperature has been proven to improve the microstructure of the UHPFRC and is capable of developing high early age compressive and flexural strength as well as high fracture energy compared to curing at room temperature [11].

3.3.5 Consistency of the Mix Design

The consistency of the mix design was monitored through the compressive strength of the UHPFRC cubes. For every batch of casting, the 100 mm and 50 mm cubes were tested for 7 and 28 days strength. The results from the compressive strength tests are discussed in Chapter 5. The cubes were tested in accordance with BS EN 12390-3 [12] for 7 day and 28 day compressive strength using the Tonipact 3000 kN compression testing machine as shown in Figure 3.5.

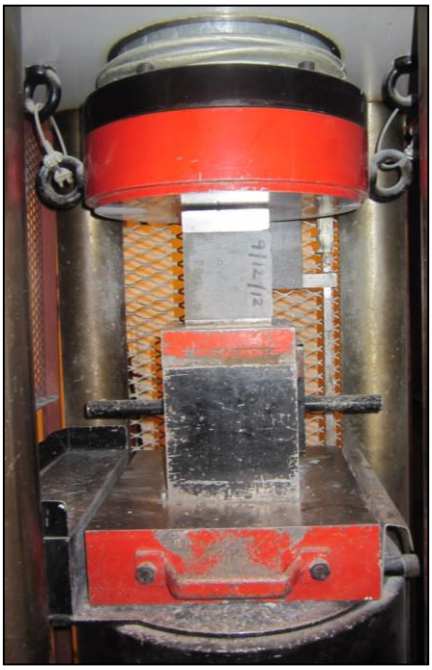

Figure 3.5: Tonipact 3000 kN compression testing machine.

3.4 Static Pressure Tests on UHPFRC Slabs

Static pressure tests were performed in order to produce 23 pre-damaged UHPFRC slabs that were used in the subsequent impact and point load static tests. All static tests were conducted after the 28 days cube strength was achieved.

3.4.1 Pulse Pressure Loading Rig

The static pressure test was carried out using the Pulse Pressure Loading Rig (PPLR) developed at the University of Liverpool [13] as shown in Figure 3.6. It consists of two pressure loading chambers and a 50 mm thick central support frame with 500 mm × 500 mm opening that serves as the loaded area. The pressure chambers and the central plate are held together using eight 24 mm diameter studs. This facility is specially designed for dynamic tests as well as static tests that involve pressure up to 800 kN/m^2. The amount of air filling the pressure chambers can be controlled manually.

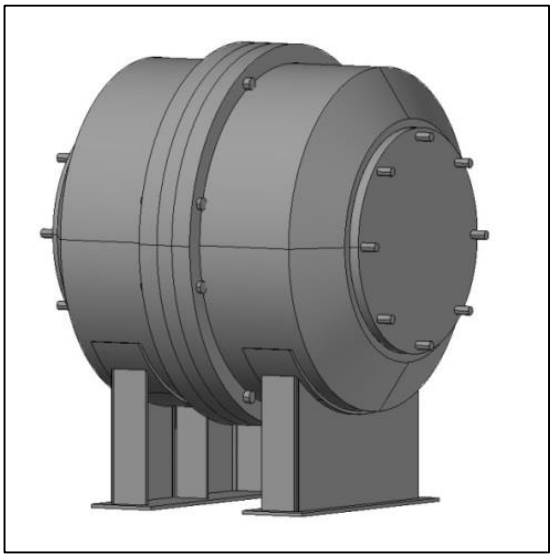

(a)

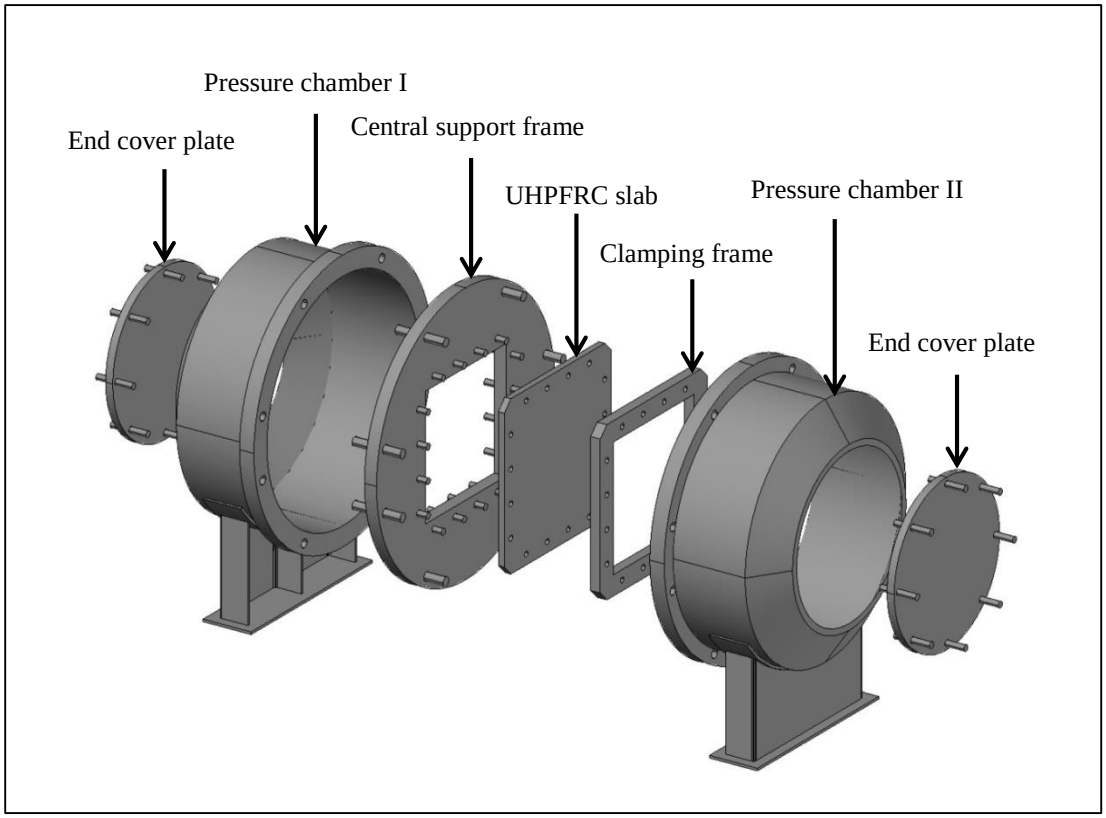

(b)

Figure 3.6: Pulse pressure loading rig (PPLR) showing (a) general view; (b) expanded view.

3.4.2 Trial Test

Considering that the static pressure test on UHPFRC slabs using the PPLR was the first ever to be carried out, a series of trial tests were conducted on the existing UHPFRC slabs with different fibre content. Table 3.2 shows the details of the slab specimens with respect to the fibre mix and the age of the slabs. These tests provided initial information and detected blind spots on the static pressure tests where the results were used to further enhance future work. The main areas of investigations were the yield line pattern, collapse load and the effect of the boundary conditions.

Table 3.2: Details of the existing UHPFRC slabs

Slab	Fibre type	Fibre content (%)	Test age (days)
1	Straight (S)	2%S	1,023
2	Straight (S)	2%S	1,023
3	Straight (S)	2%S	1,023
4	Straight (S)	2%S	1,187
5	Straight (S) & Hooked-end (H)	2%S + 2%H	1,050
6	Straight (S) & Hooked-end (H)	2%S + 2%H	1,050
7	Straight (S) & Hooked-end (H)	3%S + 3%H	1,328
8	Straight (S) & Hooked-end (H)	3%S + 3%H	1,005
9	Straight (S)	6%S	1,326

Sixteen off 20 mm diameter studs were first secured to the central plate. The UHPFRC slab was placed over the studs and hand-tightened to their position. A single non-spring loaded Linear Variable Differential Transformer (LVDT) was placed in the middle of the slab using a hook and loop tape. A final check was carried out to ensure that all the cables connecting to the measuring devices were not tangled and all other essential sensors were properly protected. Finally, the PPLR was closed by tightening eight 25 mm studs. The pressure chamber II was pressurized with air and observed on the Remote Pressure Control Panel. At the same time, the deformation of the UHPFRC panel was also monitored on the Multimeter via the voltage readings. The data collection was carried out manually at every 5 psi intervals.

Slab 1 and Slab 9 were tested until failure (no deformation was captured for Slab 1). Other slabss were pressure loaded until a certain level of cracks was formed. The results in the form of pressure-deformation curves are presented in Figure 3.7.

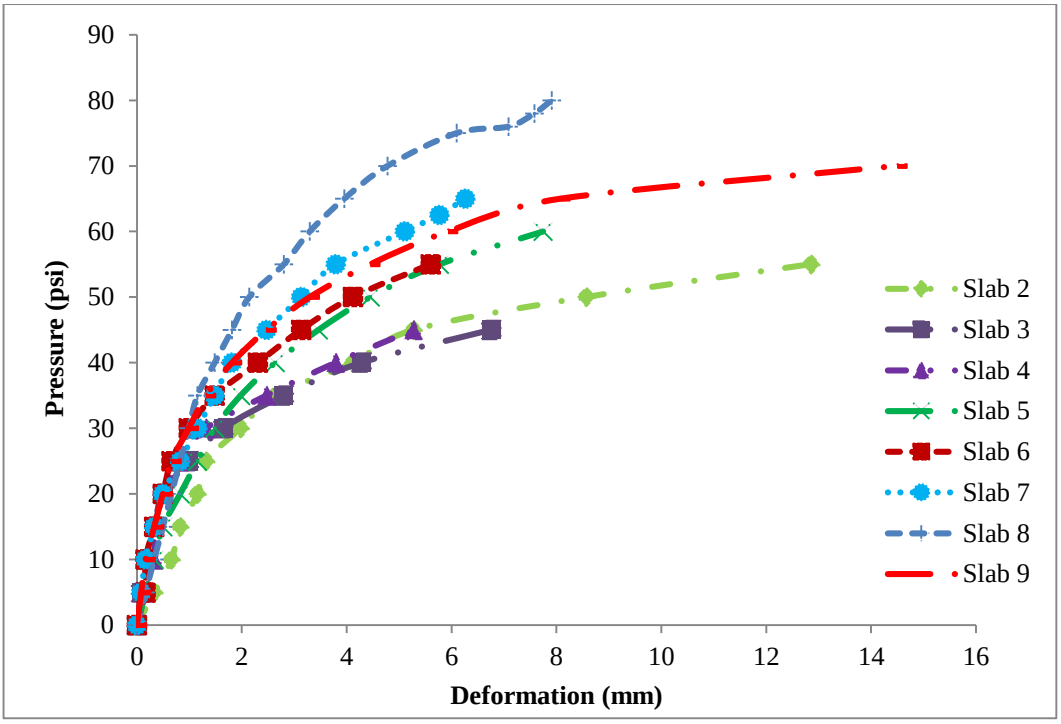

Figure 3.7: Graphs showing the pressure-deformation relationship of the static pressure tests.

The pressure-deformation behaviour for all the slabs can be divided into two, namely linear (between 20-30 psi) and non-linear. Significant deformations can be seen at higher load intensities. Slabs with higher fibre content are invariably able to support higher pressure loads as indicated by the lower deflections. The failure loads for Slab 1 and Slab 9 were 65 psi and 85 psi, respectively. For Slab 1, the load was first applied up to 60 psi and then depressurized for physical inspection. A clear and common yield line clearly formed on the bottom face of the slab due to the sagging moment, as shown in Figure 3.8.

Figure 3.8: Bottom face of Slab 1 after pressure testing showing a typical yield line formation pattern of a square slab under uniform load.

The pressure load was then continuously applied on Slab 1 until it reached 65 psi and at that moment, a loud bang could be heard from the PPLR. This signified the total failure of Slab 1. Reading on the Remote Pressure Control Panel also showed a sudden pressure drop nearing 0 psi. Upon further inspection, it was found that most of the unsupported middle slab was broken to pieces, leaving some part of the frame on the support line still intact as shown in Figure 3.9 (a) and (b). Physical inspection of the broken UHPFRC pieces showed that almost all the fibres suffered pull-out action as shown in Figure 3.9 (c).

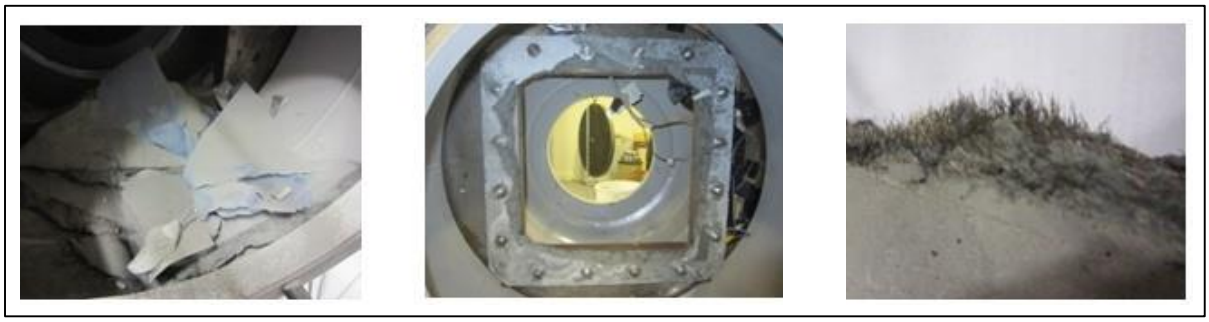

(a) (b) (c)

Figure 3.9: Slab 1 after total failure showing (a) broken pieces; (b) remaining frame; (c) fibre pull-out.

The slabs containing 2% fibre subjected to 45 psi and 50 psi exhibited almost identical crack formation on the bottom face as shown in Figure 3.10 (a) and (b). Minor crack lines were developed originating from the centre and propagated halfway towards the corner. Fine crack lines caused by hogging moment were also observed along the support line, however these cracks were found to be very close to the studs as shown in Figure 3.10 (c). Ideally, this crack should be located about 40 mm inwards from the centre of the studs, similar to the boundary of the loaded area on the bottom face. This finding proved that the boundary conditions have some degree of fixity but cannot be considered as fully fixed.

(a)

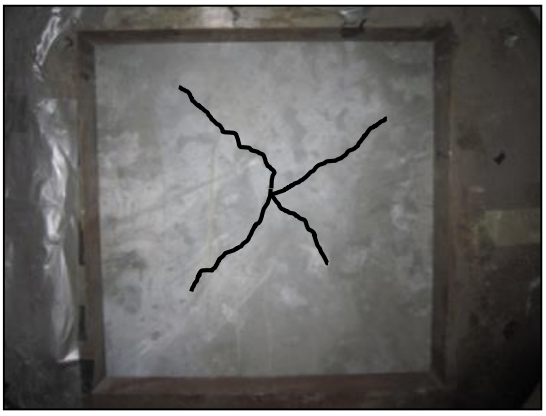

(b)

(c)

Figure 3.10: Photos of the tested slabs showing (a) crack on the bottom face of Slab 2 at 50 psi; (b) crack on the bottom face of Slab 3 at 45 psi and; (c) crack close to the studs (top face) of Slab 3.

Based on the results of the trial tests, the following observations are noted:

1. The failure of UHPFRC slabs tested using the PPLR were catastrophic with no adequate warning prior to the failure observed on the Multimeter.

2. Pre-damaging the UHPFRC slabs between the elastic range and failure load is possible provided that a suitable cut-off pressure or deformation limit is chosen. For this test, the pressure between 45-50 psi/0.31- 0.345 MPa or the deformation between 6-7 mm were found to be appropriate in this study.

3. The PPLR can be used to investigate the behaviour of UHPFRC panels at high pressure intensity although first cracking load and strain softening/hardening are not able to be captured. The condition of the UHPFRC slabs can only be inspected at loading intervals by opening the PPLR.

4. The present boundary condition is not fully fixed and further work is required to increase the degree of fixity. Clamping the UHPFRC panel with a thick steel frame and the use of a torque wrench for applying uniform force for the 20 mm studs are part of the options.

5. Taking the pressure and deformation readings manually at 5 psi intervals may not yield enough data to produce a smooth curve. A device that can record both data simultaneously should be used to improve the data quality.

The overall experimental procedures, the detail results and discussions of all tested UHPFRC slabs with various fibre content under this trial test were compiled and can be found in Zaini *et al.* [14].

3.4.3 Improvement on the Static Pressure Test

Upon placing the slab onto the 20 mm studs similar to the procedure adopted in the trial test, a 660 mm × 660 mm × 40 mm thick steel clamping frame with 500 mm × 500 mm opening was added to the assembly. Following that, all the 20 mm studs were tightened to 100 Nm torque force via a torque wrench. It is expected that the clamping method shall improve the boundary condition along the edges to be closer to a fixed boundary condition. However, it is worth mentioning that a true fully fixed boundary condition requires the slab to be monolithically casted with the support, which in this case was impossible to be achieved. The overall arrangement of the panel and the clamping frame inside the PPLR is shown in Figure 3.11.

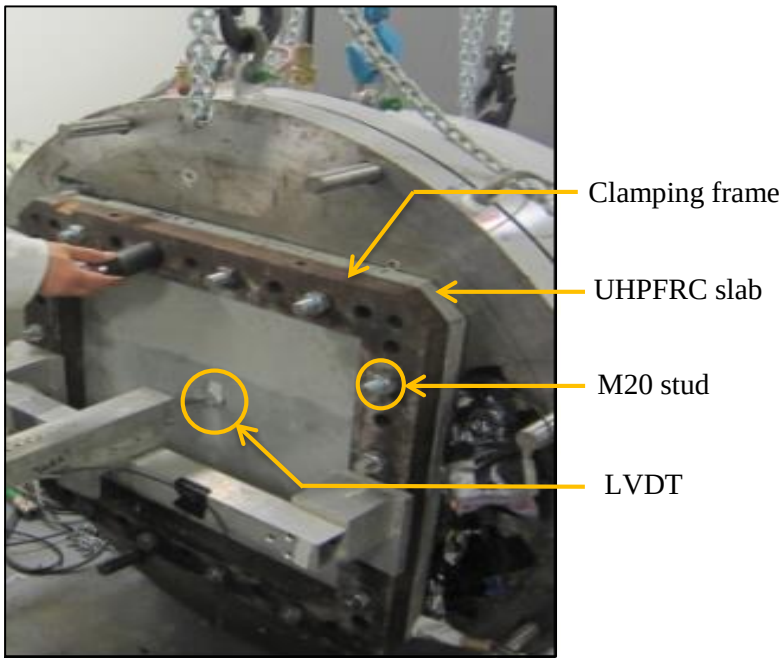

Figure 3.11: Overall assembly of the test set-up inside the PPLR.

In order to increase the number of data points and improve the quality of the pressure-deformation curve, a camera in the video mode was used to record the reading from the Remote Pressure Control Panel and the Multimeter simultaneously as shown in Figure 3.12.

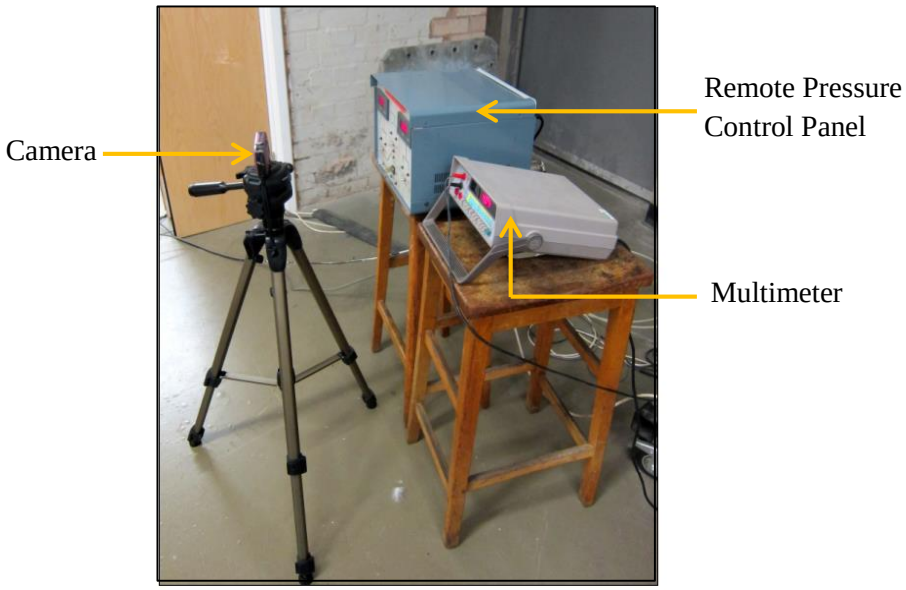

Figure 3.12: Set-up for recording the pressure and deformation simultaneously.

The PPLR was then loaded up to the pressure of 50 psi or 6 mm deformation whichever occurred first. Upon reaching the limit, the pressure was immediately released and ventilated until 0 psi. Following that, the PPLR was opened to retrieve the pre-damaged slabs. However, during the first and second test, it was found that the slabs had cracked and deformed excessively at 50 psi while still not reaching 6 mm deformation as shown in Figure 3.13. Furthermore, a sharp drop in the Remote Pressure Control Panel reading was also observed indicating that the air from pressure chamber II had leaked into pressure chamber I. Consequently, in the following pre-damaging exercise, the limit of the maximum deformation was reduced to 4 mm. This phenomenon may be due to the change in the design mix where the use of the same quantity of superplasticiser Auracast 200 may have, to some degree, reduced the bending strength of the slabs.

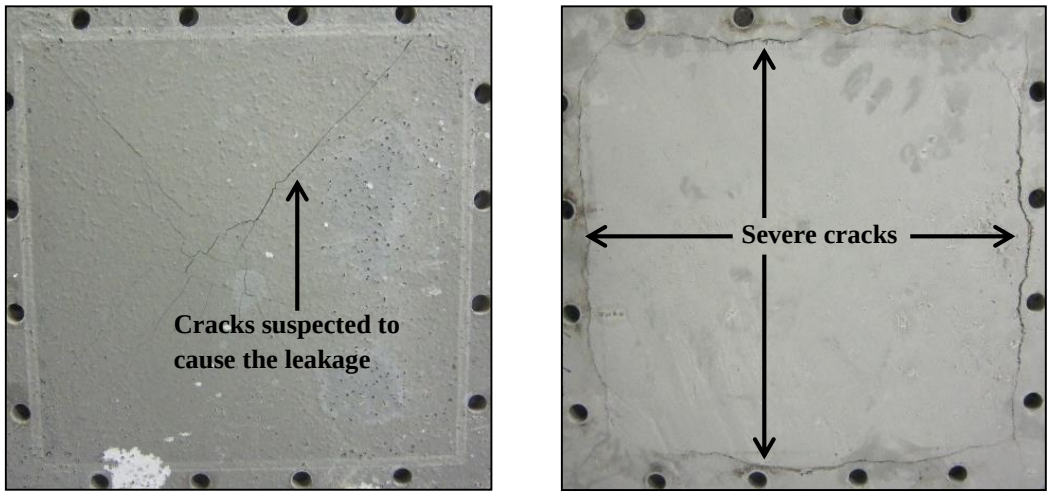

(a) (b)

Figure 3.13: Slab loaded at 50 psi showing cracks (a) at the centre of the bottom face; (b) along the edges of the top face.

3.5 Impact Test

Instrumented drop impact tests were conducted using an in-house impact rig following the recommendation stated in ACI 544.2R [15]. In order to study the sensitivity of the impact location with respect to its initial condition, impact tests were carried out at the centre, edge and corner of the slab. Additional tests to study the influence of impact angle were also conducted via oblique impact. However, the obliquity was set only to be 10°. Oblique angle higher than this was not possible within the scope of the project.

3.5.1 Impact Rig

The main component of the impact rig consists of a 150 × 90 × 23.9 kg/m C-Channel column that served as a vertical guide for the impactor. Maximum drop height that can be allowed using this rig is approximately 3.0 m depending on the overall length of the impactor. The lifting and drop mechanism is operated by means of a locking pin connected to a manually driven winch and a switch panel. For the purpose of aligning the impactor into position, rails made of two 20 mm × 10 mm steel plates were placed on each internal side of the C-Channel. The overall assembly of the impact rig is shown in Figure 3.14.

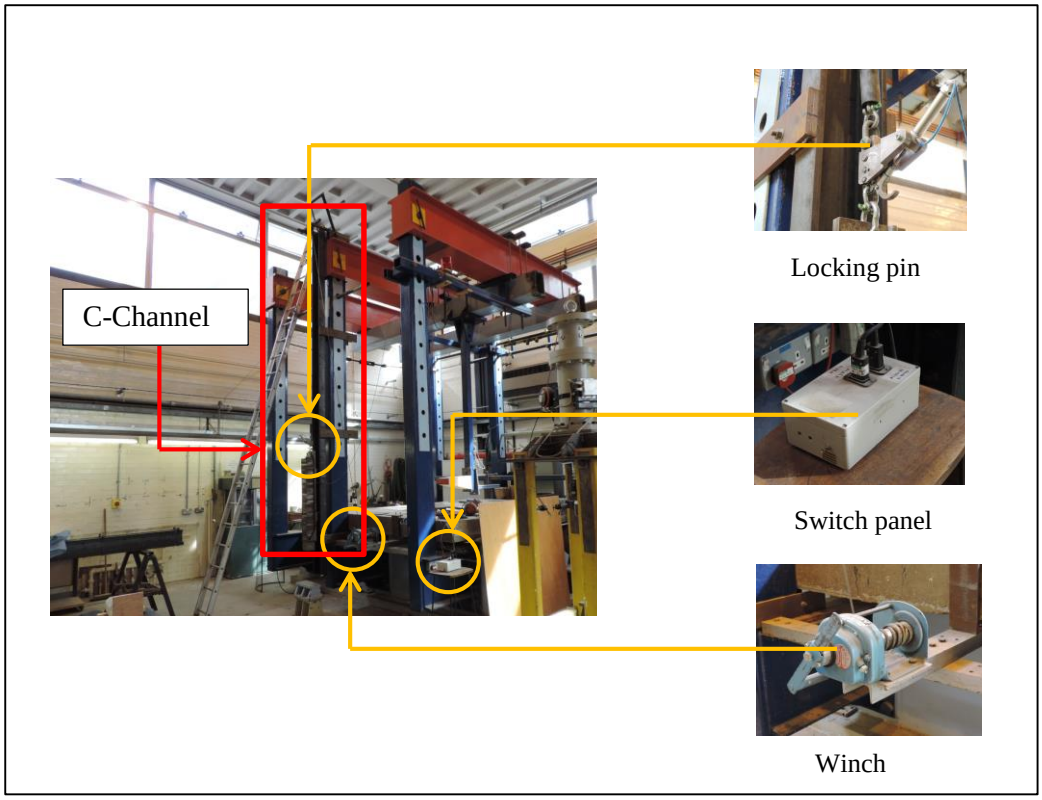

Figure 3.14: In-house impact rig and the main components.

3.5.2 Impactor

Figure 3.15 shows the schematic drawings of the impactor used in the impact tests. The main frame of the steel impactor consists of a 70 mm × 70 mm × 290 mm length solid steel block followed by a 50 mm × 50 mm × 5 mm thick square hollow section (SHS). The SHS allows additional weight to be filled up in case the impact energy is found to be relatively low. Two pairs of 20 mm diameter steel sliders were welded to the hollow section. The diameter of the slider only allows 2 mm clearance between the slider and railing. A hanger made with 6 mm diameter steel bar is welded at the end of the SHS.

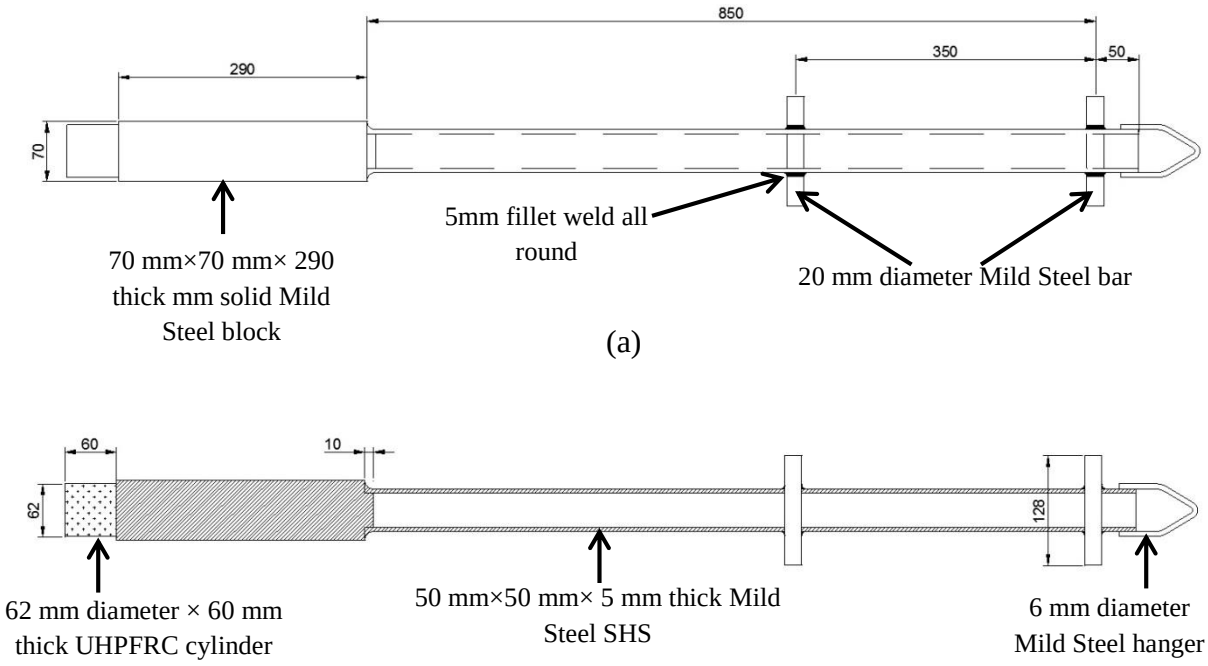

Figure 3.15: Schematic drawing of the impactor showing the (a) elevation; (b) sectional view.

In order to simulate the impact of a concrete column, a 62 mm diameter × 60 mm thick UHPFRC cylinder was attached to the solid steel block using double sided tape. The overall weight of the impactor was 15.67 kg. For the oblique impact test, apart from the double sided tape, the UHPFRC cylinder was also secured to the steel block using additional 2 mm thick plates and screws. Photos showing different method of attaching the UHPFRC cylinder to the steel impactor are shown in Figure 3.16.

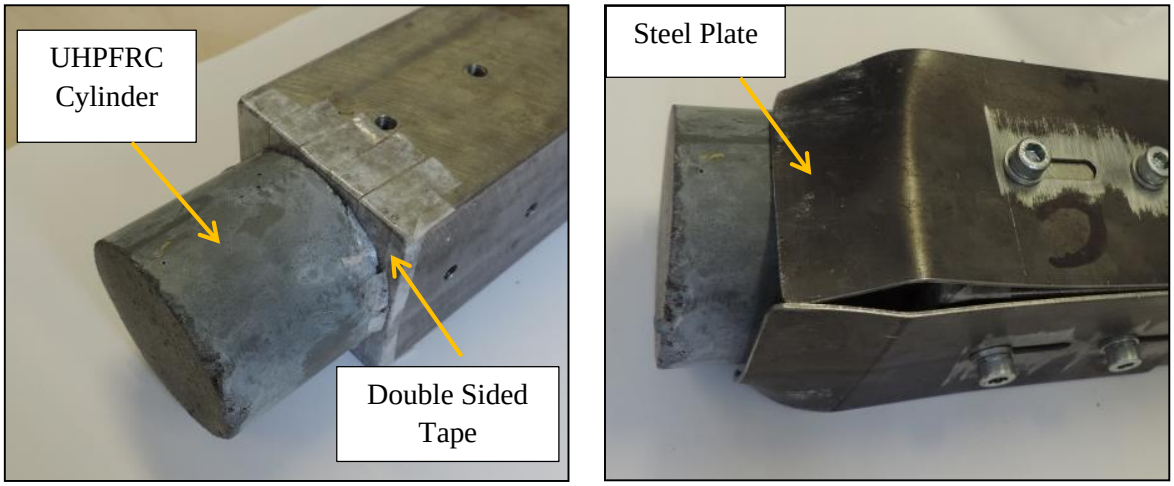

(a) (b)

Figure 3.16: Methods of attaching UHPFRC cylinder (a) double sided tape for the central, edge and corner impact; (b) additional plates and screws for the oblique impact.

3.5.3 Impact Test Arrangement

In order to maintain the same boundary condition as in the static test, the UHPFRC slab was placed in between two clamping frames. The top clamping frame was the same frame used in the pre-damaging exercise. On the other hand, a 800 mm × 800 mm × 50 mm thick with 500 mm × 500 mm opening steel frame was used as the bottom clamping frame and rested on a 12 mm thick medium density fibre board. The fibre board served to dampen the floor vibration upon impact. Finally, the clamping frames and the slab were secured by applying 100 Nm torque force along all the 20 mm studs. This arrangement was used for the central, edge and corner impact only. As for the oblique impact test, an additional frame was designed to cater for the 10° obliquity. The slab, the clamping frames set-up as well as the frame for the central and oblique impact test are shown in Figure 3.17(a) and (b), respectively.

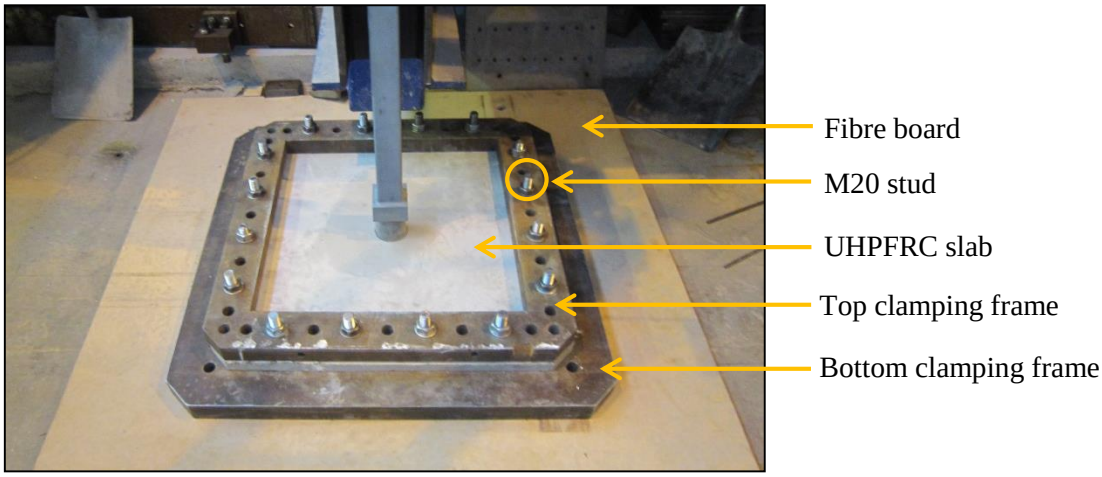

(a)

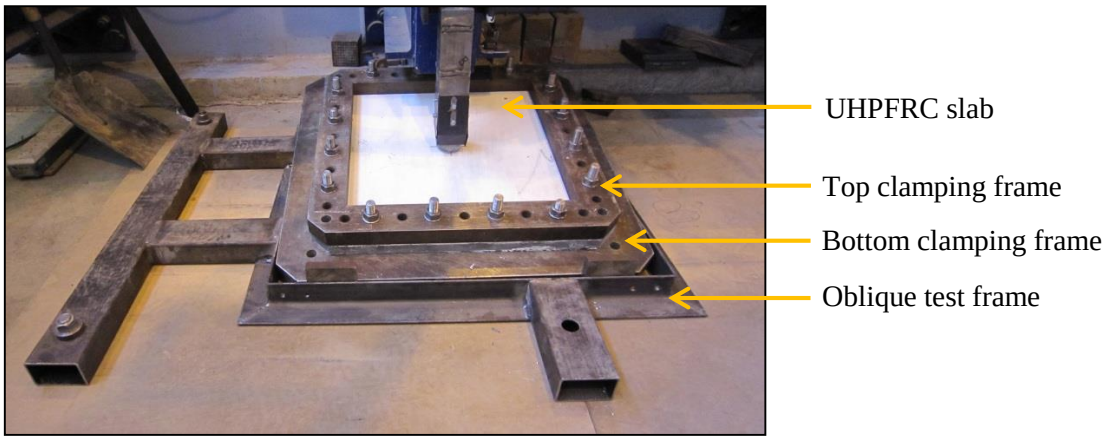

(b)

Figure 3.17: Frames arrangement for (a) normal, edge and corner impact cases; (b) oblique impact case.

The impact tests at central, edge and corner of the slab were conducted using three different impact energies by setting the drop height to be 2.8 m, 2.3 m and 1.5m. However, the oblique impact tests were carried out at 2.8 m drop height only. The edge impact was set at 175 mm in the y-direction from the centroid while the corner impact was set at 175 mm in both x- and y- directions (247.5 mm measured diagonally from the centroid) as shown in Figure 3.18. The oblique impact was set by tilting the slab with 10° angle. This condition changed the contact area from circular end of the UHPFRC cylinder to a point contact. The impact tests were conducted until slab failure, which was taken as full perforation or when the appearance of significant shear punching cracks.

After every strike, the measurement of the permanent deformation on the top face of the slab was recorded using Vernier calliper and stiff ruler. Other measurements such as the velocity, maximum deformation and contact force upon impact were derived from the Laser Doppler Velocimeter (LDV) data. Sketches showing the various impact conditions and the marking for the measurement of the permanent deformation are shown in Figure 3.18.

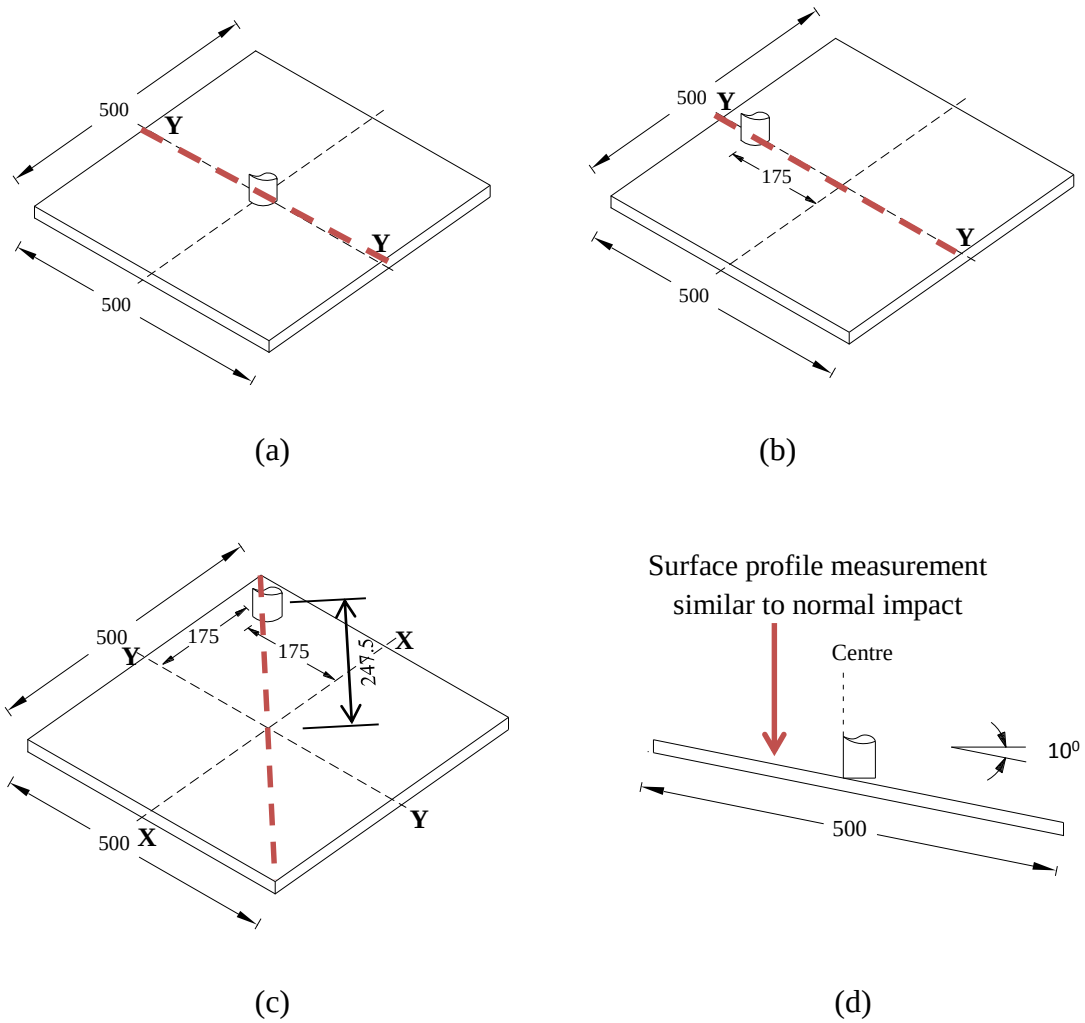

Figure 3.18: Details of impact conditions and location of the surface profile measurement (permanent deformation) for (a) centre; (b) edge; (c) corner; (d) oblique impact.

Digital photos were also taken in order to inspect the crack propagation and failure pattern on both faces of the slab. This exercise requires the test specimens to be detached from the clamping systems and may cause relaxation to the boundary of the fixed edges. In order to reduce such effect, the photos were taken at selected intervals. The tests were carried out on each slab until failure, taken as the full perforation of the slab or when the slabs were at the verge of failure where a clear shear punching crack and gaps can be observed. As such, multiple strikes to fail the slabs were expected. Similar concept was also adopted by Farnam *et al.* [16].

Due to the limited number of test specimens produced, each set of tests involved a set of two slabs. However, for the test involving central impact at 2.8 m drop height, three undamaged and pre-damaged slabs were tested first with the intention to check the ability of the test set up to produce repeatable results. Outline of the impact tests are given in Table 3.3.

Table 3.3: Outline of the impact tests.

Impact Scenario/Type of Slab	Number of UHPFRC Slabs
Central impact (undamaged slabs)	7
Central impact (pre-damaged slabs)	7
Edge impact (undamaged slabs)	6
Edge impact (pre-damaged slabs)	6
Corner impact (undamaged slabs)	6
Corner impact (pre-damaged slabs)	6
10° Oblique Impact (undamaged panels)	2*
10° Oblique Impact (pre-damaged panels)	2*

* Note: conducted at 2.8 m drop height only

The marking of the specimens was set based on the sequence Impact Location/Angle-Slab Type-Drop Height-Slab Number-Strike Number. The details of the marking are shown in Table 3.4.

Table 3.4: Details of the specimen marking.

Item	Marking	Notes
Impact location/angle	CEN	Centre
	EDG	Edge
	COR	Corner
	OBL	Oblique
Slab type	UD	Undamaged
	PD	Pre-damaged
Drop height (m)	1.5, 2.3 or 2.8	
Slab number	Pn (n = 1, 2, 3….)	Not shown for average data
Strike number	Sn (n = 1, 2, 3…)	Not shown for average data

3.6 Laser Doppler Velocimeter

A Laser Doppler Velocimeter (LDV) was used to measure the velocity of the impactor as well as the maximum deformation of the slab and contact force between the impactor and the slabs. LDV is a non-contacting instrument and as such, will not influence the system or become influenced by it [17]. Unlike load cells, the magnitude of the unknown contact force is not bounded to the capacity of the instrumentation. The main component of the LDV consists of:-

i) Laser system (two beams, red colour Helium-Neon laser, continuous wave with 632 nm wavelength)

ii) Bragg Cell (shifting the frequency of laser beam)

iii) Optic unit (transmitting and receiving optics) with lenses

iv) Fibre-optic cable

v) Burst Spectrum Analyzer (BSA) signal processor model 57N21.

The two laser beams produced were focused together via a lens on the optic unit. This backscatter-type LDV required some reflected beams impinging the impactor to be collected at the same lens for further processing. For this reason, a 25 mm width × 200 mm long high intensity reflective tape was placed on the surface of the SHS. The focal length from the lenses to the reflective tape was set at 400 mm. A computer was linked to the BSA via an interface card and setting of the BSA prior to the impact test was performed using BSA Flow software. The schematic arrangement of the LDV system is shown in Figure 3.19.

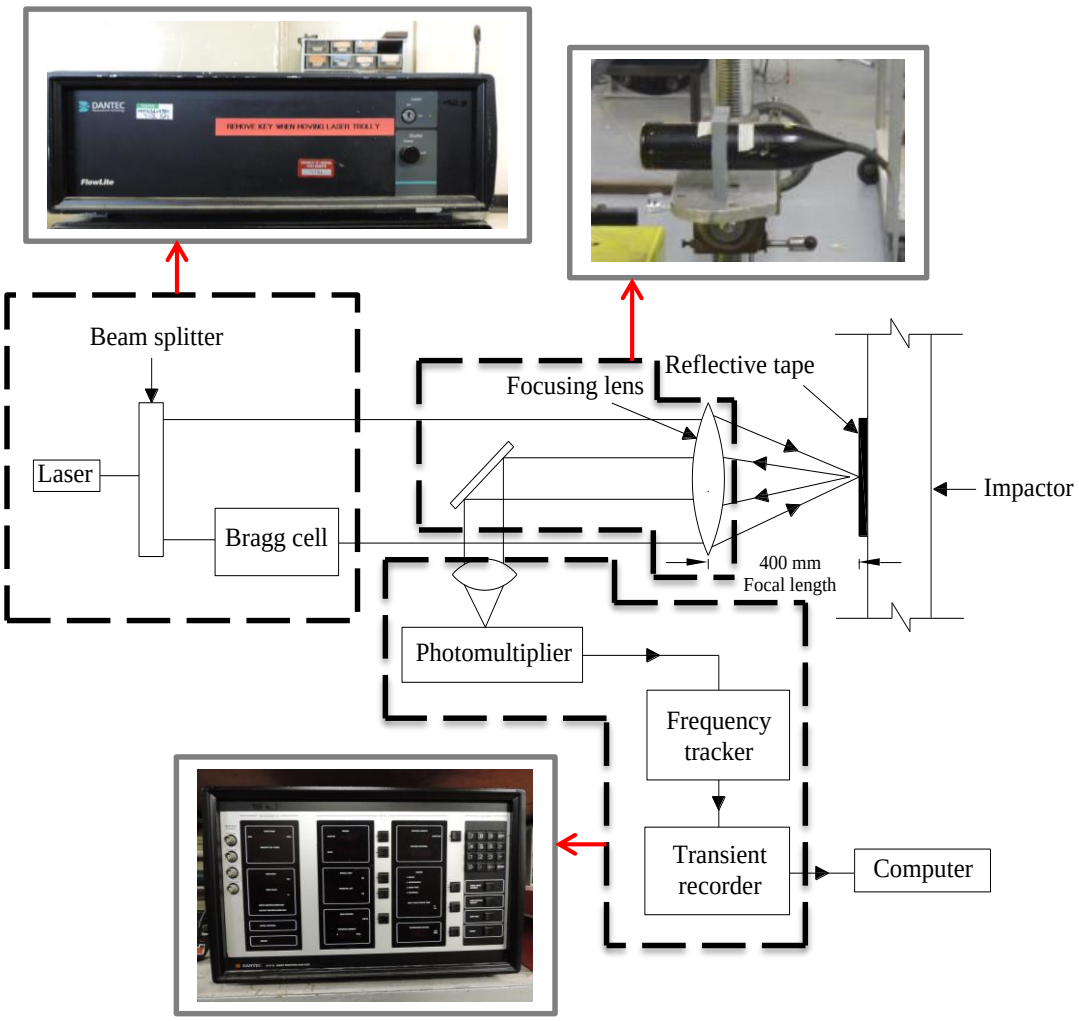

Figure 3.19: Schematic arrangement of the Laser Doppler Velocimeter.

3.6.1 Setting the Burst Spectrum Analyser

A Burst Spectrum Analyser (BSA) was used to analyse the real time signal from the LDV and loading the values in computer storage. The setting was carried out based on the recommendations from the User's Guide Manual [18].

The highest theoretical velocity from a 2.8 m drop height was calculated to be 7.41 m/s. By setting the velocity centre and velocity span to be 3.31 m/s and 13.2 m/s respectively, the BSA will take readings for any velocity in the range of -3.29 m/s and +9.91 m/s. The negative and positive velocities reflect the change in the direction (upward and downward movement of the impactor).

The record length defines the number of samples taken to the processor for analysis every time a digitized signal is detected. The choices were limited to 8, 16, 32 and 64. The high voltage and signal gain parameters were used to enhance the data quality and reduce signal noise. The signal's quality can be affected by the level of voltage supplied and gained in the signal amplifier, both through the photo-multiplier embedded in the BSA. The optimum value may be higher or lower depending on the laser power, LDV optics and position of the measurement volume. In this experiment, 848 V and 35 dB were selected.

In the case of measuring the velocity of a solid surface, the Doppler signals are expected to be in the form of quasi-continuous data rather than a burst-like signal. As such, the data collection mode is set to be continuous. High data collection may be required in order to capture the arrival velocity, impact and rebound phenomena. Sampling criterion was taken as 100,000 data points with maximum measurement interval 10 seconds, whichever came first. The general setting of the BSA is shown in Table 3.5.

Table 3.5: General setting of the BSA.

Context	Parameter	Value	Units
BSA Range/Gain	Velocity Range - Centre	3.31	m/s
	Velocity Range – Span	13.2	m/s
	Record Length	16	-
	High Voltage	848	V
	Signal Gain	35	dB
	Calibration	6.61	m/s
BSA Data Collection/Buffering	Data Collection Mode	Continuous	-
	Output Buffer Mode	Burst	-
	Number of Burst	100,000	-
	Measurement Intervals	10	S
	Validation Level	0	-
	Dead Time	0	ms
	Duty Cycle	100	%

3.6.2 Filtering Velocity-Time Raw Data

The pattern of a typical velocity-time raw data from a low velocity impact test using LDV and plotted in EXCEL is shown in Figure 3.20, and typically consists of 80,000 data points. The presence of a band-type data with random spikes rather than a single continuous line indicates that the true signals are superimposed with some noise. Assuming that V_A is the average velocity representing the true signals, the influence of noise has resulted in fluctuation of V_A with values above and below V_A. Filtering of such noise is a pre-requisite before the raw data can be used.

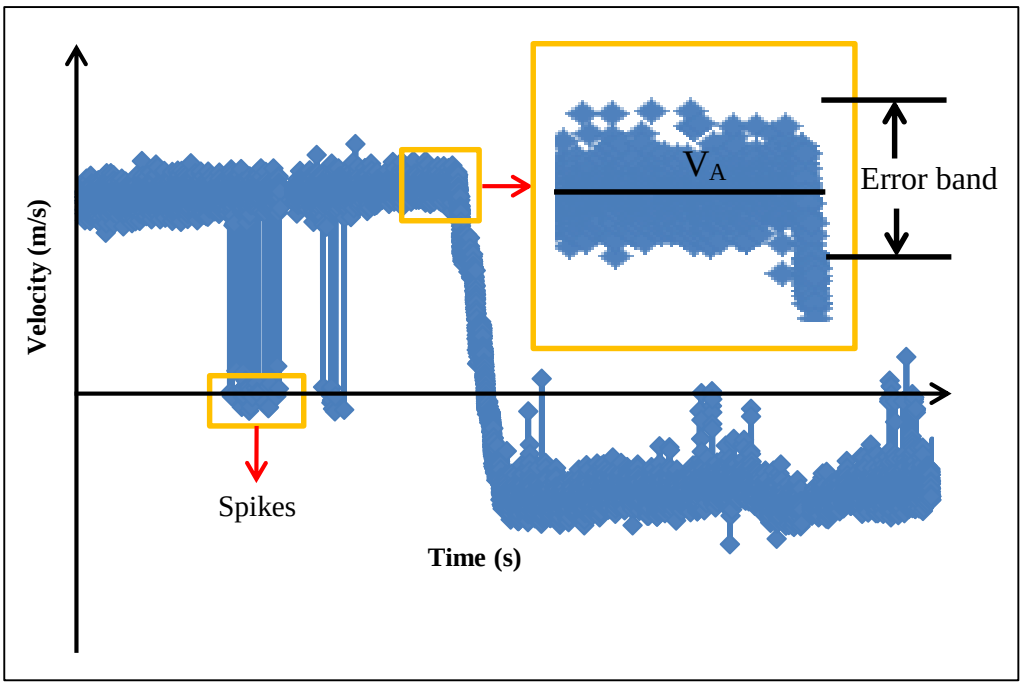

Figure 3.20: Typical velocity-time raw data from LDV.

There are many methods and filter types in signal processing. Some typical filter methods include Chebyshev, Butterworth and Bessel, while filter type would fall either under Low Pass, High Pass, Band Pass or Notch Pass. Each filter method has different properties and characteristics [19-24]. Figure 3.21 shows the frequency response curve for each type of filter. The main characteristic of the Butterworth filter is that the pass band is maximally flat (without any ripples) and gradual out-of-band attenuation. On the other hand, the Chebyshev filter is mathematically designed to achieve a faster and steeper out-off-band attenuation but at the expense of having ripples in the pass-band (non-linear phase response) that could lead to significant distortion in the signal. The Bessel filter has a flat pass band but very slow roll-off rate in the stop band that can cause time delay in the output. In this study, a Fourth Order Low Pass Butterworth Filter was selected for its smooth response and low overshoot advantages. The extremely flat pass band also resembled the pass band of an ideal filter. A similar filtering approach has been noted in some low velocity impact studies [25-26].

.

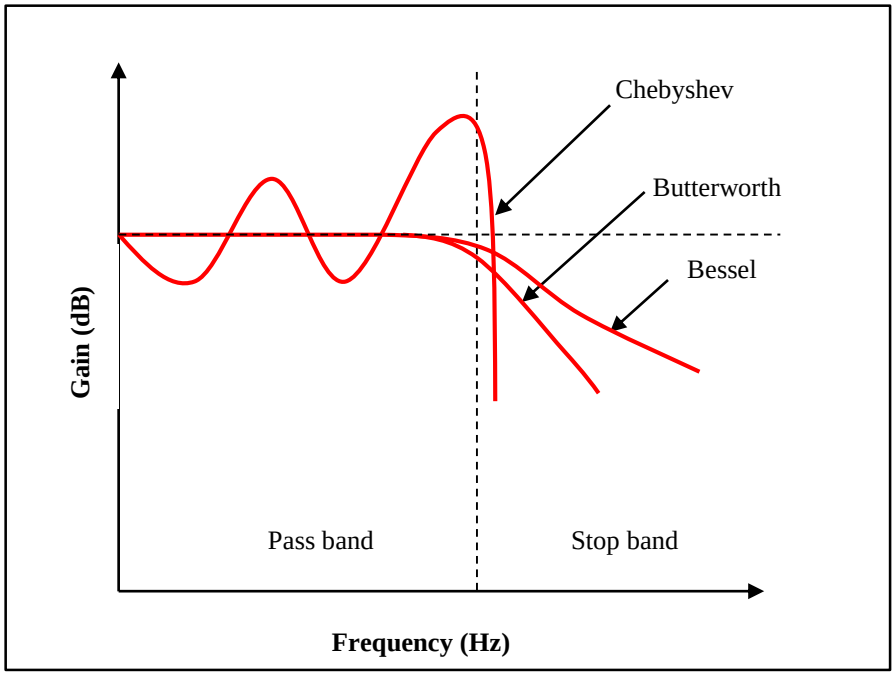

Figure 3.21 : Frequency response curve for different types of filter method.

The signal processing was performed using the Impression 6.0 software developed by Nicolet Instrument Technologies Inc. This software was selected because it is able to perform several tasks in signal processing such as spectrum analysis and filtering. Prior to the filtering process, the full data set was reduced to a suitable range within the event of contact and rebound. For example, the 80,000 data points in Figure 3.20 were reduced to 10,000 as shown in Figure 3.22.

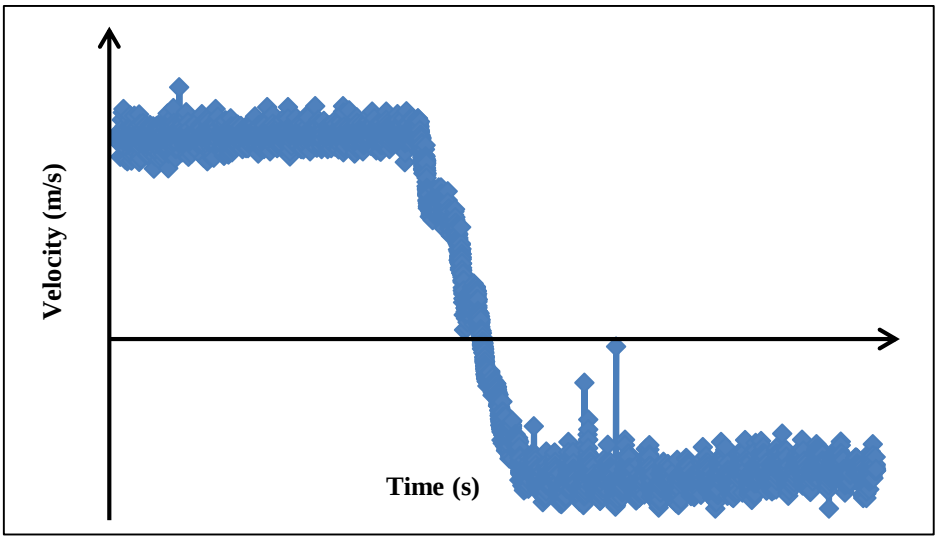

Figure 3.22: Reduced velocity-time raw data.

The reduced data set was then transferred to the Impression 6.0 software for linear interpolation in order to obtain an equal time step. Following that, the spectrum analysis using Fourier Transformation was carried out where the velocity data in the time domain was transformed into the frequency domain. Investigation into the possible source of noise and estimation of the cut-off frequency was carried out in this stage. Finally, the reduced data was filtered using the Fourth Order Low Pass Butterworth Filter. It is worth mentioning that the algorithm in the Fourier Transformation and the Butterworth Filter require equal time step. The flow chart showing the filtering process is presented in Figure 3.23.

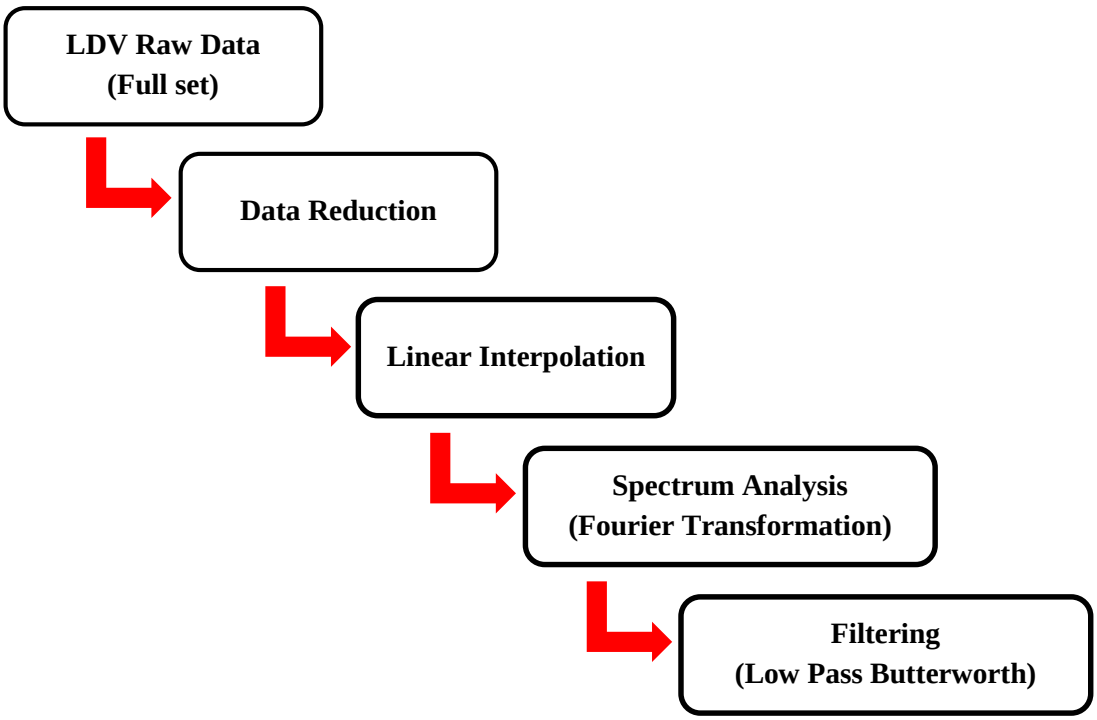

Figure 3.23: Flowchart showing the overall filtering process.

It is worth mentioning that the derivation of the contact force is related to the accuracy of the acceleration-time history that is being reflected in the slope of the velocity-time graph. The acceleration-time history was determined by performing a single differentiation to the velocity-time history from filtered LDV data. This technique is more preferable compared to a double differentiation technique that needs to be carried out by using optical displacement devices [27].

Wu and Chang [28] reported that an accurate determination of the acceleration history can be obtained by recording a large number of data during the short duration impact event, typically around 1000 data points. In statistical theory, as the sample becomes larger, the variability in the data becomes less and hence increases the accuracy of the results [29]. This larger sample will produce negligible effect when being linearly interpolated prior filtering process. Similarly, it can be expected that the filtering process will not significantly reduce the

accuracy of the velocity-time data and as such the derivation of acceleration-time and force-time data using the equation of motion can be justified.

According to Birch and Jones [17], peak forces are difficult to be measured under dynamic conditions with high-magnitude and short duration loading, regardless of the type of devices being used. This is due to the presence of reflected stress waves and vibrations in the system that may combine or act individually to produce a false peak. This phenomenon limits the investigation for determining the true peak force during an impact event. However, for comparison purposes, Birch and Jones [17] proved that the peak force derived from LDV data possessed strong similarity compared to the direct measurement from a load cell when filtered using the same cut-off frequency of 1000 Hz.

As the force-time history depends on the slope of the velocity-time raw data, the accuracy is highly dependent on the size of the data set and the continuity between each data especially in an impact event where the impact duration can be extremely short. Any missing data or a large gap in the time step between each data could affect the slope of the velocity-time history. This condition is possible when the target (impactor) vibrates excessively during motion and contact. The movement of the target normal to the lens affects the frequency shift of the reflected beams. As such, LDV should not be used if this situation cannot be avoided or improved.

3.7 Processing Filtered Velocity-Time Data

The filtered velocity-time data was processed to obtain relevant measurements in the impact study such as the impact velocity, maximum deformation and contact force. The impact velocity was taken as the velocity of the impactor at the instance of contact with the slab and taken directly from the filtered LDV data.

3.7.1 Maximum Deformation

In this case, the movement of the impactor was assumed to represent the deformation history of the slab at the point of contact and within the contact period. This can be achieved by calculating the area under the curve from the velocity-time history using the numerical integration as follows:-

$$s(t) = \int v\, dt\,, \tag{3.1}$$

where

$s(t)$ = deformation with respect to time.

The maximum deformation upon impact was taken as the total area under the curve that had a positive velocity-time relationship within the contact period.

3.7.2 Contact Force

The contact force-time history of the impact test was determined by firstly transforming the velocity-time data into an acceleration-time relationship and multiplied by the mass of the impactor using Newton's Second Law as follows:-

$$F(t) = m \times a(t), \tag{3.2}$$

where

$F(t)$ = force (N) with respect to time,

m = mass of the impactor (kg), and

$a(t)$ = acceleration (m/s^2) with respect to time.

The peak contact force was taken as the maximum value shown in the graph showing the force-time relationship.

3.7.3 Measuring the Maximum and Permanent Deformation

In order to gauge the true maximum and permanent deformation of the pre-damaged slabs, the datum of such measurement was taken along the profile of the existing permanent deformation produced under the pre-damaging exercise. The datum shown in Figure 3.24 (a) is the example for the midpoint measurement only. On the other hand, the datum for the undamaged slabs was taken as the original profile of the slabs as shown in Figure 3.24 (b).

(a)

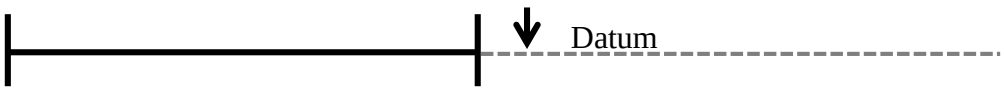

(b)

Figure 3.24: Datum for measuring the maximum and permanent deformation for (a) pre-damaged slab; (b) undamaged slab.

Consequently, the maximum and permanent deformation values were used to calculate the ductility ratio using the following equation from McCann and Smith [30]:-

$$Ductility\ Ratio\ = \frac{y_{max}}{y_{max} - y_{per}}\ , \tag{3.3}$$

where

y_{max} = maximum deformation (mm), and

y_{per} = permanent deformation (mm).

The denominator of the equation is commonly known as the 'elastic limit'.

3.8 Static Point Load Test

Static tests using a point load were performed on damaged and pre-damaged slabs using the hydraulic bending frame. The tests were conducted for the purpose of developing the resistance function and used in the numerical analysis. In this test, the boundary condition and the contact condition are kept similar to the impact test as shown in Figure 3.25. In order to avoid a punching effect onto the UHPFRC cylinder upon loading, the actuator was mounted with a steel block with a larger diameter than the cylinder. In this case, a 75 mm diameter steel block was used. The test was carried out under displacement control condition imposing a constant displacement rate of 40μm/s. The forces were evaluated from the 300 kN capacity ZWICK load cell. A ± 25mm nominal stroke LVDT was placed centrally at the bottom face of the slab to measure the deformation. The results and discussion on the static test are presented in Chapter 6.

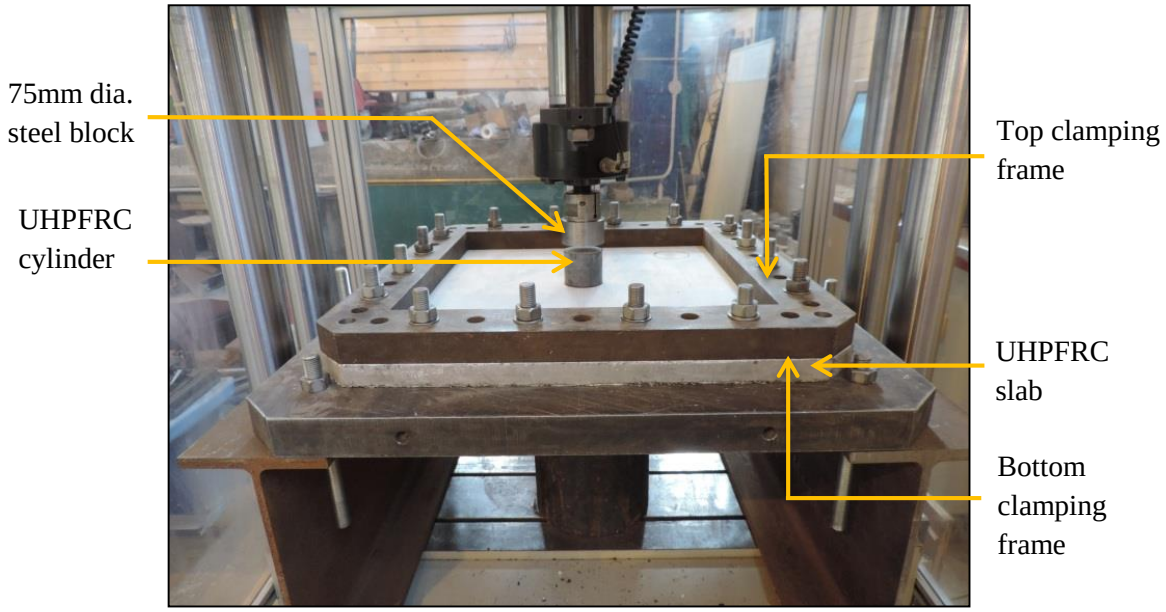

Figure 3.25: Static test set-up.

3.9 Summary of Chapter 3

This chapter presented the details of the experimental procedures involving the preparation of the UHPFRC slab (both undamaged and pre-damaged), the static pressure test, the impact test and the static point load test. The information gained from a series of trial tests on the existing UHPFRC slabs improved the preparation and quality of the pre-damaged specimens, shown by the consistency in the pressure-deformation curves. The impact resistance, responses and stiffness degradation of the pre-damaged slabs compared to the undamaged slabs were examined via low velocity drop-weight tests. In order to investigate the sensitivity of the impact location and angle, the drop tests were set at centre (normal and 10° oblique angle), edge and corner of the slab. Arrangements of the test set-up, including the modifications to cater for the oblique impact were also shown. This chapter also presented the pre-requisite procedures involving data reduction, interpolation and spectrum analysis prior filtering the raw velocity-time data from the LDV readings. Following that, the data was filtered using a Low Pass Butterworth Filter technique and processed to obtain the velocity at impact, maximum deformation and contact force. Finally, this chapter also presented the procedures and arrangement for the static point load test on the slabs using the bending test frame where the results from these tests were used to develop resistance functions for SDOF modelling.

3.10 References

[1] S. G. Millard, T. C. K. Molyneaux, S. J. Barnett and X. Gao, "Dynamic enhancement of blast-resistant ultra high performance fibre-reinforced concrete under flexural and shear loading," *International Journal of Impact Engineering*, *37*(4), pp. 405-413, 2010.

[2] A. M. T. Hassan, S. W. Jones and G. H. Mahmud, "Experimental test methods to determine the uniaxial tensile and compressive behaviour of ultra high performance fibre reinforced concrete (UHPFRC)," *Construction and Building Materials*, vol. 37, pp. 874-882, 2012.

[3] G. H. Mahmud, Z. Yang and A. M. T. Hassan, "Experimental and numerical studies of size effects of Ultra High Performance Steel Fibre Reinforced Concrete (UHPFRC) beams," *Construction and Building Materials*, vol. 48, pp. 1027-1034, 2013.

[4] British Standards Institution, *Cement composition, specifications and conformity criteria for common cements*, BS EN 197-1, 2011.

[5] British Standards Institution, *Ground granulated blast furnace slag for use in concrete, mortar and grout: Definitions, requirements and conformity criteria*, BS EN 15167-1, 2006.

[6] P. K. Mehta and O. E. Gjorv, "Properties of Portland cement concrete containing fly ash and condensed silica-fume," *Cement and Concrete Research*, vol. 12, no. 5, pp. 587-595, 1982.

[7] K. Habel, M. Viviani, E. Denarie and E. Bruhwiler, "Development of the mechanical properties of an ultra-high performance fiber reinforced concrete (UHPFRC)," *Cement and Concrete Research*, vol. 36, no. 7, pp. 1362-1370, 2006.

[8] British Standards Institution, *Silica fume for concrete: Definitions, requirements and conformity criteria*, BS EN 13263-1, 2005.

[9] British Standards Institution, *Aggregates for concrete*, BS EN 12620, 2002.

[10] S. J. Barnett, J. F. Lataste, T. Parry, S. G. Millard and M. N. Soutsos, "Assessment of fibre orientation in ultra high performance fibre reinforced concrete and its effect on flexural strength," *Materials and Structures*, vol. 43, no. 7, pp. 1009-1023, 2010.

[11] S. L. Yang, S. G. Millard, M. N. Soutsos, S. J. Barnett, and T. T. Le, "Influence of aggregate and curing regime on the mechanical properties of ultra-high performance fibre reinforced concrete (UHPFRC)," *Construction and Building Materials*, vol. 23, no. 6, pp. 2291-2298, 2009.

[12] British Standards Institution, *Testing hardened concrete. Compressive strength of test specimens*, BS EN 12390, 2009.

[13] G. K. Schleyer, N. J. Underwood, H. M. Do, J. K. Paik and B. J. Kim, "On pulse pressure loading of plates with holes," *Central European Journal of Engineering*, vol. 2, no. 4, pp. 496-508, 2012.

[14] S. S. Zaini, G. K. Schleyer, S. J. Barnett and N. J. Underwood, "High pressure static test on UHPFRC panels using pulse pressure loading rig," presented at the Awam International Conference on Civil Engineering, Malaysia, Aug. 28-30, 2012.

[15] American Concrete Institute, *Measurement of properties of fiber reinforced concrete*, ACI 544.2R-89, 1989.

[16] Y. Farnam, S. Mohammadi and M. Shekarchi, "Experimental and numerical investigations of low velocity impact behavior of high-performance fiber-reinforced cement based composite," *International Journal of Impact Engineering*, vol. *37, no.* 2, pp. 220-229, 2010.

[17] R. S. Birch and N. Jones, "Measurement of impact loads using a laser Doppler velocimeter," *Journal of Mechanical Engineering Science*, vol. 204, no. 1, pp. 1-8, 1990.

[18] DANTEC Measurement Technology, *BSA/FVA Flow Software: Installation and User's Guide*, DANTEC Measurement Technology, Denmark, 2000.

[19] R. Kaszynski, R and J. Piskorowski, "New concept of delay equalized low-pass Butterworth Filters," presented at the IEEE International Symposium on Industrial Electronics and Applications, Montreal, Quebec, July 9-13, 2006, pp. 171-175.

[20] W. Menzel and F. Bogelsack, "Bessel low pass filter in mixed planar waveguide techniques," presented at the 29th European Microwave Conference, Munich, Oct. 5-7, 1999, pp. 191-194.

[21] C. Matos and M. D. Ortigueira, "Fractional filters: An optimization approach," in *Emerging Trends in Technological Innovation*, L. M. Camarinha-Matos, P. Pareira and L. Rebeiro, Eds. Berlin: Springer, 2010, pp. 361-366.

[22] R. Shelton and A. Adkins, "Noise bandwidth of common filters," *IEEE Transactions on Communication Technology*, vol. 18, no. 6, pp. 828-830, 1970.

[23] D. E. Johnson, *Introduction to filter theory*, New Jersey: Prentice-Hall. 1976.

[24] R. Samar, "Digital filters for gain stabilization of flexible vehicle dynamics," presented at the 17th International Federation of Automatic Control World Congress, Seoul, July 6-11, 2008.

[25] K. C. G. Ong, M. Basheerkhan and P. Paramasivam, "Resistance of fibre concrete slabs to low velocity projectile impact," *Cement and Concrete Composites*, vol. 21, no. 5, pp. 391-401, 1999.

[26] L. S. Sutherland and C. G. Soares, "Scaling of impact on low fibre-volume glass–polyester laminates," *Composites Part A: Applied Science and Manufacturing*, vol. *38, no.* 2, pp. 307-317, 2007.

[27] E. Wu, H. J. Sheen and L. C. Chang, "Penetration force measurement of thin plates by Laser Doppler Anemometry," *Experimental Mechanics*, vol. 34, no. 2, pp. 93-99, 1994.

[28] E. Wu and L. C. Chang, "Woven glass/epoxy laminates subjected to projectile impact," *International Journal of Impact Engineering*, vol. 16, no. 4, pp. 607-619, 1995.

[29] S.K. Kachigan, *Statistical analysis*, New York: Radius Press. 1986.

[30] D. M. McCann and S. J. Smith, "Resistant design of reinforced concrete structures", *STRUCTURE Magazine*, pp. 22-26, 2007.

CHAPTER 4

NUMERICAL PROCEDURES

4.1 Introduction

This chapter presents the procedures and techniques involved in deriving the input parameters required to model the response of the slabs under low velocity impact. It covers both the finite element (FE) and analytical simulation accordingly.

The non-linear dynamic FE simulation in this study employed the ANSYS Explicit Dynamics Release 13.0 software package developed by ANSYS Incorporated. Explicit Dynamics is one of the applications in ANSYS Workbench and capable of performing non-linear dynamic analysis. In general, ANSYS Explicit Dynamics offers engineering solutions for simulating physical events that occur in a short period of time and may involve complete material failure. The solution method employs the Lagrange formulations in the ANSYS solver. The FE simulation also utilized the RHT Concrete Model embedded in the ANSYS Explicit Dynamics to represent the material model for UHPFRC. The calibrations of several input parameters based on the available test data are presented in detail.

As for the analytical simulation, the single-degree-of-freedom (SDOF) model was used for the slab subjected to the central impact only. This approach has been proven to be able to predict the response of slabs subjected to dynamic loading condition. This chapter explains the procedures to establish the SDOF parameters from the point load static test and recommendations from other research. This chapter also covers the procedure to derive the SDOF parameters theoretically for the undamaged slab only.

4.2 Development of the Model Geometry for FE Simulation

The assemblage of the full FE model in some low velocity drop test simulations can be very extensive depending on the complexity of the experimental work set up. Such complexity normally is embedded in the geometry of the specimen, impactor, boundary conditions as well as the connections itself. Discretization or meshing of the model into elements also requires careful selection of the mesh densities and connections in order to achieve reliable results and reduce the computational time. Where possible, simplification of the model can be justified without affecting the results significantly.

Three different geometries of the FE model that represent the UHPFRC slab subjected to the central impact are shown in Figure 4.1. The first geometry in Figure 4.1 (a) consists of UHPFRC slab, top and bottom clamping plate as well as the main component of the impactor. This geometry was then simplified by removing the two clamping frames, trimming the UHPFRC slab down to 500 mm × 500 mm and eliminating the hollow section forming the top part of the impactor as shown in Figure 4.1 (b). The reduction of the total mass of the impactor was balanced by increasing the density of the solid block to 10,700 kg/m^3. It is worth mentioning that Explicit Dynamics does not support single point mass where the impactor can be further simplified by assigning a single mass entity on the concrete cylinder to replace the steel portion. In order to reduce the computational time, the model was further simplified by introducing a symmetry plane, hence removing half of the model geometry as shown in Figure 4.1 (c).

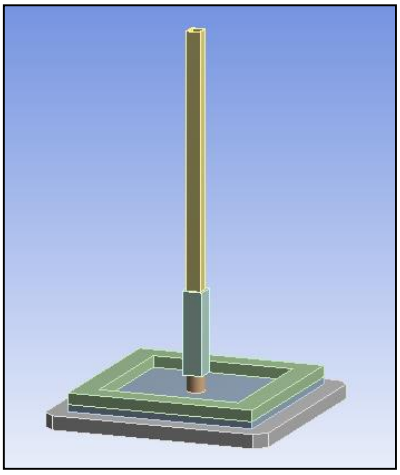

(a)

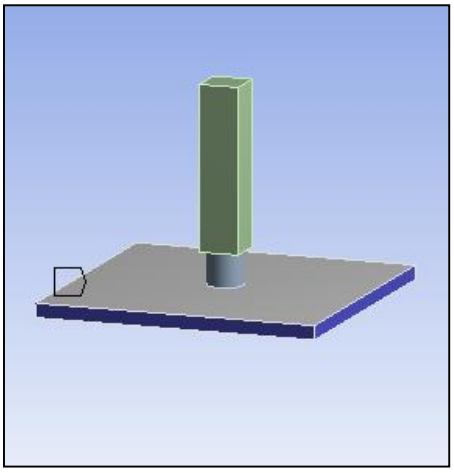

(b)

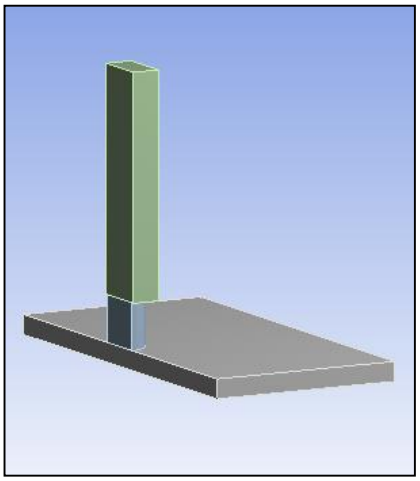

(c)

Figure 4.1: Geometry of FE model for central impact: (a) full model with clamping plates and impactor; (b) simplified full model (c) half-symmetry model.

In ANSYS Explicit Dynamics, the program will automatically select the appropriate element type based on the geometry of the model. In this case, the meshes were created using *SOLID 186*, a higher order 3-D solid element. This element is a quadratic element defined by 20 nodes. Each node has 3 degree of freedom, allowing translation in x, y and z directions.

4.3 Mesh Refinement

In a static analysis, mesh sensitivity analysis is performed to ensure that the accuracy of the results are not affected by the mesh size and can be compromised with the computational efficiency. Technically, finer mesh pattern will produce better results, although not necessarily more accurate. As the mesh becomes finer, the strains asymptotically approach a converged value where insignificant difference between successive runs is observed. In a static analysis, the error in the equilibrium condition is solved exactly at the nodes but only approximately along the element edges. On refining the mesh, this error is reduced to a point where the FE solution reaches a converged stable value provided there is no geometric discontinuity.

In a dynamic problem, stress and strain are a function of time and are caused by dynamic waves permeating through the solid medium. As the mesh is refined, higher frequency dynamic waves are propagated through the entire mesh and may not asymptotically approach a converged solution. Therefore, the mesh refinement in Explicit Dynamics is carried out normally for computational efficiency. Nevertheless, a significantly high volume mesh would affect the accuracy of the results. Also, the required degree of accuracy varies with the experimental demand. As such, a mesh sensitivity analysis was conducted on one of the FE models using an impact velocity of 5.0 m/s at the centre of the slab. Due to the fact that the contact between the impactor and the slab can be activated immediately, the simulation time was shortened to 0.015 s only. The results from this analysis are presented in section 6.2.1.

.

4.4 Edge Condition

The experimental work used studs and clamping frames to create a fully fixed edge condition. However, this technique is not able to assure perfectly fully fixed edges where, technically the slab needs to be cast monolithically with the support. It can be expected that the slab may slightly move horizontally during the impact event due to the presence of 2.5 mm clearance on each side between the stud and the opening.

In the FE model, the edge condition was modified using both the *Fixed Support* and *Displacement* commands together. As the size of the element along the edges was set to be 5 mm, five elements were generated along the thickness of the slab as shown in Figure 4.2 (a). The surface of the top and bottom element representing the support boundary was allowed to displace horizontally while keeping the vertical movement to be fixed as shown in Figure 4.2 (b). The other three surfaces of the remaining element were restraint in all directions as shown in Figure 4.3 (c). A sensitivity analysis was conducted to investigate the effect of using this approach and slab models with fully fixed edges. The results are presented in section 6.2.3.

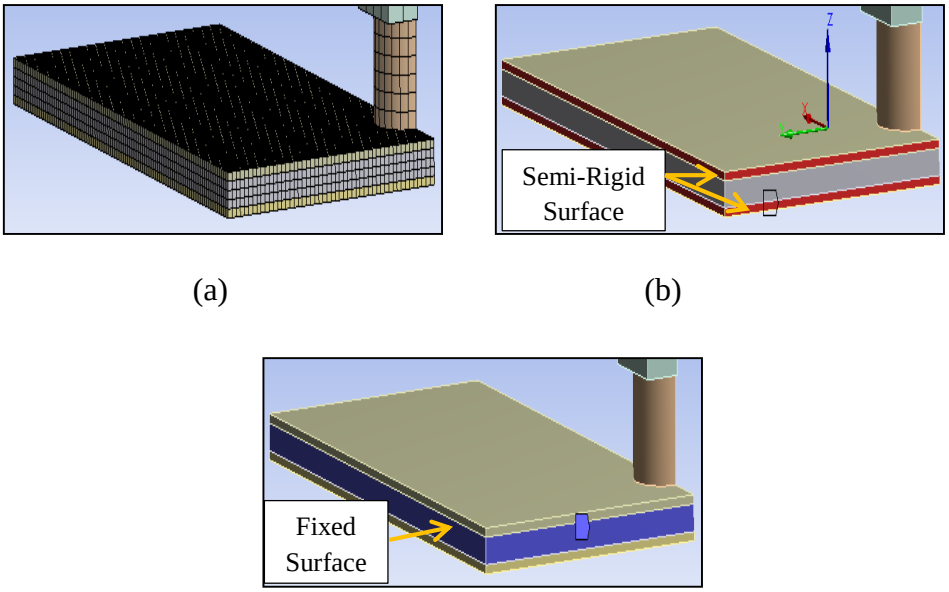

Figure 4.2: Modelling the support condition showing (a) five elements along the thickness of the slab; (b) top and bottom element with partially fixed surfaces; (c) fixed support surfaces.

4.5 Modelling the Pre-damaged Slab

The overall impact test involved undamaged and pre-damaged slabs. Unlike the impact test, the pre-damaging exercise was conducted under quasi-static pressure load. The load-deformation response duration was significantly longer and cannot be treated under dynamic environment. Explicit Dynamics package in ANSYS Workbench only allows dynamic analysis. However, it allows the package to be coupled with static analysis within the Workbench such as Static Structure, where Implicit Solver is used. Such combination may not be reliable unless two different sets of material properties, each one for static and dynamic simulation, can be maintained throughout the analysis.

A longer loading duration to simulate the quasi-static environment is also impractical and might be impossible in Explicit Dynamics as it involves millions of time increments. One of the possible methods in *Explicit Dynamics* for quasi-static loading is by introducing a static damping coefficient that can remove the dynamic effects. However, the damping coefficient cannot be assigned periodically or between intervals. Therefore, any attempt to couple a quasi-static environment together with a true dynamic condition in a single run will cause the end result to be inaccurate as the damping has influenced the actual dynamic response.

An attempt was made to overcome this constraint by setting the loading into two phases within the total simulation time as shown in Figure 4.3. In Phase 1, the slab was loaded with higher pressure but shorter loading duration. In order to avoid the overlapping of the response between the pressure loading and the impact load, the height of the impactor was raised to allow for the development of the permanent deformation. As the pressure loading declined, the impactor moved closer to the slab. The vibration effect developed by the pressure loading was reduced by extending the simulation time to 0.2 s until a steady state vibration was reached. The same running time was also used by Kishi *et al.* [1] in his impact study.

The impact loading in Phase 2 was set immediately after Phase 1 was ended. At this stage, the impactor hit the slab at its deformed geometry. The simulation time for the impact event was also extended to 0.2 s until a steady state vibration was achieved. At this stage, the impactor has already re-bounded. Similar to Phase 1, the permanent deformation under the impact loading was taken as the average value at the steady state vibration of the slab. Figure 4.3 shows the loading arrangement and the anticipated deformation pattern with respect to the overall running time for the impact simulation of the pre-damaged slab.

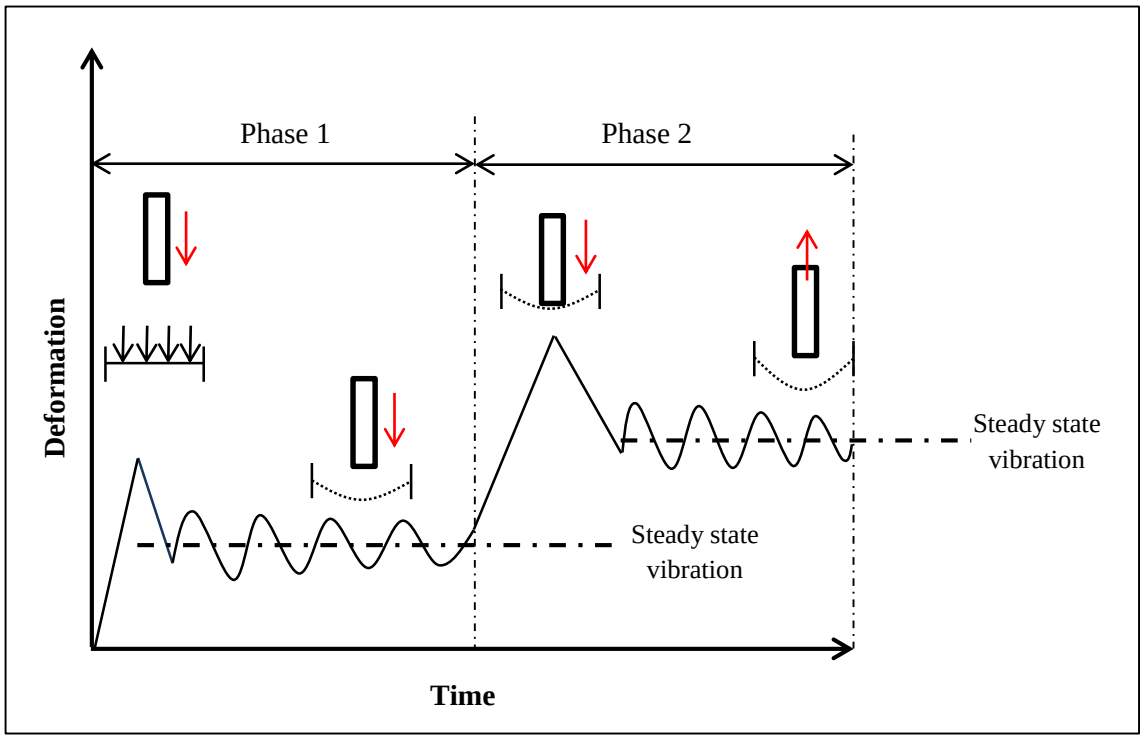

Figure 4.3: Loading arrangement in two phases for simulating the low velocity impact of the pre-damaged slab.

A sensitivity analysis was carried out in order to determine the most suitable pressure loading arrangement that was able to develop a similar maximum and permanent deformation with the actual pre-damaged slabs. The analysis was conducted on the FE model (slab only) by varying the peak pressure and rise time within a period of 0.2 s as shown in Figure 4.4. The results pertaining to this exercise are presented in section 6.2.2.

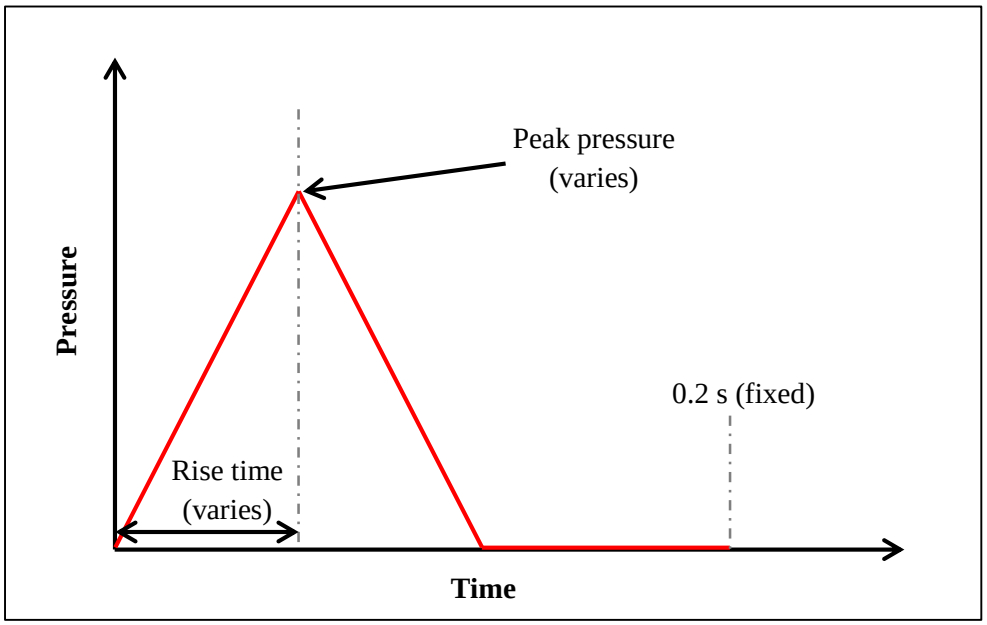

Figure 4.4: Pressure loading and rise time in the sensitivity analysis.

4.6 RHT Input Parameters

ANSYS Explicit Dynamics has the capability for modelling concrete under dynamic loading using the RHT material model [2-3] apart from other models such as the Drucker-Prager and the Johnson-Holmquist model. The RHT constitutive model is an advanced plasticity and shear damage model. It was first developed at the Ernst-Mach Institute in 1997. Later, the work became the PhD thesis of Dr. Riedel in the year 2000 with the support and guidance from Professor Thoma and Professor Hiermaier which led to the initial 'RHT' concrete model [4].

Similar to other hydrodynamic codes, the study of the dynamic response of materials and structures involves the governing equations and in ANSYS Explicit Dynamics they are established through the principle of conservation of mass, momentum and energy. The finite element analysis itself is a study of continuum, therefore another two relationships describing the material behaviour is required, namely the Equation of State (EoS) and a constitutive material model. RHT concrete model combines the *Strength Model* and *Failure Model* [4-7] that form the constitutive material model in a single formulation:

$$F_{fail}\left(P, \sigma_{eq}, \theta, \varepsilon_p, \dot{\varepsilon}_p\right) = \sigma_{eq} - \left[f_c \times Y^*\left(\varepsilon_p, P^*, \dot{\varepsilon}_p\right) \times F_{CAP}\left(P^*\right) \times R_3\left(\theta\right)\right] \tag{4.1}$$

$$Y^*\left(\varepsilon_p, P^*, \dot{\varepsilon}_p\right) = f_c\left[\varepsilon_p, {Y^*}_{TXC}\left(P^*, F_{RATE}\left(\dot{\varepsilon}_p\right)\right)\right] \tag{4.2}$$

where

σ_{eq} = equivalent stress,

f_c = uniaxial compressive strength,

$Y^*\left(\varepsilon_p, P^*, \dot{\varepsilon}_p\right)$ = pre-peak yield surface on the compressive meridian,

P = pressure,

P^* = pressure normalised by the uniaxial compressive strength,

θ = Lode angle,

ε_p = plastic strain,

$\dot{\varepsilon}_p$ = plastic strain rate,

F_{CAP} = pressure dependent elastic cap function,

$R_3(\theta)$ = third invariant dependency,

$Y^*{}_{TXC}\left(P^*, F_{RATE}(\dot{\varepsilon}_p)\right)$ = pressure and rate dependent peak surface on the compressive meridian and

$F_{RATE}(\dot{\varepsilon}_p)$ = strain rate dependency.

The strain rate independent compressive meridian in RHT formulation is developed through the following equations:

$$Y^*{}_{TXC}(P^*) = A(P^* - P_s{}^*)^n \tag{4.3}$$

$$P_s{}^* = \frac{1}{3} - \left(\frac{1}{A}\right)^{\frac{1}{n}} \tag{4.4}$$

A and *n* are the failure surface parameters that define the shape of the failure surface as a function of pressure. On the other hand, P_s* is the spall strength. The curve produced from equation (4.3) is required to go through the point of uniaxial compression and this part is explained in section 4.6.2.3.

Strain rate effects are incorporated into the equation through the increases in peak strength. Two different terms are used for compression and tension, defined as:

$$F_{RATE} = \begin{cases} \left(\frac{\dot{\varepsilon}}{\dot{\varepsilon}_0}\right)^{\delta} \\ \left(\frac{\dot{\varepsilon}}{\dot{\varepsilon}_0}\right)^{\alpha} \end{cases} \tag{4.5}$$

where

F_{RATE} = represents the dynamic increase factor (DIF) as the function of strain rate $\dot{\varepsilon}$,

α and δ = user defined parameters and

$\dot{\varepsilon}_0$ = reference strain rate (quasi-static).

The minimum value F_{RATE} is 1.0. This rate enhancement factor is applied to the peak strength surface using the equations:

$$Y^*_{TXC}\,(P^*, F_{RATE}(\dot{\varepsilon})) = A_{dyn}\left(P^* - P^*_{s,dyn}\right)^n \tag{4.6}$$

$$A_{dyn} = AF_{RATE}^{\,1-n} \tag{4.7}$$

$$P^*_{s,dyn} = F_{RATE}\left(\frac{1}{3} - \frac{1}{A}^{\frac{1}{n}}\right) \tag{4.8}$$

Figure 4.5 shows a typical deviatoric section plane of a strength surface. In the case of concrete material, the deviatoric section changes from triangular shape at low pressure (brittle condition) to a circular shape at high pressure (ductile condition). In RHT concrete model, the transition is represented through the third invariant dependent term $R_3(\theta)$ and evaluated by the following equations:

$$R_3(\theta) = \frac{2(1-\psi^2)cos\theta + (2\psi-1)(4(1-\psi^2)cos^2\theta + 5\psi^2 - 4\psi)^{\frac{1}{2}}}{4-(1-\psi^2)cos^2\theta + (1-2\psi)^2} \tag{4.9}$$

$$\psi = \psi_0 \times B_Q \times P^* \tag{4.10}$$

$$\cos(3\theta) = \frac{3(3)^{\frac{1}{2}} \times J_3}{(2)^{\frac{3}{2}} \times (J_2)^{\frac{1}{2}}} \tag{4.11}$$

where

ψ = ratio of a material tensile strength to compressive strength,

ψ_0 = tensile to compression meridian ratio at zero pressure,

B_Q = rate at which the fracture surface transits from a triangular to a circular form with increasing pressure and

J_2 & J_3 = second and third invariants of the deviatoric stress tensor.

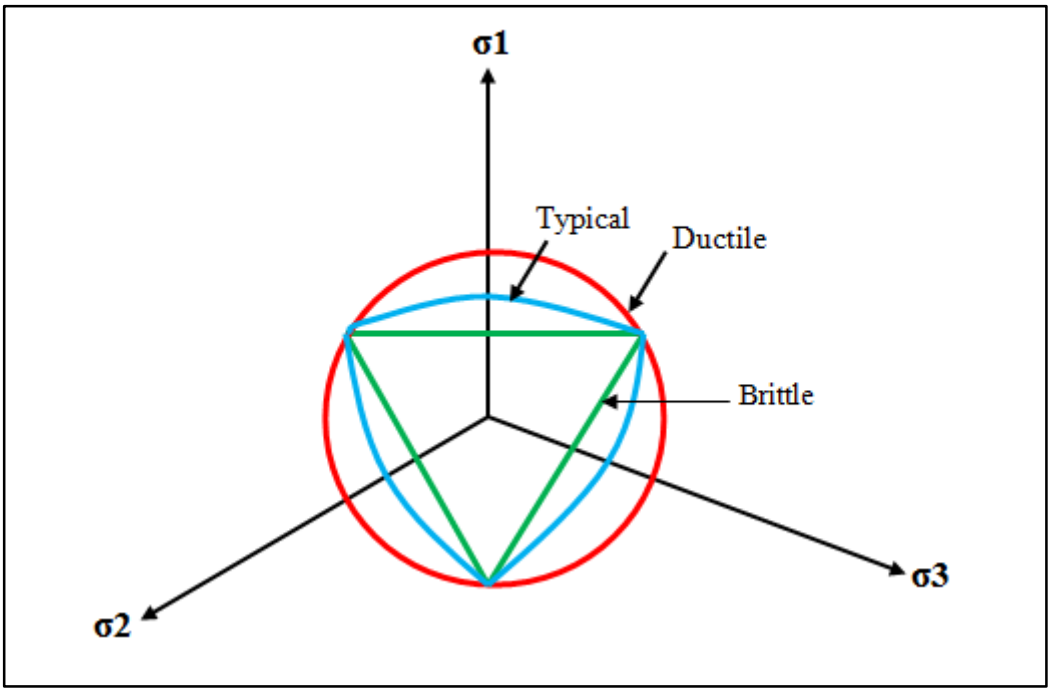

Figure 4.5: Deviatoric cross section of a strength surface.

Figure 4.6 illustrates the concept of strain hardening based on a uniaxial compression curve. In order to allow for strain hardening behaviour, an elastic limit surface and a hardening slope is introduced. The elastic limit surface is scaled down from the peak surface by the normalised elastic strength parameters (user defined). The pre-peak yield surface is defined through the interpolation between the elastic and peak surfaces based on the ratio of elastic and plastic shear moduli using:

$$Y^* = \frac{\varepsilon_p}{\varepsilon_{p,pre}} (Y^*_{TXC} - Y^*_{el}) \tag{4.12}$$

$$\varepsilon_{p,pre} = \frac{Y^*_{TXC}}{3G} \times \frac{G}{G - G_{pl}} \tag{4.13}$$

where

Y^*_{el} = initial elastic limit scaled down from peak surface,

ε_p = plastic strain, accumulated as soon as elastic surface is exceeded,

$\varepsilon_{p.pre}$ = pre-peak plastic strain,

G = shear modulus and

G_{pl} = plastic shear modulus.

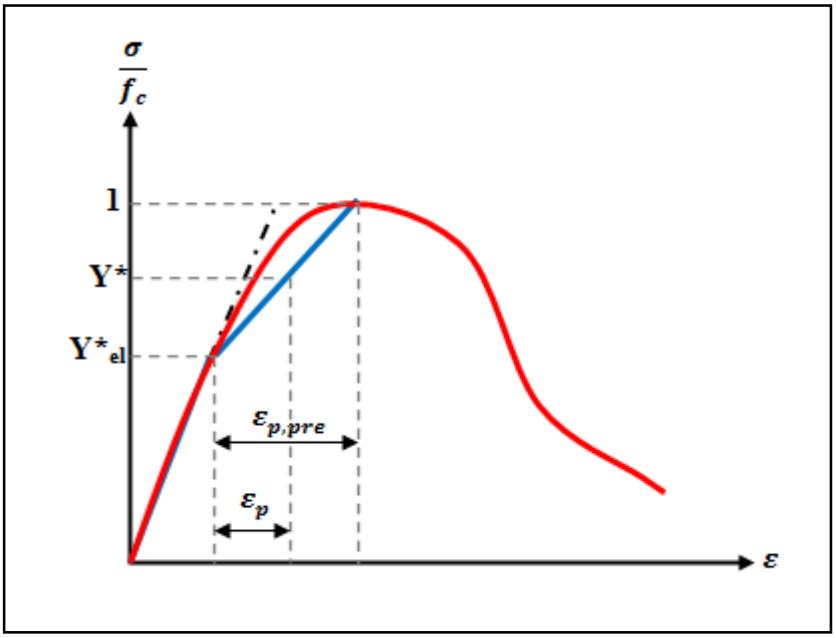

Figure 4.6: Concept of strain hardening in RHT concrete model.

Damage is assumed to accumulate due to the shear induced cracking once the peak yield has been exceeded. A damage index *D* is used to determine the value of the current strength surface using the relationship:

$$D = \sum \frac{\Delta \varepsilon_p}{{\varepsilon_p}^{fail}} \tag{4.14}$$

$${\varepsilon_p}^{fail} = MAX\left(D1(P^* - htl^*)^{D2}, {\varepsilon_{p,min}}^{fail}\right) \tag{4.15}$$

$$htl^* = -\frac{f_t}{f_c} \times \frac{f_s}{f_c} \times \psi_0 \left(\frac{\frac{f_t}{f_c}}{3\left(\psi_0 \frac{f_s}{f_c} - \frac{f_t}{f_c}\right)} \right) \tag{4.16}$$

where

D = damage index (ranging from zero to unity),

$D1$ & $D2$ = damage constants,

${\varepsilon_p}^{fail}$ = pressure dependent plastic strain to failure,

${\varepsilon_{p,min}}^{fail}$ = minimum strain to failure (complete damage at low pressure),

htl^* = normalised hydrodynamic tensile limit,

$\frac{f_t}{f_c}$ = normalised tensile strength and

$\frac{f_s}{f_c}$ = normalised shear strength.

The strength of the completely crushed material in the present model is defined through the reduction in strength (strain softening) using equation:

$$Y_{res} = (B \times (P^*)^m) \quad (4.17)$$

where

Y_{res} = residual strength surface and

B & m = residual strength parameters.

On the other hand, the current shear modulus of the crushed material $G_{fractured}$ is defined through:

$$G_{fractured} = (1 - D)G + DG_{residual} \quad (4.18)$$

where

$G_{residual}$ = residual shear modulus at fracture (post-damage shear).

RHT concrete model requires substantial amount of input parameters as shown in Table 4.1. However, the uniqueness is that some parameters are derived based on normalized values and can safely be used for a wide range of concrete strength. Default values for plain concrete with compressive strength of 35 MPa and 140 MPa are provided in the code as a guideline. It is worth mentioning that 18 default values are identical.

The default parameters in thee RHT Concrete model are derived based on normal and high strength plain concrete, without the inclusion of fibres and as such some default values are not valid for UHPFRC material. Although no specific characterization tests were conducted in this study, the derivation of several input parameters were carried out based on the work by other researchers as presented in the following sections.

Table 4.1: RHT input parameters and the default values for concrete grade C35 and C140.

Parameter	**Feature**	**C35**	**C140**
Compressive strength f_c (MPa)	Fracture surface	35	140
Normalized tensile strength	Fracture surface	0.1	0.1
Normalized shear strength	Fracture surface	0.18	0.18
Failure surface parameter *A*	Fracture surface	1.6	1.6
Failure surface parameter *n*	Fracture surface	0.61	0.61
Tension/compression meridian ratio	Fracture surface	0.6805	0.6805
Brittle to ductile transition	Fracture surface	0.0105	0.0105
Hardening slope	Strain hardening	2.0	2.0
Normalized elastic strength 1	Strain hardening	0.70	0.70
Normalized elastic strength 2	Strain hardening	0.53	0.53
Cap on elastic surface	Compaction damage	Yes	Yes
Residual strength constant *B*	Strain softening	1.6	1.6
Residual strength exponent *m*	Strain softening	0.61	0.61
Compressive strain rate exponent α	Fracture surface	0.032	0.00909
Tensile strain rate exponent δ	Fracture surface	0.036	0.0125
Maximum fracture strength ratio	Residual strength	1×10^{20}	1×10^{20}
Damage constant *D1*	Shear induced damage	0.04	0.04
Damage constant *D2*	Shear induced damage	1	1
Minimum strain to failure	Erosion strain	0.01	0.01
Residual shear modulus fracture	Post-damage shear	0.13	0.13
Shear modulus (MPa)	Elastic Response	16,700	22,060
Bulk modulus (MPa)	Linear Equation of State	35,270	35,270

4.6.1 Compressive Strength, Normalised Tensile Strength and Normalised Elastic Strength 1

These parameters were determined from the work of Hassan *et al.* [8] where the same design mix was used. It was reported that the compressive and tensile strength of UHPFRC were 150 MPa and 9.1 MPa, respectively. As such, the ratio between tensile and compressive strength was taken as 0.061. This Normalised Tensile Strength value is lower compared to the default value of 0.1 in the RHT concrete model as well as in the general relationship between compressive and tensile strength for plain concrete reported by Neville [9].

Figure 4.7 [8] shows the graph of the direct tensile strength versus strain reproduced from Hassan *et al.* [8]. The tensile strength of the UHPFRC dog bone specimen is in a linear relationship approximately up to 6.8 MPa before strain hardening takes place. Once the peak tensile strength is reached, the tensile strength decreases gradually, commonly known as the strain softening branch. The ratio of the elastic strength over the maximum tensile strength is estimated to be 0.75. This Normalised Elastic Strength 1 value is higher compared to the default value for grade 35 and 140 concrete in the RHT concrete model possibly due to the influence of strain hardening.

Figure 4.7: Direct tensile test [8].

4.6.2 Input Parameters from Tri-axial Tests

The tri-axial test on UHPFRC-type material was taken from the work of Farnam *et al.* [10]. Several types of concrete class ranging from high strength to UHPFRC were tested at various confinement pressures. SIFCON 5, a UHPFRC class with cylindrical compressive strength of 146.6 MPa was selected due to its closeness to the current UHPFRC strength. It should be highlighted that currently very limited data can be found pertaining to the behaviour of UHPFRC under tri-axial loading condition.

4.6.2.1 Normalised Shear Strength

The normalised strength was determined from the Mohr Circle failure envelope diagram where the half circles were plotted using two normal pressure points (σ_n), namely the confinement pressure (CP) and the maximum axial pressure as shown in Figure 4.8 [10]. The average of these two points serves as the origin of the half-circle. A common tangent line that best fits all three half circles was drawn and extended until it touches the y-axis. In this case, the minimum shear strength was estimated to be 37 MPa at σ_n = 0 and normalised with the unconfined compressive strength of 146.6 MPa. This Normalized Shear Strength was calculated to be 0.25.

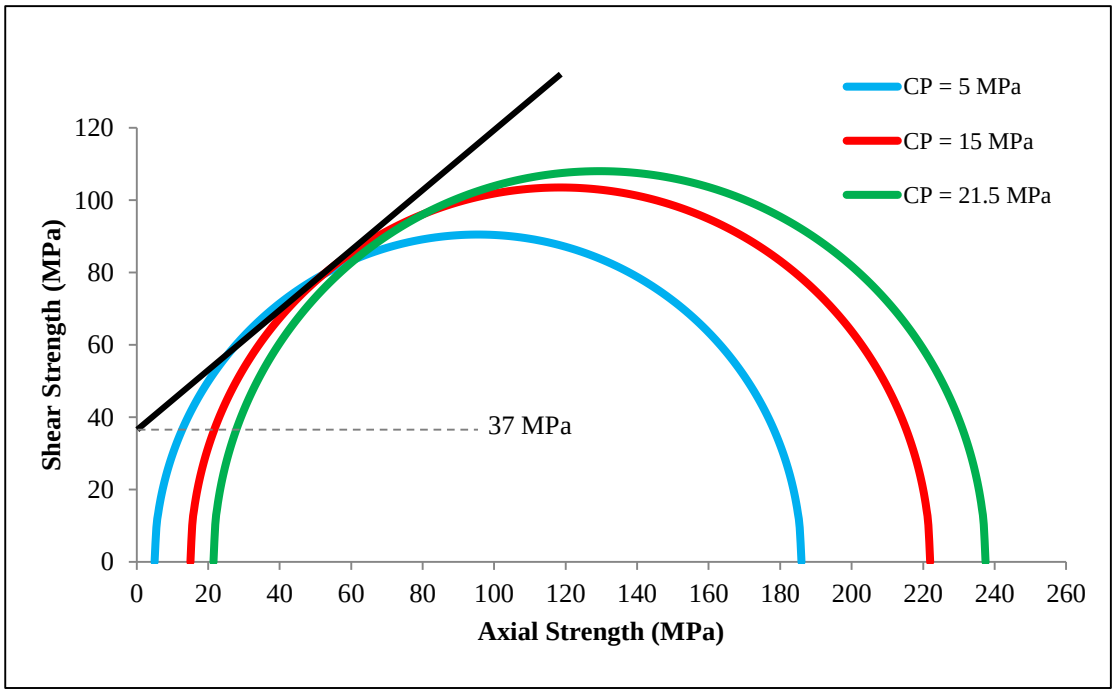

Figure 4.8: The Mohr Circles constructed from the tri-axial test by Farnam *et al.* [10].

4.6.2.2 Normalised Elastic Strength 2

Figure 4.9 [10] shows the tri-axial test results for SIFCON 5 reported by Farnam *et al.* [10]. The elastic strength was estimated by assuming the end of the linear relationship of the stress-strain curve and given in Table 4.2 [10].

Figure 4.9: Tri-axial results for SIFCON 5 at different confinement pressure [10].

Table 4.2: Elastic strength of SIFCON 5 at various confinement pressure [10].

Type	$\sigma_2 = \sigma_3$ (MPa)	Elastic Strength (MPa)	σ_1 (MPa)	Normalised Elastic Strength 2
SIFCON 5	0	100	146.6	0.68
	5	125	181	0.69
	15	140	207	0.68
	21.5	150	216	0.69

The ratio of the elastic strength over maximum axial stress is consistent within the values of 0.68-0.69 but relatively higher compared to the default value of 0.53. Tan [11] explained this situation and reported that the presence of fibres in the UHPFRC matrix had increased the elastic range with the development of strain hardening as opposed to plain concrete as shown in Figure 4.10 [11]. The ratio of 0.68 was used in this study.

Figure 4.10: Stress-strain curve for plain concrete under tri-axial test showing insignificant strain hardening [11].

4.6.2.3 Failure Surface Parameters (*A* and *n*)

Other parameters that can be derived from the tri-axial test are associated with the failure and residual surface along the compression meridian. In RHT concrete model, the peak surface on the compression meridian is represented through the equations:-

$$Y^*{}_{TXC}\,(P^*) \quad = \quad A(P^* - P_s{}^*)^n \tag{4.19}$$

and

$$P_s{}^* \quad = \quad \frac{1}{3} - \left(\frac{1}{A}\right)^{\frac{1}{n}} \quad , \tag{4.20}$$

where

$P_s{}^*$ = normalised hydrodynamic tensile limit,
A = failure surface constant (user defined value), and
n = failure surface exponent (user defined value).

The failure surface must satisfy the condition where it is required to pass through the point of uniaxial compression at coordinate ($\frac{1}{3}$, 1). Such condition has restricted the manipulation of equation (4.19) because any changes made to the parameters *A* and *n* apart from the default values will shift the uniaxial compression coordinate away from ($\frac{1}{3}$, 1).Therefore, the default values A = 1.6 and n = 0.61 must be used. Furthermore, the default values produced a reasonably good agreement with the tri-axial results as shown in Figure 4.11 and Table 4.3 where the maximum difference was calculated to be 12%.

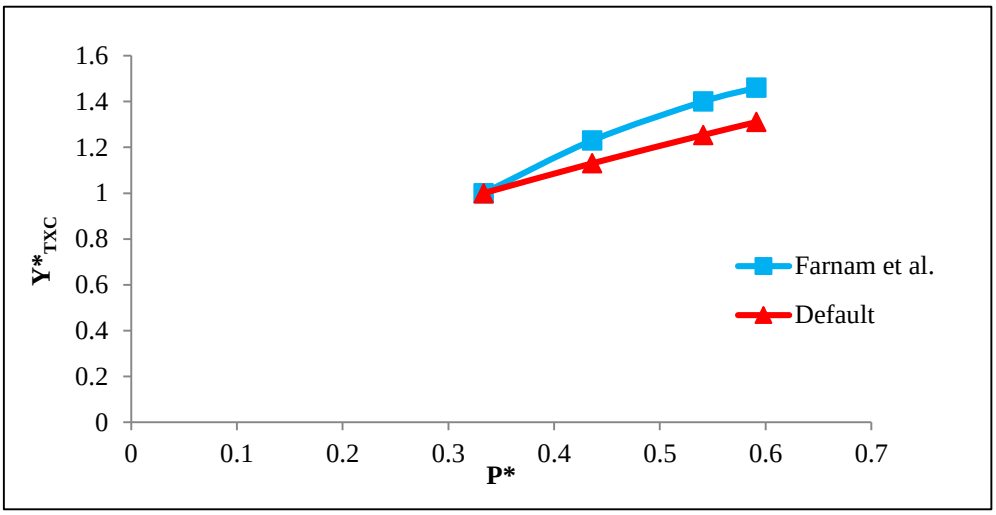

Figure 4.11: Comparison between the failure surfaces plotted using the default values and the experimental results by Farnam *et al.* [10].

Table 4.3: Percentage difference for the failure surface measurement using the default values compared with the experimental results by Farnam *et al.* [10].

Average stress (MPa)	***P****	***Y***$_{TXC}$* **(experiment)**	***Y***$_{TXC}$* **(default *A* & *n*)**	**Difference (%)**
48.67	0.33	1.00	1	0
63.67	0.44	1.24	1.13	8.87
79.00	0.54	1.42	1.25	11.97
86.33	0.59	1.48	1.31	11.49

4.6.2.4 Residual Strength Parameters (*B* and *m*)

In ANSYS, the residual surface, y_{res} , is calculated from the following equation:-

$$y_{res} = B \times (P^*)^m \tag{4.21}$$

where *B* and *m* are user input values (default values 1.6 and 0.61, respectively).

A typical stress-strain response for plain concrete under tri-axial loading and the corresponding failure surfaces on the compression meridian is illustrated in Figure 4.12 (a) and Figure 4.12 (b), respectively. Upon loading at a specified confinement pressure, the stress-strain curve will first reach the elastic surface (point 1). At this stage, if the axial stress is released then the material will return to its initial form as no permanent deformation or fracture is formed. With increase in the axial pressure, the material will reach its maximum strength/failure surface where crushing of the concrete will take place and cracks will develop (point 2). Once the failure surface is reached, RHT formulation will then scale it down towards the residual strength/surface where the concrete still maintains a certain level of shear strength (point 3) contributed by the friction between the crushed particles.

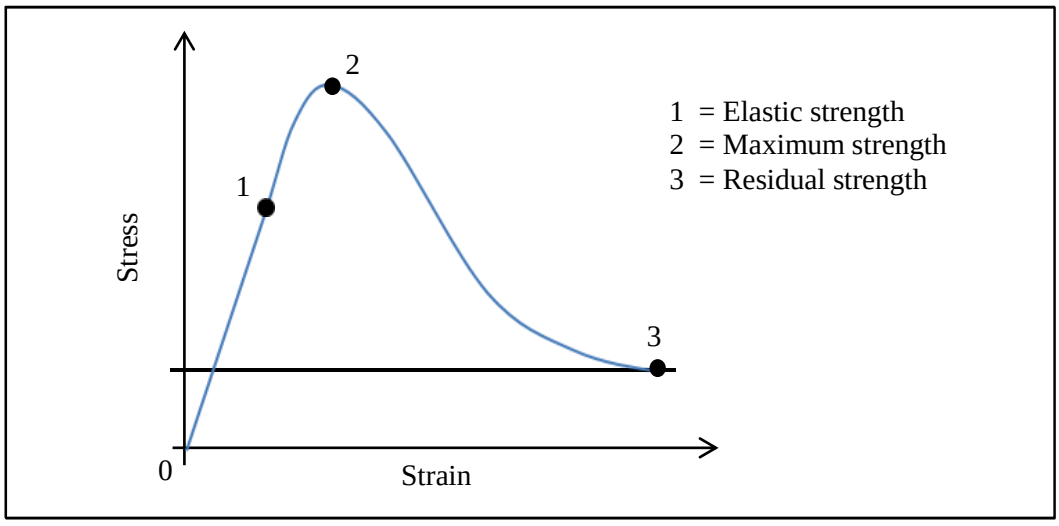

(a)

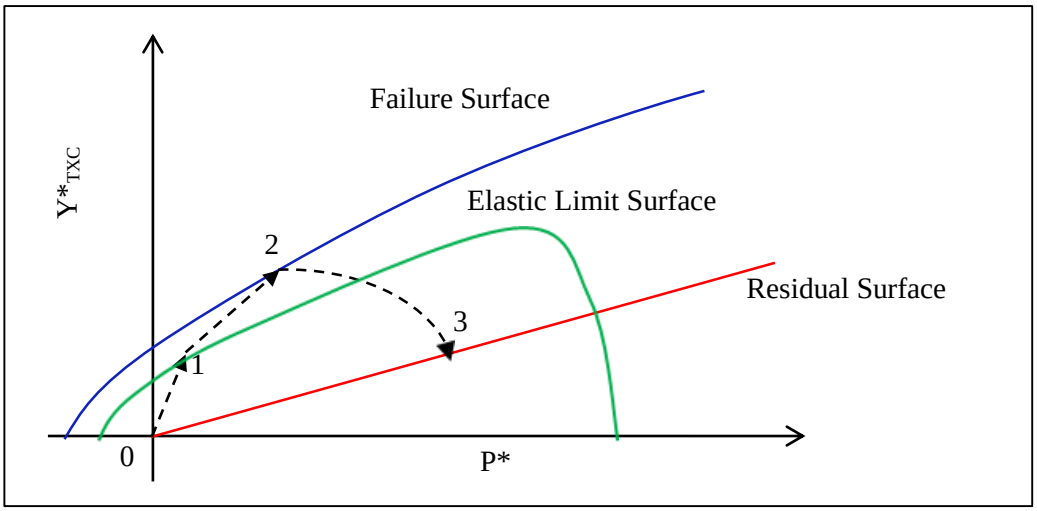

(b)

Figure 4.12: Correlation between tri-axial results and material response shown by (a) stress-stress diagram; (b) surface strength along the compression meridian.

In a typical tri-axial test involving plain concrete, the residual strength can be captured after the softening branch as shown in Figure 4.13 [10]. In this case, a complete stress path is achieved. However, this response may not be achievable for UHPFRC material where the UHPFRC still resists the radial stress without complete failure even at zero stress due to its enhanced tensile strength [12] as shown earlier in Figure 4.9. As a result, the final residual strength and the post-peak behaviour for UHPFRC material may be difficult to achieve in a tri-axial test and the default values need to be calibrated accordingly.

Figure 4.13: Tri-axial test result for plain high strength concrete [10].

In order to demonstrate the consequences of using the default values, the curves for the residual surfaces were plotted using equation (4.21) together with P^* from the tri-axial test [10] as shown in Figure 4.14. It can be seen that the curve for the residual surface calculated using B = 1.6 is in the higher region compared to the elastic surface, therefore not following the material response along the compression meridian as shown earlier in Figure 4.11 (b). Tu and Lu [6] explained that this inconsistency was due to the simplification made on the deviatoric cross-section plane in the principle stress space. The RHT concrete model used the standard circular deviatoric cross-section in its algorithm as opposed to the more realistic triangulated cross-section. This simplification has caused unnecessary strain hardening after the peak failure surface is reached rather than the softening branch, as normally expected.

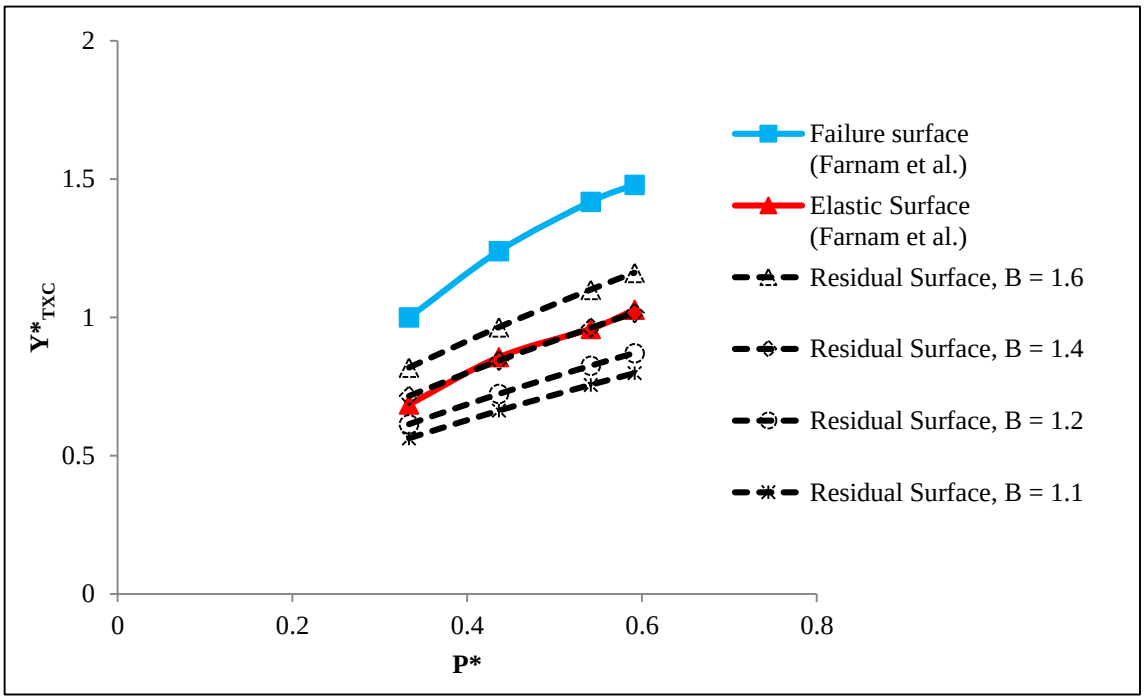

Figure 4.14: Position of the residual surface along the compression meridian by varying the parameter B with respect to the failure and elastic surface.

One possible way to overcome this issue without altering the shape of the residual surface is to reduce the constant *B* [6]. Obviously, the constant *B* can take many values as long as the residual surface falls below the elastic regime. As shown in Figure 4.14, the residual surface coincides with the elastic surface when *B* = 1.4. Similarly, when *B* = 1.2, the residual surface is still significantly close to the elastic surface at the lowest *P** value and moves away from it when *B* = 1.1. As such, the initial value for B is taken as 1.1 and calibrated until a fair agreement with the experimental data is reached. Using a lower value for *B* will only reduce the residual strength and expedite the failure of the material.

4.6.3 Strain Rate Effect

Concrete, regardless of its class is sensitive to the loading condition especially in the high strain rate range where the apparent strength of concrete is increased. One possible explanation is that the bulk strength of concrete increases with the strain rate as reported by Tu and Lu [6]. This strength enhancement is indicated by the ratio of the dynamic to static strength either in tension or compression, commonly known as the Dynamic Increase Factor (DIF).

In the RHT concrete model, the strain rate effect ($\dot{\varepsilon}$) is incorporated through the following equation:-

$$\text{DIF}\ (\dot{\varepsilon}) = \begin{cases} \left(\frac{\dot{\varepsilon}}{\dot{\varepsilon}_0}\right)^{\delta} \\ \left(\frac{\dot{\varepsilon}}{\dot{\varepsilon}_0}\right)^{\alpha} \end{cases}, \qquad (4.22)$$

where

$\dot{\varepsilon}_0$ = quasi-static strain rate ($3 \times 10^{-5}\ s^{-1}$) for compression and ($3 \times 10^{-6}\ s^{-1}$) for compression.

δ = strain rate exponent in tension (user defined parameter), and

α = strain rate exponent in compression (user defined parameter).

4.6.3.1 Strain Rate Effect in Tension

Habel and Gauvreau [13] conducted direct tensile tests on UHPFRC dog bone specimens at different strain rates ranging from 8×10^{-7} s^{-1} to 2×10^{-2} s^{-1}. Maalej *et al.* [14] conducted the same test on hybrid-fibre reinforced ECC coupons with strain rate ranging from 2×10^{-6} s^{-1} to 2×10^{-1} s^{-1}. The DIF derived from the experimental work is plotted together with the DIF from the RHT formulation as shown in Figure 4.15.

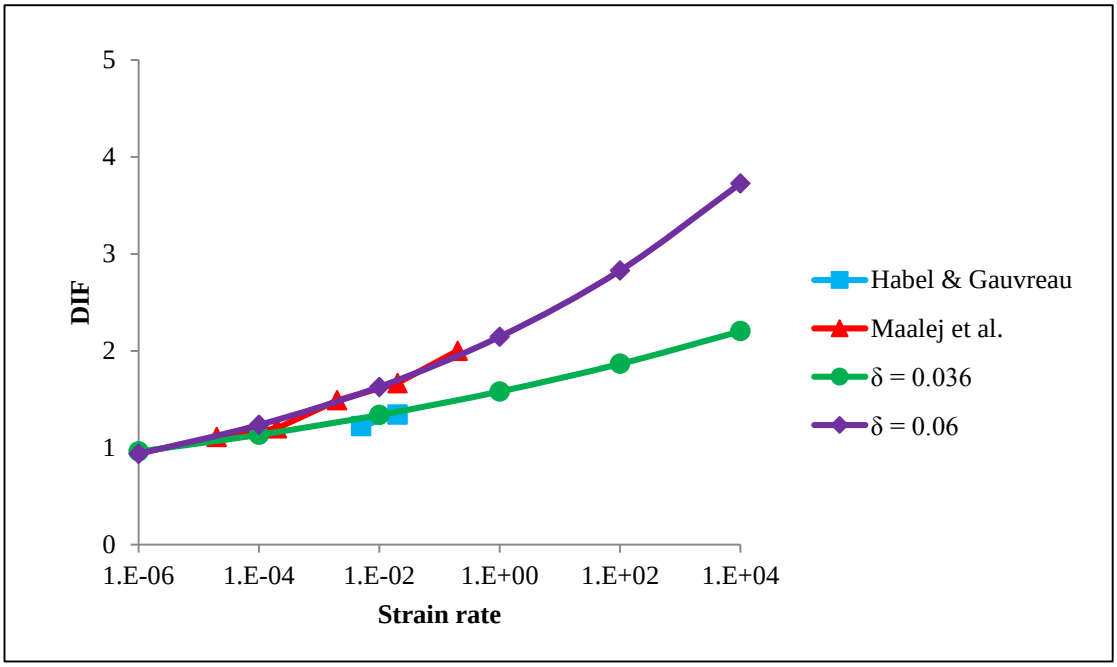

Figure 4.15: DIF for UHPFRC in tension by varying parameter δ compared to the experimental results by Habel and Gauvreau [13] and Maalej *et al.* [14].

It can be seen that the work by Maalej *et al.* [14] fits well with $\delta = 0.06$. The work by Habel and Gauvreau [13] lies along the curve where $\delta = 0.036$ is used. However, since the DIF derived here is based on reference strain in the order of 10^{-7} s^{-1} compared to 10^{-5} s^{-1} in the

RHT formulation, a fair comparison cannot be made. Nevertheless, the value for δ is taken as 0.06 similar to the results obtained by Maalej *et al.* [14].

At higher strain rate, the strain rate enhancement becomes more significant and consequently a bi-linear DIF-strain rate relationship needs to be introduced, as proposed by Malvar and Ross [15]. Modification to the RHT formulation is carried out by incorporating sub-routine as reported by Leppanen [2], Tu and Lu [6] and Nystrom and Gylltoft [16]. However, the bi-linear relationship is not necessarily required in a low velocity impact study using a drop hammer due to the fact that the strain rate will not be greater than the order of 10^0 s^{-1}. Such value of strain rate was shown in the work by Habel and Gauvreau [13] and Millard *et al.* [17] in their low velocity impact tests. In this lower region, the relationship is relatively linear and as such, the standard RHT formulation is valid.

4.6.3.2 Strain Rate Effect in Compression

Tu and Lu [6] commented on the default value in the RHT concrete model for DIF in compression and suggested that the values embedded in the code are acceptable for a large range of strain rate. The closest experimental work regarding the compressive strain rate sensitivity for UHPFRC can be referred to Ngo and Mendis [18]. The graph developed from the said work together with a series of graphs with different α values is shown in Figure 4.16. It can be seen that the graph developed using $\alpha = 0.01$ matches the experimental work at strain rate lower than 10^1 s^{-1} and starts to branch out at higher strain rate values. On the other hand, using a higher value of α will only create a significant gap between the RHT formulation and the experimental work.

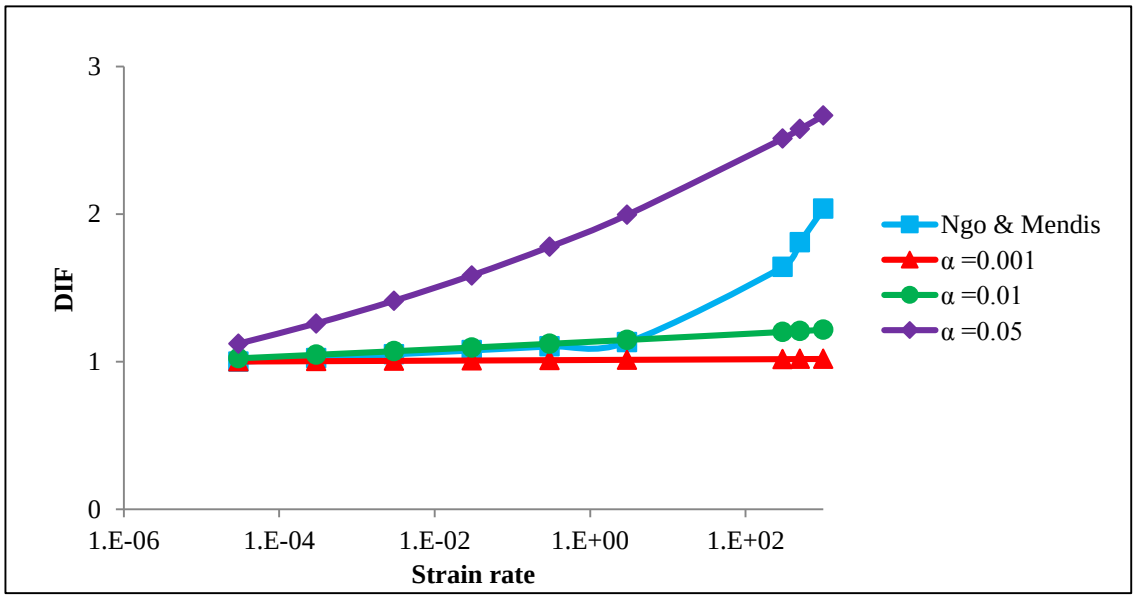

Figure 4.16: DIF for UHPFRC in compression by varying parameter α compared to the experimental results by Ngo and Mendis [18].

4.6.4 Shear and Bulk Modulus

The Bulk Modulus (K) and Shear Modulus (G) is calculated based on the equations:-

$$K = \frac{E_c}{3(1-2v)} \tag{4.23}$$

and

$$G = \frac{E}{2(1+v)}, \tag{4.24}$$

where

E_c = Young Modulus of Elasticity, and

v = Poisson Ratio.

The value of $E = 45.55 \times 10^3$ MPa and $v = 0.213$ is obtained from Hassan *et al.* [8] and Hassan and Jones [19], respectively. Substituting these two values in equations (4.7) and (4.8) give the values of K = 26,450 MPa and G = 18,775 MPa.

Bulk Modulus relates the change in stress to the volumetric strain and a simple form of the linear Equation of State (EoS). Technically, a more comprehensive EoS is normally employed for dynamic analysis especially if the experiment involves high strain rate loading regime such as blast load or projectile impacting a solid. Under low velocity impact, where the concrete compression is expected to be low, a linear EoS is assumed to be valid. Farnam *et al.* [10] also used an EoS corresponding to a linear pressure versus volumetric strain data.

4.6.5 Minimum Strain to Failure

The full stress-strain diagram for the direct tensile strain for a UHPFRC dog bone specimen by Hassan *et al.* [8] is reproduced and shown in Figure 4.17. It can be seen that there are two parts showing a descending trend and thus the exact end of the plastic behaviour prior to softening is difficult to justify. Farnam *et al.* [10] used the value 0.012 for high performance fibre reinforced concrete (HPFRC) based on a direct tensile test on high-performance fibre-reinforced concrete. Assuming that the end of the plastic behaviour of the stress-strain curve in Figure 4.17 lies along the first descending branch, the same value of 0.012 can be adopted in this study.

Figure 4.17: Tensile stress-strain diagram reproduced from Hassan *et al.* [8].

4.6.6 Failure Model

The RHT concrete model uses a hydrodynamic-tensile-failure-model as the default. Failure will take place when the hydrodynamic pressure exceeds a specified value. Researchers such as Leppanen [2] and Nystrom and Gylltoft [16] introduced a modified crack-softening failure via fracture energy. However, this type of failure model could only be activated when coupled with the principal stress failure model. The activation of the principal stress failure model will automatically turn off the tensile strain rate exponent δ. Combining two separate failure models will end up with an 'either'/'or' situation where it depends on how the two failure models overlap each other. To avoid such complication, the default hydrodynamic-tensile-failure-model is used throughout the FE work.

4.6.7 Overall Parameters in RHT Concrete Model for UHPFRC

The overall parameters used in this study are shown in Table 4.4. Some parameters remain the same as the default values or similar to the parameters in Table 2.5 due to unavailability of characterization tests.

Table 4.4: Overall RHT input parameters for UHPFRC material.

Parameter	Unit	Value	Remarks
Compressive strength f_c (MPa)	MPa	150	[a]
Normalised tensile strength	-	0.061	[a]
Normalized shear strength	-	0.25	[b]
Failure surface parameter *A*	-	1.6	[b]
Failure surface parameter *N*	-	0.61	[b]
Tension/compression meridian ratio	-	0.6805	[c]
Brittle to ductile transition	-	0.0105	[c]
Hardening slope	-	2	[c]
Normalised elastic strength 1	-	0.75	[a]
Normalised elastic strength 2	-	0.68	[b]
Cap on elastic surface	Yes/No	Yes	[c]
Residual strength constant *B*	-	N/A	[d]
Residual strength exponent *M*	-	0.61	[b]
Compressive strain rate exponent α	-	0.01	[e]
Tensile strain rate exponent δ	-	0.06	[f]
Maximum fracture strength ratio	-	1×10^{20}	[c]
Damage constant *D1*	-	0.04	[c]
Damage constant *D2*	-	1	[c]
Minimum strain to failure	-	0.012	[g]
Residual shear modulus fracture	-	0.13	[c]
Shear modulus (MPa)	MPa	18,775	[h]
Bulk modulus (MPa)	MPa	26,450	[h]

[a] Data from Hassan *et al.* [8]

[b] Data from Farnam *et al.* [10]

[c] Default in RHT concrete model

[d] Refer to Chapter 5

[e] Data from Ngo and Mendis [18]

[f] Data from Habel and Gauvreau [13] and by Maalej *et al.* [14]

[g] Data from Farnam *et al.* [10]

[h] Data from Hassan and Jones [19]

4.7 Analytical Model

The analytical model to predict the deformation of UHPFRC plates subjected to the central impact in this study was represented by a single-degree-of-freedom (SDOF) model, a type of spring-mass model. This model evaluates the structural response using only one physical degree of freedom, in this case the vertical movement of the UHPFRC slab as shown in Figure 4.18. The SDOF model developed from experimental data was used to predict the response of the undamaged and pre-damaged slabs. On the other hand, the SDOF model developed theoretically was used to predict the response of the undamaged slabs only.

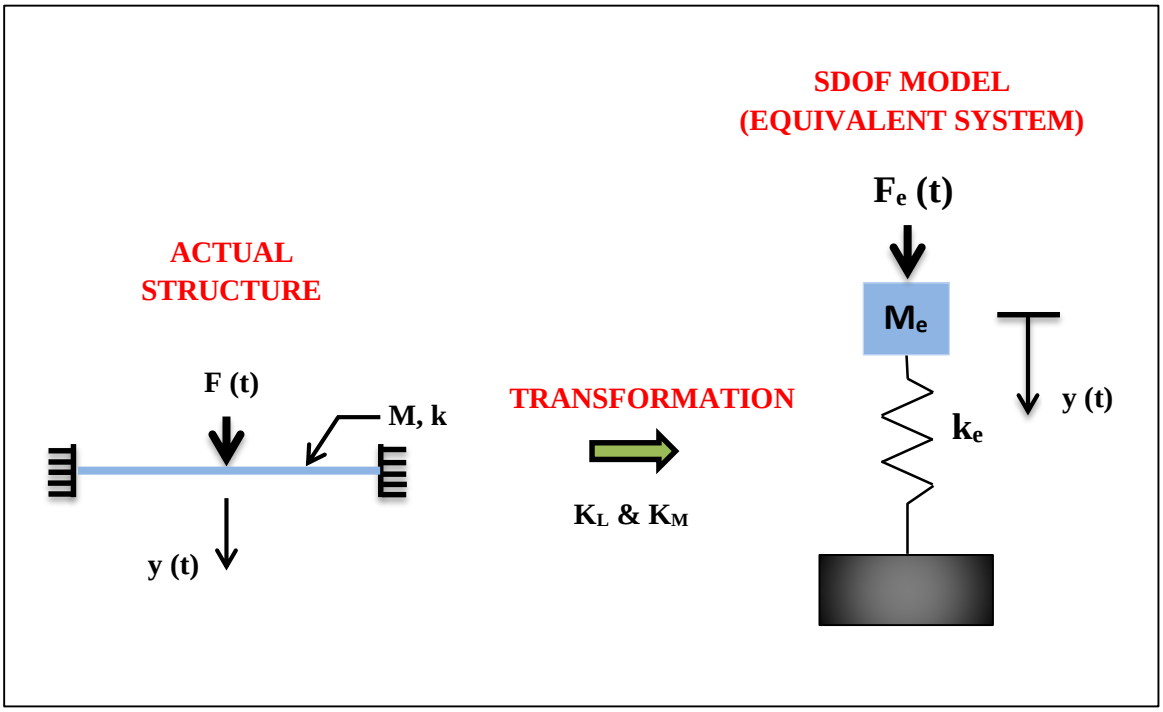

Figure 4.18: Equivalent spring-mass system.

The distributed mass of the slab has an infinite degree of freedom and technically should be represented by a series of lumped masses. However, the number of degrees of freedom is directly related to the number of lumped masses being considered. In the above model, only one direction is allowed and as such, only one lumped mass is considered.

The lumped mass in SDOF and the actual distributed mass are equated on the assumption that both masses have the same kinetic energy. Similarly, the force acting on the SDOF system and the force acting on the slab are equated assuming that the work done by both are the same. The equivalency is achieved through the introduction of load factors, K_L and mass factor, K_M as shown in the following equations:-

$$k_e = k \times K_L \ , \tag{4.25}$$

$$M_e = M \times K_M \ , \tag{4.26}$$

$$F_e(t) = F(t) \times K_L \ , \tag{4.27}$$

where

k = stiffness of the plate (N/m),

M = distributed mass of the slab (kg),

$F(t)$ = force (N),

M_e = equivalent single lumped mass (kg),

k_e = equivalent spring stiffness (N/m),

$F_e(t)$ = equivalent force (N),

K_L = load factor

= 1.0 for any single point load case, and

K_M = mass factor.

4.7.1 Transformation Factors

The transformation factors K_L and K_M were determined based on the deformed shape of the slab. Ideally, the profile of the maximum deformation should be used. Due to the constraint of using LDV (single point measurement) it was assumed that the permanent deformation profile of the slab represents the governing mode of failure. As the impact test involved a point load impact, the load factor K_L was taken as 1.0 [20]. The mass factor K_M is determined upon plotting the permanent deformation profile of the slab where the profile was idealized following any of the deformed shape as listed in Table 4.5.

Table 4.5: Deformed shape and shape function for square a slab.

Deformed shape	Strain range	Shape function (w)	Equation
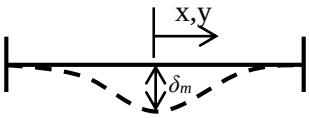	Elastic	$\frac{\delta_m}{4}\left(1+cos\frac{\pi x}{X}\right)\left(1+cos\frac{\pi y}{Y}\right)$	(4.28)
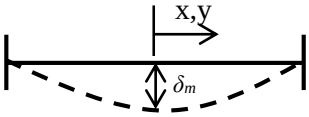	Elastic-plastic	$\delta_m cos\left(\frac{\pi x}{2X}\right)\left(cos\frac{\pi y}{2Y}\right)$	(4.29)
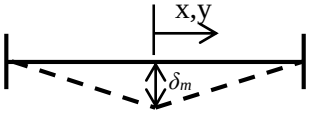	Plastic	$\delta_m\left(1-\frac{x}{2X}\right)\left(1-\frac{y}{2Y}\right)$	(4.30)

Note: X, Y = half span of the slab in x-axis and y-axis, respectively.

x,y = any point along the half span in x-axis and y-axis, respectively.

The mass transformation factor K_M was calculated by equating the kinetic energy of the actual slab $KE_{(S)}$ with the SDOF system $KE_{(SDOF)}$ using the following equations:-

$$KE_{(S)} = \frac{1}{2} \times 4t\rho \int_0^X \int_0^Y \dot{w}^2 \, dxdy \, , \tag{4.31}$$

$$KE_{(SDOF)} = \frac{1}{2} \times M_e \dot{w}^2 \, , \tag{4.32}$$

$$K_M = \frac{M_e}{M} \, , \tag{4.33}$$

where

t = thickness of the slab,

ρ = density of the UHPFRC, and

$\dot{w}$ = velocity of the slab.

Note:

1. Solving equation (4.31) will solve KE as a function of M and $\dot{w}$.

2. Parameter $\dot{w}$ will be removed when equating equation (4.31) and (4.32)

4.7.2 Resistance Functions

The stiffness and resistance forces are among the parameters required in order to perform SDOF analysis. These parameters were obtained from the load-deformation curve of the static test described in Section 3.8. Figure 4.19 illustrates the approach to obtain a bi-linear resistance function from a load-deformation curve produced from a static test. This approximation provides the parameters k (elastic stiffness) and R_m (maximum resistance force) for the SDOF analysis. This approach however is not incorporating any strain softening behaviour. In the case where a tri-linear function is used, another approximation is carried out to transform it into the basic bi-linear resistance function.

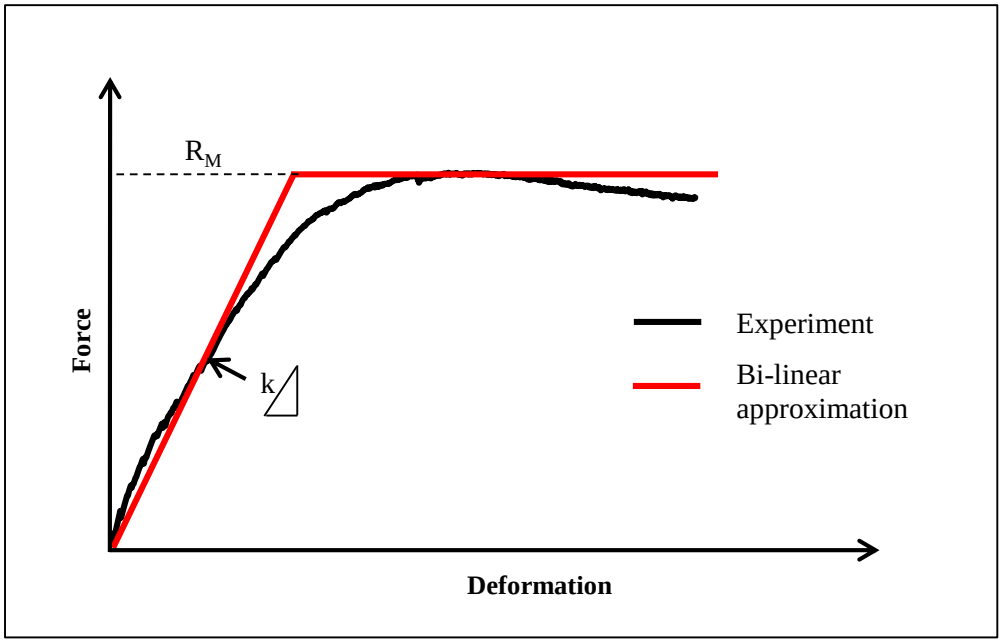

Figure 4.19: Transforming load-deformation curve from static test to a bi-linear resistance function.

4.7.3 Governing Equations in SDOF

Solving the equivalent SDOF model was carried out using the Newmark time-steping numerical integration with linear acceleration method in Microsoft EXCEL 2010 and coupled with a resistance function from the actual static load test. The free body diagram for the SDOF model is shown in Figure 4.20 together with a bi-linear resistance function.

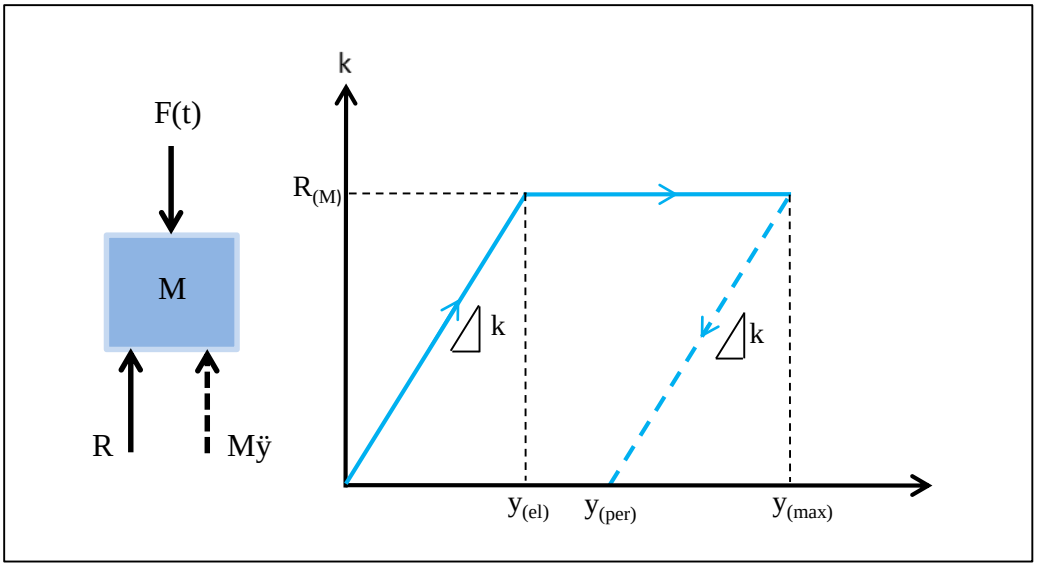

Figure 4.20: SDOF Free body diagram and the corresponding bi-linear resistance function.

From the equation of motion,

$$M\ddot{y} + R - F(t) = 0 \tag{4.34}$$

$$M\ddot{y} + ky - F(t) = 0 \qquad 0 < y < y_{el} \tag{4.35}$$

$$M\ddot{y} + R_{(M)} - F(t) = 0 \qquad y_{el} < y < y_{max} \tag{4.36}$$

$$M\ddot{y} + R_{(M)} - k(y_{max} - y) - F(t) = 0 \qquad y_{(per)} < y < y_{(max)} \tag{4.37}$$

The time step integration method was deployed to solve equations (4.35) to (4.37). The differential equation of motion is solved in a step-by-step manner starting from $t = 0$ where the displacement y and velocity dy/dt at this point are known. In this case $y = 0$ at $t = 0$ and the velocity at $t = 0$ is the velocity before impact recorded by the LDV.

This study used the velocity of the slab (v_e) as one of the input parameters in the SDOF analysis. The velocity was derived based on the assumption that plastic collision had occurred between the slab and the impactor [21] where the two bodies moved together at the same velocity during contact. From the law of conservation of momentum,

$$v_s = \frac{m_2}{m_2 + K_{M(s)} m_1} v_i \tag{4.38}$$

where

v_s = velocity of the slab,

v_i = velocity of the impactor,

m_1 = mass of the slab (15.25 kg)

m_2 = mass of the impactor (15.67 kg), and

$K_{M(S)}$ = mass transformation factor of the slab.

The assumption on the plastic collision as shown in equation (4.38) produced a new mass m_3 during contact and calculated as:

$$m_3 = m_2 + K_{M(S)} m_1 \tag{4.39}$$

The overall input parameters required in the SDOF analysis is shown in Table 4.6.

Table 4.6: Overall SDOF parameters.

Parameters	Symbol
Slab stiffness*	k_1
Slab velocity	v_s
Slab mass	m_1
Resistance force*	R_M
Impactor velocity	v_i
Impactor mass	m_2
Load transformation factor	K_L
Mass transformation factor	K_M

*Note: For tri-linear resistance function k_1 = slab stiffness in the elastic range, k_2 = slab stiffness in the elastic-plastic range, R_1 = resistance force at the end of elastic range and R_M = maximum resistance force.

4.7.4 Theoretical Resistance Function (stiffness and resistance force)

The theoretical stiffness of the undamaged UHPFRC slab was derived based on the elastic theory of thin plates with small deflections. The bending strain energy in a slab undergoing an elastic deformation is given by

$$4\int_0^X\int_0^Y\int_{-z}^{z}\left(\frac{1}{2}E\,\in_{xx}^2+\frac{E}{2(1+\upsilon)}\in_{xy}^2+\frac{1}{2}E\,\in_{yy}^2\right)dx\,dy\,dz. \tag{4.40}$$

Similarly, the bending strains are given by

$$\in_{xx}=z\left(\frac{\partial^2 w}{\partial x^2}\right)\qquad \in_{xy}=2z\left(\frac{\partial^2 w}{\partial x\partial y}\right)\qquad \in_{yy}=z\left(\frac{\partial^2 w}{\partial y^2}\right), \tag{4.41}$$

where

X,Y = half span of the slab in x-axis and y-axis, respectively,

x,y = any point along the half span in x-axis and y-axis, respectively,

z = half slab thickness,

E = Modulus of Elasticity,

υ = Poisson Ratio, and

w = shape function (see Table 4.5)

Assuming that the energy loss in bending is negligible, the potential energy (U) stored in the slab is taken as

U = Bending strain energy – Work done

U = Bending strain energy – $F\delta$. (4.42)

At equilibrium,

$$\frac{dU}{d\delta} = 0 \,. \tag{4.43}$$

The slab stiffness is determined by solving equations (4.41) to (4.43) and equating the solution with the Hooke's Law

$$F = k\delta \tag{4.44}$$

The Modulus of Elasticity (*E*) in bending was estimated from a static 3-point bending test by re-arranging the equation

$$\delta = \frac{FL^3}{48EI} \quad \text{to be} \tag{4.45}$$

$$E = \frac{FL^3}{48\delta I} \ , \tag{4.46}$$

where

F = Force (N),
L = support to support distance (mm),
I = second moment of area (mm^4), and
δ = deflection (mm).

The results of the 3-point bending test on a UHPFRC beam with the same mix design conducted by Mahmud *et al.* [22] were used. The test involved three notched beams measuring 150 mm × 150 mm section and 500 mm support to support distance. The experimental work measured the load versus crack mouth opening displacement (CMOD) and was transformed into load versus deflection values using the following relationship as recommended by BS EN 14651 [23]:

$$\delta = 0.85\ CMOD + 0.04 \tag{4.47}$$

Figure 4.21 shows the load-CMOD curve from Mahmud *et al.* [22] together with the equivalent load-deformation curve using equation (4.47). The elastic load-deformation relationship was considered up to 32.23 kN with a deflection of 0.0925 mm. Incorporating these values in equation (4.46) provides the value for $E = 21.51 \times 10^3$ MPa.

Figure 4.21: Load-CMOD curve [22] and the equivalent load-deformation curve.

Finally, the maximum resistance force (R_M) was calculated based on the assumption that the crack lines follow the concept of the yield-line theory for a fully fixed slab subjected to a concentrated load as shown in Figure 4.22.

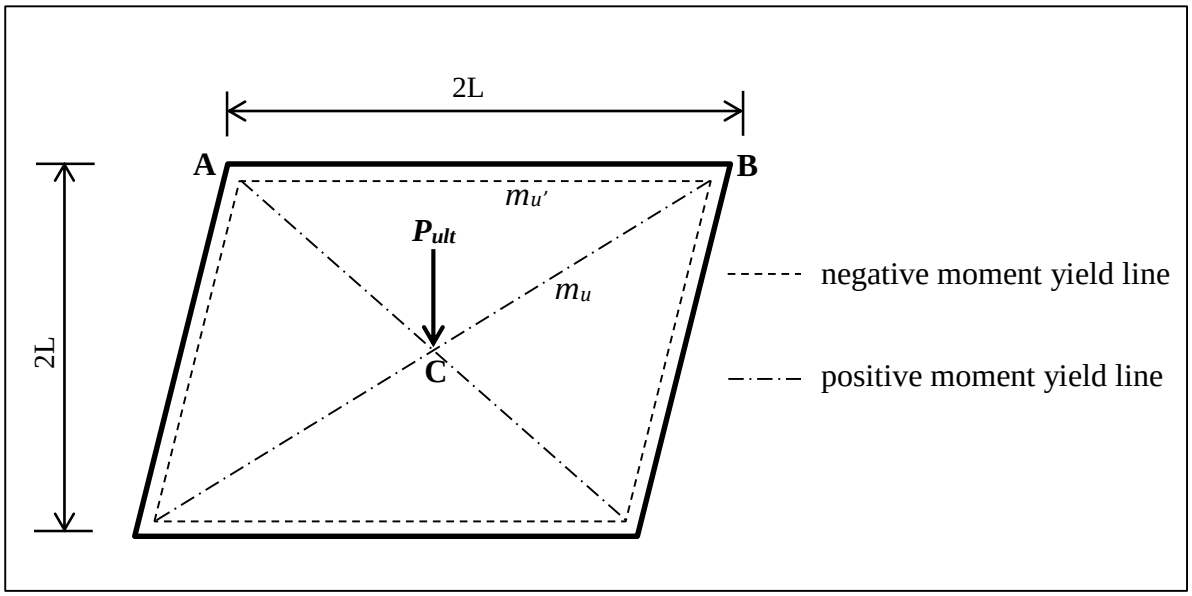

Figure 4.22: Yield-lines for a fully fixed square slab subjected to a concentrated load.

By using the Work Method and considering the segment ABC:-

Work done = Internal Energy

$$\frac{R_M}{4} \times L = 2L \times (m_u + m_{u'})$$

$$R_M = 8\,(m_u + m_{u'}) \quad ; \quad m_u = m_{u'} = M_{ult}$$

$$R_M = 16\,M_{ult} \tag{4.48}$$

where

M_{ult} = ultimate moment of resistant,

P_{ult} = ultimate load at collapse = R_M ,

m_u & m_u' = positive and negative moment of resistance, respectively.

The ultimate moment of resistant (M_{ult}) was then calculated based on the plastic solution proposed by Spasojevic [24]:

$$M_{ult} = \left(3 - \frac{2\sqrt{2}f_{ct}}{\sqrt{f_{ct}\left(E_c\varepsilon_{fct} + \sqrt{f_{ct}\left(2E_c\varepsilon_{fct} - f_{ct}\right)}\right)}} \right) . f_{ct} . \frac{t^2}{6} , \quad (4.49)$$

where,

f_{ct} = tensile strength (MPa),

E_c = Young modulus of elasticity (MPa),

$\varepsilon_{f_{ct}}$ = maximum tensile strain at the end of the pseudo-plastic tensile plateau, taken as 0.025 (as in Figure 4.17), and

t = slab thickness (mm).

.

4.8 Summary of Chapter 4

This chapter presented the numerical simulation procedures to predict the response of the UHPFRC slabs under low velocity impact. ANSYS Explicit Dynamics R13.0 software package were used for the FE simulations involving a single impact event. The modifications adopted in generating the 3-D models from the actual test set up were shown. Such modifications involve reducing the length of the impactor, simplifying the support condition and reducing the mesh quantity by utilising half model. This chapter also presented the concept of developing the pre-damaged condition to the slab prior activating the impact loading. The modelling of the pre-damaged effect in the dynamic simulation was carried out by selecting a higher pressure loading with shorter load duration compared to the actual static condition. RHT concrete model was used to represent the dynamic properties of the UHPFRC materials. The input parameters for using RHT concrete model were identified and several parameters were calibrated using available test data. The results from the calibration exercise were discussed. Finally, in the analytical modelling, the methods to derive the SDOF parameters from a static test, theoretical equations and other published work were also presented.

4.9 References

[1] N. Kishi, S. G. Khasraghy and H. Kon-No, "Numerical simulation of reinforced concrete beams under consecutive impact loading," *ACI Structural Journal*, vol. 108, no. 4, pp. 444-452, 2011.

[2] W. Riedel, K. Thoma, S. Hiermaier and E. Schmolinske, "Penetration of reinforced concrete by BETA-B-500 numerical analysis using a new microscopic concrete model for hydrocodes," presented at the 9th International Symposium on Interaction of the Effects of Munitions with Structures, Berlin, May 3-7, 1999.

[3] J. Leppanen, "Concrete subjected to projectile and fragment impacts: Modelling of crack softening and strain rate dependency in tension," *International Journal of Impact Engineering*, vol. 32, no. 11, pp. 1828-1841, 2006.

[4] W. Riedel, "10 Years RHT: A Review of concrete modelling and hydrocode applications," in *Predictive modeling of dynamic processes* – a tribute, K. Thoma and S. Hiermaier, Ed. London: Springer, 2009, pp. 143-165.

[5] ANSYS Incorporated, *ANSYS Workbench User's Guide*, ANSYS Incorporated, USA, 2010.

[6] Z. Tu and Y. Lu, "Modifications of RHT material model for improved numerical simulation of dynamic response of concrete," *International Journal of Impact Engineering*, vol. 37, no. 10, pp. 1072-1082, 2010.

[7] Z. Tu and Y. Lu, "Evaluation of typical concrete material models used in hydrocodes for high dynamic response simulations," *International Journal of Impact Engineering*, vol. 36, pp. 132-146, 2009.

[8] A. M. T. Hassan, S. W. Jones and G. H. Mahmud, "Experimental test methods to determine the uniaxial tensile and compressive behaviour of ultra high performance fibre reinforced concrete (UHPFRC)," *Construction and Building Materials*, vol. 37, pp. 874-882, 2012.

[9] A. M. Neville, *Properties of concrete*, 5th ed. London: Prentice Hall/Pearson Education Limited, 2011.

[10] Y. Farnam, M. Moosavi, M. Shekarchi, S. K. Babanajad and A. Bagherzadeh, "Behaviour of slurry infiltrated fibre concrete (SIFCON) under triaxial compression," *Cement and Concrete Research*, vol. 40, no. 11, pp. 1571-1581, 2010.

[11] T. H. Tan, "Effects of triaxial stress on concrete," presented at the 30th Conference on Our World in Concrete and Structures, Singapore, Aug. 23-24, 2005.

[12] J. M. Magallanes, Y. Wu, K. B. Morrill and J. E. Crawford, "Feasibility studies for a plasticity-based constitutive model for ultra-high performance fiber-reinforced concrete," presented at the 21st International Symposium on Military Aspects of Blast and Shock, Jerusalem, Israel, Oct. 4-8, 2010.

[13] K. Habel and P. Gauvreau, "Response of ultra-high performance fiber reinforced concrete (UHPFRC) to impact and static loading," *Cement and Concrete Composites*, vol. 30, no. 10, pp. 938-946, 2008.

[14] M. Maalej, S. T. Quek and J. Zhang, "Behavior of hybrid-fiber engineered cementitious composites subjected to dynamic tensile loading and projectile impact," *Journal of Materials in Civil Engineering*, vol. *17, no.* (2), pp. 143-152, 2005,

[15] L. J. Malvar and C. A. Ross, "Review of strain rate effects for concrete in tension," *ACI Materials Journal*, vol. *95, no.* 6, pp. 735-739, 1998.

[16] U. Nystrom and K. Gylltoft, "Comparative numerical studies of projectile impacts on plain and steel-fibre reinforced concrete," *International Journal of Impact Engineering*, vol. 38, no. 2, pp. 95-105, 2011.

[17] S. G. Millard, T. C. K. Molyneaux, S. J. Barnett and X. Gao, "Dynamic enhancement of blast-resistant ultra high performance fibre-reinforced concrete under flexural and shear loading," *International Journal of Impact Engineering*, *37*(4), pp. 405-413, 2010.

[18] T. Ngo and P. Mendis, "Modelling reinforced concrete structures subjected to impulsive loading using concrete lattice model," *Electronic Journal of Structural Engineering*, vol. 8, pp. 80-89, 2008.

[19] A. M. T. Hassan and S. W. Jones, "Non-destructive testing of ultra high performance fibre reinforced concrete (UHPFRC): A feasibility study for using ultrasonic and resonant frequency testing techniques," *Construction and Building Materials*, vol. *35*, pp. 361-367, 2012.

[20] J. M. Biggs, *Introduction to Structural Dynamics*. New York: McGraw-Hill Book Company, 1964.

[21] K. Fujikake, B. Li and S. Soeun, "Impact response of reinforced concrete beam and its analytical evaluation," *Journal of Structural Engineering*, vol. *135, no.* 8, pp. 938-950, 2009.

[22] G. H. Mahmud, Z. Yang and A. M. Hassan, "Experimental and numerical studies of size effects of Ultra High Performance Steel Fibre Reinforced Concrete (UHPFRC) beams," *Construction and Building Materials*, vol. 48, pp. 1027-1034, 2013.

[23] British Standards Institution. Test method for metallic fibre concrete – Measuring the flexural tensile strength (limit of proportionality (LOP), residual), *BS EN 14651:2005+A1:2007*, 2007.

[24] A. Spasojevic, D. Redaelli and A. Muttoni, "Thin UHPFRC slabs without conventional reinforcement as light-weight structural elements," presented at the fib Symposium, London, June 22-24, 2009.

CHAPTER 5

EXPERIMENTAL RESULTS AND DISCUSSIONS

5.1 Introduction

This chapter presents the test results starting from the preparation of the UHPFRC specimens, the pre-damaging exercise and the low velocity impact tests. In total, 48 slabs were successfully cast and 23 slabs were pre-damaged using the PPLR. A total of 42 panels were tested under the low velocity impact and four were used for developing the resistance curve from the static point load tests. The impact response of the pre-damaged slabs with regards to the impact resistance, deformations and local material degradation are evaluated and compared with the undamaged slabs. The sensitivity of the impact location and impact angle are also assessed and discussed accordingly.

5.2 Consistency of the Design Mix

The UHPFRC panels were prepared in 16 batches. For each batch, a maximum of 3 panels can be prepared together with cubes for checking the mix consistency. The average compressive strength test results for 7 day and 28 day curing were found to be 157.1 MPa (standard deviation 2.95 MPa) and 165.2 MPa (standard deviation 2.77 MPa), respectively.

The average density of the cubes was recorded to be 2,440 kg/m^3 (standard deviation 8.78 kg/m^3). Low standard deviations observed for all results indicated a low variance in the design mix used. The details of the density and compressive strength test record are given in Appendix A.

5.3 Preparation of Pre-damaged UHPFRC Slabs using the PPLR

As discussed earlier in Section 3.4.3 the new cut-off values for the pressure and deformation were set to be 50 psi (0.345 MPa) and 4 mm, respectively. Figure 5.1 shows the pressure-deformation curves for the 23 slabs prepared via the pre-damaging exercise. It can be seen that the linear elastic relationship extends to approximately 20-25 psi (0.138-0.172 MPa) before developing non-linear behaviour. Once the cut-off limit was reached, mostly governed by the 4 mm deformation, the pressure was released to 0 psi. The graphs also show

that the response follows almost the same trend from the loading to the unloading stage hence producing consistent and repeatable pre-damaged specimens.

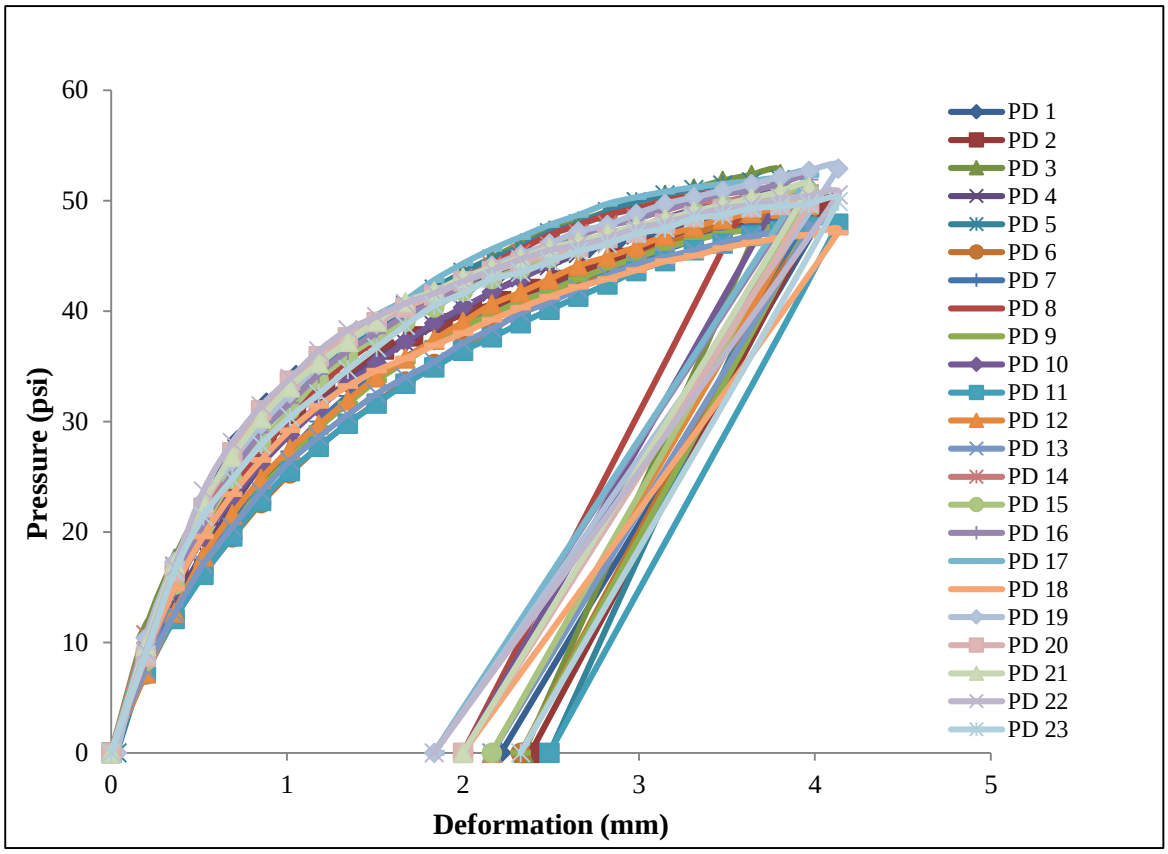

Figure 5.1: The overall pressure-deformation results for the pre-damaging exercise.

The average maximum deformation was 3.99 mm (standard deviation 0.10 mm) and the average maximum pressure was 50.04 psi/0.35 MPa (standard deviation 1.67 psi). As for the permanent deformation, the average was 2.04 mm (standard deviation 0.23 mm). The pre-damaging exercise also managed to produce similar crack patterns on both surfaces. On the top face (loaded face), cracks along the edges were formed due to the hogging moment while on the bottom face the cracks spread diagonally towards the four corners as shown in Figure 5.2. Also noted in Figure 5.2 (a) was the shifting of the cracks along the edges away from the alignment of the studs compared to the previous trial test result shown in Figure 3.10 (c). The location of these crack lines was now closer to the boundary of the loaded face and closely resembled the yield lines of a uniformly loaded square slab with fixed edges.

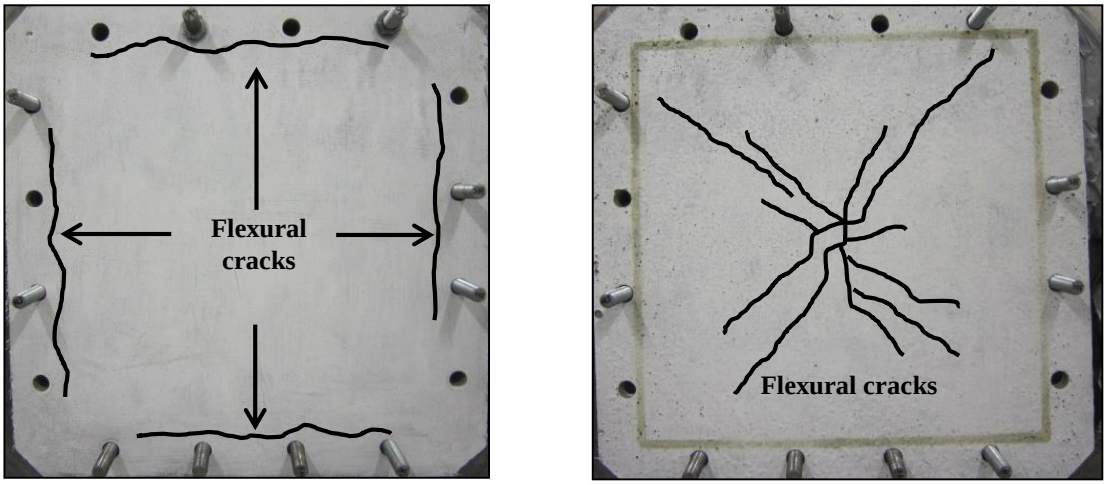

(a) (b)

Figure 5.2: Typical crack pattern formed on the (a) top; (b) bottom face of the slab.

5.4 Impact Tests

The impact tests were conducted on 42 panels, 21 each representing the damaged and undamaged panels. For simplicity and clarity of presentation, only average values for each impact case is shown. The full results are given in Appendix B.

5.4.1 Number of Strikes at Failure

The graphs showing the number of strikes required to fail the undamaged and pre-damaged slabs are shown in Figure 5.3 (a) and 5.3 (b), respectively. At the same drop heights, corner impact shows the lowest impact resistance, followed by edge, central and oblique impact. The maximum difference in terms of the number of strikes to fail the slab between the undamaged and pre-damaged slabs was found to be relatively low, typically between 1 and 3.

It is also noted that the relationship between the number of strikes and the drop height for central impact is in the form of a polynomial expansion. This relationship shows a significant increase in the number of strikes to fail the slab as the drop height is reduced. On the contrary, the corner and edge impact (asymmetrical impact) show almost a linear relationship, suggesting that the asymmetrical impact is not significantly influenced by the change in the drop height. A similar relationship is also observed for the pre-damaged slabs. The results also show that the oblique impact for both types of slab exhibits a higher impact resistance compared to the central impact. This phenomenon suggests that a lower amount of impact energy was transferred to the slab upon impact.

The early findings revealed that, although initially exposed to 77% of their maximum static resistance, the pre-damaged slabs showed high residual strength and were able to withstand between 50% and 85% impact resistance of the undamaged slabs. The change to the impact location and angle also show strong influence on the impact resistance of both types of slabs.

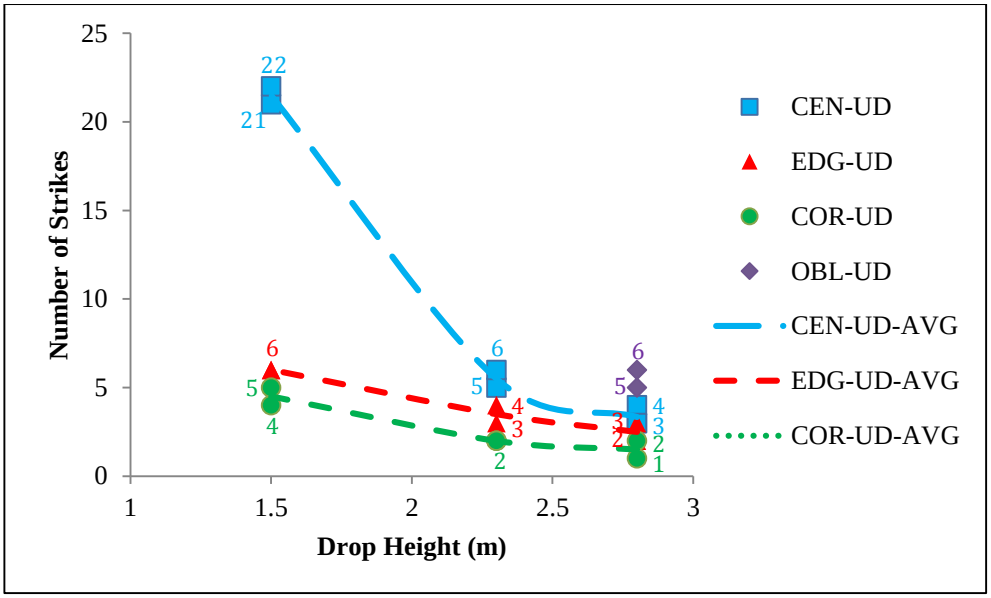

(a)

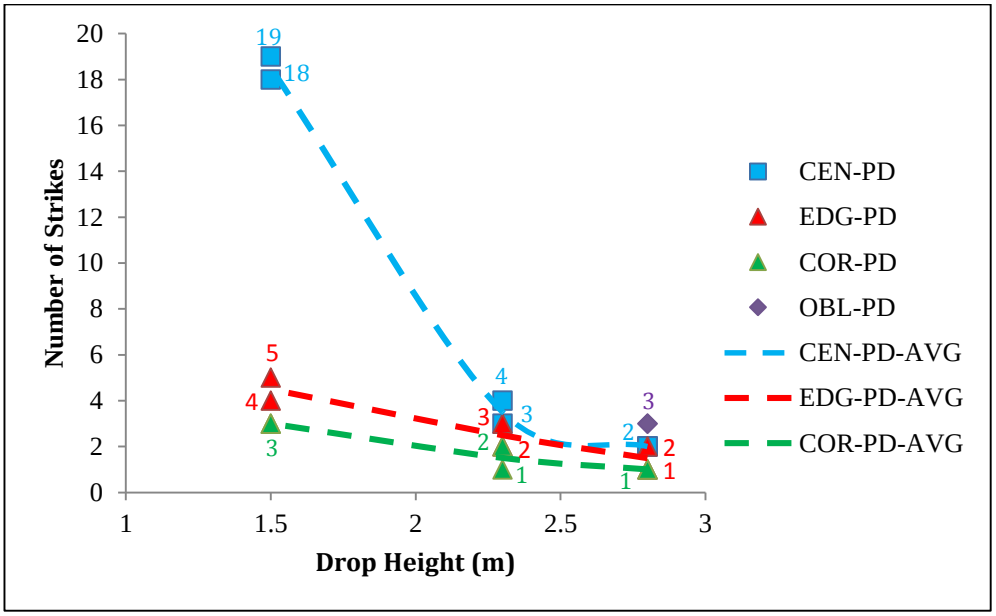

(b)

Figure 5.3: Drop height versus number of strike variations according to different impact scenario for (a) undamaged slabs; (b) pre-damaged slab.

5.4.2 Crack Propagation and Failure Pattern for the Slabs Subjected to Central Impact Case

The development and propagation of flexural and shear cracking for UHPFRC slabs impacted from 1.5 m drop height are shown in Figure 5.4. Initially, a fine circular crack with local indentation and edge cracks were formed on the top face as shown in Figure 5.4 (a). In successive strikes, the circular crack propagated deeper through the thickness of the section and started to develop the punching shear failure. Consequently, the edge cracks propagated further towards the corner. At this stage, the edge cracks exhibited significantly wider crack width as shown in Figure 5.4 (b). Finally, a shear punching failure occurred at the centre of the slab while the edge cracks formed a closed loop along the edges.

On the bottom face, fine flexural cracks first developed within the vicinity of the impact location. In successive strikes, the flexural cracks propagated towards the corners while a shear punching crack initiated at the centre of the slab, indicated by the concentration of macrocracks as shown in Figure 5.4 (b). At the final strike, shear punching failure occurred where severe gaps were observed between the un-detached shear plug and the slab as shown in Figure 5.4 (c). In addition, edge cracks also developed along the edges. Upon inspection, these cracks were found to be the progression of the edge cracks from the top face.

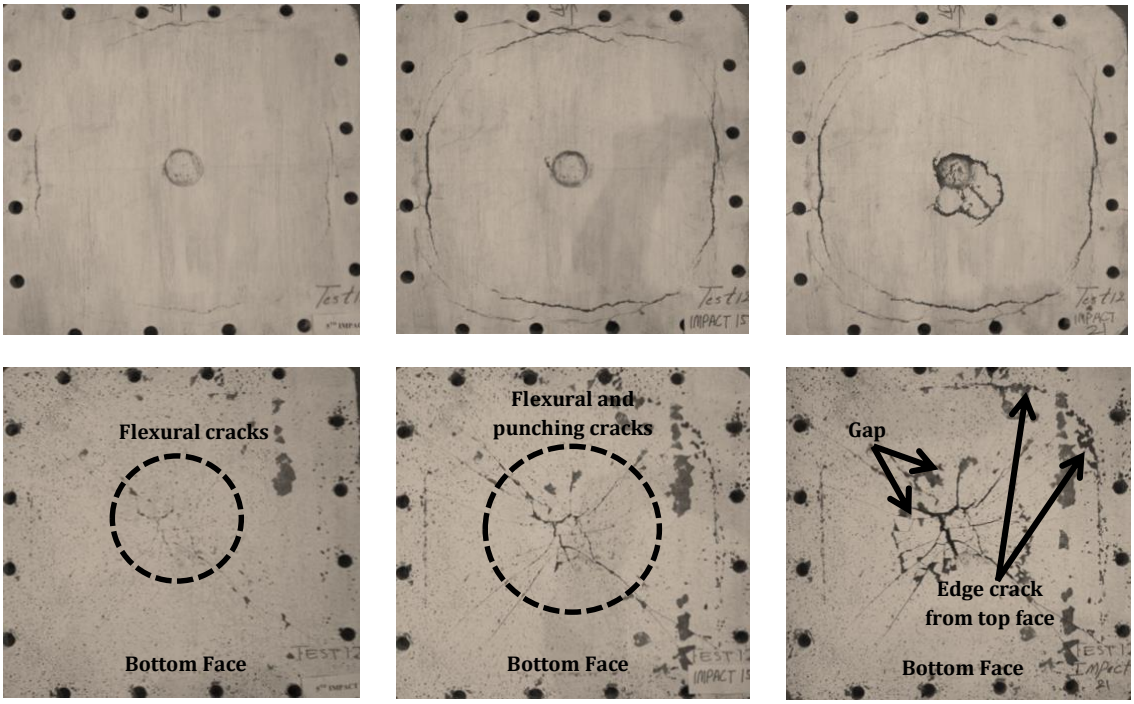

(a) (b) (c)

Figure 5.4: Crack propagation and failure pattern on top (above) and bottom (below) for undamaged UHPFRC slab subjected to central impact at 1.5 m drop height after (a) 5th strike; (b) 15th strike; (c) 21st strike (at failure).

The failure patterns for the undamaged slab impacted from 2.3 m and 2.8 m drop heights are shown in Figure 5.5 (a) and (b), respectively. At failure, the cracks along the edges on the top face and the flexural cracks on the bottom face were less propagated with smaller crack width compared to the slabs impacted from 1.5 m drop height. This observation indicates that shear failure mode is more dominant as the drop height is increased. In the case of 2.3 m drop height, a complete perforation occurred. The dislodged shear plug formed a circular hole on the top face and the failure plane dispersed radially to the bottom face forming a larger circle as shown in Figure 5.5 (a). The shear punching failure of the slab impacted from 2.8 m drop height was similar in form to the 1.5 m drop height.

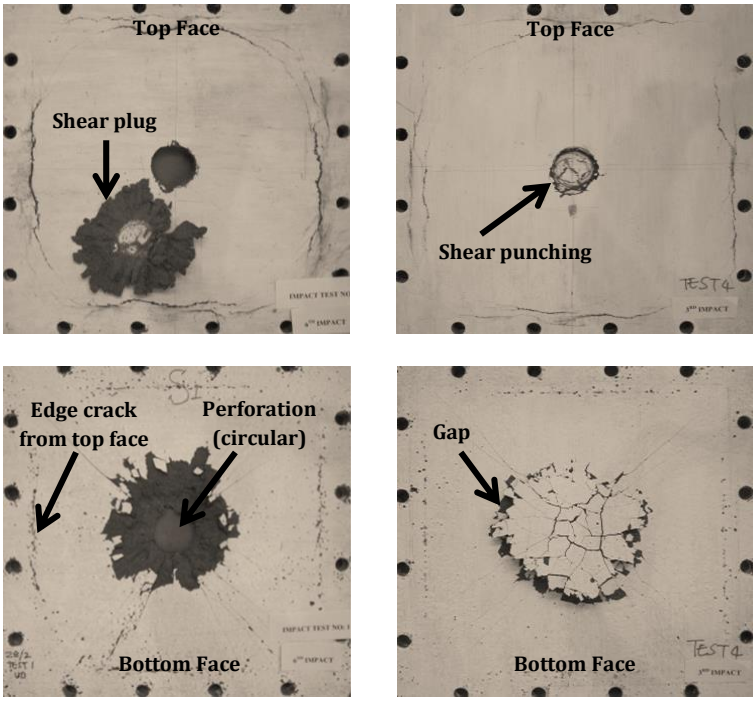

(a) (b)

Figure 5.5: Final failure pattern on top (above) and bottom (below) for undamaged UHPFRC slab subjected to central impact at (a) 2.3 m drop height (6th strike); (b) 2.8 m drop height (3rd strike).

In the case of pre-damaged slabs impacted from 1.5 m drop height, the propagation of the cracks and the failure pattern were found to be similar to the undamaged slab as shown in Figure 5.6. As expected, the shear punching failure developed earlier where the complete circular crack was observed at the 12th strike compared to the 15th strike for the undamaged slab. The progression of the cracks along the edges after the 15th strike was relatively insignificant and can be justified by comparing Figure 5.6 (b) and Figure 5.6 (c). Similarly, the progression of the edge cracks from the top face to the bottom face was also found to be less significant.

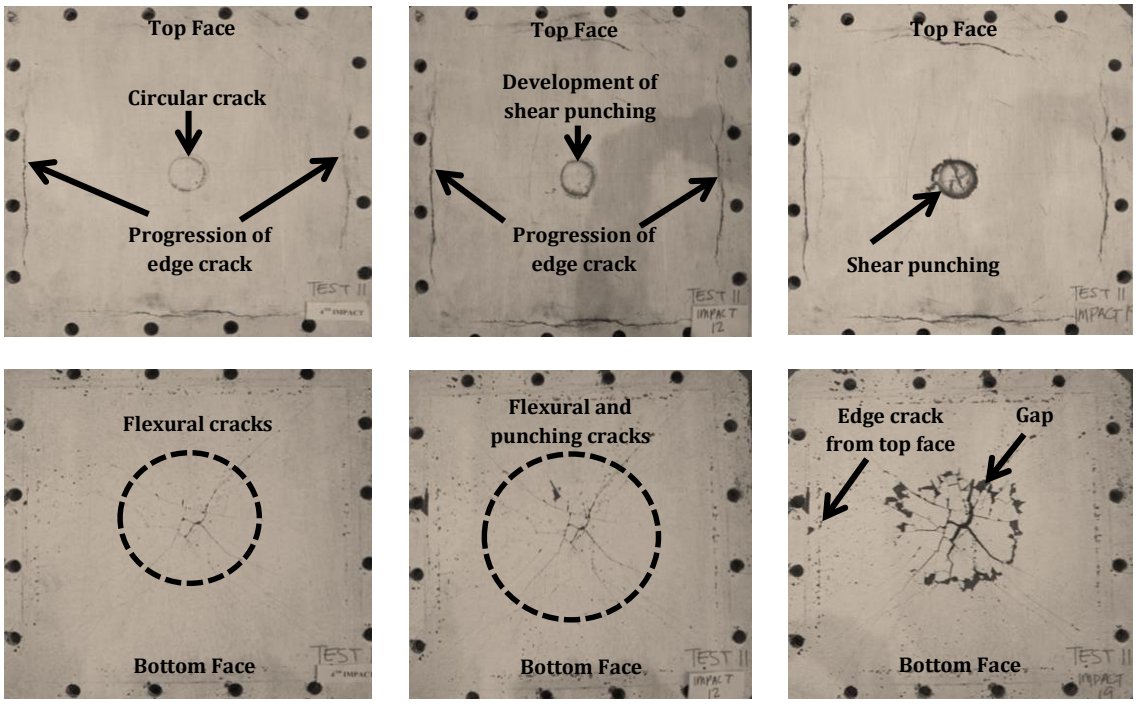

(a) (b) (c)

Figure 5.6: Crack propagation and failure pattern on top (above) and bottom (below) for pre-damaged UHPFRC slab subjected to central impact at 1.5 m drop height after (a) 4th strike; (b) 12th strike; (c) 19th strike (at failure).

Figure 5.7 (a) and (b) show the final crack pattern for the pre-damaged slabs subjected to 2.3 m and 2.8 m drop height, respectively. The immediate failure shown by the slab especially when impacted from 2.8 m drop height, caused the existing cracks along the edges to remain almost unchanged as shown in Figure 5.7 (b). The shape of the shear plugs were similar to the one produced by the undamaged slab.

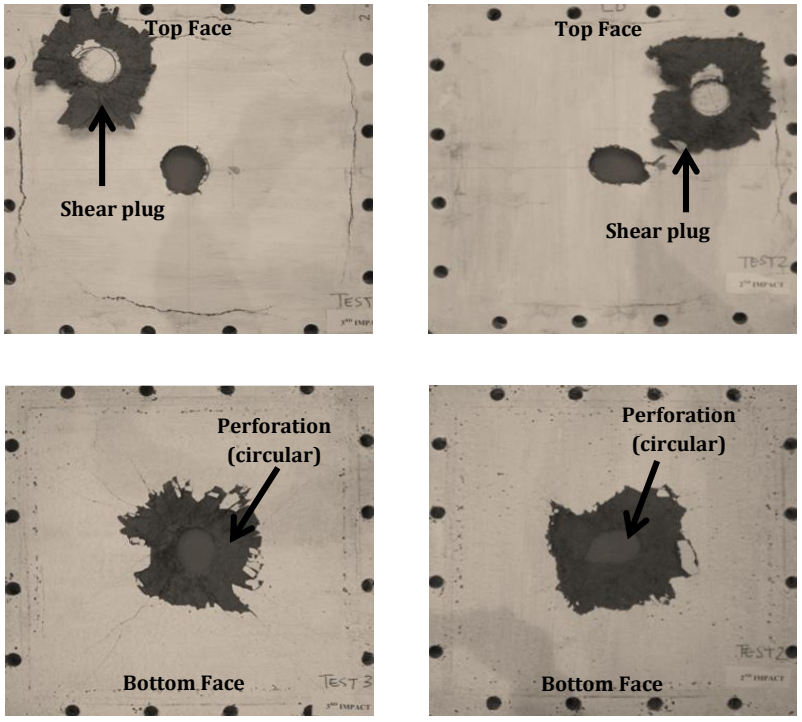

(a) (b)

Figure 5.7: Final failure pattern on top (above) and bottom (below) for pre-damaged UHPFRC slab subjected to central impact at (a) 2.3 m drop height (3rd strike); (b) 2.8 m drop height (2nd strike).

The overall crack propagation and failure pattern of the pre-damaged slabs subjected to the same drop height were almost similar with the undamaged slabs. In the case where perforation had occurred, the size of the shear plug was also found to be almost the same. The results also showed that under multiple impacts, both type of slabs had eventually failed locally in a punching shear mode and at the same time developed substantial amount of edge cracks especially when impacted at 1.5 m drop height. In some cases, these edge cracks were able to progress deeper and extended to the bottom face. As expected, increasing the drop height had resulted in a higher degree of localised damage. This effect can be seen in both types of slab impacted from 2.8 m drop height where the new cracks were largely concentrated within the impact location.

5.4.3 Crack Propagation and Failure Pattern for the Slabs Subjected to Edge Impact Case

The crack pattern and failure mode of the slab impacted from 1.5 m drop height is shown in Figure 5.8. The punching shear failure on the top face started with the development of a half circle shear crack at the impact location as shown in Figure 5.8 (a). In successive strikes, this crack extended halfway towards the nearest corners before rotating downwards and initiating the shape of the shear punching failure. At failure, the shear punching area resembled the shape of a half-circle as shown in Figure 5.8 (c). Also noted was the presence of fine edge cracks along the two clamped edges adjacent to the impact location.

The dispersion of the shear crack from the top face reached the clamped edge on the bottom face together with a region of fine flexural cracks located underneath the impact location as shown in Figure 5.8 (a). In successive strikes, the edge crack propagated further until it reached the two corners while the flexural cracks spread towards the middle of the slab as shown in Figure 5.8 (b). At failure, a clear half-circle shear punching area was observed together with a slight progression of the flexural cracks underneath the impact location.

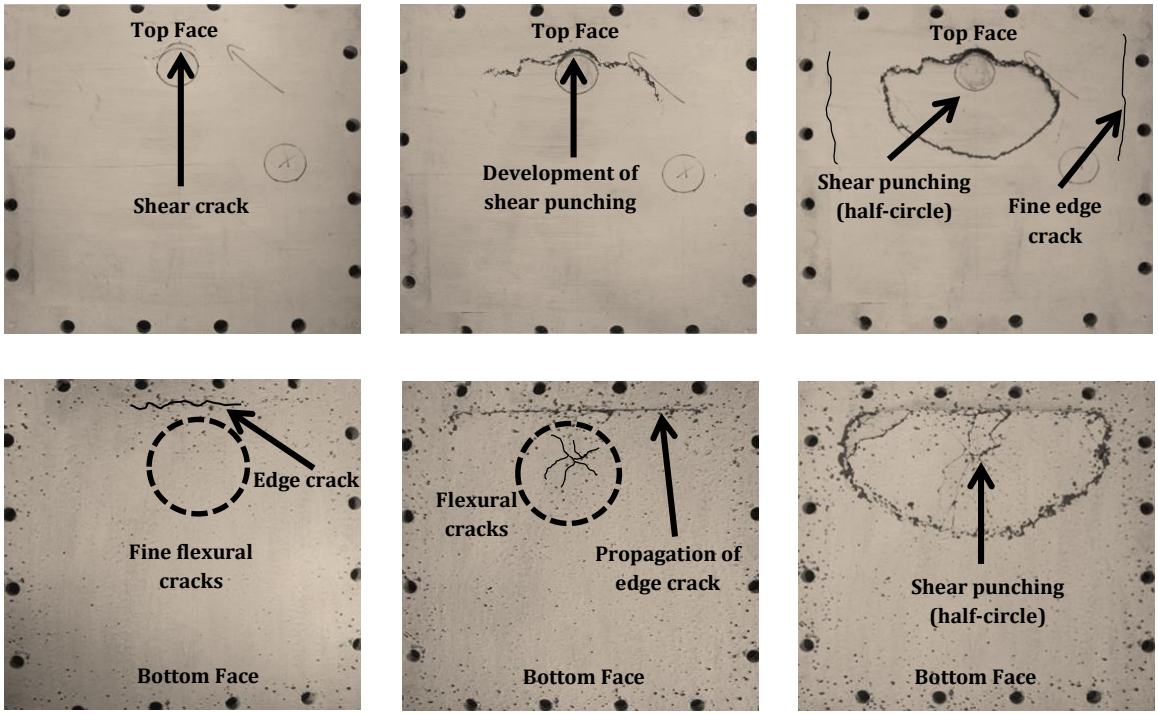

(a) (b) (c)

Figure 5.8: Crack propagation and failure pattern on top (above) and bottom (below) for undamaged UHPFRC slab subjected to edge impact at 1.5 m drop height after (a) 1st strike; (b) 3rd strike; (c) 6th strike (at failure).

The failure pattern for the undamaged slab impacted from 2.3 m and 2.8 m drop heights are shown in Figure 5.9 (a) and (b), respectively. Unlike the case at 1.5 m drop height, the failure for these slabs were more localised where the size of the shear punching area on both faces was relatively smaller and insignificant crack propagation was developed elsewhere. This phenomenon suggested that the impact energy supplied by the impactor was mostly absorbed and used within the impact vicinity hence expediting the shear punching failure.

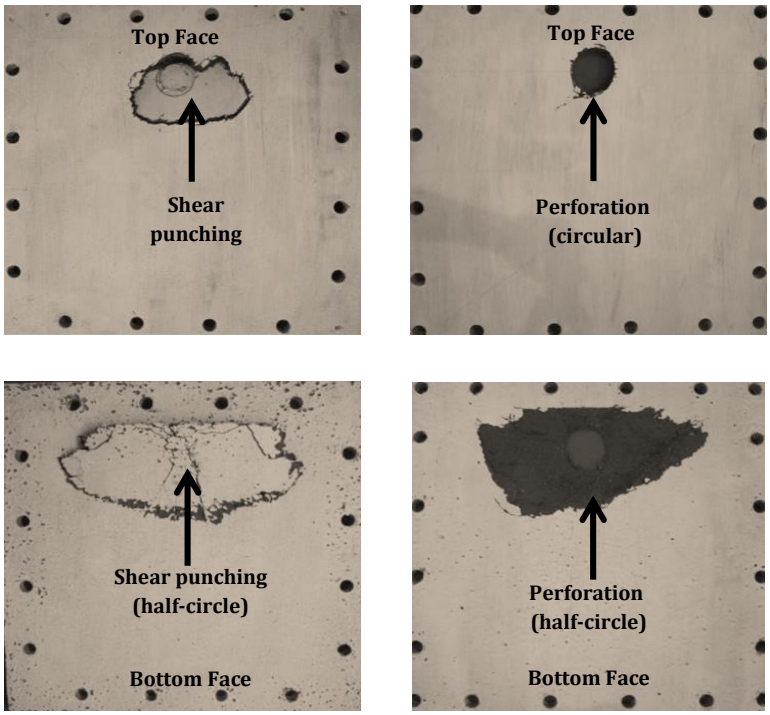

(a) (b)

Figure 5.9: Final failure pattern on top (above) and bottom (below) for undamaged UHPFRC slab subjected to edge impact at (a) 2.3 m drop height (4th strike); (b) 2.8 m drop height (2nd strike).

In the case of the pre-damaged slabs impacted from 1.5 m drop height, a half-circle shear crack was developed at the impact location on the top face as shown in Figure 5.10 (a). The initial cracks formed along the edges on the top face and at the centre of the bottom face had not significantly propagated. In successive strikes the circular shear crack on the top face transformed into a shear plug with extended shear cracks without affecting a large area as shown in Figure 5.10 (b) and Figure 5.10 (c). On the bottom face, an edge crack was initially formed and propagated further in subsequent strikes as shown in Figure 5.10 (b). Fine flexural cracks were also generated at the area underneath the impact location and propagated towards the middle part of the slab, similar to the undamaged slab. At failure, a shear plug taking the shape of a circular segment was formed while the edge crack extended towards the middle of the slab as shown in Figure 5.10 (c).

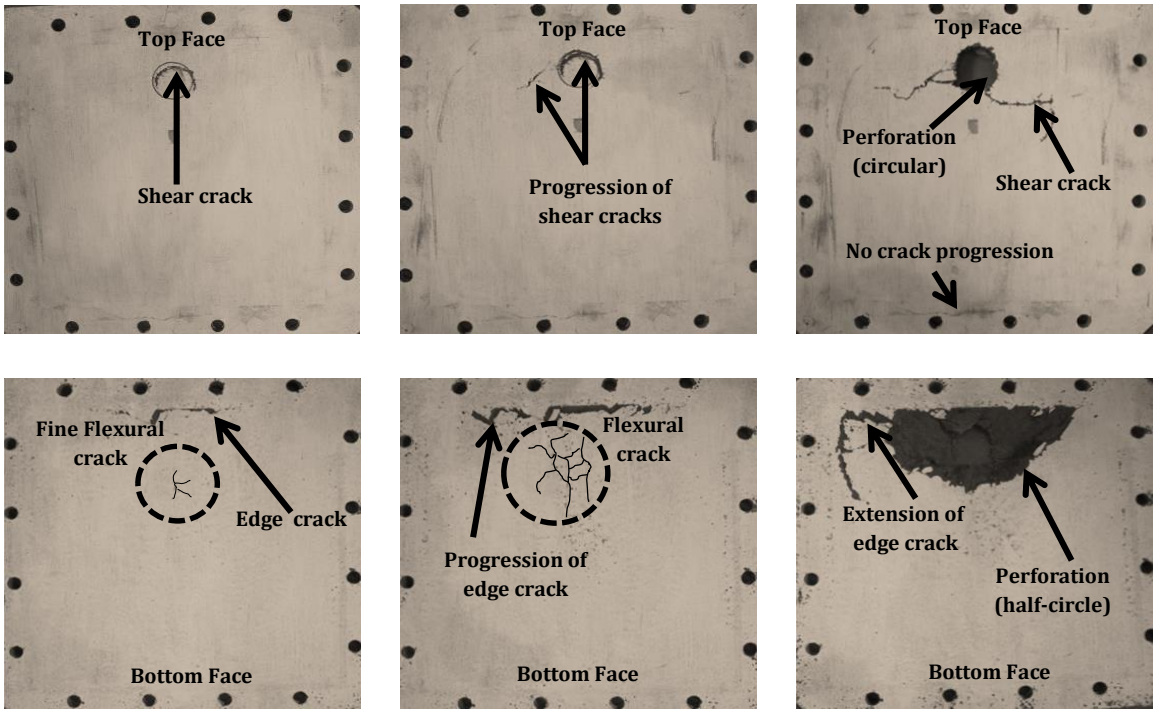

(a) (b) (c)

Figure 5.10: Crack propagation and pattern on top (above) and bottom (below) for pre-damaged UHPFRC slab subjected to edge impact at1.5 m drop height after (a) 1st strike; (b) 3rd strike; (c) 5th strike (at failure).

Figure 5.11 (a) and (b) show the final failure pattern for the pre-damaged slabs impacted from 2.3 m and 2.8 m drop heights, respectively. It can be seen that the failure pattern for these slabs was relatively similar to the pre-damaged slab impacted at 1.5 m drop height although the shear punching area was slightly irregular. No significant propagation or new crack development was observed elsewhere except within the vicinity of the impact location.

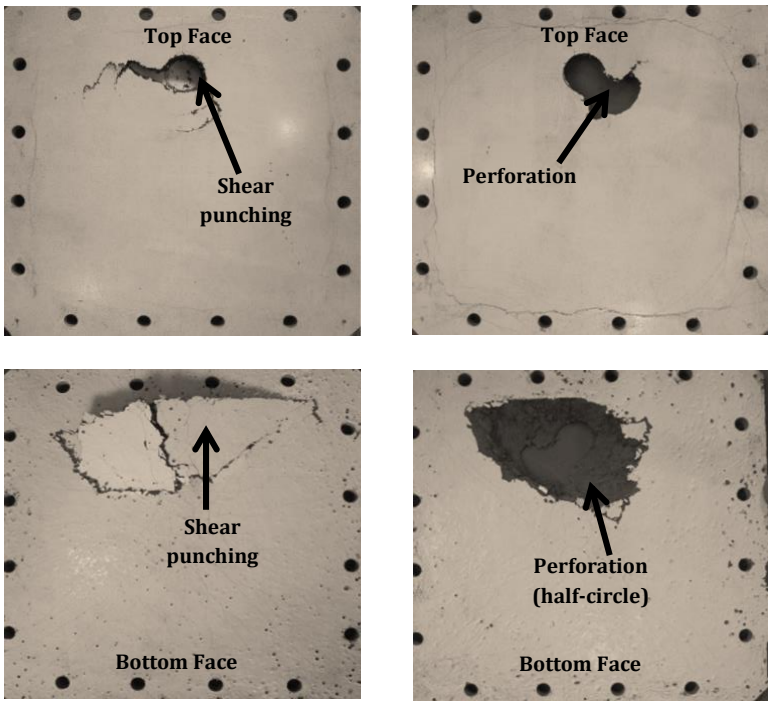

(a) (b)

Figure 5.11: Final failure pattern on top (above) and bottom (below) for pre-damaged UHPFRC slab subjected to edge impact at (a) 2.3 m drop height (3th strike); (b) 2.8 m drop height (2nd strike).

The crack propagation and failure pattern for the pre-damaged slabs were almost similar to the undamaged slabs. Although the pre-damaged slabs carried initial cracks along the impacted edge, the mode of failure was still governed by shear punching suggesting that the pre-damaged condition has no obvious influence on the overall damage scenario. When both types of slabs were impacted from 1.5 m drop height, the crack along the impacted edge had extended further compared to the crack developed from impact at 2.3 m and 2.8 m drop height. As a result, the area of the punching failure for the slabs impacted at 1.5 m drop height became larger. In all cases, the crack propagation along the other three edges on the top face of the slabs was insignificant.

5.4.4 Crack Propagation and Failure Pattern for the Slabs Subjected to Corner Impact Case

The crack development and failure pattern for the undamaged slab subjected to corner impact from 1.5 m drop height is shown in Figure 5.12. On the top face, a shear crack that took the shape of a half circle at the impact location together with fine cracks located closer to the corner of the slab were formed. At failure, the circular shear crack propagated deeper forming a shear punching failure as shown in Figure 5.12 (b). Insignificant development of edge cracks was observed.

On the bottom face, shear cracks had developed at the corner of the slab together with fine flexural cracks underneath the impact location as shown in Figure 5.12 (a). At failure, the corner crack formed a shear punching area almost the shape of a circular quadrant. No significant flexural cracks were developed or propagated elsewhere on both faces of the slab.

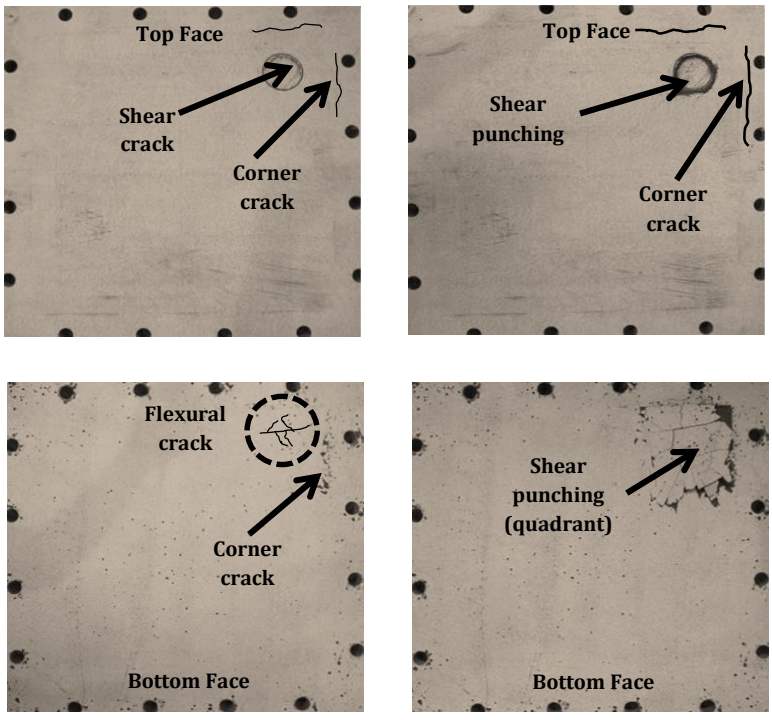

(a) (b)

Figure 5.12: Crack propagation and failure pattern on top (above) and bottom (below) for undamaged UHPFRC slab subjected to corner impact at 1.5 m drop height after (a) 2nd strike; (b) 4th strike (at failure).

A very similar trend was also observed for the slabs impacted from 2.3 m and 2.8 m drop heights as shown in Figure 5.13 (a) and (b), respectively. The final failure pattern showed similar punching shear area, formation of corner cracks and insignificant progression of edge cracks.

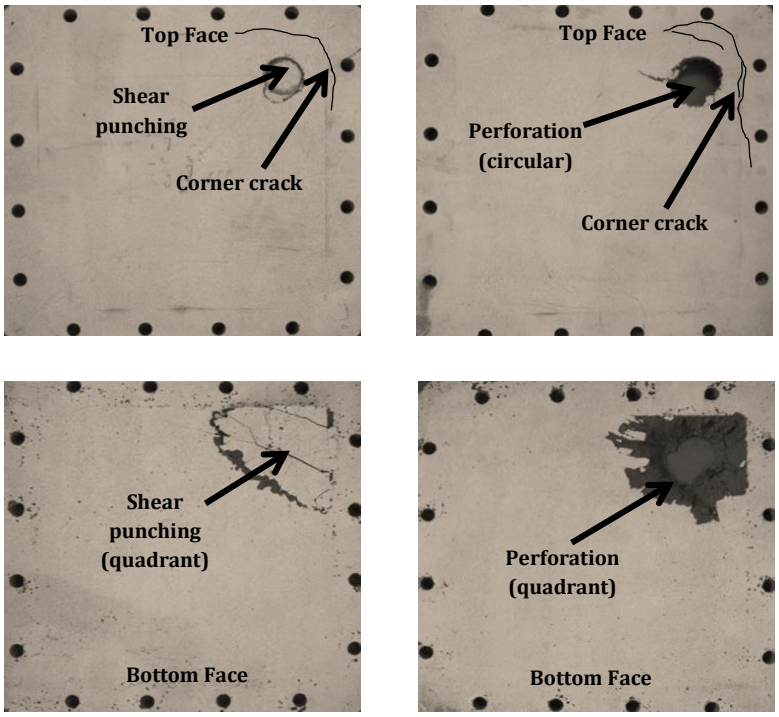

(a) (b)

Figure 5.13: Final failure pattern on top (above) and bottom (below) for undamaged UHPFRC slab subjected to corner impact at (a) 2.3 m drop height (2nd strike); (b) 2.8 m drop height (2nd strike).

Figure 5.14 shows the crack propagation and failure pattern for the pre-damaged slab impacted from 1.5 m drop height. Similar to the undamaged slab, a half-circle shear crack and corner cracks were formed at the impact location. The existing cracks along the edges of the top face and the flexural cracks at the centre of the slab show some degree of propagation, more obvious compared to the undamaged slab. However, at failure, these cracks remain unchanged. The shape of the shear punching area or the shear plug was also relatively similar to the undamaged slabs.

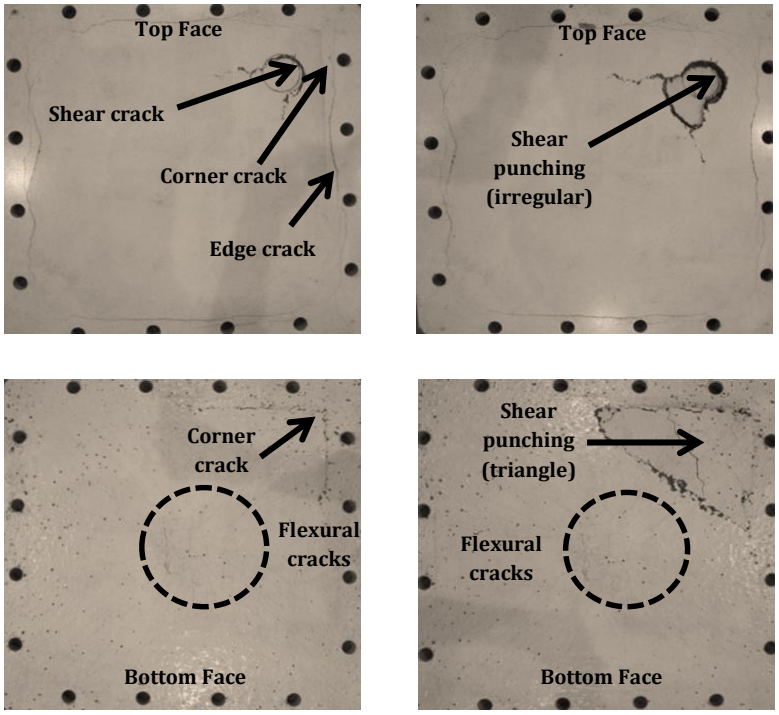

(a) (b)

Figure 5.14: Crack propagation and final failure pattern on top (above) and bottom (below) for pre-damaged UHPFRC slab subjected to corner impact at 1.5 m drop height after (a) 2nd strike; (b) 3rd strike (at failure).

In the case of the slabs impacted from 2.3 m and 2.8 m drop height, the sudden perforation of the slabs had caused the damage to be concentrated within the vicinity of the impact location as shown in Figure 5.15. On the top face, apart from the circular perforated area, cracks at the corner of the slab were also formed. However, insignificant progression of cracks was observed along the edges. A perfect circular-quadrant shear plug can be seen on the bottom face of the slab as shown in Figure 5.15 (b).

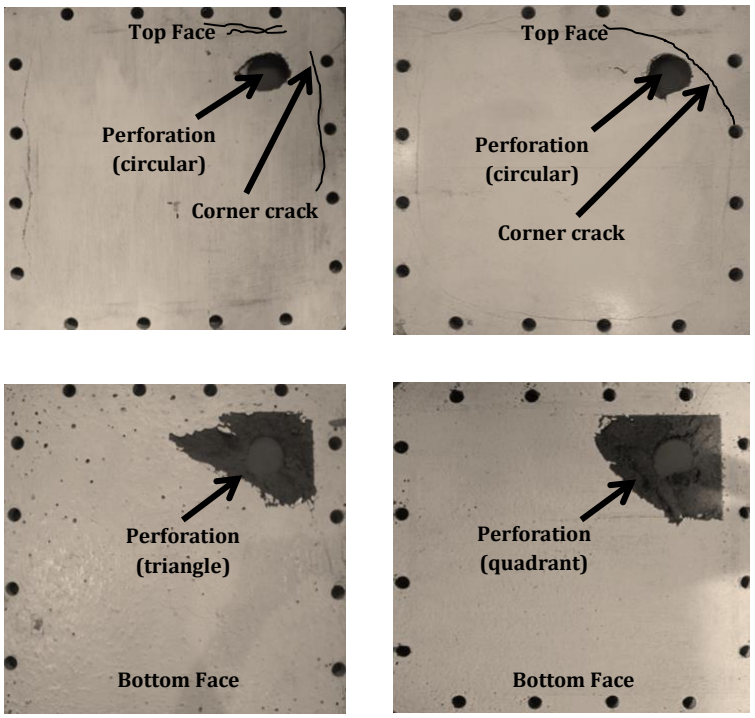

(a) (b)

Figure 5.15: Final failure pattern on top (above) and bottom (below) for pre-damaged UHPFRC slab subjected to corner impact at (a) 2.3 m drop height (2nd strike); (b) 2.8 m drop height (1st strike).

The results from the corner impact show that the crack propagation and final failure pattern of the pre-damaged slabs were relatively similar to the undamaged slabs. In all cases, the damage was more localised having similar size of punching shear area. This observation suggests that the failure of the slabs subjected to the corner impact is highly governed by the punching shear compared to the central and edge impact. Similarly, it can also be seen that the crack propagation and failure pattern for the slabs are not significantly influenced by the drop height.

5.4.5 Crack Propagation and Failure Pattern for the Slabs Subjected to Oblique Impact Case

The crack development and failure pattern for the undamaged slab subjected to oblique impact from 2.8 m drop height is shown in Figure 5.16. During the first strike, a half-circle shear crack line was formed on the top face as shown in Figure 5.16 (a). Also noted was the presence of dark half-circle marking at the impact location. Upon inspection, it was found that the surface of the marking was coarse suggesting that friction with the impactor had taken place during contact with the impactor. This area was also indented with the deeper section being located at the tip of the half circle. At the same time, cracks had formed along the edges of the slab and were more obvious at the two edges located on the left and right of the slab.

In subsequent strikes, the shear punching area developed where deeper indentation was observed at the impacted area. In the final strike, shear punching failure taking the shape of a half circle occurred as shown in Figure 5.16 (c). Along the edges, wider cracks developed and propagated further towards the corner.

On the bottom face, flexural cracks were initially formed underneath the impact location. In subsequent strikes, these cracks then propagated further towards the two corners that are closer to the impact location as shown in Figure 5.16 (b). At failure, an irregular shear punching area was formed.

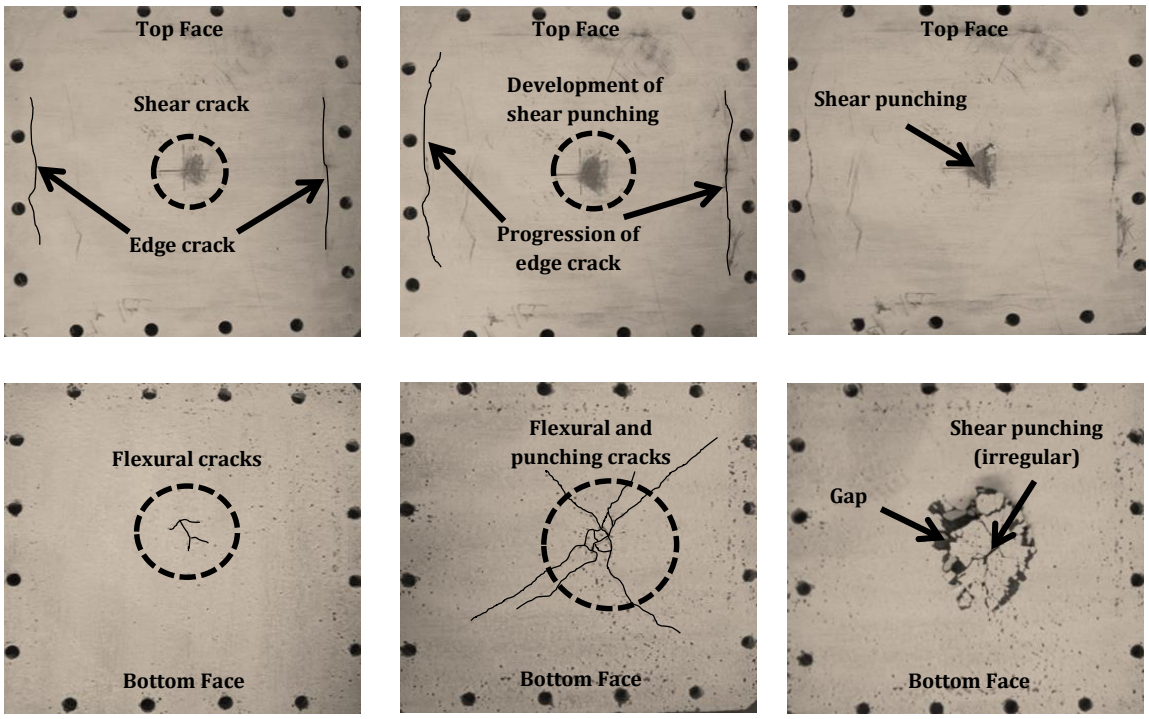

(a) (b) (c)

Figure 5.16: Crack propagation and failure pattern on top (above) and bottom (below) for pre-damaged UHPFRC slab subjected to 10° oblique impact at 2.8 m drop height after (a) 1st strike; (b) 3rd strike; (c) 5th strike (at failure).

Unlike the undamged slab at failure, the pre-damaged slab showed a circular shear punching area on the top face as shown in Figure 5.17 (a). However, the deeper section is still at the centre of the slab which was similar to the undamaged slab. The existing cracks along the edges also propagated and almost formed a closed loop. The most severe cracks were located at the edge closest to the impact location. On the bottom face, the shear punching area was almost rectangular as shown in Figure 5.17 (b). The formation of this punching shear area and shape was influenced by the existing flexural cracks developed earlier at the middle of the slab during the pre-damaging exercise.

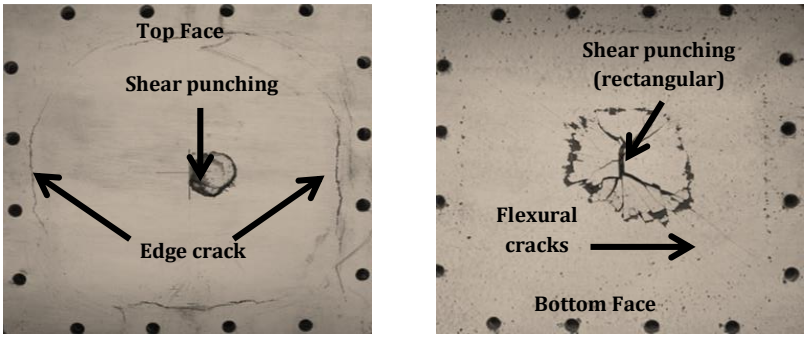

(a) (b)

Figure 5.17: Final failure pattern for pre-damaged UHPFRC slab subjected to 10° oblique and impacted at 2.8 m drop height after the 3rd strike showing (a) top face; (b) bottom face.

5.4.6 Discussion on the Failure Patterns with Respect to Progressive Collapse Risk

The failure patterns observed in the experimental work described previously for the undamaged and pre-damaged slabs can be related to two possible threats as listed below.

i) **Local punching of the slab only**. This type of failure is likely to take place when both types of slab are impacted at higher drop height or when the impact location is closer to the edge and corner of the slab. Such failure is caused by a single or relatively lower number of impacts from a failed column. It can be seen that local and immediate punching failure produced a smaller shear plug. The impact from a small fragment onto a slab generates a lesser impact demand and is unlikely to trigger a progressive collapse. On the other hand, failure of a plain concrete slab under low velocity impact can be global and catastrophic where larger fragments can be produced [1] as shown in Figure 5.18 (a). The failure of a reinforced concrete slab may not show a global failure but the spalling or perforation can be accompanied by a large shear plug as shown in Figure 5.18 (b) and (c), respectively [2]. In the actual structural slab, the local punching and large scabbing creates a threat to equipment, machinery and occupants located underneath within the vicinity of the impact location.

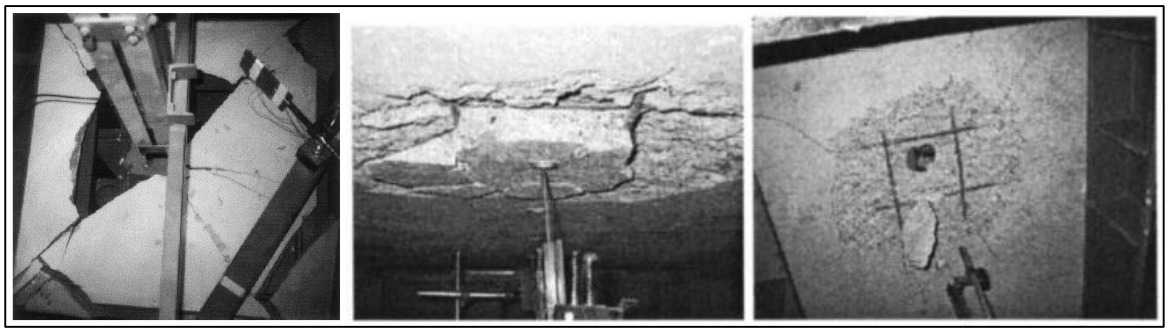

(a) (b) (c)

Figure 5.18: Typical low-velocity impact failure showing (a) larger fragments for plain concrete [1]; (b) serious spalling for reinforced concrete [2]; (c) perforation with large shear cone for reinforced concrete [2].

ii) **Potential detachment of the slab edge(s)**. This type of event is likely to take place when the drop height is relatively lower than in (i) and the impact location is at the centre (both normal and oblique) or closer to the edge of the slab. In the case of the slab subjected to the central impact, the cracks on the loaded face progress through the thickness until reaching the bottom face of the slab. This situation can cause full detachment of the slab edges from the supporting beams as shown in Figure 5.19 (a). Eventually, the whole piece of slab may fall down and impact the floor below. The removal of the slab also reduces the lateral stability of a structure. Partial detachment of the slab edge is reflected in the case of edge impact. When the edge of an actual square or rectangular slab is partially detached from the supporting beams, a portion of the slab's dead and live load is transferred to the respective beams as shown in Figure 5.19 (b). These beams are at risk of failure if they are not designed to carry the unexpected load. The situation can be worse if the edge impact occurs along the short span of a one-way slab as shown in Figure 5.19 (c). The loss of support along the short span can cause the slab to become cantilevered and significantly changes the reinforcement demand. Inability to meet the demand may cause the cantilevered end to fail, impacting the lower floor and initiating a progressive collapse.

Partial detachment of the slab at the corner of a two-way and one-way slab may not pose significant threat to the floor system. However, the effect can be severe if the corner impact occurs close to the slab-column connection of a flat slab as shown in Figure 5.19 (d). A study by Micaleff *et al.* [3] showed that a surge in the loading rate at this area increased the punching shear strength and reduced the deformation capacity. The stiffer behaviour may lead to pure punching shear failure and the current empirical formulae are unable to predict this behaviour. Similarly, a direct punching may also occur if the design shear strength and reinforcement capacity is inadequate to cater for this punching shear section as shown in Figure 5.19 (d)

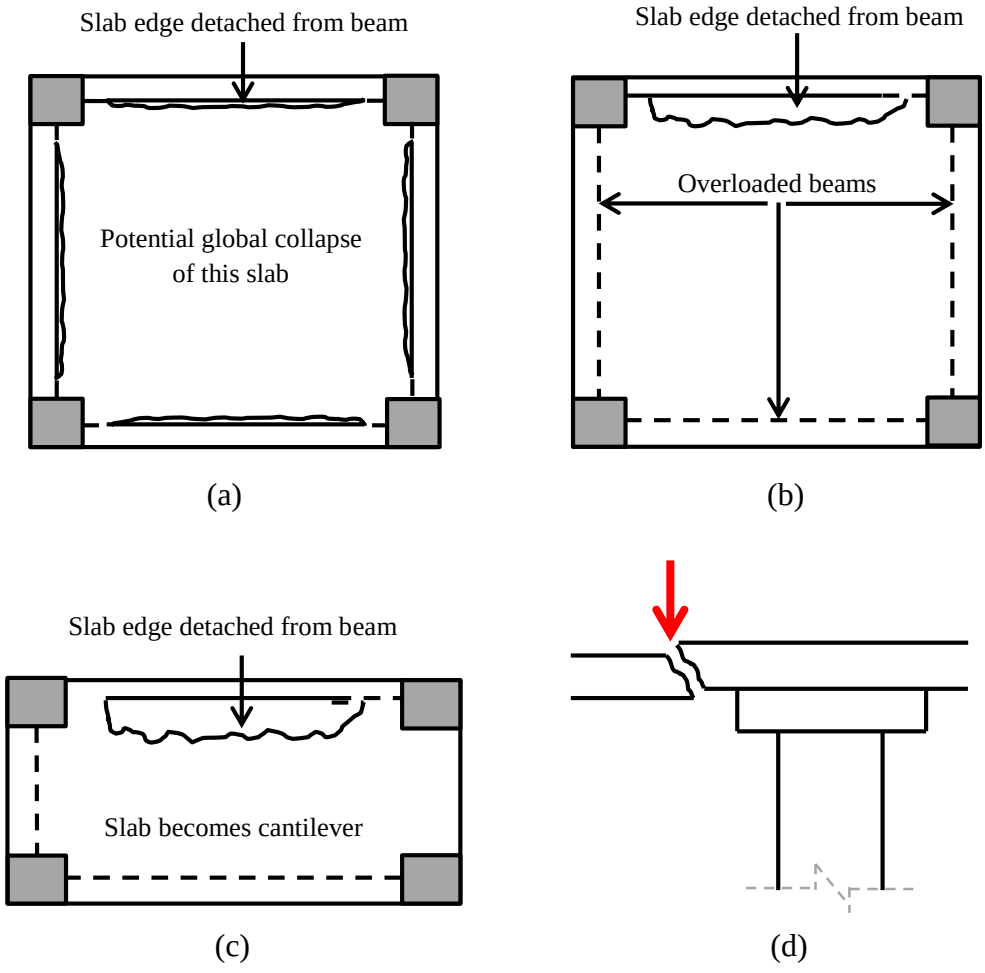

Figure 5.19: Potential risk of progressive failure for (a) square slab impacted at centre; (b) square slab impacted at edge; (c) one-way slab impacted at edge; (d) flat slab impacted at corner (rupture).

5.4.7 Cumulative Impact Energy

The impact resistance of the slabs can also be analysed by measuring the impact energy instead of number of strikes. Moreover, this approach is technically more meaningful and has the advantage when included in fundamental equations. This is particularly true as shown in equation (2.1) where the energy component (velocity and mass) is embedded in the formulation to determine the minimum thickness of the slab against perforation.

Currently, there is no standard term being used in the literature to date to describe the total impact energy required at failure of a test specimen. Some of the random terms available are 'energy to perforation' [4], 'impact energy at complete failure' [5], and 'energy absorbed' [6]. These terms refer to the kinetic energy of the impactor immediately prior to impact. The actual term for 'energy absorbed' represents the net kinetic energy supplied by the impactor to the test specimen after considering all the energy losses such as friction and damping [7].

This study covers multiple impact scenarios where an accumulation in the energy supplied per strike is expected. As such, a new term called 'cumulative impact energy' (CIE) is defined here in order to avoid the misconception in the representation of the energy. The word 'cumulative' describes the increase in the amount of energy with respect to the number of strikes. It is noted that some of this impact energy (kinetic energy) will be retained in the impactor on rebounding. In this case, the rebound energy can be determined by plotting the full force-deformation history of the impact event. However, the investigation of the retained energy in the impactor, the energy loss and the final absorbed energy by the UHPFRC slab is not part of this work scope. In order to provide a simple and straight-forward comparison between different impact events without considering perforation or rebound condition, only the kinetic energy supplied by the impactor was considered in this study. As such the term 'impact energy' represents the energy supplied by the impactor before impact [4-6] and the cumulative impact energy can be calculated using the equation

$$E_{cie} = \frac{1}{2} \times m \times {v_i}^2 \times n \ , \tag{5.1}$$

where

v_i = the average velocity before contact (m/s),

n = number of strikes, and

m = mass of the impactor (kg).

The charts showing the CIE for undamaged and pre-damaged slabs under various impact conditions are shown in Figure 5.20 (a) and Figure 5.20 (b), respectively. In order to compare the impact energy demand of the pre-damaged slabs with the undamaged slabs, the total CIE of the pre-damaged slabs in Figure 5.20 (b) was normalized with the total CIE of the undamaged slabs in Figure 5.20 (a). The normalised value for central impact was calculated to be 0.86, 0.64 and 0.6 at 1.5 m, 2.3 m and 2.8 m drop height, respectively. In the case of edge impact, the normalised value was calculated to be 0.75, 0.71 and 0.6. Similarly for slabs subjected to the corner impact, the normalised value was 0.67, 0.75 and 0.67. Finally, for the oblique impact, the normalised value was 0.54.

The high value shown in the calculation suggests that the pre-damaged slabs are able to withstand a significant amount of impact energy similar to the undamaged slabs. Although the value drops as the energy per strike is increased, the overall results still show a value more than 0.5. As such, in most cases, the pre-damaged slabs were able to absorb a relatively high impact energy considering that the slabs initially carried damage beyond the elastic limit. The lowest value shown by the oblique impact suggests that the pre-damaged slabs were weakest when impacted in the form of a point contact.

The sensitivity of the impact location and impact angle can be clearly seen by comparing the total CIE between the central impact with the rest of the tests, both for undamaged and pre-damaged slabs. It can be seen in Figure 5.20 (a) and Figure 5.20 (b) that the total CIE is the highest under the central impact compared to the edge and corner impact. The results indicate that moving the impact location from the centre of the slab closer to the clamped edges could significantly expedite the failure. Moreover, the relatively small increase in the energy

demand shown by the edge and corner impact indicates that the impact at these locations is not significantly influenced by the drop heights compared to the central impact. Finally, the slabs subjected to the oblique impact at 2.8 m drop height exhibited the highest total CIE both for the undamaged and pre-damaged slabs suggesting that the point contact increased the energy demand of the slabs.

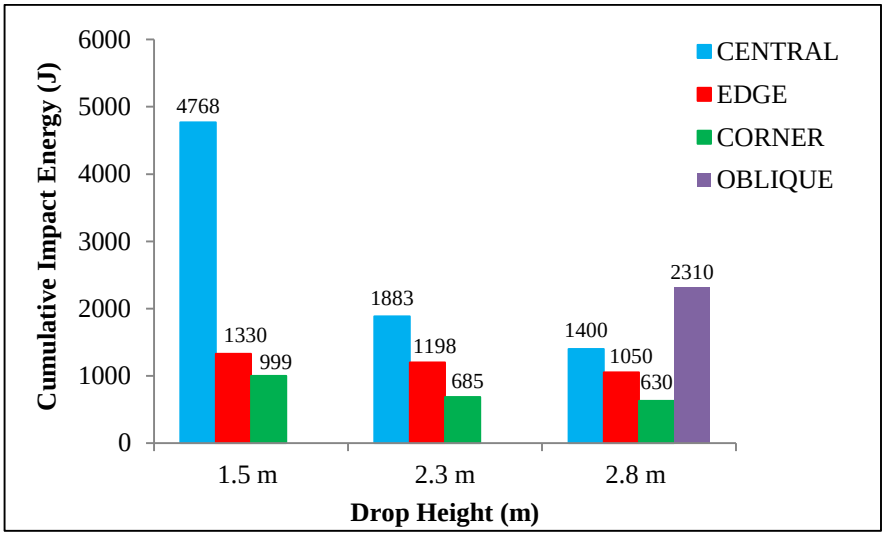

(a)

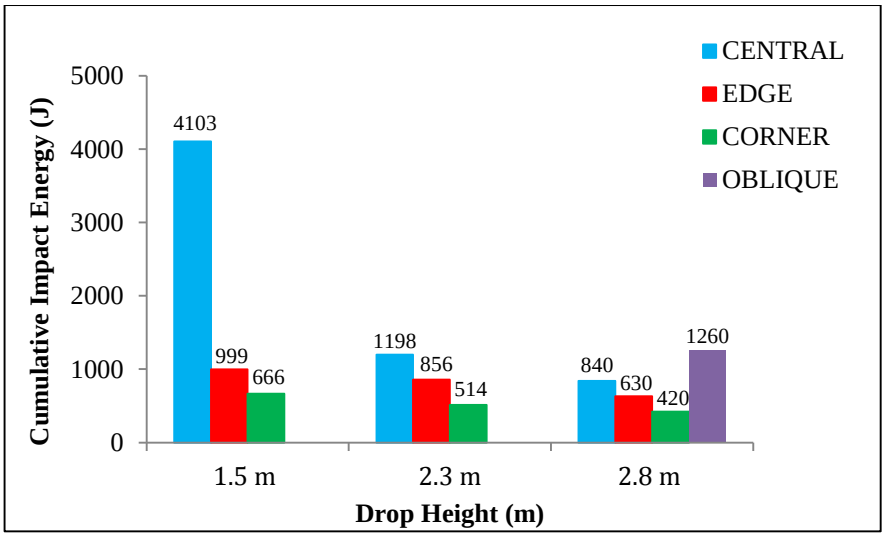

(b)

Figure 5.20: Comparison between the cumulative impact energy to failure for central, edge, corner and oblique impact cases at respective drop heights for (a) undamaged slabs; (b) pre-damaged slabs.

The investigation on the normalised CIE of the pre-damaged slab is extended in a preliminary investigation to determine the minimum thickness of the slab against perforation by modifying equation (2.1). In the case of the undamaged slab subjected to a central impact at 2.8 m drop height, the minimum thickness of the UHPFRC slab was calculated to be 16.8 mm. In the experimental work, the slab thickness was 25 mm and survived at least three strikes before perforation. Theoretically, a lower thickness than 25 mm can be used in order to survive perforation at the first strike. As such, a more refined study is required in this area in order to effectively utilise equation (2.1).

Similarly, knowing that the lowest normalised CIE of the pre-damaged slab was 0.6, equation (2.1) was modified to be:-

$$e = \left(\frac{V_0}{v_i}\right)^{0.25} \left(\frac{m{v_i}^2}{0.6df_c}\right)^{0.5} \left(1 + 5.39V_f\right)^{0.38} \quad (5.1)$$

The minimum thickness for the pre-damaged slab subjected to a single impact at the centre of the slab was calculated to be 21.7 mm. Due to the fact that the pre-damaged slab with 25 mm thickness survived the first strike at 2.8 m drop height but perforated at the second strike, the calculated value shows a close agreement with the experimental result with a factor of 1.15. The full set of calculations is given in Appendix C.

In the case of edge and corner impact case, a different set of equations should be used. This is particularly true due to the fact that the edge and corner impact only require a small amount of total CIE in order to perforate at all drop heights compared to the central impact case. As such, it is not possible to modify equation (2.1) and equation (5.1) by introducing a reduction factor to the impact energy components.

5.4.8 Maximum Deformation

The raw data representing the velocity-time history for one of the pre-damaged slabs subjected to a central impact at 2.8 m drop height (first strike) and superimposed by the idealised signal is shown in Figure 5.21 (a). For clarity, the frequency spectrum up to 2000 Hz for both signals (y-axis is in log 10 scale) is shown in Figure 5.21 (b). The idealized data represents the original shape of the amplitude-frequency distribution without any interference (commonly known as noise) from the system such as vibration from the slab and the impactor. As such, the influence of the noise on the raw data, if any, can be investigated.

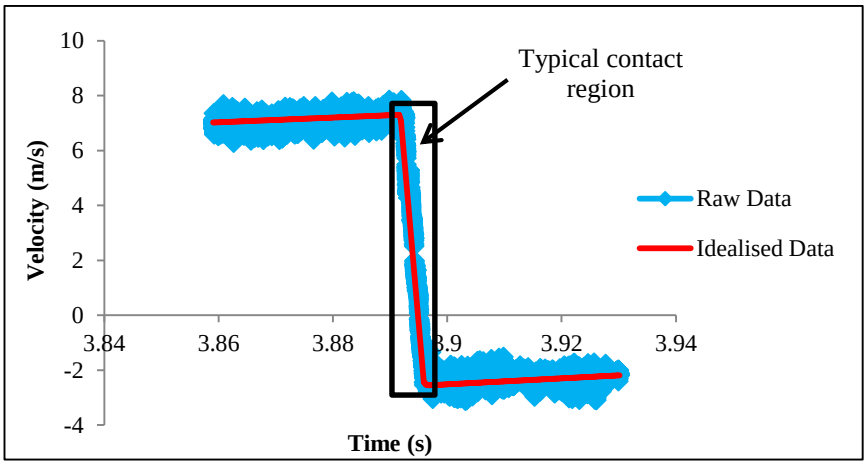

(a)

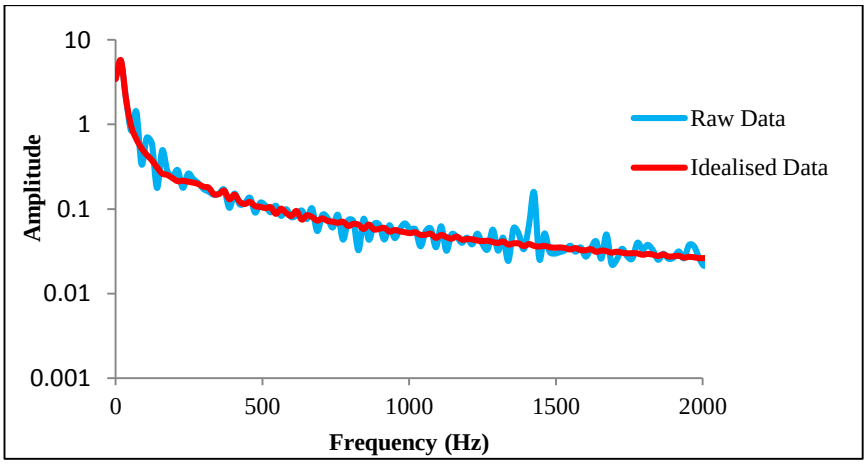

(b)

Figure 5.21: Velocity-time history of the raw and idealised signal in (a) time domain; (b) frequency domain (up to 2000 Hz only).

The graphs in Figure 5.21 (b) show that the frequency spectrum of the raw data matches the overall shape of the idealized data. The idealized data contains high amplitude data at low frequency range up to approximately 100 Hz and low amplitude data after the 500 Hz similar to the raw data. A smooth transition curve between these two sets of frequencies is also observed. As such, the noise embedded in the raw data is not influencing the overall amplitude-frequency distribution. However, the raw data contains several spikes or ripples at the lower frequency range (between 70 and 250 Hz) and also at approximately 1400 Hz. The low frequency noise can be contributed by the natural vibration of the slab, calculated to be 116 Hz using the equation

$$f_n = \frac{1}{2\pi} \times \sqrt{\frac{k}{m}} \quad , \tag{5.2}$$

where

f_n = natural frequency (Hz),

k = elastic stiffness of the slab (refer to Section 6), and

m = mass of the slab (kg).

On the other hand, the high frequency noise in the raw data can be associated with the sound wave travelling up and down the impactor and the natural vibration of the impactor. However, both calculations are complex and may require other measuring devices not within the scope of this study.

A second order Butterworth Low Pass Filter with 1000 Hz cut-off frequency was selected for all filtering work. This approach retains data with low frequency while attenuates the data with higher frequencies. As shown in Figure 5.21 (b), any attempt to remove the noise at the lower frequency range using a Low Pass Filter will also affect the true data. Figure 5.22 shows the filtered data superimposed on the raw data. It can be seen that the proposed 1000 Hz cut-off frequency follows the trend of the average reading with reasonable accuracy especially within the contact region.

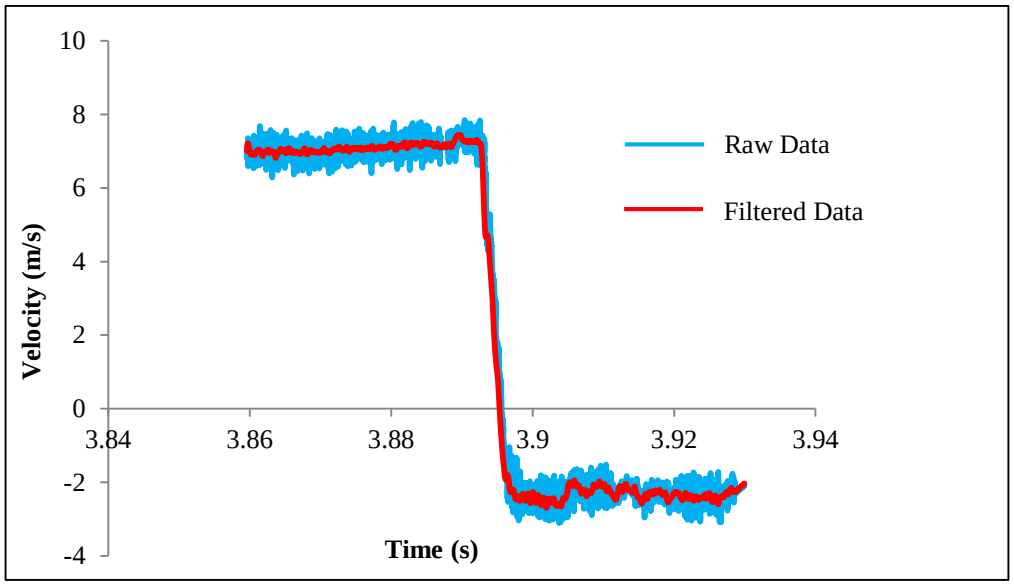

Figure 5.22: Superimposing the raw and the filtered data using Low Pass Butterworth Filter at 1000 Hz cut-off frequency.

The velocity from the overall filtered velocity-time data was averaged for clarity and consistency in the following presentations. In general, the average impact velocities for the impactor travelling from 1.5 m, 2.3 m and 2.8 m were calculated to be 5.32 m/s (standard deviation 0.025), 6.62 m/s (standard deviation 0.033) and 7.32 m/s (standard deviation 0.025). As such, the impact energy when the impactor is dropped from 1.5 m, 2.3 m and 2.8 m was averaged at 222 J, 342 J and 420 J, respectively.

Samples of the deformation-time history obtained from the processed LDV data are shown in Figure 5.23 (a) and Figure 5.23 (b). The first graph represents a condition where the impactor strikes the slab and moves downward until a maximum deformation is achieved. As there is no perforation to the slab, the impactor starts to move upward (rebound) from this point and later detaches from the slab at the end of the contact time. The second graph (b) shows a condition where the slab has failed, signified by the increasing deformation throughout the contact time and hence no true maximum deformation can be recorded. The number of data points recorded in all cases was between 900-1200 within typically 5 ms. The relatively large number of data points collected during the contact event can be expected to provide good accuracy in determining other measurements such as deformation and contact force.

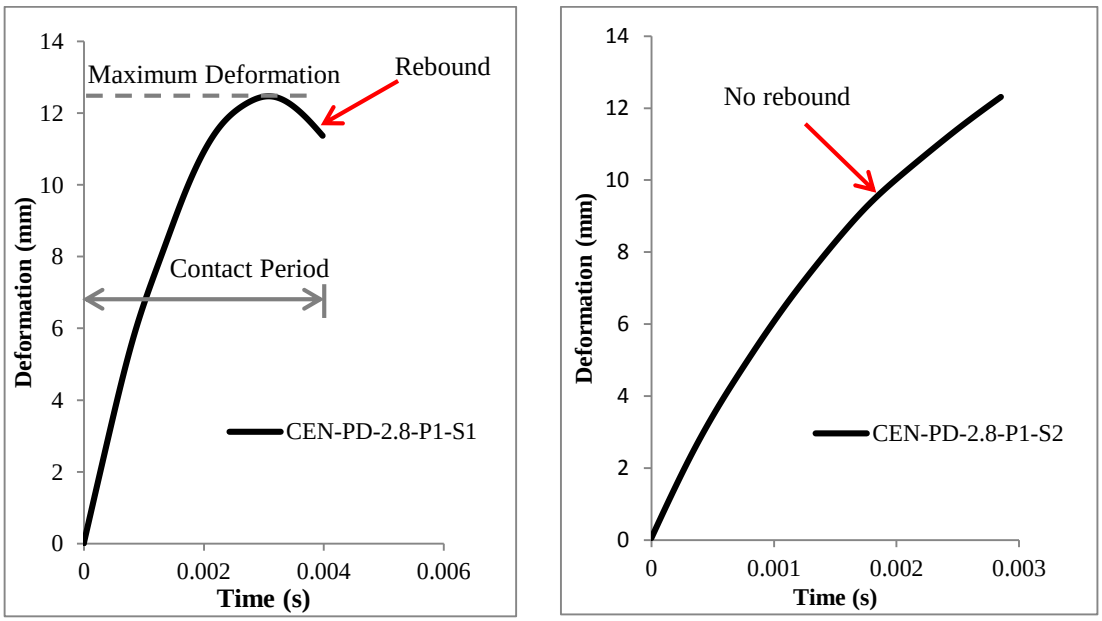

(a) (b)

Figure 5.23: Deformation-time history from LDV showing (a) a rebound condition; (b) at failure.

Figure 5.24 (a) to Figure 5.24 (c) shows the relationship between the average maximum deformation and the CIE for the undamaged and pre-damaged slabs impacted at various drop heights. It is worth mentioning that although CIE is used, the deformation trend can also be visualised with respect to the number of strikes. In each figure, the impact cases are presented

with respect to the same drop height and as such, every point shown by the marker also represents the strike. The same concept is applied in other graphs involving CIE values.

As expected, in all cases the maximum deformation of the pre-damaged slabs was found to be higher than the undamaged slabs. This is obviously due to the initial damage and deformation carried by the pre-damaged slabs. All pre-damaged slabs impacted at 1.5 m drop height showed relatively similar deformation trend compared to the undamaged slabs as shown in Figure 5.24 (a). At the same CIE, the similarity between the two graphs was more obvious for the slabs subjected to the edge and corner impact where the divergence is relatively small compared to the slabs subjected to the central impact. However, the differences in terms of the final maximum deformation between the pre-damaged and undamaged slabs were 4.3% for the slabs subjected to the central impact compared to 5.3% and 29.0% for the edge and corner impact, respectively.

The deformation of the pre-damaged slabs continues to follow the trend of the undamaged slabs when the drop height is increased to 2.3 m and 2.8 m as shown in Figure 5.24 (b) and Figure 5.24 (c), respectively. This is particularly true when comparing the value of the maximum deformation at the same CIE. When impacted at 2.3 m drop height, the differences in terms of the final maximum deformation between the two types of slab increased to 18.9% and 8.4% for the slabs subjected to the central and edge impact. However, the difference showed by the slabs subjected to the corner impact reduced to 17.8 %. Similar trend is also observed when the slabs were impacted from 2.8 m drop height especially up to the final CIE of the pre-damaged slabs. No comparison can be made for the corner impact as the pre-damaged slabs had failed at the first strike.

Similarly, the deformation of the pre-damaged slabs subjected to the oblique impact from 2.8 m drop height was also able to follow the trend of the respective undamaged slabs at the same CIE. However, the difference in terms of the maximum deformation at the respective CIE between both types of slab was relatively higher and calculated to be 32.0 %.

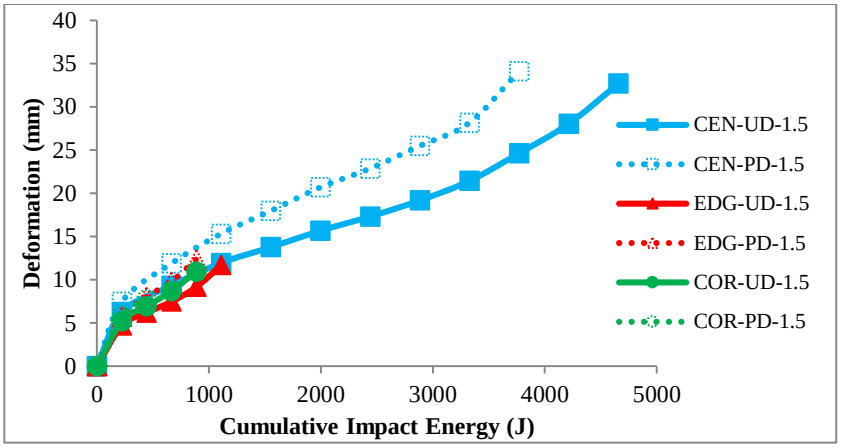

(a)

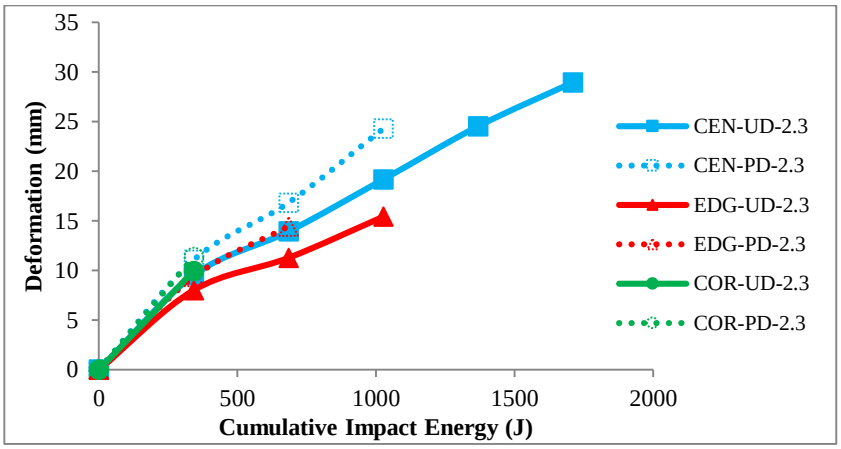

(b)

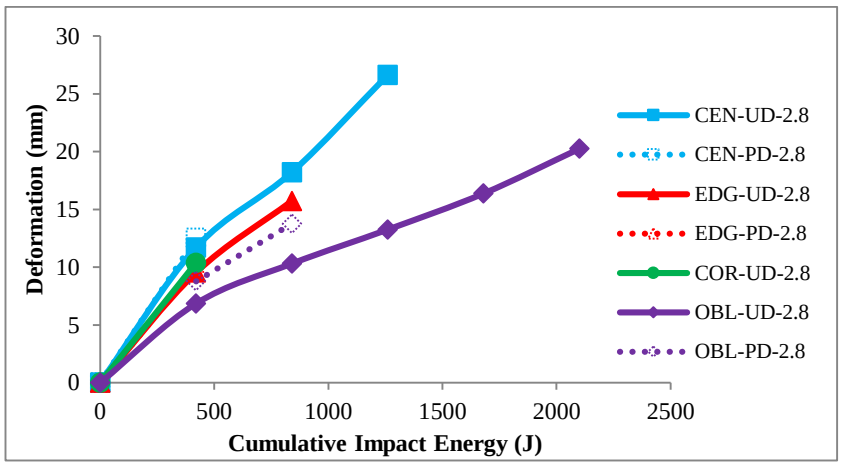

(c)

Figure 5.24: Relationship between the maximum deformation and CIE for the slabs impacted at (a) 1.5 m; (b) 2.3 m; (c) 2.8 m drop height.

The ability to withstand multiple impacts and at the same time show a similar deformation trend with the undamaged slab in most of the impact scenarios suggests that the pre-damaged slabs possess substantially high reserve strength. The phenomenon can be observed by comparing the final maximum deformation between both types of slab where the differences are shown to be small especially when the energy per strike (drop height) is low. Although the difference increases with respect to the energy per strike, the deformation trend is still shown to be similar up to the final CIE of the pre-damaged slabs.

The similarity in the deformation trend suggests that the initial cracks at the centre of the slabs and along the edges had not significantly influenced the deformation trend of the pre-damaged slabs when impacted at the same location with the undamaged slabs. These results correlate well with the trend in the crack propagation of the pre-damaged slabs as shown earlier in Figure 5.4 to Figure 5.16. The initial cracks developed under the pre-damaging exercise allowed the stress from the impact loading to be effectively transferred between the existing crack planes hence showing similar crack propagation with the undamaged slabs. Such behaviour provides an indication that the pre-damaged slabs still possess a high degree of fibre bridging strength although they have been pre-damaged at a relatively high static pressure.

While there is little difference in terms of the maximum deformation between the pre-damaged and undamaged slabs for the central, edge and corner impact condition, there is a noticeable difference for the 10° oblique impact condition. The reason for this difference could be associated to the intense point loading imposed by the edge of the impactor and the influence is obvious when there are concentrated flexural cracks at the bottom face of the slab within the vicinity of the impact location.

The maximum deformation of the edge and corner impact (before failure) normalised with respect to the central impact is shown in Table 5.1. At 1.5 m drop height, the values were low and increased at 2.3m and 2.8 m drop height for all impact cases. Also, the slabs subjected to the corner impact showed a lower value compared to the edge impact, both for the undamaged and pre-damaged slabs. In most cases, the normalised values are less than 1.0. As for the oblique impact, the values are generally high compared to the corner and edge impact.

This phenomenon indicates that the slabs subjected to the corner and edge impact exhibited significantly lower maximum deformation at failure compared to the central impact and this is particularly true when the energy per strike is relatively low. The low deformation value at failure is more significant when the impact location is set closer to the corner. These results suggest that at lower energy per strike, the mode of failure of the edge and corner impact is governed by shear mode compared to the flexural mode as in the case of the central impact condition. At higher drop height, the ratio increase as a result from a relatively similar shear punching failure observed in all slabs.

The introduction of 10° obliquity shows a different pattern in the overall test results. In the case of the undamaged slabs, the final ratio is less than 1.0. This may indicate a slightly stronger influence on the shear punching failure. However, due to the fact that the slabs require almost double the CIE compared to the central impact, it can be justified that the oblique impact case exhibited slow punching shear development at subsequent impact. Although the pre-damaged slabs showed a ratio slightly more than 1.0, this may not give a clear indication that the response is governed by flexural failure. This is due to the fact that at the same CIE, the maximum deformation of the oblique impact was lower than the central impact as shown in Figure 5.24 (c). Considering that the oblique contact condition can cause a high stress concentration area that is more favourable to punching failure mode, the slightly higher ratio seen in the pre-damaged slabs can also be related to the slow punching shear development at subsequent impact.

Table 5.1: Final maximum deformation of the edge, corner and oblique impact normalised with respect to the central impact.

Drop Height (m)	Pre-damaged			Undamaged		
	EDGE/ CEN	COR/ CEN	OBL/ CEN	EDGE/ CEN	COR/ CEN	OBL/ CEN
1.5	0.36	0.23	-	0.36	0.33	-
2.3	0.59	0.47	-	0.53	0.34	-
2.8	0.98	-	1.10	0.59	0.39	0.76

These findings raise the need to consider the sensitivity of the impact location when designing a slab subjected to abnormal loading condition. As the slab subjected to asymmetrical impact is not able to deform extensively, the failure can be almost immediate without prior indication of yielding yet possess potential to trigger a progressive collapse as discussed earlier in section 5.4.6. On the other hand, a slab subjected to an oblique impact also shows lower maximum deformation but requires more impact energy before failure, therefore most likely not considered to be the worst case scenario compared to the central impact.

Currently, the acceptance criteria for a slab to mitigate progressive collapse under dynamic loading is based on the degree of support rotation and ductility ratio [8]. It is therefore possible to extend the support rotation criteria as a form of an acceptance criteria to the undamaged and pre-damaged UHPFRC slabs subjected to low velocity impact. This can be done by transforming the maximum deformation into support rotation angle. However, the support rotation may only be valid for the central impact due to the presence of a single support rotation value as shown in Figure 5.25 (a) by examining the profile of the permanent deformation. In the case of asymmetrical impact, angles (θ_2 and θ_3) may be developed as shown in Figure 5.25 (b). This is due to the fact that the failure mode of the asymmetrical impact cases is highly governed by punching failure. As such, more thorough investigations need to be conducted in order to use the support rotation as the acceptance criteria for asymmetrical impact cases.

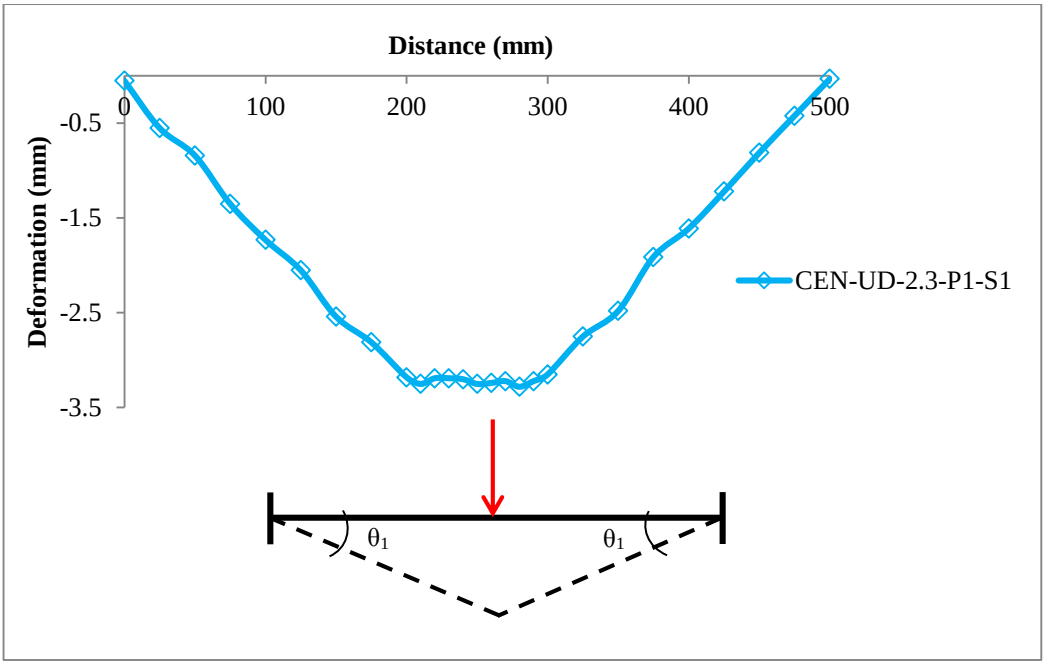

(a)

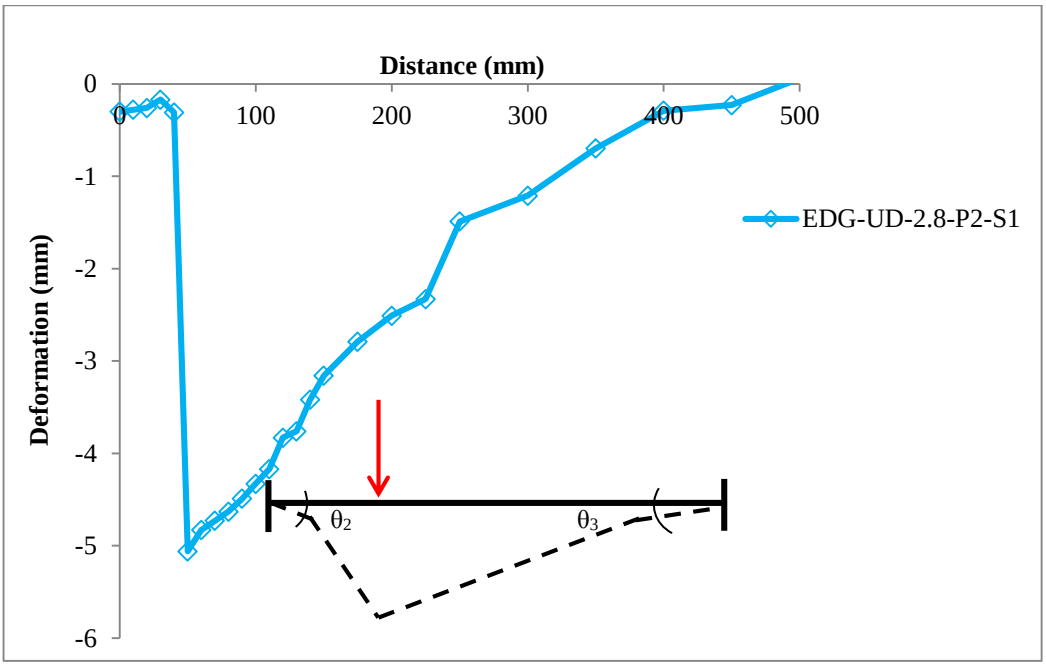

(b)

Figure 5.25: Support rotation (based on the permanent deformation profile) for (a) central impact with equal angle; (b) asymmetrical impact with variable angles.

5.4.9 Ductility Ratio

Ductility is the ability of the structural member to sustain large inelastic deformations without excessive strength deterioration [9] and as such characterised by the deformation capacity of a member after yielding. This behaviour is normally investigated in a static test [10-11] or in a dynamic test involving cyclic loading [12-13]. On the other hand, for dynamic condition, the basic ductility ratio formulation as given in equation (3.3) is used in this study to investigate the stiffness degradation of the material. A high ductility ratio indicates that the slab is approaching failure and a ratio 1.0 indicates that the behaviour is perfectly elastic with no degradation on the stiffness. A graph with a sharp slope indicates a lower phase of stiffness recovery and likewise a faster rate of stiffness degradation that reduce the elastic response of the slabs.

The relationship between the average ductility ratio and the CIE is shown in Figure 5.26 (a) to Figure 5.26 (c). It can be seen that in all cases, the ductility ratio of the slab increases with the accumulation of the impact energy and this is particularly true for all cases. Also, the ductility ratio of the pre-damaged slabs is higher than the undamaged slabs at the same CIE. At 1.5 m drop height, the graphs for the pre-damaged slabs show a relatively similar trend with the undamaged slab as shown in Figure 5.26 (a). A similar behaviour was also observed when the drop height was increased to 2.3 m especially up to the same CIE as shown in Figure 5.26 (b) and also in the case of the oblique impact as shown in Figure 5.26 (c). However, at 2.8 m drop height, the ductility ratio for the rest of the pre-damaged slabs showed relatively stronger divergence compared to the trend of the undamaged slabs.

The similarity in the trend is also reflected in the final ductility ratio between both types of slab. At 1.5 m drop height the difference is calculated to be 6.7%, 9.0% and 9.5% for the central, edge and corner impact, respectively. However, at 2.3 m drop height, the trend changes and the difference is 21.05, 23.0% and 3.7% for the central, edge and corner impact, respectively. Similarly, at 2.8 m drop height, the difference is 23.0%, 26.2% and 24.6% for the central, edge and oblique impact, respectively. No comparison can be made for the corner impact as the slabs had failed after the first strike.

The similarity shown between the pre-damaged and undamaged slabs in the development of the ductility ratio suggests that the pre-damaged slabs were still able to recover some degree of stiffness after successive impact. The residual stiffness of the pre-damaged slabs was substantially high allowing the slabs to withstand additional impact energy relatively similar to the undamaged slabs. This performance continued until a total degradation of the stiffness occurred at the localized impact location and this behaviour was obvious when the energy per strike was low. The difference in terms of the final ductility ratio between both types of slab also shows to be relatively small indicating that the pre-damaged slabs had attained a similar degree of final stiffness to the undamaged slabs before failure. The ability of the pre-damaged slabs to recover the stiffness diminished at higher drop heights.

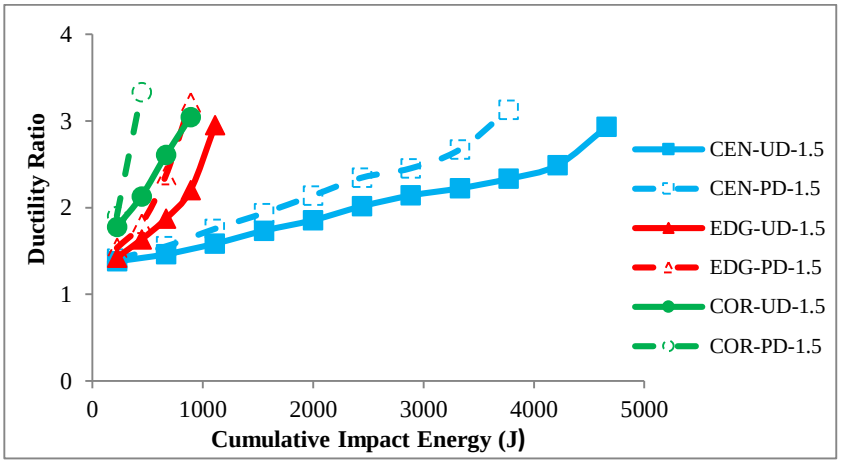

(a)

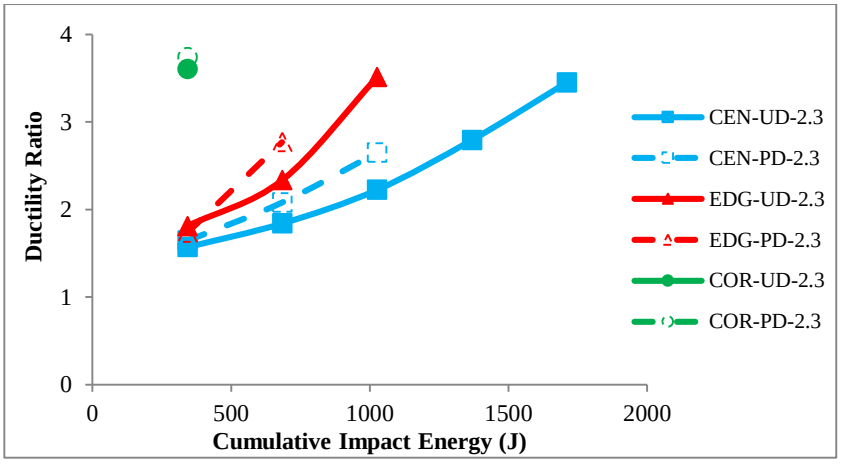

(b)

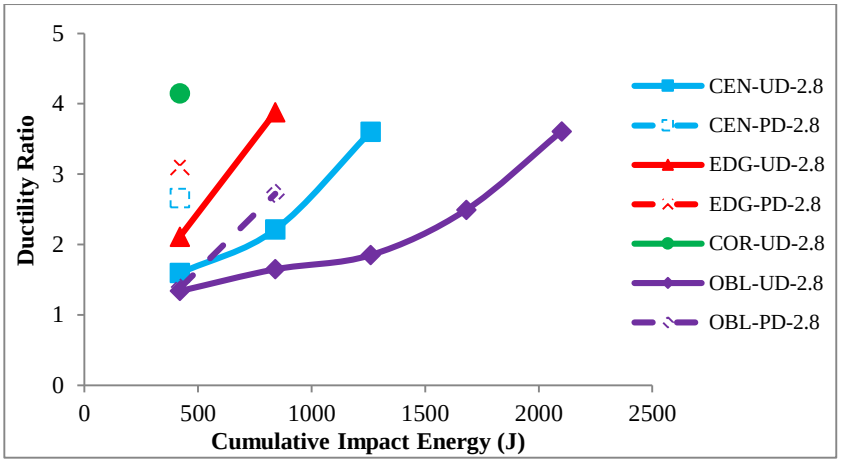

(c)

Figure 5.26: Relationship between the ductility ratio and CIE for the slabs impacted at (a) 1.5 m; (b) 2.3 m; (c) 2.8 m drop height.

On the other hand, the change in impact location shows that the ductility ratio for asymmetrical impact achieved its maximum value at significantly low CIE compared to the central impact. The results suggest a rapid degradation of the stiffness of the slabs at the impact location after successive strikes and this is particularly true for all cases. In other words, the slabs subjected to the asymmetrical impact were not able to recover substantial degree of stiffness after successive strikes compared to the central impact. The inability for these slabs to recover the stiffness is reflected in the trend of the permanent deformation. As reported by Jensen *et al.* [14], the range of the elastic limit (the denominator of equation (3.3)) is more likely to be influenced by the magnitude of the permanent deformation. As shown in Figure 5.27, the slabs subjected to the asymmetrical impact exhibit high permanent deformation values at the respective CIE compared to the central impact in all the impact cases. These graphs contradict the pattern shown in the maximum deformation (refer to Figure 5.24) where the slabs subjected to the central impact continuously show higher maximum deformation values after successive impacts.

Unlike the trend shown in the measurement of the maximum deformation, the permanent deformation shown by the asymmetrical impact was higher compared to the central impact at the same CIE. This trend reflects a situation that these slabs were physically unable to return

to their original position where the final position (permanent deformation) is relatively closer to the maximum value. Similarly, this situation also provides a strong indication that the ability of these slabs to recover the stiffness is diminishing in subsequent impact.

This trend also indicates that the response of a slab subjected to the asymmetrical impact is signified by low maximum and high permanent deformation values. This is particularly true based on the deformation trends displayed by the asymmetrical impact. Similarly, this statement can be used to represent an impact response that is more likely to be governed by shear failure mode compared to flexural governing failure.

The change in the impact angle to 10° obliquity showed a lower ductility ratio compared to the central impact and particularly true at the same CIE. Although this may indicate a response with a high stiffness recovery in successive impacts but it is unlikely to be related to the high stress concentration area generated during the oblique contact as discussed earlier. Moreover, the maximum deformation of the slabs subjected to the oblique impact showed the lowest values compared to other impact conditions. As such, the results provide strong indication that mechanics of the energy transfer during the oblique contact influence the response of the impact.

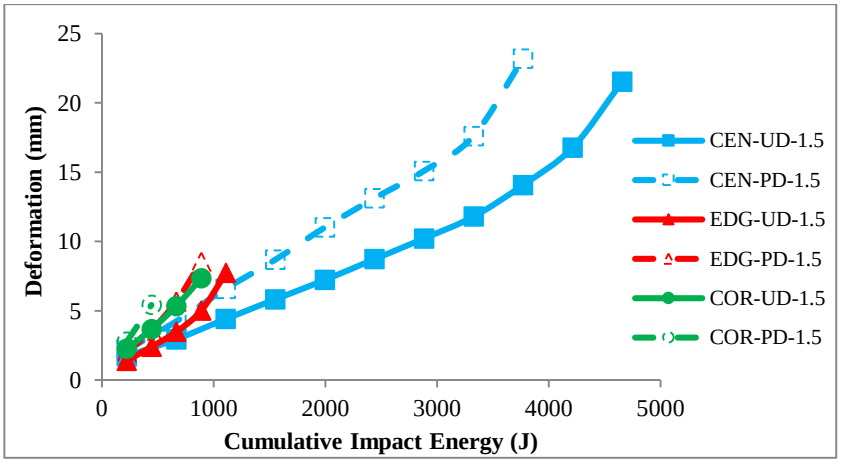

(a)

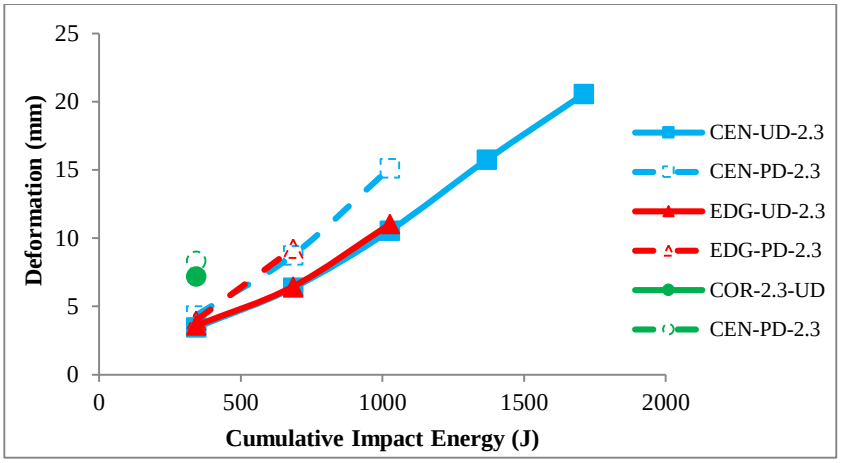

(b)

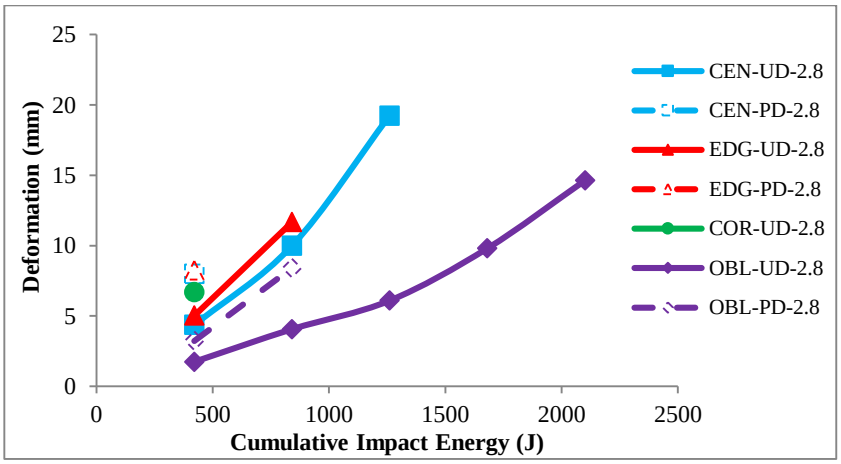

(c)

Figure 5.27: Relationship between the permanent deformation and CIE for the slabs impacted at (a) 1.5 m; (b) 2.3 m; (c) 2.8 m drop height.

It is also noted that the final ductility ratios for the asymmetrical impact are more than 1.0 when normalised with the central impact case as shown in Table 5.2. The results provide a qualitative indication that the final local stiffness of these slabs is lower than the central impact case and hence expedited the failure. The effect is obvious at higher drop heights where a stronger influence from the shear mode of failure had significantly retarded the ability of the slab to recover the stiffness.

The normalised final ductility ratio for the slabs subjected to the oblique impact shows a ratio slightly higher than 1.0. These results suggest that the final local stiffness for the slab subjected to the oblique impact is slightly lower or relatively similar with that of the central impact case. Technically, a lower stiffness could cause the slab to fail at lower CIE due to punching failure as in the case of the edge and corner impact. However, the expected punching failure for the oblique impact occurred only at significantly higher total CIE compared to the central impact reflecting a slow development of punching failure. Again, this finding shows a strong influence on the amount of energy transferred during the oblique contact. Further discussion is provided in section 5.6. It is worth mentioning that the reduction in the local stiffness can be associated with the degree of local damage which subject is investigated further in section 5.4.10.

Table 5.2: Final ductility ratio of the edge, corner and oblique impact normalised with respect to the central impact.

Drop Height (m)	Pre-damaged			Undamaged		
	EDGE/ CEN	COR/ CEN	OBL/ CEN	EDGE/ CEN	COR/ CEN	OBL/ CEN
1.5	1.03	1.06	-	1.01	1.04	-
2.3	1.05	1.41	-	1.02	1.05	-
2.8	1.17	-	1.02	1.08	1.15	1.003

In terms of design, ACI 349-1 [15] and ASCE Manual 58 [16] use ductility ratio as the acceptance criteria for a concrete member subjected to blast loading. This approach can also be extended to design a UHPFRC slab as the material possesses a relatively higher ductility compared to normal concrete. However, due to the brittleness of the matrix in UHPFRC, more investigations need to be carried out in order to establish a suitable ductility ratio that does not artificially limit the true degree of response.

5.4.10 Peak Force

The graphs from the filtered LDV data showing the relationship between the average contact force and the deformation of the selective slabs impacted at 2.8 m drop height during the first strike are shown in Figure 5.28. It can be seen that the contact forces for the central, edge and corner impact reach a maximum value in the first peak after impact. On the contrary, such pattern is not observed in the case of the oblique impact where the highest peak force is established in the second peak. The deformations increase until the maximum value and finally, the rebound takes place. The zero force shown on the x-axis indicates that there is no longer a contact interface between the impactor and the slab. In this study, the peak force is taken as the maximum force from the first peak. The same consideration was also used by Fujikake [17] and Habel and Gauvreau [18]. Beyond this point, the forces are basically descending and fluctuate by displaying multiple peaks, also known as the secondary peaks [1].

For the same impact location, the undamaged slabs show slightly stiffer response compared to the pre-damaged slabs based on the slope of the elastic force-deformation relationship. However, the difference in the slope representing the elastic behaviour is not significant suggesting that the pre-damaged slabs still possess similar elastic behaviour before reaching the peak force. On the contrary, when 10° obliquity is introduced, the pre-damaged slab showed significant reduction in the elastic stiffness. The pre-damaged slabs also produce longer contact duration, which indicates their lower stiffness [19] compared to the undamaged slabs.

The highest peak force the undamaged slabs subjected to the corner impact followed by edge, central and oblique cases. These results reflect the difference in the local stiffness at different impact locations. In this case, a higher peak force indicates a higher local stiffness at the particular impact location.

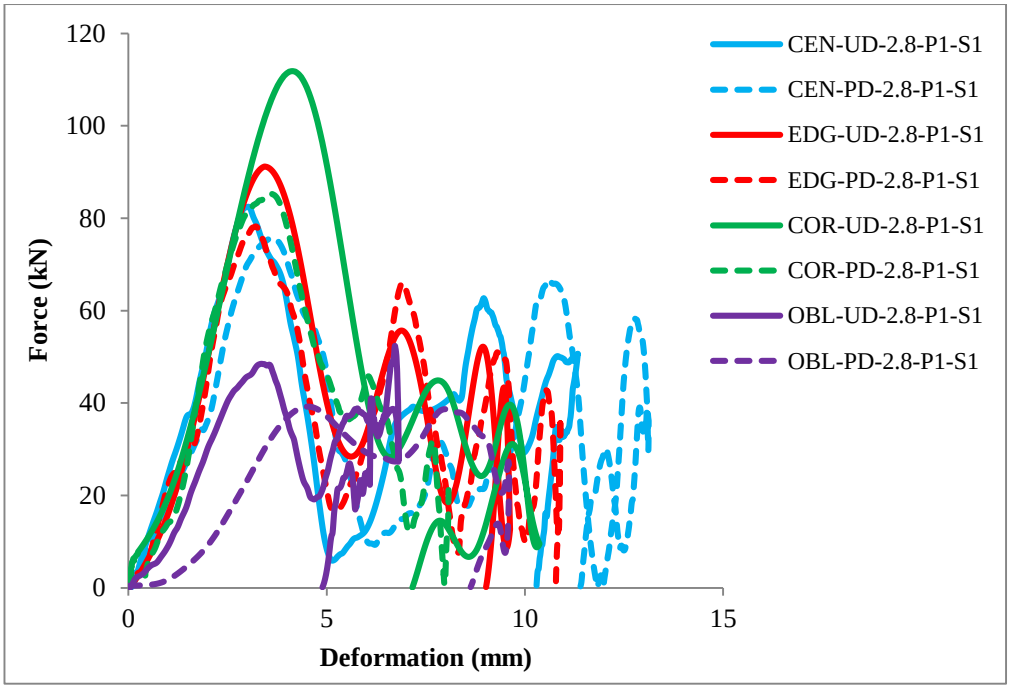

Figure 5.28: Selective results showing the relationship between the contact force and deformation for slabs impacted at 2.8 m drop height.

The graphs showing the relationship between the average peak force and cumulative impact energy are shown in Figure 5.29. At 1.5 m drop height, the reduction in the peak force for the pre-damaged slabs show similar pattern with the undamaged slabs. As the CIE increases, the graphs for the pre-damaged slabs show no significant divergence from the undamaged slabs as shown in Figure 5.29 (a). The similar trend was also observed when the slabs are impacted at 2.3 m drop height. At 2.8 m drop height the similarity also continued for the central, edge and oblique cases. However, unlike the oblique impact, the difference in the peak force at the same CIE is higher compared to the 2.3 m and 1.5 m drop height. No clear trend was observed for corner impact although the difference in the peak force is shown to be relatively high.

The effect of the material degradation was immediately shown after the first strike where all the peak forces representing the pre-damaged slabs were lower compared to the undamaged slabs. Apparently, the initial crack in the pre-damaged slab cushioned the impact hence reducing the peak force. In successive impacts, the pre-damaged slabs suffered higher

material degradation but the process was not abrupt and the graph of the declining peak force maintained a similar slope with the undamaged slabs. The similarity in the pattern of the peak force shown by both types of slab also reflect that the pre-damaged slabs are undergoing a similar material degradation process with the undamaged slabs and particularly true within the region of the impact point. These results correlate well with the photographic evidence shown in Figure 5.4 to Figure 5.17 where the crack propagation of the pre-damaged slabs shows relatively similar pattern with the undamaged slabs throughout the impact exercise.

The similarity between both types of slab also can be observed by comparing the final peak force. At 1.5 m drop height, the difference in terms of the final peak force is 7.0%, 10.0% and 8.0% for the central, edge and corner impact cases, respectively. Similarly, as the drop height is increased to 2.3 m, the difference also showed a slight difference and calculated to be 6.5%, 10.8% and 39.7% for the central, edge and corner impact cases, respectively. At 2.8 m drop height, the difference is calculated to be 10.2%, 17.0% and 29.8% for the central, edge and oblique impact cases, respectively. However, as the pre-damaged slabs for corner impact survived only one strike compared to two strikes for the undamaged slab, the ratio showed a different trend and increased to 79.1%. It is worth mentioning that the ratios cannot be used to quantify the internal damage but rather to explain and elaborate the observation qualitatively.

The relatively similar final peak force shown in most of the graphs indicates that the internal damage of the pre-damaged slabs before failure is almost at the same degree with the undamaged slabs especially when the energy per strike is relatively low. However, this similarity is affected by the increase in the drop height possibly due to a more rapid development in the internal damage of the pre-damaged slabs and stronger influence from the governing punching shear failure in successive strikes. The photographic evidences were also concurrent with the above finding where the localised failure pattern and the punching shear area between both types of slab were relatively similar.

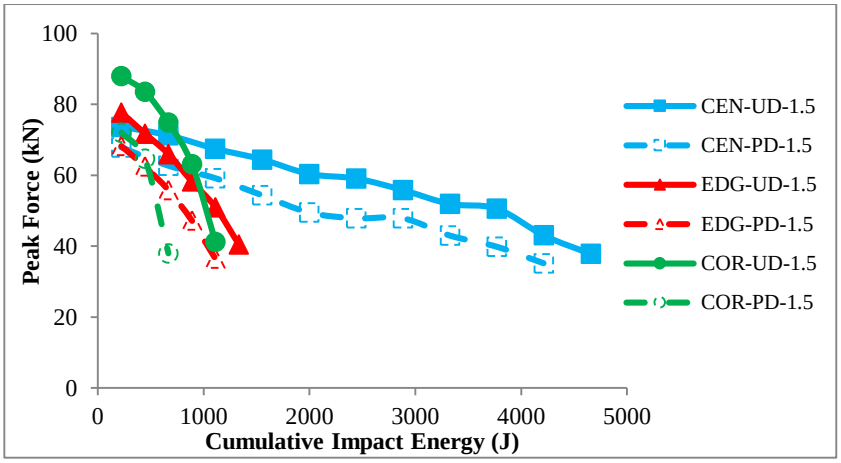

(a)

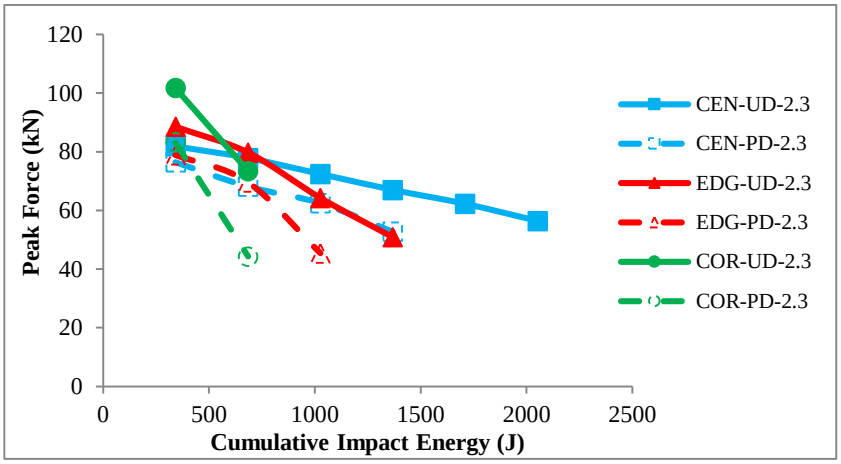

(b)

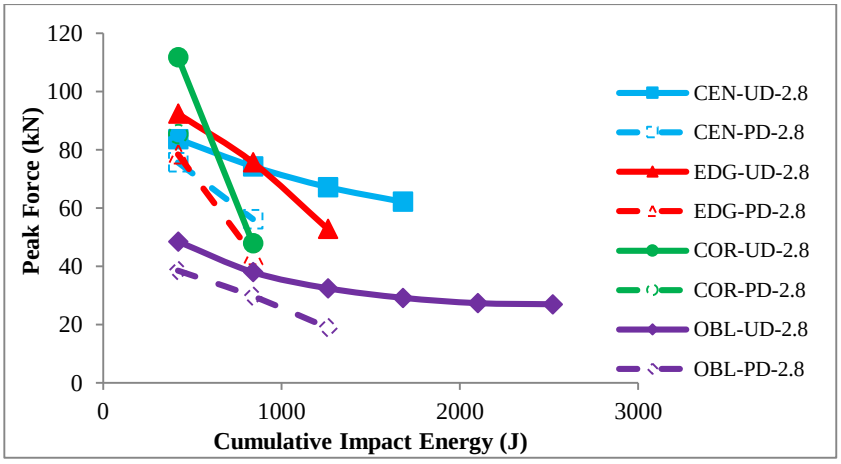

(c)

Figure 5.29: Relationship between the peak force and CIE for the slabs impacted at (a) 1.5 m; (b) 2.3 m; and (c) 2.8 m drop height.

On the contrary, with the change in the impact location, the peak force for the slabs subjected to the corner and edge impact dropped dramatically compared to central impact and particularly true at all drop heights. At 1.5 m drop height, the graph for the central impact shows a steady decline from the first until the last strike. On the other hand, the asymmetrical impact produced higher peak force at the first strike and start developing a sudden drop after successive strikes. The reduction rate in the peak force for the corner impact is higher compared to the edge impact as shown in the declining pattern of the slopes. A similar trend is also observed when the drop height is increased to 2.3 m and 2.8 m. Also noted is the slight reduction in the slope of the graphs with respect to the increase in the drop height and this is particularly true for all impact cases. The slabs subjected to the oblique impact show a relatively gentler slope than the central impact case however, the declining pattern is similar.

As mentioned earlier, the high peak force shown by the asymmetrical impact at the first strike is related to the localised stiffness and this is particularly true for the undamaged slabs. The force generated during the contact between the slab and the impactor had caused internal damage to the slab, mainly within the vicinity of the impact area. In successive strikes, the sudden reduction in the peak force and the sharp inclination of the graphs indicate a rapid development in the internal damage. As a result, the slabs subjected to the asymmetrical impact suffer a higher degree of internal damage compared to the central impact. The presence of 10° obliquity shows no immediate internal damage.

Table 5.3 shows the normalised value of final peak force for the edge and corner impact. At 1.5 m drop height, in most of the impact cases, the normalised values are slightly higher than 1.0. However, the trend changes at higher drop heights where the values decrease and shown to be lower than 1.0. These results suggest that at lower drop height, the degree of the internal damage due to the asymmetrical impact is slightly lower or almost similar compared to the undamaged slabs.

However, at higher drop heights, the values decrease and this trend indicates that these slabs are suffering from a higher degree of internal damage and possibly due to the influence from the punching shear effect. Although the oblique impact showed the lowest values, the trend does not reflect a higher degree of internal damage compared to the central impact case. This statement is also supported by the fact that the slope of the graphs representing the oblique impact exhibits a gentle drop. As such, the low values are likely to be influenced by the amount of impact energy absorbed by the slab.

Table 5.3: Final peak force of the edge, corner and oblique impact normalised with respect to the central impact.

Drop Height (m)	Pre-damaged			Undamaged		
	EDGE/ CEN	COR/ CEN	OBL/ CEN	EDGE/ CEN	COR/ CEN	OBL/ CEN
1.5	1.13	1.09	-	1.07	1.30	-
2.3	0.86	0.84	-	0.90	1.30	-
2.8	0.78	-	0.41	0.85	0.77	0.43

As discussed earlier in Section 5.4.2 to 5.4.5, the formation of shear plug started with the development of circular or half-circle shear cracks and indentation on the top face depending on the impact location and angle. In some cases (asymmetrical impact cases at higher drop heights), shear plug was formed after the first strike while others required multiple strikes. In the case of multiple strikes, the shear plug was formed by inclined cracking through the remainder of the slab. Dinic and Perry [19] reported that the formation of shear plugging is dependent on the magnitude of the peak force and the 'input kinetic energy' (kinetic energy supplied by the impactor prior to contact). In their study involving reinforced concrete slab of different thickness and various impact energy, they showed that both the peak force and input kinetic energy have to reach a certain critical value for shear plugging to occur. In other words, if a critical contact force is reached but the input kinetic energy is less than the critical value required, shear plugging will not take place. The study of critical peak force to cause shear plugging or perforation involving slab specimens with different thickness and performed under a single impact case is beyond the scope of this study.

Although the 'true' peak force may not be captured using the LDV or any other device (refer to section 3.6.2), the derived peak forces from the filtered LDV data were used to compare and relate the development of localized material degradation with respect to the CIE at various impact conditions. The use of 1000 Hz cut-off frequency throughout the whole filtering process and the fact that an ample number of data points were captured within the short duration contact event justified the value of the derived peak forces for this exercise.

5.5 Discussion on the Residual Strength of the Pre-damaged UHPFRC Slabs

The experimental work showed that the pre-damaged slabs were able to demonstrate a high residual strength and without sharp deterioration even after being exposed to 77% of the maximum static pressure capacity. The high residual strength of the pre-damaged slabs was reflected in their ability to absorb high CIE and to follow the response pattern of the undamaged slabs with a high degree of similarity. Moreover, the pre-damaged slabs were able to recover some degree of stiffness and extend the localized internal damage relatively similar to the undamaged slabs which was particularly true at lower drop heights. The inclusion of 2% fibres (by volume) in the mix effectively maintained a lower strength reduction through the fibre bridging although the matrix had cracked.

The response of UHPFRC under quasi-static uniaxial tensile testing as shown in Figure 4.16 is reproduced in Figure 5.30 to incorporate the tensile mechanical response for UHPFRC as reported by Graybeal *et al.* [20]. A similar tensile mechanical response can be expected under the dynamic loading in this test due to the fact that it produces similar fibre pull-out failure as shown in Figure 5.31. It can be seen that the mobilisation of the cracking strength ended at significantly lower strain compared to the mobilisation of the fibre bridging strength where the failure involves strain at relatively high magnitude. In this static test, the ratio of the strain at the end of the cracking strength to the strain at the end of the fibre bridging strength is about 0.1. This low ratio reflects that the strength of the UHPFRC slabs is mainly contributed by the fibre bridging strength. In the case of the pre-damaged slabs, the existing cracks that were produced by the pre-damaging exercise might only diminished the strength contributed by the matrix and the reserve strength was gained from the fibre bridging

capability in the softening branch of the response. The existing cracks were able to transfer the stress between the crack planes effectively by extending the crack propagation and producing wider crack width similar to the trend shown by the undamaged slabs.

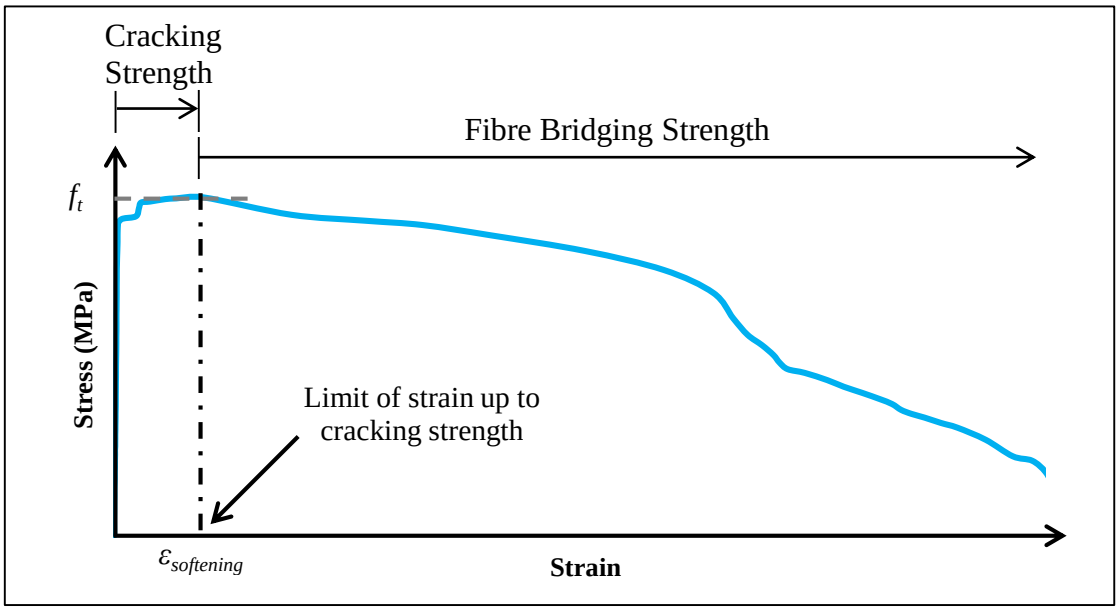

Figure 5.30: Strength contribution from the matrix and fibre bridging under tensile loading.

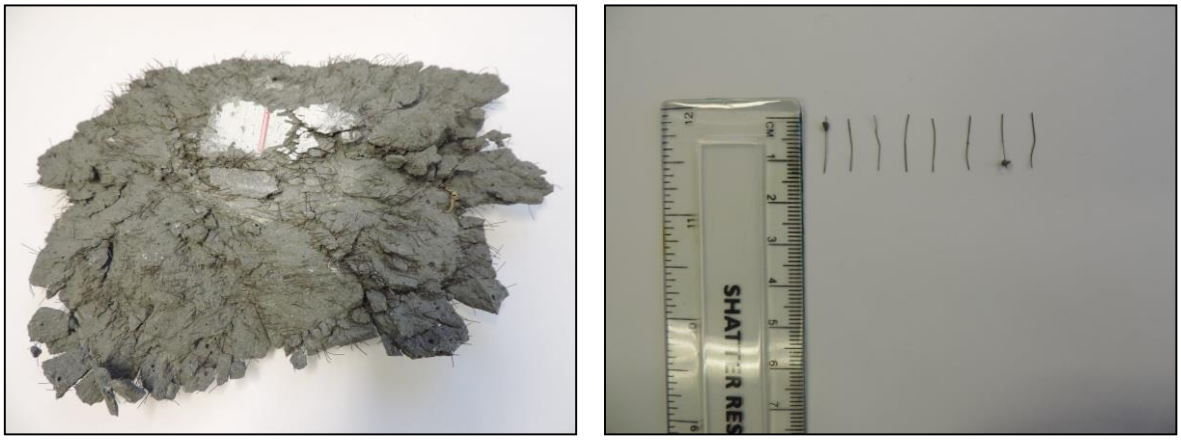

(a) (b)

Figure 5.31: Fibre pull-out failure showing (a) shear plug; (b) length of the pull-out fibres (13 mm long).

The pre-damaging exercise at this high pressure is expected not to have significantly affected the shear capacity of the slabs. This expectation is based on the study conducted by Ahmed and Ansell [21] on the residual shear capacity of pre-cracked high strength fibre concrete. In their study, a crack size of 0.25 mm was introduced (hence pre-cracked) along the shear plane of the specimens under flexural loading and later tested for the residual shear strength under push-off static test. The reduction in the shear strength was reported between 25% and 45% compared to the undamaged specimens. Although the test did not relate the crack size with flexural capacity of the specimens, the result provides an indication that the pre-damaged specimens are able to transfer shear stress across an open crack. They attributed the low reduction in the shear capacity of the pre-damaged specimens to the pull-out resistance of the fibres across the shear plane that had led to a considerable residual load-carrying capacity in the event of shear failure.

5.6 Discussion on the Sensitivity of the Impact Location

The differences in terms of the total CIE, the deformations, stiffness recovery and strength degradation shown by the asymmetrical impact case with respect to the central impact case showed that the impact location significantly influenced the response of the slabs.

The locations for the eccentric impact were located close to the clamped edges. At these locations, a higher degree of constraint against rotation was developed compared to the central impact location. As a result, the area closer to the clamped edges was not able to deform excessively upon absorbing the impact energy compared to the central location. Following that, the impact energy was largely absorbed within the vicinity of the impact location and led to a shear dominant mode of failure. This response was observed through the crack propagation as shown in Figure 5.8 to Figure 5.15 where the slabs subjected to the asymmetrical impact generated less flexural cracks. The punching shear that governed the mode of failure also expedited the local internal damage hence significantly reduced the impact resistance of the slabs. The internal damage also reduced the local stiffness and had caused the response to be less elastic where higher permanent deformations were developed compared to the central impact case as shown earlier in Figure 5.27.

The results also recorded high peak forces (or inertia forces) for the asymmetrical impact case compared to the central impact case. The presence of a high inertia force expedites the fracture process [22] of the slab. The localised inertia force also governs the dominant mode of failure where high inertia force results in a shear localized failure rather than flexural failure [23].

The difference in the response of the slabs between the asymmetrical and central impact can also be linked to the relative degree of localised strain generated at the particular impact location. Although there was no strain rate measurement conducted in this study, the concept can be extended by qualitatively relating the strain rate with the governing mode of failure and the CIE. For example, at 1.5 m drop height, the undamaged slabs subjected to the central impact required 4,768 J of CIE before failure compared to 1,400 J when impacted at 2.8 m

drop height. Obviously, the strain rate for the slab impacted at 2.8 m drop height was higher than those at 1.5 m drop height as the strain rate is affected by the impact velocity [24]. As such, the localised strain generated at the impact location for the 2.8 m drop height was significantly higher compared to the 1.5 m drop height. In the case of the asymmetrical impact, the CIE before failure was lower than 1,400 J as shown in Figure 5.18. Consequently, it can be deduced that the localised strains generated by the asymmetrical impact at any drop height in this study were relatively similar or even higher compared to the central impact at 2.8 m drop height. The high localised strain experienced by the slabs had expedited the internal damage hence reducing the impact resistance.

5.7 Discussion on the Sensitivity of the Impact Angle

The high total CIE to failure, the reduction in the deformations, the high stiffness recovery and reduced localized internal damage shown by the oblique impact case compared to the central impact case are closely related to the loss of energy during the impact event. The presence of obliquity significantly reduced the contact area between the impactor and the slab as shown in Stage I of Figure 5.32 (a). At the instant of impact, a high stress concentration area was developed at the contact interface. At the start, it was expected that the oblique impact would produce lower impact resistance due to this high stress concentration area that could expedite the punching failure. Instead, the slabs were able to withstand more strikes and withstand higher CIE than the central impact case.

In Stage II, as a result of the high stress concentration area, the impactor penetrated into the slab causing local shear indentation and global deflection. At this stage, the high stress concentration caused some degree of damage at the tip of the UHPFRC cylinder and extended upward along the line of contact on the UHPFRC cylinder as shown in Figure 5.32 (b). Such response contributed some amount of energy loss during the impact event.

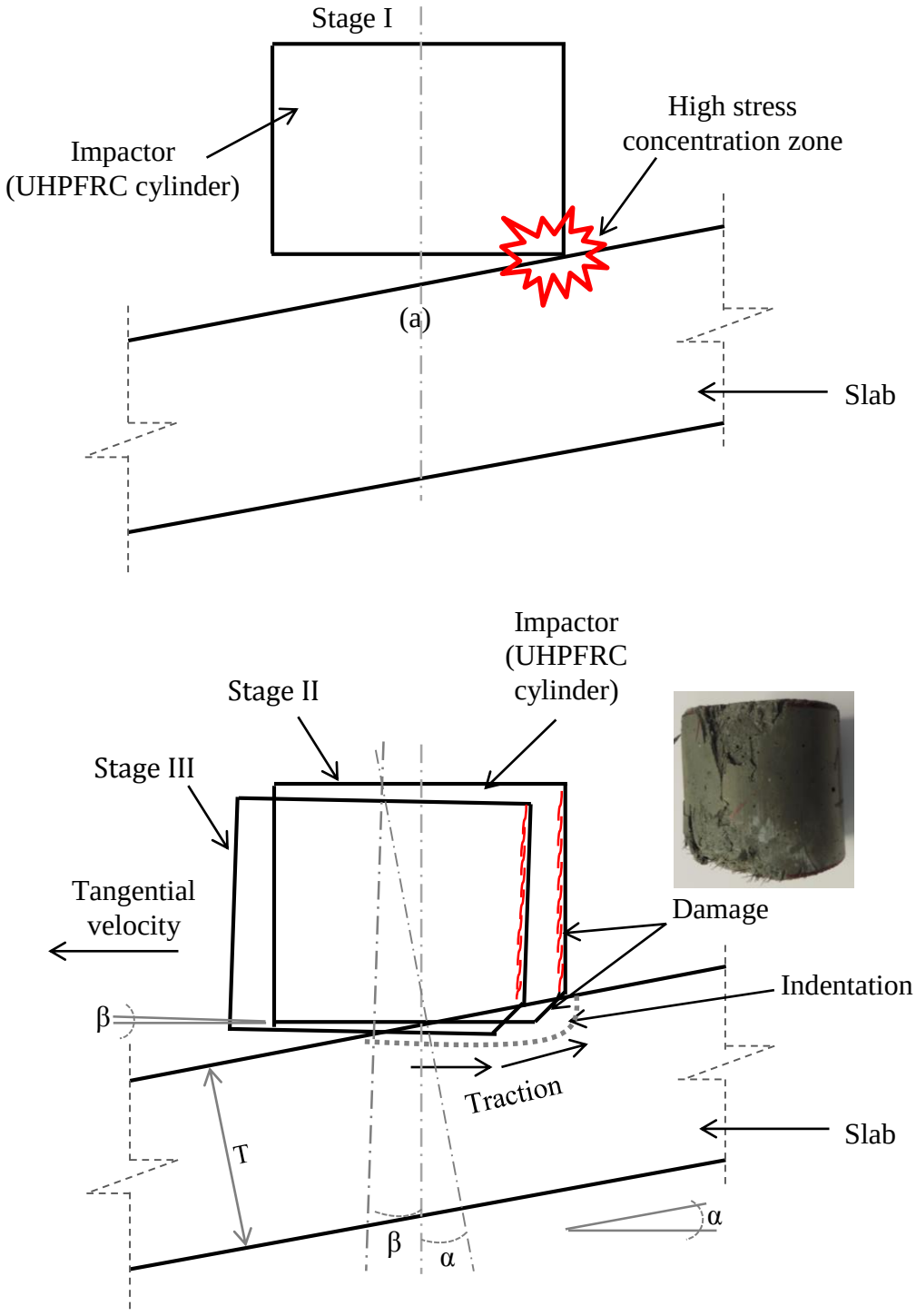

Figure 5.32: Contact stages during oblique impact showing (a) development of high stress concentration area at the contact interface; (b) traction between the impactor and the slab surface.

The traveling velocity of the impactor during the oblique impact resolves into instantaneous normal and tangential components [25-26]. The tangential velocity kept the impactor in motion while still in contact with the slab as shown in Stage III of Figure 5.32 (b). The movement of the impactor against the slab surface gave rise to a traction force which reduced the impact energy. This argument is supported by the evidence shown in Figure 5.33 (a), where a dark half-circular area was found at the contact interface after the impact event. The rough surface developed within that area suggested that traction between two surfaces had taken place. This type of marking was found to be different compared to the slabs subjected to the central impact that only showed a marking in the form of a dark circular ring as shown in Figure 5.33 (b).

(a) (b)

Figure 5.33: Different marking regime observed at the impact location for (a) oblique impact showing traces of traction after the 1st strike; (b) central impact showing circular shear crack.

The loss of energy due to traction in oblique impact depends on other factors such as the magnitude of the tangential velocity, the coefficient of restitution between the contacting bodies and the degree of obliquity [27] and is beyond the scope of this work.

The reduction in the CIE can also be associated with the effective thickness of the slab. In the oblique impact, the thickness was increased to $T/\cos(\alpha)$ compared to T in the central impact as shown in Figure 5.31 (b). Furthermore, there is a possibility that an angular directional change was made to the impactor as a result of the asymmetric resistance that caused the impactor to tilt by $\beta°$. This angular directional change took place at the angle developed between the submerged face and the impactor during the localised indentation of the specimen. The tilting of the impactor by $\beta°$ increased the effective thickness from $T/\cos(\alpha)$ to $T/\cos(\alpha + \beta)$. In any case, these effective depths are always higher than T which is the original thickness normal to the impact surface. The assumption of the angular directional change can be seen in the work published by Ipson and Recht [28] and Chen *et al.* [29].

The findings show that, unlike the central impact, the energy supplied by the impactor in the oblique impact was not fully transferred to the slab. Instead, part of the energy was lost due to the damage induced to the UHPFRC impactor and the traction at the impact interface. The damage exhibited on the UHPFRC cylinder was due to the presence of high stress concentration at the tip of the cylinder and the fact that the cylinder is also deformable. A different set of results can be expected if the impactor is non-deformable hence more energy will be transferred to the slab although this may not be the realistic case for an actual structure.

The reduction in the impact energy transferred to the slab and the increase in the effective thickness resulted in more strikes to failure compared to the central impact condition. Therefore, at the same CIE, the slabs subjected to the oblique impact produced lower maximum and permanent deformation as well as lower rate of the stiffness degradation. At the same time, the lower impact energy dissipated in the slab under oblique impact caused the response to be more elastic compared to the central impact condition.

5.8 Summary of Chapter 5

The experimental results from the series of impact tests on undamaged and pre-damaged UHPFRC slabs were presented in Chapter 5. The new arrangement made to the experimental set-up after initial testing had improved the preparation of the pre-damaged slabs. A similar degree of initial damage was produced and the cracks along the edges were now developed along the boundary line. In the impact tests, the resistance and response of the pre-damaged slabs show relatively similar trend with the undamaged slabs especially at low impact energy per strike, indicating that the pre-damaged slabs possess a substantial amount of reserve strength. These findings agreed with the photographic evidence that showed that the presence of the initial damage only expedited the failure but was unlikely to change the crack pattern and final failure mode. The high reserve strength shown by the pre-damaged slabs were discussed and showed to contribute by to remarkable fibre bridging action of UHPFRC materials.

The sensitivity of the impact location and the change in the contact condition were investigated. The results had raised a concern on the need to consider the sensitivity of the impact location due to the fact that the slabs subjected to asymmetrical impact exhibited significantly low impact resistance compared to the central impact. This finding is reflected in the results showing that the total CIE at failure was not considerably affected by the increase in the drop height. Moreover, the general failure pattern of these slabs indicated a potential risk to trigger progressive collapse especially when an actual slab detaches from the support and impacts the floor below. The rapid degradation of the strength was associated with the higher degree of constraint developed along the clamped edges that had led to a high inertia force and localised strain.

The change in the contact condition had influenced the impact resistance and response of the slabs. With an introduction of 10° obliquity upon contact, these slabs exhibited higher resistance compared to the central impact case. Although the general failure pattern included a potential loss of edge support, the failure would require high CIE and hence may not be the worst case scenario in the impact study. Further investigation revealed that the high resistance exhibited by these slabs may be related to the loss of impact energy due to the traction and

fracturing process of the impactor (UHPFRC cylinder). The increase in the effective thickness of the slab also had improved the impact resistance and response.

In order to avoid perforation due to a single concentric impact, equation (2.1) showed the potential to be used for predicting the minimum thickness of a undamaged UHPFRC However, the validity of equation (2.1) require more refine study. This can be achieved by conducting low velocity impact test on various UHPFRC slab thickness. By incorporating a reduction factor into equation (2.1) based on the normalised CIE of the pre-damaged slab, a conservative value on the minimum thickness to avoid perforation was obtained. Equation (2.1) and equation (5.1) however, cannot be used directly for the asymmetrical impact case.

Currently, there are no guidelines to design a slab subjected to a combined blast loading and low velocity impact loading. Generally, the acceptance criteria for a slab subjected to a blast load is based on the limit of the support rotation and ductility ratio. In this study, these two values can be obtained experimentally for UHPFRC slab subjected to a combination of static pressure and low velocity impact loading. As such, it is possible to develop a suitable acceptance criteria for a slab subjected to blast and impact loading condition. However, more investigations are required in order to have a broad range of data especially in order to determine the damage level that can be associated with the magnitude of the support rotation or ductility ratio.

Similarly, there is no reference for the design of a slab subjected to asymmetrical impact loading. As shown in the experimental work, to some degree, the response from an asymmetrical impact on a slab may trigger a progressive collapse event. As such, an acceptance criteria for a slab subjected to this type of impact loading condition should also be taken into consideration. This study only considers two asymmetrical impact locations and might not represent the worst case scenario.

5.9 References

[1] K. C. G. Ong, M. Basheerkhan and P. Paramasivam, "Resistance of fibre concrete slabs to low velocity projectile impact," *Cement and Concrete Composites*, vol.21, no. 5, pp. 391-401, 1999.

[2] J. Zhang, M. Maalej, M and S. T. Quek, "Performance of hybrid-fiber ECC blast/shelter panels subjected to drop weight impact," *Journal of Materials in Civil Engineering*, vol. 19, no. 10, pp. 855-863, 2007.

[3] K. Micallef, J, Sagaseta, M. F. Ruiz and K. Muttonni, "Assessing punching shear failure in reinforced concrete flat slabs subjected to localised impact loading," *International Journal of Impact Engineering*, vol. 71, pp. 17-33, 2014.

[4] H. Masuya, M. Yamamoto, M. Toyama and Y. Kajikawa, "Experimental study on the perforation of steel fiber reinforced concrete slab by impact," *Structures and Materials*, vol. 8, pp. 205-214, 2000.

[5] K. Marar, O. Eren and T. Celik, "Relationship between impact energy and compression toughness energy of high-strength-fiber-reinforced concrete," *Materials Letters*, vol. *47, no. 4-5*, pp. 297-304, 2001.

[6] H. S. Rao, V. G. Ghorpade, N. V. Ramana and K. Gnaneswar, "Response of SIFCON two- way slabs under impact loading," *International Journal of Impact Engineering*, vol. 37, no. 4, pp. 452-458, 2010.

[7] Y. Deng, C. Y. Tuan, Y, Xiao, "Flexural behavior of concrete-filled circular steel tubes under high strain-rate impact loading," *Journal of Structural Engineering*, vol. 138, no. 3, pp.449-456, 2012.

[8] D. M. McCann and S. J. Smith, Resistant Design of Reinforced Concrete Structures, *STRUCTURE Magazine*, pp. 22-26, 2007.

[9] M, Said and T. M. Elrakib, "Enhancement of shear strength and ductility for reinforced concrete wide beams due to web reinforcement," *HBRC Journal*, vol. 9, no. 3, pp. 235-242, 2013.

[10] P. Richard and M. H. Cheyrezy, "Reactive powder concretes with high ductility and 200-800 MPa compressive strength," *ACI Special Publication,* vol. 144, pp. 507-518, 1994.

[11] P. Rossi, A. Arca, E. Parant, and P. Fakhri, "Bending and compressive behaviours of a new cement composite," *Cement and Concrete Research,* vol. *35, no.* 1, pp. 27-33, 2005.

[12] R. Park and R. A. Sampson, "Ductility of reinforced concrete column sections in seismic design," *Journal of American Concrete Institute,* vol. 69, no. 9, pp. 543-551, 1972.

[13] P. Zohrevand and A. Mirmiran, "Cyclic behavior of hybrid columns made of ultra high performance concrete and fiber reinforced polymers," *Journal of Composites for Construction,* vol. 16, no. 1, pp. 91-99, 2012.

[14] J. Jensen, A. Tomaszewicz and G. Markeset, G. (1998, June). "Impact Resistance of Fibre Reinforced High Strength Concrete Slabs," presented at the *Second International Conference on Concrete Under Severe Conditions,* Tromsø, Norway, June 21-24, 1998.

[15] American Concrete Institute, *Code requirements for nuclear safety related concrete structures*, ACI 349-01, 2001.

[16] American Society of Civil Engineers, *Structural analysis and design of nuclear plant facilities*, Manual No. 58, 1980.

[17] K. Fujikake, "Impact performance of ultra-high performance fiber reinforced concrete beam and its analytical evaluation," *International Journal of Protective Structures,* vol.5, no. 2, pp. 167-186, 2014.

[18] K. Habel and P. Gauvreau, "Response of ultra-high performance fiber reinforced concrete (UHPFRC) to impact and static loading," *Cement and Concrete Composites,* vol. 30, pp. 938-946, 2008.

[19] G. Dinic and S. H. Perry, "Shear plug formation in concrete slabs subjected to hard impact," *Engineering Fracture Mechanics*, vol. 35, no. (1), pp. 343-350, 1990.

[20] B. A. Graybeal, F. Baby, P. Marchand and F. Toutlemonde, "Direct and flexural tension test methods for determination of the tensile stress–strain response of UHPFRC," in *International Symposium on UHPC and Nanotechnology for High Performance Construction Materials: Proceedings of 3rd Hipermat ,* Kassel, Germany, M. Schmidt, E. Fehling, C. Clotzbach, S, Frohlich and S. Piotrowski, Eds. Kassel University Press, 2012, pp. 395-418.

[21] L. Ahmed and A. Ansell, "Direct shear strength of high-strength fibre concrete," *Magazine of Concrete Research*, vol. 62, no. 5, pp. 379-390, 2010.

[22] Y. Liu and H. Zhou, "High velocity impact test of a C-Mn steel and inertia effect," *Engineering Fracture Mechanics*, vol. 48, no. 2, pp. 299-304, 1994.

[23] S. G. Millard, T. C. K. Molyneaux, S. J. Barnet and X. Gao, "Dynamic enhancement of blast-resistant ultra high performance fibre-reinforced concrete under flexural and shear loading," *International Journal of Impact Engineering*, vol. 37, no. 4, pp. 405-413, 2010.

[24] K. T. Ramesh, "High rates and impact experiments," in *Springer Handbook of Experimental Solid Mechanics*, W. N. Sharpe, Jr., Springer, 2008, pp. 929-960.

[25] E. E. Osuke and R. J. Rogers, "An experimental study of friction during planar elastic impact," *Journal of Pressure Vessel Technology*, vol. 123, pp. 493-500, 2001.

[26] W. J. Stronge, R. James and B. Ravani, "Oblique impact with friction and tangential compliance," *Philosophical Transactions of the Royal Society of London Series A: Mathematical, Physical and Engineering Sciences*, vol. 359, pp. 2447-2465, 2001.

[27] R. M. Brach, "Classical planar impact theory and the tip impact of a slender rod," *International Journal of Impact Engineering*, vol. 13, no. 1, pp. 21-33, 1993.

[28] T. W. Ipson and R. F. Recht, "Ballistic penetration resistance and its measurement," *Experimental Mechanics*, vol. 15, no. 7, pp. 249-257, 1975.

[29] X. W. Chen, S. C. Fan and Q. M. Li, "Oblique and normal perforation of concrete targets by a rigid projectile," *International Journal of Impact Engineering*, vol. 30, no. 6, pp. 617-637, 2004.

CHAPTER 6

NUMERICAL RESULTS AND DISCUSSIONS

6.1 Introduction

This chapter presents and discusses the results from the numerical simulations. The finite element package ANSYS Explicit Dynamics R13 and a SDOF model were used to predict the response of the UHPFRC slabs subjected to the first strike. The response from the numerical analysis was compared and validated with the experimental work reported in Chapter 5. As for the SDOF model, the work was expanded into deriving the input parameters using a theoretical approach.

6.2 Sensitivity Analysis

Prior to the actual FE simulation work, a sensitivity analysis was carried out on the mesh, loading arrangement and the RHT input parameter *B* as a pre-requisite for the evaluation of confidence in the FE results.

6.2.1 Mesh Sensitivity Analysis

Figure 6.1 shows the influence of varying the mesh size on the maximum deformation and computational time. It can be seen that maximum deformations were slightly influenced by the size of the mesh compared to the computational time. The reduction from 20 mm to 2.5 mm mesh size gave a difference of 10%. On the other hand, a mesh smaller than 5.0 mm exhibited insignificant change in the magnitude of the maximum deformation but increased the computational time enormously. As such, the 5.0 mm mesh size was used for all FE models.

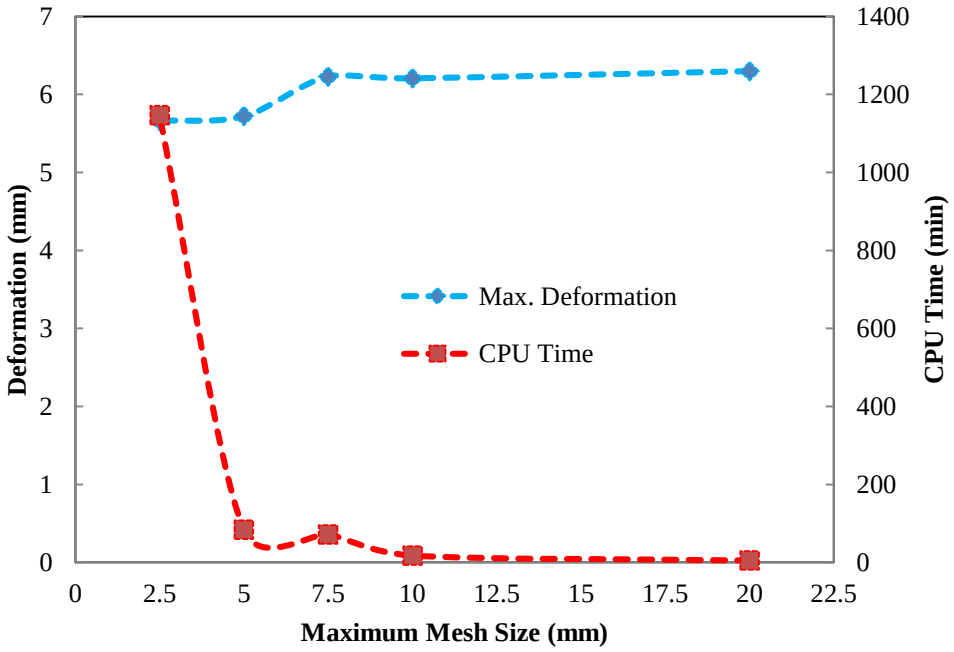

Figure 6.1: Mesh sensitivity analysis showing the variation in the maximum deformation and computational time versus maximum element size.

6.2.2 Loading Arrangement Sensitivity Analysis

The analysis on sensitivity of the loading condition was conducted by varying the magnitude of the peak pressure and rise time as well as monitoring the deformation of the slab model. Figure 6.2 shows the variation of the maximum and average permanent deformation response with the loading condition. In the first trial, the pressure load and rise time was set at 0.345 MPa (similar to the static loading) and 0.04 s, respectively. As expected, the maximum and average permanent deformation was lower than the values obtained from the pre-damaging exercise and only reached 1.76 mm and 0.51 mm, respectively. The slab model also showed no significant vibration after the peak deformation.

The pressure loading was then doubled to 0.69 MPa but with a reduced rise time of 0.02 s. This loading arrangement increased the maximum deformation excessively to 6.42 mm but reasonably managed to capture the permanent deformation at 1.95 mm. The slab also vibrated after reaching the peak deformation. The deformation of the slab model stabilised as the vibration decayed until the end of the simulation time. Although this load arrangement was able to provide a reasonable permanent deformation value, but the excessive maximum deformation showed in the result could cause higher internal damage to the slab model and as such, considered to be not suitable in the analysis. As these exercises were performed on a trial and error basis, many possibilities can be encountered by adjusting the peak pressure and rise time.

After experimenting with a range of different loading conditions, the closest results that matched the experimental data were obtained at a peak pressure and rise time of 0.495 MPa and 0.04 s, respectively. The maximum and average permanent deformation was 4.23 mm and 1.98 mm, respectively. The slab model showed low amplitude vibration after the descending branch and stabilized after about 0.10 s.

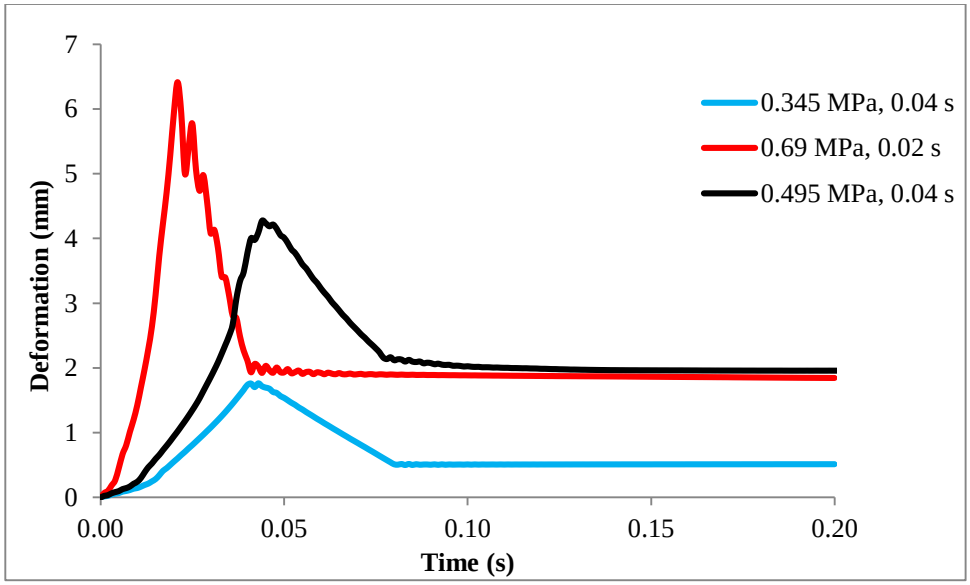

Figure 6.2: Response of the FE slab models in various loading arrangements.

Figure 6.3 shows the permanent deformation profile of the slab in the Y-Y and X-Y directions after applying the high pressure load. These profiles were plotted due to the fact that the FE simulation only recorded the real time maximum deformation value regardless of the location. In this case, the deformation at the end of the first 0.2 s (applicable to the pre-damaged edge and corner impact cases) was adjusted accordingly, in order to represent the final permanent deformation at the point of interest.

In Figure 6.3 (a), the location of the edge impact was identified and the maximum deformation at that particular point was recorded to be 0.9 mm. Similarly, the location for the corner impact was identified and recorded to be 0.58 mm as shown in Figure 6.3 (b). These values were used as a datum to measure the true maximum and permanent deformation of the pre-damaged slab models after impact loading in the FE analyses. In the case of central impact condition, the permanent deformation value of 1.96 mm was used (refer to Figure 6.2).

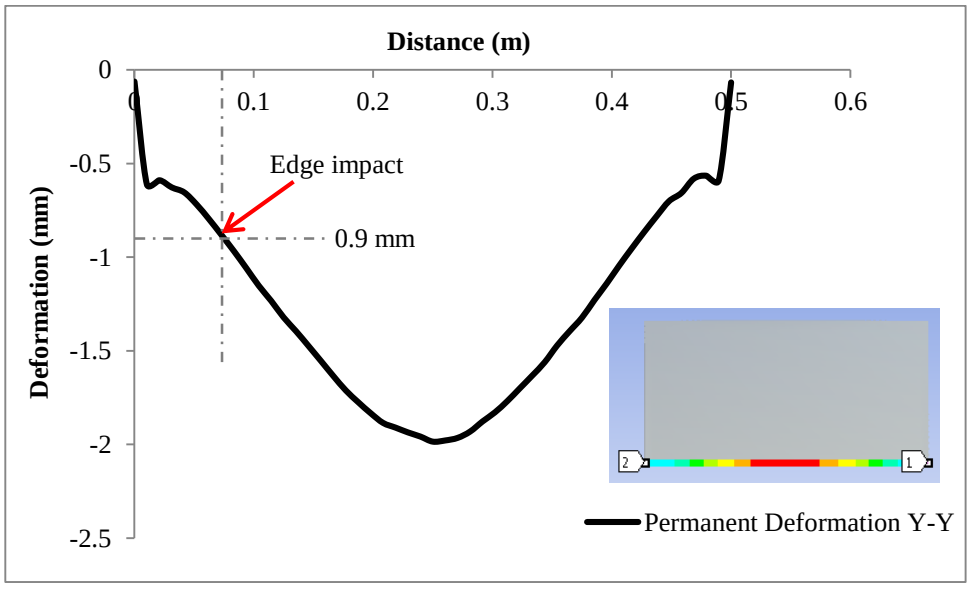

(a)

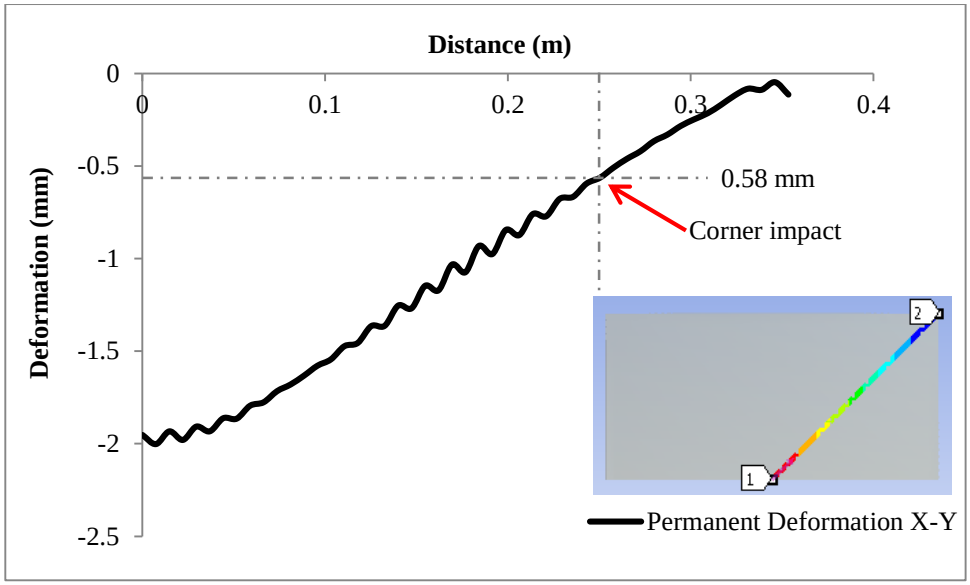

(b)

Figure 6.3: FE surface profile (permanent deformation) in (a) Y-Y axis; (b) X-Y axis.

6.2.3 Parameter B Sensitivity Analysis

In order to investigate the sensitivity of the parameter *B*, the resistance of the slabs against perforation at the first drop weight strike in the FE simulations was validated with the experimental data as shown in Table 6.1. It can be seen that the overall results for using *B* = 1.1 exhibits five failures in the form of perforation to the slab model. Three of these failures match the results from the experimental data. On the other hand, using *B* = 1.0 produces nine failures and only four match the experimental data.

In the sensitivity analysis, the FE models were not able to simulate the impact resistance of the slab subjected to the oblique impact, both for the undamaged and pre-damaged slabs. This result can be improved by increasing the value of parameter *B*. However, as shown earlier in Figure 4.12, increasing *B* higher than 1.1 will only move the residual strength surface closer to the elastic surface hence affecting the appropriate failure path. On the contrary, reducing parameter *B* will increase the number of failures to other slab models. As such, the parameter *B* was taken as 1.1 for the FE simulation. Further discussion on the failure of oblique simulation is provided in the following section.

Table 6.1: Overall impact resistance of the slab models using B = 1.1 and B = 1.0.

Impact Type	Slab Type	Drop Height (m)	Response after the 1st strike					
			EXP		FE (B =1.1)		FE (B = 1.0)	
			DEF	PEF	DEF	PEF	DF	PF
CEN	UD	1.5	✓		✓		✓	
		2.3	✓		✓		✓	
		2.8	✓		✓		✓	
CEN	PD	1.5	✓		✓		✓	
		2.3	✓		✓		✓	
		2.8	✓		✓			✓
EDG	UD	1.5	✓		✓		✓	
		2.3	✓		✓		✓	
		2.8	✓		✓			✓
EDG	PD	1.5	✓		✓		✓	
		2.3	✓		✓		✓	
		2.8	✓	✓		✓		✓
COR	UD	1.5	✓		✓		✓	
		2.3	✓		✓			✓
		2.8	✓	✓		✓		✓
COR	PD	1.5	✓		✓		✓	
		2.3	✓	✓	✓			✓
		2.8		✓		✓		✓
OBL	UD	2.8	✓			✓		✓
OBL	PD	2.8	✓			✓		✓

DEF = Deflected, PEF = Perforated

6.2.4 Support Condition Sensitivity Analysis

Table 6.2 shows the results of the overall impact resistance for the FE models using partially and fully fixed edges. It can be seen that the FE models constructed with fully fixed edges showed four additional failures compared to the partially fixed slab models. Generally, the fully fixed edges were not able to simulate the impact resistance at higher drop heights especially when the impact location is closer to the edge and corner of the slab where a higher degree of restraint was developed compared to the experimental condition.

It is worth mentioning that the partially fixed edges that were used in this study may not perfectly represent the actual boundary condition however, it was able to reduce the degree of fixity along the edges. A more detailed study using frequency measurement of the slab during impact and calibration of the stiffness of the clamped edges may be required as suggested by Agardh [1]. However, this approach requires the fixing of accelerometers on the bottom face of the slab and was not possible with the current experimental set-up.

Table 6.2: Overall impact resistance of the slab models with partially and fully fixed edges.

Impact Type	Slab Type	Drop Height (m)	Response after the 1st strike			
			Partially Fixed		Fully Fixed	
			DEF	PEF	DEF	PEF
CEN	UD	1.5	✓		✓	
		2.3	✓		✓	
		2.8	✓		✓	
CEN	PD	1.5	✓		✓	
		2.3	✓		✓	
		2.8	✓		✓	
EDG	UD	1.5	✓		✓	
		2.3	✓		✓	
		2.8	✓			✓
EDG	PD	1.5	✓		✓	
		2.3	✓		✓	
		2.8		✓		✓
COR	UD	1.5	✓		✓	
		2.3	✓			✓
		2.8		✓		✓
COR	PD	1.5	✓		✓	
		2.3	✓			✓
		2.8		✓		✓
OBL	UD	2.8		✓		✓
OBL	PD	2.8		✓		✓

DEF = Deflected, PEF = Perforated

6.3 Results from the FE Analysis

The FE simulations were performed on a single computer with an Intel Core Xeon 5450 processor running at 3.0 GHz. The maximum computational time for the simulation involving the undamaged and pre-damaged FE model was around 14 and 62 hours, respectively.

The impact resistance of the FE models against perforation was formerly validated with the experimental work as shown in Table 6.1. All FE models, with the exception of the corner and oblique impact, were not perforated at the first strike similar to at least one of the actual test results. The failure of the undamaged slab due to corner impact at 2.8 m drop height can be justified due to the fact that one of the actual slab specimens had failed at the first strike. However, the FE model was not able to simulate the impact resistance under oblique condition. In the experimental work, the undamaged slab subjected to the oblique impact condition failed after five to six strikes compared to only one strike in the FE model.

The inability to simulate the oblique impact case is examined through the impact sequence (graphical output) as shown in Figure 6.4. It can be seen that the damage at the tip of the impactor and the top face of the slab started immediately upon contact as shown in Figure 6.4 (b). The damage extended to the bottom face of the slab and at this time almost half of the lower part of the impactor was affected as shown in Figure 6.4 (c). Instead of re-bound (as in the experimental work), the impactor progressed further into the slab extending a larger damaged area to the bottom of the slab as shown in Figure 6.4 (d). Finally, the impactor progressed further and perforated the slab model as shown in Figure 6.4 (e). The red marking indicates the completely damaged elements that are no longer intact within the model. The severe damage to the UHPFRC cylinder in the FE simulation is also not in accordance with the actual damage condition of the impactor as shown earlier in Figure 5.31. Majidi *et al.* [2] compared the gross damage area of Chopped Strand Mat (CSM) laminate subjected to normal and oblique impact tests and concluded that the impact of inclined plates is less damaging owing to the reduction in the normal force. Similar comments were also given by Hampson and Moatamedi [3]. Although using a different material and test set-up compared to this study, the findings by these researchers indirectly support the experimental results from this study.

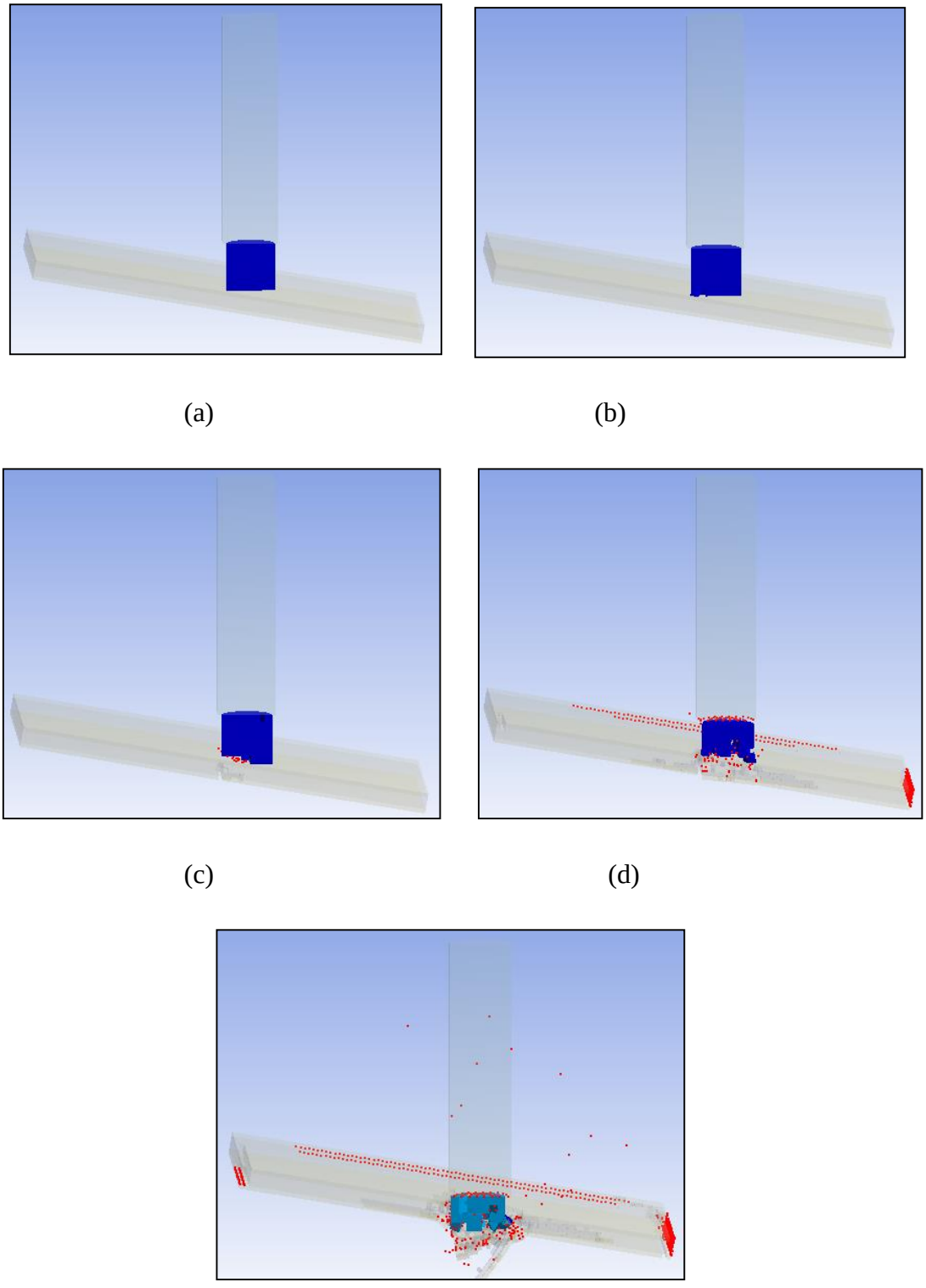

(a) (b)

(c) (d)

(e)

Figure 6.4: Impact sequence for the oblique simulation showing (a) impactor and slab before contact; (b) contact; (c) development of damage to the tip of the UHPFRC cylinder and bottom of the slab; (d) severe damage to the UHPFRC cylinder and bottom of the slab (e) perforation of the slab model and crack along the edges.

The premature damage due to this type of contact condition has also been investigated through numerical simulation studies reported by other researchers. Borvik *et al.* [4] performed numerical simulations involving high velocity projectiles with conical, hemispherical and blunt nose penetrating 12 mm thick steel plates. In the early stage of the finite element simulation work using a uniform mesh 0.25 mm × 0.25 mm, they were unable to simulate the response of the conical projectile. In their investigation, they reported that the FE meshes were highly distorted due to the high hydrostatic compression of the elements in front of the conical tip and created negative mesh volume. This phenomenon was not observed for the simulation involving blunt and hemispherical projectiles.

They also reported that, depending on the specific impact conditions, there may be various modes of failure and energy absorbing mechanisms. As such, it is vital that the numerical models are able to take these effects into account in order to produce reliable results. The problem was rectified by introducing adaptive meshing coupled with sub-routine programming in which the mesh was refined upon error condition or other information output by the solver.

In the present FE simulation, uniform meshes were used for all models. Although it has been reported that the use of a uniform mesh is known to be accurate and robust for problems involving small to moderate deformation [5], the technique may not be suitable to simulate normal and oblique impact under the same procedure as shown in this study. The presence of eccentricity between the centroid of the impactor and the slab at contact and the contact between the same materials as shown in Figure 6.5 may have developed a highly complex response that requires modification to the algorithm in ANSYS Explicit Dynamics. This phenomenon requires further investigation.

The sudden failure showed by the oblique impact simulation is not fully understood. Currently, there is very limited information on FE simulation work especially involving low velocity oblique impact on concrete or UHPFRC material. Almost all oblique impact simulations are involved with high velocity projectile [6-8] and as such limited further investigation into this issue.

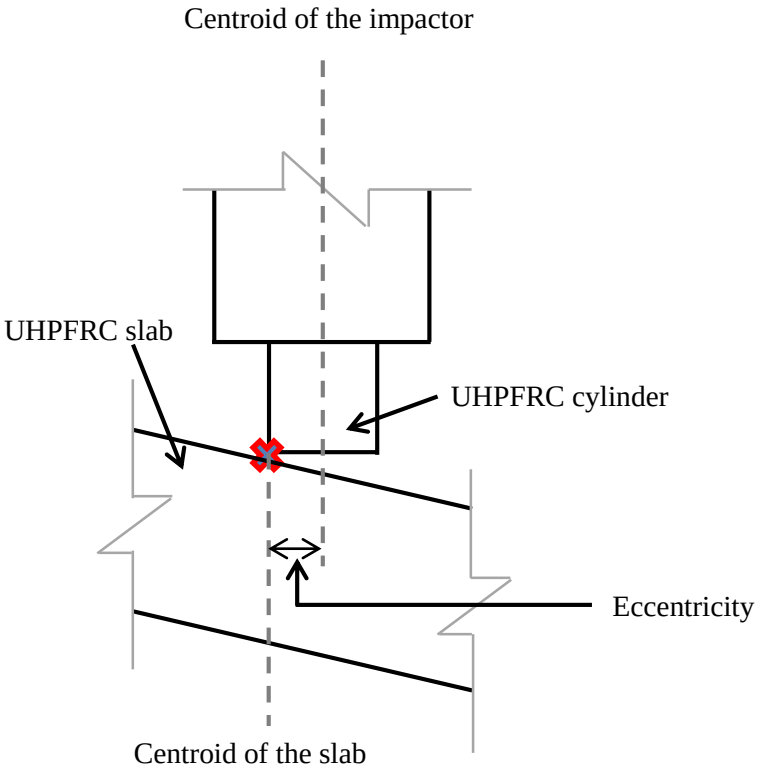

Figure 6.5: Eccentricity between the contact point and the centroid of the impactor.

6.3.1 Timescale of the impact event

This section investigates the timescale of the impact event for undamaged (rebound) and pre-damaged slab (punching shear failure). In this case, the results from the edge impact were used for comparison. Figure 6.6 shows the impact sequence for the undamaged slab model subjected to edge impact case at 2.8 m drop height. At t = 0 ms, the contact between the UHPFRC cylinder occurred as shown in Figure 6.6 (a). Following that, at t = 1.1 ms, the impactor moved downward and started deforming the slab model. The deformation arrived to the maximum value at t = 3.0 ms as shown in Figure 6.6 (c). Upon reaching the maximum deformation, the impactor moved upward (rebound process) and at the same time reducing the maximum deformation as shown in Figure 6.6 (d). The complete detachment of the impactor from the slab occurred at t = 7.5 ms as shown in Figure 6.6 (e).

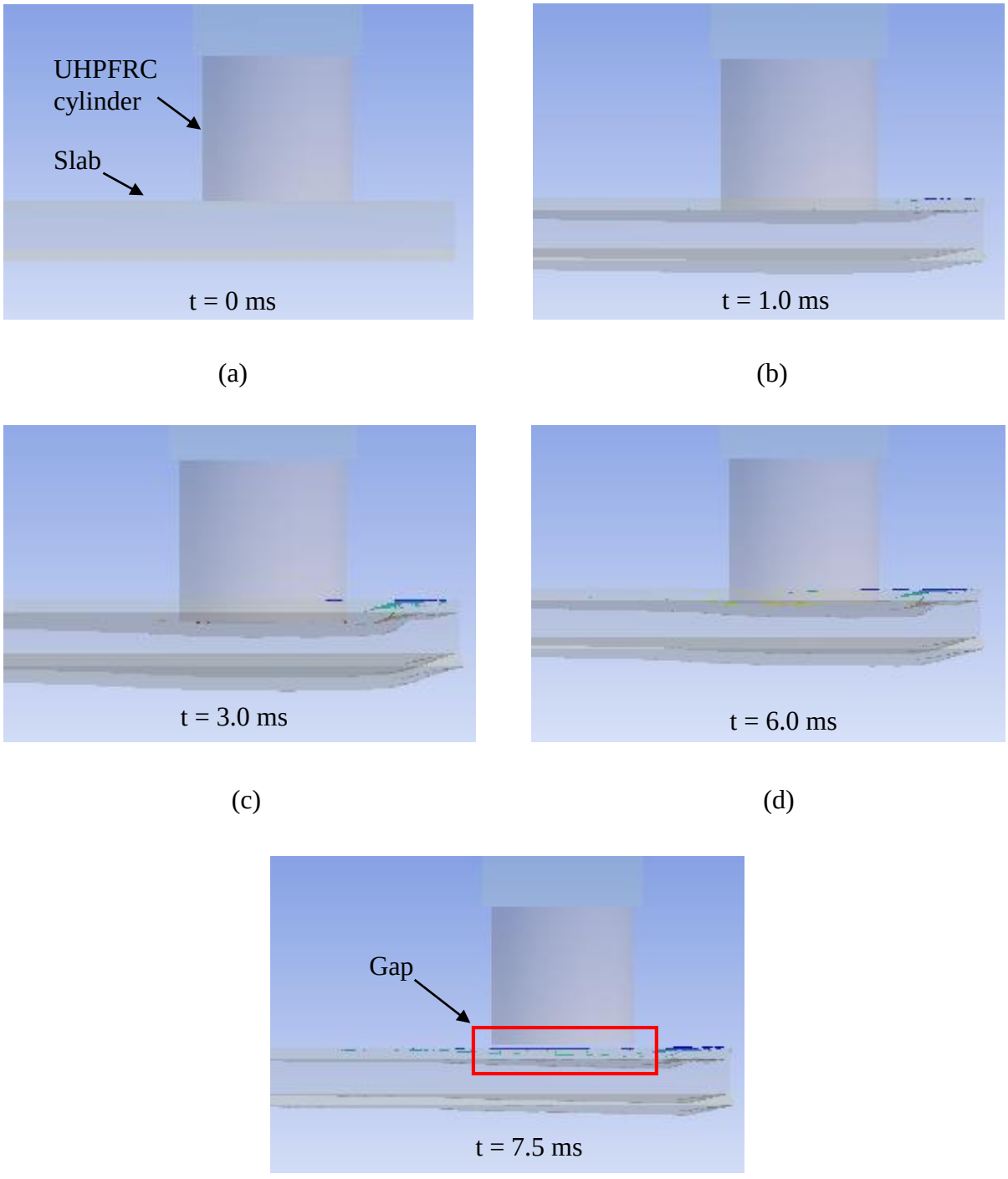

Figure 6.6: Elevation view showing the contact event for the undamaged slab model subjected to edge impact condition (a) at t = 0, contact between impactor and slab; (b) at t = 1.0 ms, impactor moves downward and increases the deformation; (c) at t = 3.0 ms, maximum deformation; (d) at t = 6.0 ms, rebound and reduction of maximum deformation, impactor moves upward; (e) at t = 7.5 ms, complete detachment.

Figure 6.7 shows the formation of shear punching failure for the pre-damaged slab model subjected to edge impact case from 2.8 m drop height. The contact between the face of the UHPFRC cylinder and the slab model was assumed to take place at t = 0 ms (ignoring the travelling time of the impactor from the drop height) as shown in Figure 6.7 (a). The red dots shown in Figure 6.7 (a) represent the eroded elements (cracks) due to the initial pressure imposed onto the slab model under the pre-damaged condition. The development of the shear punching failure occurred almost immediately at t = 0.03852 ms as shown in Figure 6.7 (b) where the UHPFRC cylinder penetrated almost half the thickness of the slab model. At 0.07704 ms, the impactor continues to progress downward forming a larger shear punching area as shown in Figure 6.7 (c).

By comparing the timescale between the pre-damaged and undamaged slab models, it can be seen that the formation of shear punching failure occured almost immediately upon contact. In this simulation exercise, the full perforation occurs in less than 0.08 ms. On the other hand, the whole process of the impact event for the undamaged slab model required 3.0 ms to reach the maximum deformation and 7.5 ms for the impactor to detach from the peripheral slab.

The sub-millisecond impact event shown by the pre-damaged slab model compared to the undamaged slab model indicates that the shear punching failure is driven by the inertial processes and is highly localised. The relatively short timescale during the impact event prevented the entire slab to respond in a flexural mode. The structural stiffness of the slab within the vicinity of the impact location was only able to withstand the impact energy.

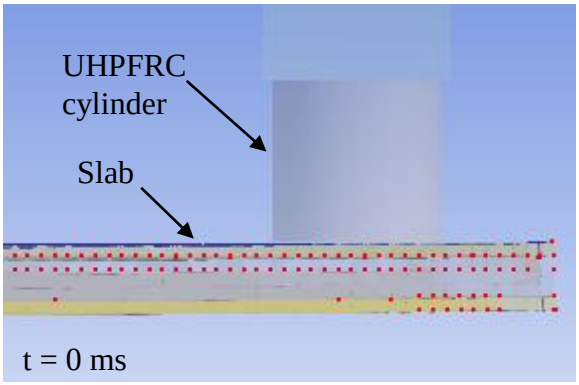

(a)

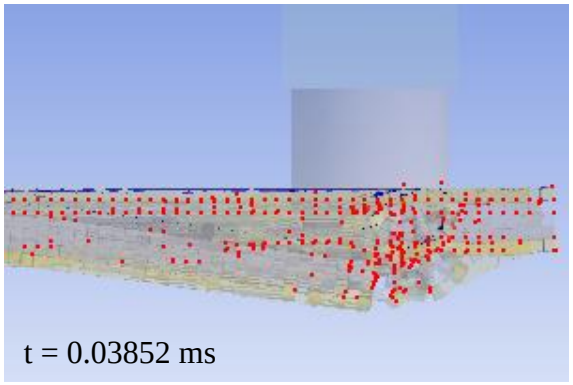

(b)

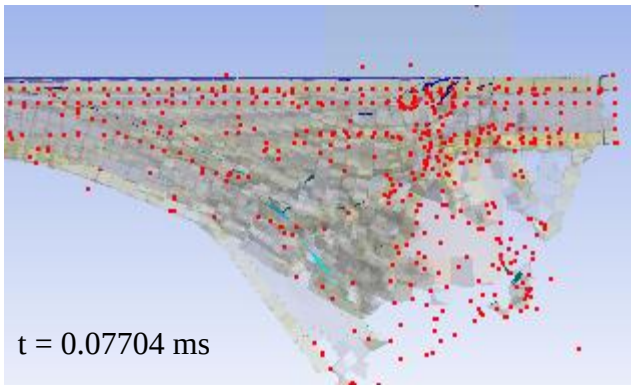

(c)

Figure 6.7: Elevation view showing the development of shear punching failure at the first strike for the pre-damaged slab model subjected to the edge impact showing (a) at t = 0 ms, contact between impactor and slab; (b) at t = 1.03852 ms, immediate formation of shear punching area; (c) at t = 1.11538 ms, spreading of shear punching failure on the bottom face.

6.3.2 Undamaged Slab Models

This section only focuses on the overall deformation results from the FE simulation and the validation exercise with the experimental data. This metric was chosen because it is a fundamental parameter in the acceptance criteria when designing a slab subjected to impact loading. In the case of the slab subjected to central impact loading, the maximum deformation can be converted to support rotation. Similarly, the results from the maximum and permanent deformation can be used to determine the ductility ratio. The values for the maximum and permanent deformation are obtained directly at the end of the simulation time.

Finite element results such as contact force are not presented in this section. In Ansys Explicit Dynamics, the measurement of the contact force is recorded using a *Tracker* where the recorded data may contain some noise. Although Ansys Explicit Dynamics allows filtering of the data (using the Butterworth filter method), the cut-off frequency cannot be guarenteed to be exactly the same as in the case of filtering the LDV data. This is due to the fact that filtering of the LDV data was performed on the velocity-time history and the contact force was derived from the filtered data using Newton's Second Law. Moreover, the simplification made to the FE model such as removing the clamping frames and modification to the impactor may create a different form of noise. The approach to determine the correct cut-off frequency based on the simplified model requires deeper investigation and was beyond the scope of this study.

Figure 6.8 shows the deformation-time history and the deformation contours (at maximum deformation and steady state vibration) for the undamaged slabs subjected to the first strike. For clarity of presentation, only the results from the highest drop height for every impact case are presented.

The maximum and permanent deformation for the undamaged slab models can be distinguished by the peak deformation and a horizontal line, respectively. It can be seen that the slab model subjected to the central impact reached the peak deformation at a relatively shorter time and vibrated over a longer period of time compared to the edge impact. Generally, the time period for each cycle of the vibration was shorter. As frequency is a function of stiffness [9], this response indicates that the local stiffness at these impact locations is higher compared to the edge and corner impact. Similarly, the deformation contour of the slab model subjected to the central impact is distributed across the slab compared to the edge and corner impact where a more localised deformation pattern was observed. These results also support the earlier discussion on the sensitivity of the impact location with respect to the local stiffness and failure pattern.

The maximum and permanent deformation values for the central, edge and oblique impact can be distinguished easily by the first peak and the final value in the deformation-time history, respectively. The deformation contour at these two locations also shows noticeable difference. However, the slab model for the corner impact showed only a small drop after the peak deformation resulting in a high permanent deformation value as shown in Figure 6.8 (c). The deformation contour for the slab also showed a similar pattern at the peak and along the horizontal portion of the graph. This phenomenon suggests that the slab is at the point of failure.

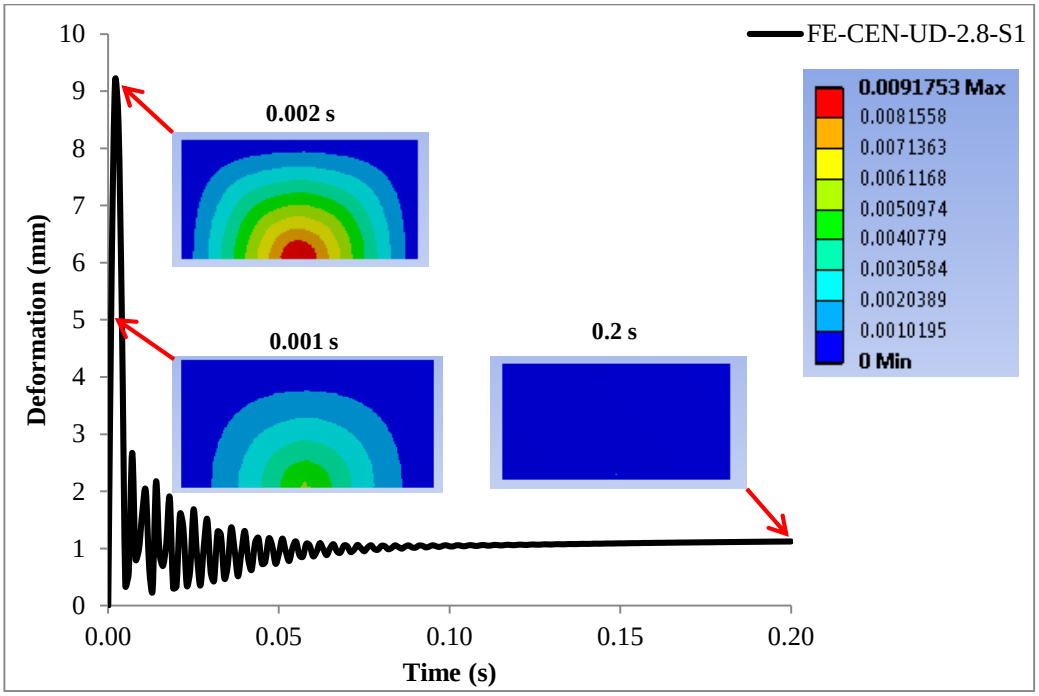

(a)

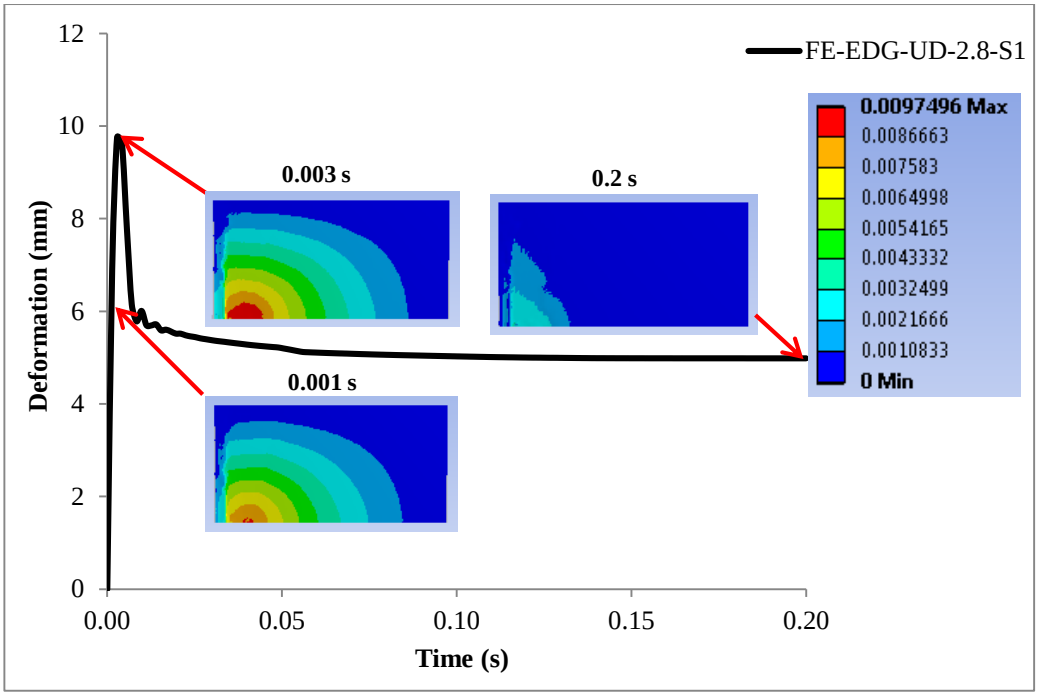

(b)

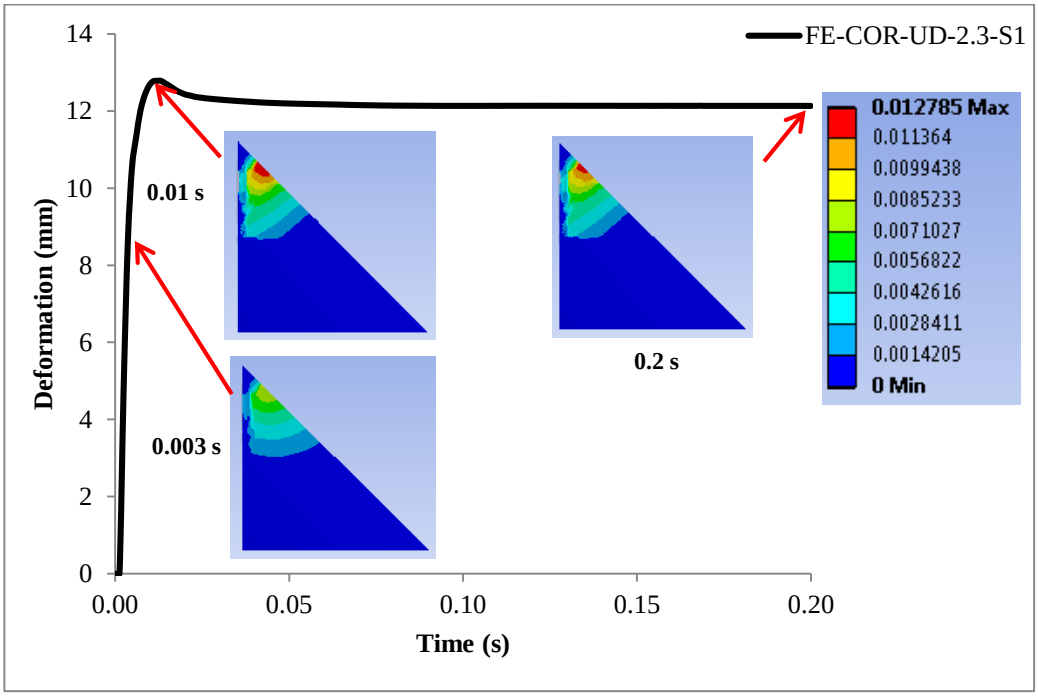

(c)

Figure 6.8: Deformation-time history and deformation contour for the undamaged slab model impacted at (a) centre; (b) edge; (c) corner.

6.3.3 Pre-damaged Slab Models

Figure 6.9 shows the deformation-time relationship and deformation contours for the pre-damaged slabs. The datum for each impact case is also included. The true maximum deformation was taken as peak deformation minus the respective datum. Similarly, the true permanent deformation value was taken as the deformation at 0.4 s minus the respective datum.

The contact between the impactor and the slab occurred at 0.2 s and the deformation reached the maximum values at the first peak. Unlike the case of the undamaged model, the maximum and permanent deformation for the pre-damaged models showed only small differences. This is particularly true for the central impact case where the maximum deformation showed insignificant decrease after 0.22 s and maintained almost a horizontal path until the end of the simulation time. The edge and corner impact cases showed a slight decrease after reaching the maximum deformation as shown in Figure 6.9 (b) and Figure 6.9 (c), respectively. The deformation contour at the maximum and permanent deformation also showed insignificant changes.

Also noted is the slightly lower maximum deformation developed by the pre-damaged slab subjected to the corner impact compared to the undamaged model (calculated to be 0.8 mm). Although this result contradict with the experimental data but with the small difference between the maximum and permanent deformation values, both slabs can be considered as approaching failure.

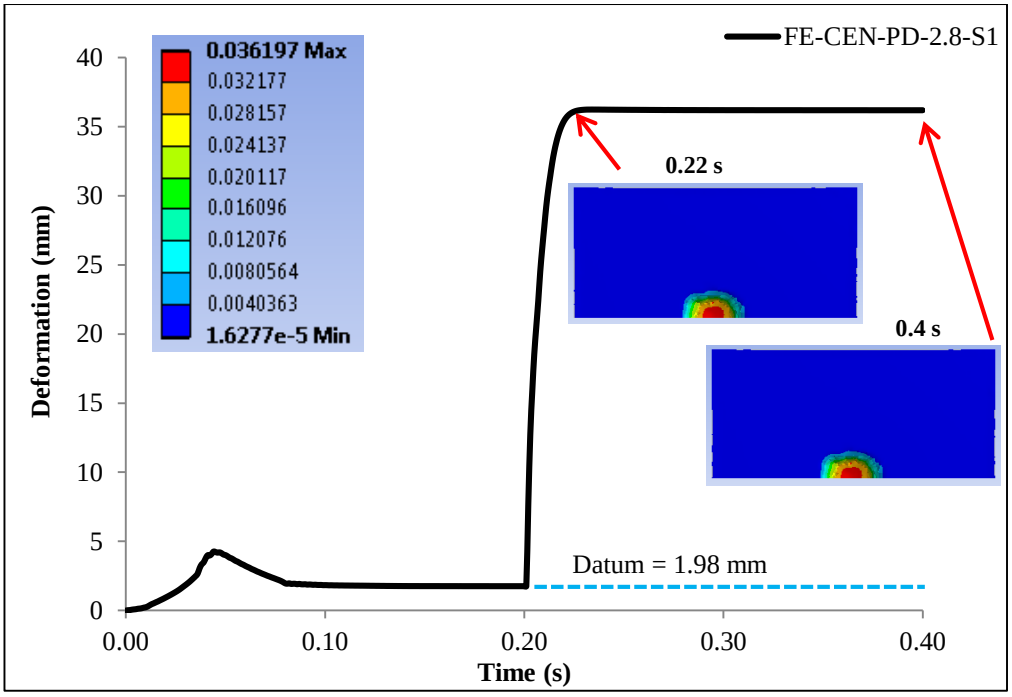
FE-CEN-PD-2.8-S1
0.036197 Max
0.032177
0.028157
0.024137
0.020117
0.016096
0.012076
0.0080564
0.0040363
1.6277e-5 Min
0.22 s
0.4 s
Datum = 1.98 mm
Deformation (mm)
Time (s)
0
5
10
15
20
25
30
35
40
0.00
0.10
0.20
0.30
0.40

(a)

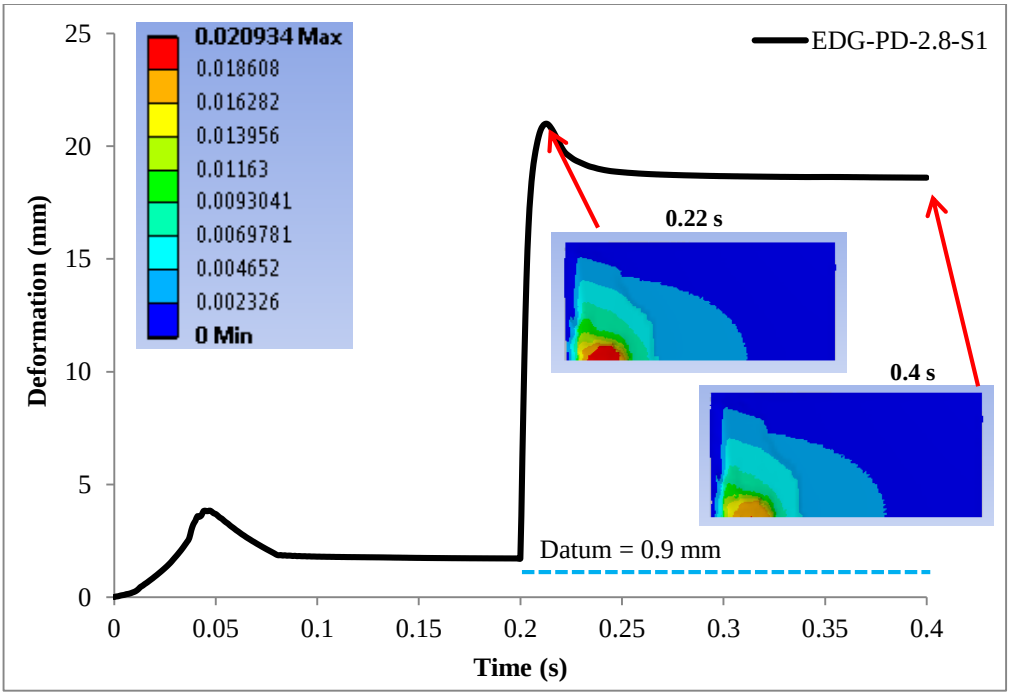
EDG-PD-2.8-S1
0.020934 Max
0.018608
0.016282
0.013956
0.01163
0.0093041
0.0069781
0.004652
0.002326
0 Min
0.22 s
0.4 s
Datum = 0.9 mm
Deformation (mm)
Time (s)
0
5
10
15
20
25
0
0.05
0.1
0.15
0.2
0.25
0.3
0.35
0.4

(b)

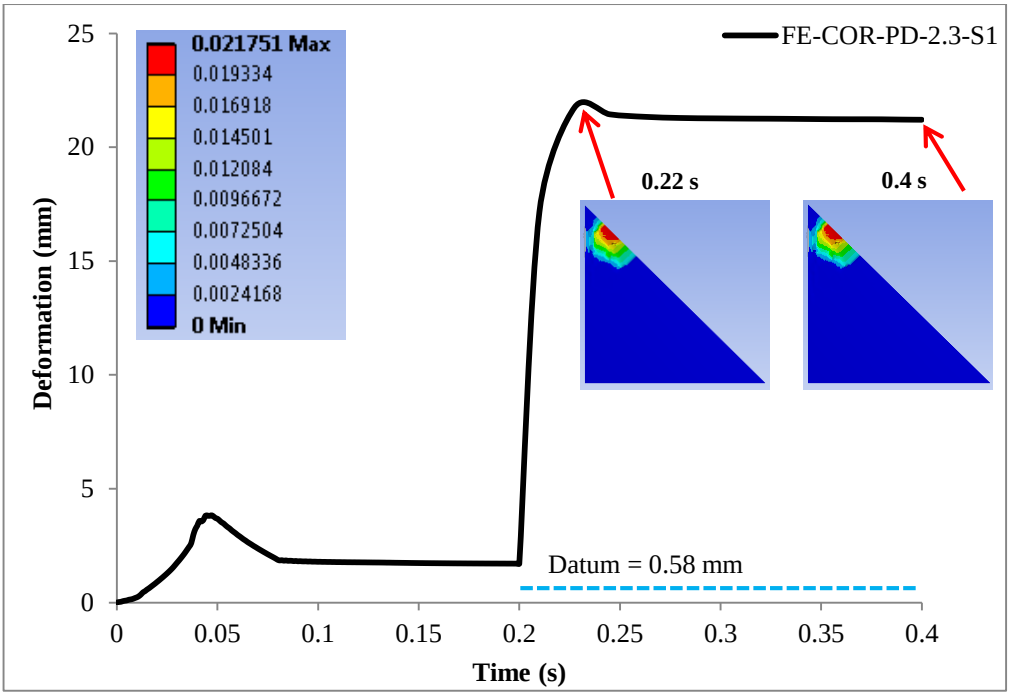

(c)

Figure 6.9: Deformation-time history and deformation contours for the pre-damaged slab model impacted at (a) centre; (b) edge; (c) corner.

6.3.4 Validation with the Experimental Data

The overall maximum deformations produced by the FE analysis were plotted together with the experimental data as shown in Figure 6.10. In the case of the undamaged slab, the results from the FE analysis showed reasonably good agreement with the experimental data and this is particularly true for the central, edge and corner impact cases as shown in Figure 6.10 (a) Figure 6.10 (b) and Figure 6.10 (c), respectively. For the central impact, the difference is calculated to be 9.1%, 19.9% and 21.5% for 1.5 m, 2.3 m and 2.8 m drop height, respectively. The FE model for the edge impact predicted the maximum deformation with reasonable accuracy and the difference is calculated to be 9.3%, 8.1 % and 2.2% for 1.5 m, 2.3 m and 2.8 m drop height, respectively.

The FE models were also able to simulate the maximum deformation of the corner impact with reasonable accuracy. At 1.5 m drop height, the FE results underestimated the experimental data with 18.1 % difference but overestimated the maximum deformation approximately 36.9% at 2.3 m drop height. Although the FE model overestimated the maximum deformation, it did not perforate and was able to withstand another strike similar to the experimental data.

In the case of the pre-damaged slabs, the FE models also showed reasonably good agreement with the experimental data at 1.5 m drop height but were not able to produce a similar agreement at higher drop heights. For the central impact, the difference is calculated to be 11.5%, 29.8% and 173.8% at 1.5 m, 2.3 m and 2.8 m drop height, respectively. The FE models for the edge impact overestimated the experimental data by 33.0%, 51.4% and 77.7% at 1.5 m, 2.3 m and 2.8 m drop height, respectively. Finally, the FE models for the corner impact underestimated the maximum deformation by 10.8% at 1.5 m drop height but overestimated the experimental data by 86.2% at 2.3 m drop height.

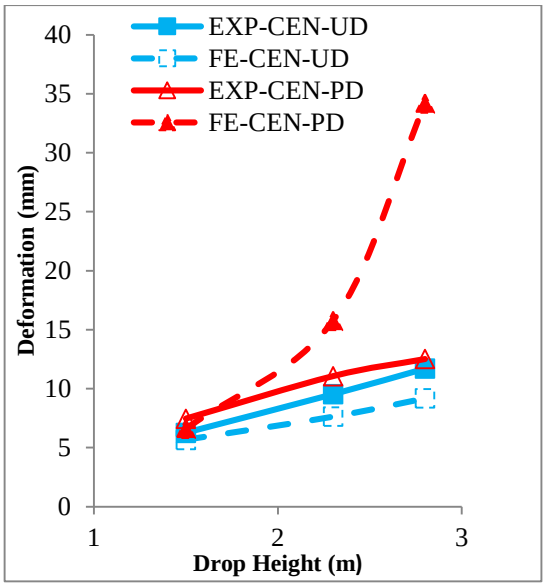

(a)

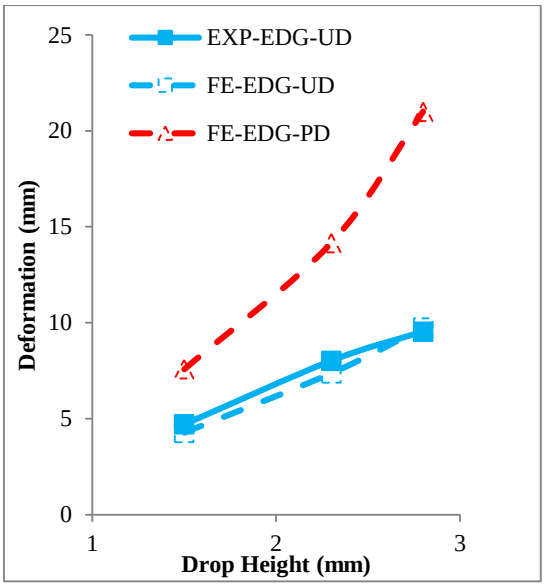

(b)

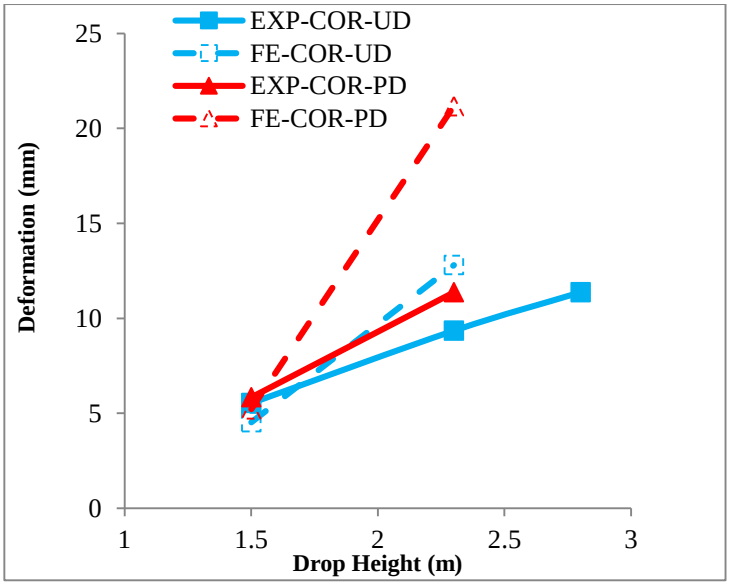

(c)

Figure 6.10: Comparison in terms of the maximum deformation between FE simulation and experimental data for undamaged and pre-damaged slabs subjected to (a) central impact; (b) edge impact; (c) corner impact.

Figure 6.11 shows the comparison between the FE simulation results and the experimental data with respect to the permanent deformation of the slabs. It can be seen that the FE results show a fair agreement with the experimental work for simulating the central and edge impact of the undamaged slabs. This is particularly true at almost all drop heights. For the central impact, the difference is calculated to be 77.5 %, 75.4% and 74.3% at 1.5 m, 2.3 m and 2.8 m drop height. Similarly for the edge impact, the difference was recorded to be 22.9%, 11.7 % and 2.4%. However, for the corner impact, the FE model shows a difference of 15.9 % with the experimental data at 1.5 m drop height but increases to 79.4 % at 2.3 m drop height.

Similarly, the pre-damaged models show less degree of accuracy for predicting the permanent deformation of the slabs and this is particularly true for the central impact and at higher drop heights. In the case of the central impact, the difference was calculated to be 190.3%, 261.9% and 326.5% at 1.5 m, 2.3 m and 2.8 m drop height respectively. The edge impact predicted the response very well at 1.5 m drop height with 2.5 % difference but significantly over predicted the response at 2.3 m drop and 2.8 m drop height with a

difference of 257.6 % and 126.6%, respectively. The corner impact also followed the same trend and the difference was calculated to be 18.8% and 148.7% at 1.5 m and 2.3 m drop height, respectively.

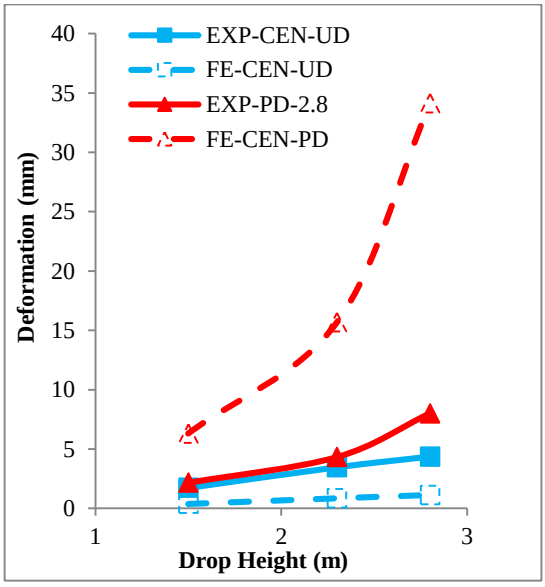

(a)

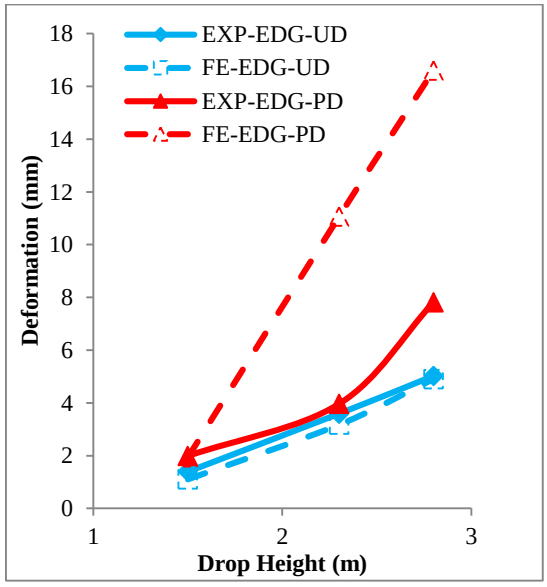

(b)

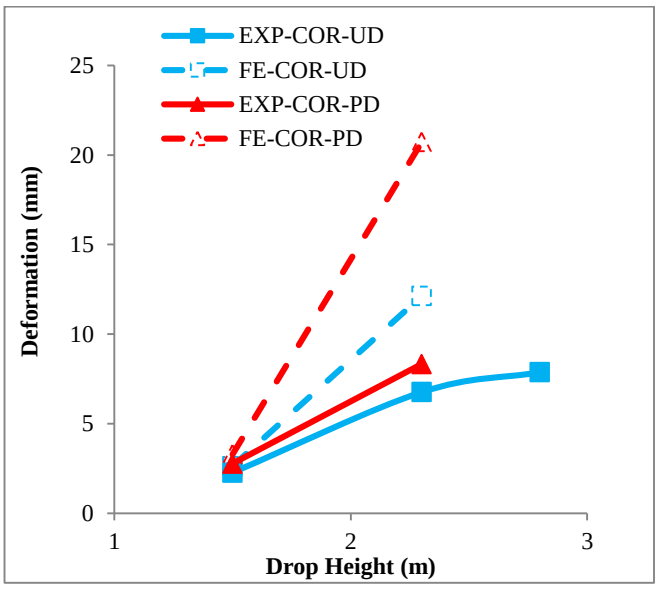

(c)

Figure 6.11: Comparison in terms of the permanent deformation between FE simulation and experimental data for undamaged and pre-damaged slabs subjected to (a) central impact; (b) edge impact; (c) corner impact.

The validation shows that the FE models predict the maximum deformation of the undamaged slabs with reasonably good accuracy in most of the impact simulations at 1.5 m and 2.3 m drop height. At the same time, the FE models also show a fair agreement with the experimental data for predicting the permanent deformation of the slabs. On the other hand, the pre-damaged model offered a fair agreement for predicting the maximum deformation but show less accuracy for predicting the permanent deformation.

In general, the FE slab model shows better accuracy for predicting the maximum deformation compared to the permanent deformation. This trend indicates that the RHT concrete model possesses low residual strength especially after being impacted at higher drop heights. In the RHT formulation, the residual strength of the material is mainly controlled by the parameter *B* and *m*. Due to limited data available in the open literature, the calibration was performed based on one characterization test. The calibrated *B* value might have caused the RHT formulation to scale down the failure surface immediately to a low residual strength surface. As a result, the strain softening of the UHPFRC material was not fully mobilised and reduced the post-peak strength of the slab. Moreover, the other parameter *m* that controls the shape of the residual surface along the compression meridian was not calibrated together with the parameter *B* and this is thought to influence the results as well. In some cases, default values were used due to the unavailability of such test data in the open literature. Similarly, there are very limited data on the FE simulation to predict the permanent deformation of a UHPFRC element subjected to dynamic loading. As such, comparison with other research work was difficult.

The relatively lower degree of accuracy shown by the pre-damaged slab model compared to the undamaged slab is thought to be associated with the method of using high pressure loading with a short rise time to replace the static loading. This method induced dynamic effects in the form of slab vibration. Impacting a vibrating element may cause higher excitation to the slab causing premature damage. However, the sensitivity analysis conducted on the slab by varying the pressure and rise time showed that the selected loading condition produced an almost horizontal deformation-time relationship after 0.1 s suggesting that the slab was not vibrating excessively.

Consequently, the FE modelling and validation exercise demonstrates the ability of a correctly calibrated RHT concrete model to simulate a complex dynamic event with damage in UHPFRC material. With further calibration and refinement to the model it is possible to achieve more accurate results that correlate to the multiple loading scenarios.

6.4 SDOF Simulation Results

Figure 6.12 shows an example of the permanent deformation profiles for the undamaged and pre-damaged slab subjected to the central impact at 2.8 m drop height. It can be seen that the deformation profiles fit the shape function of the elastic-plastic strain range as given in Table 4.5. Similar results were also shown for slabs impacted at 2.3 m and 1.5 m drop height. As such, the derivation of the resistance functions is based on the elastic-plastic formulations.

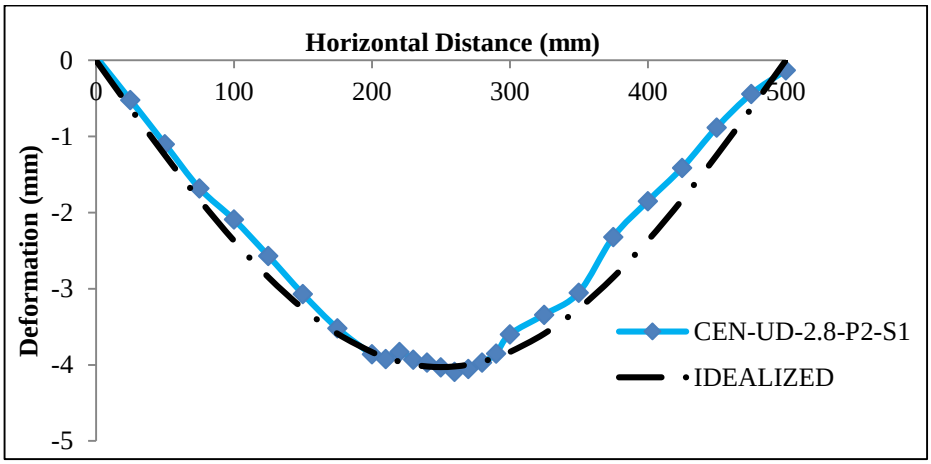

(a)

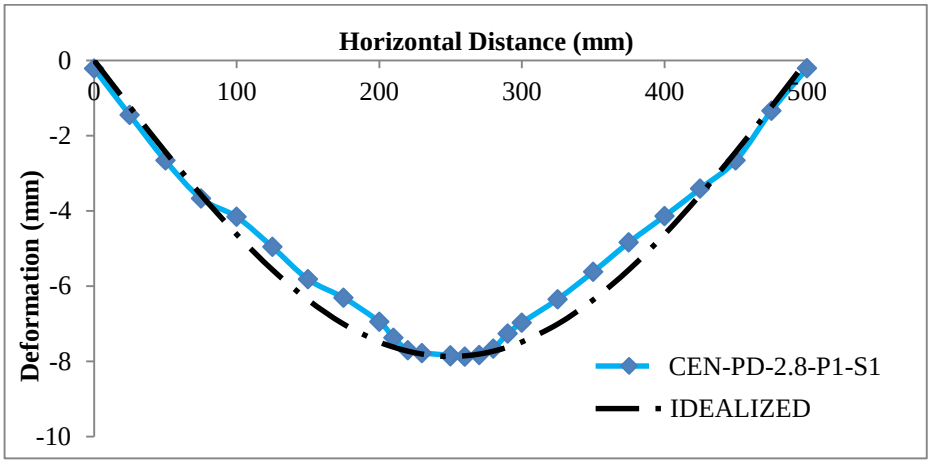

(b)

Figure 6.12: Permanent deformation profiles and the idealised elastic-plastic shape for the (a) undamaged slab; (b) pre-damaged slab.

Figure 6.13 shows the average load-deformation curves for the undamaged and pre-damaged slabs under static test together with the tri-linear resistance curve. Both the undamaged and pre-damaged slabs showed similar load-deformation relationship trend starting with linear elastic, elastic-plastic, plastic, and softening phases. However, the plastic phase for the pre-damaged slabs is over a shorter range compared to the undamaged slab and this response can be expected when the slab carries some degree of initial damage.

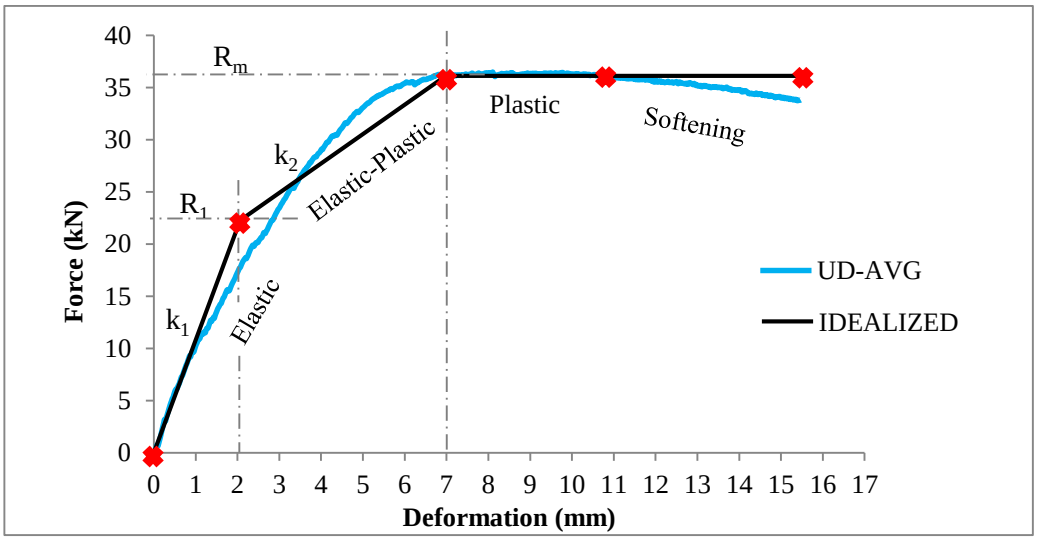

(a)

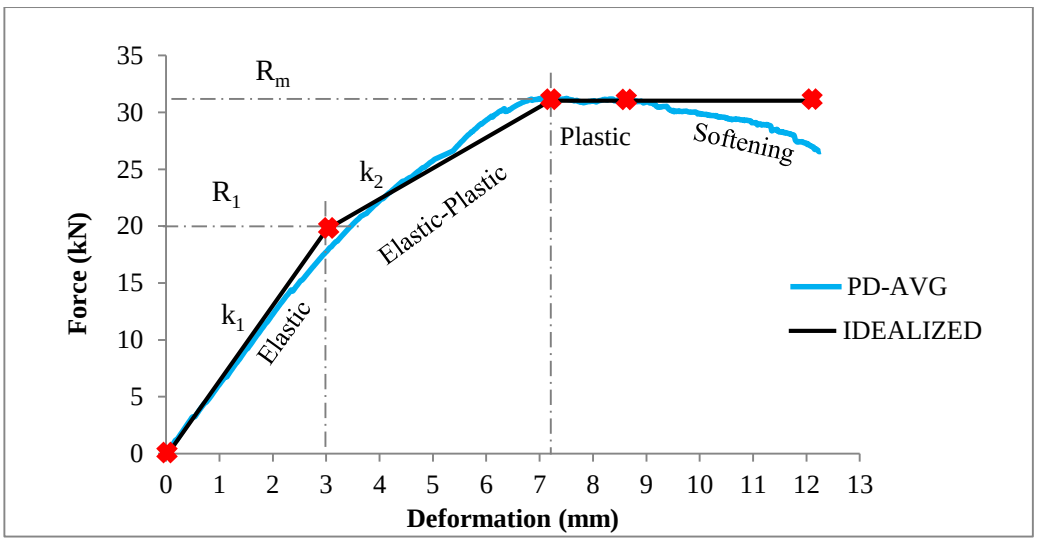

(b)

Figure 6.13: Load-deformation curves developed from the static tests and the tri-linear resistance functions for (a) undamaged slab; (b) pre-damaged slab.

Based on the tri-linear resistance curves, the stiffness and resistance forces were estimated and presented in Table 6.3. These functions shall be part of the input parameters in the SDOF analysis. As expected, the stiffness and resistance forces of the pre-damaged slabs are lower than the undamaged slabs.

Table 6.3: SDOF parameters derived from the idealised resistance curves.

Parameter	**Unit**	**Undamaged slab**	**Pre-damaged slab**
R_1	N	22,500	20,000
R_M	N	36,500	31,000
k_1	N/m	1.13×10^7	6.67×10^6
k_2	N/m	2.9×10^6	2.56×10^6

The mass transformation factor for the slab $K_{M(s)}$ was calculated by solving equations (4.31) to (4.33) based on the elastic-plastic shape function. The value for $K_{M(s)}$ was found to be 0.31, representing 31% of the actual slab mass that participated in the dynamic response of the SDOF model.

Table 6.4 shows the estimated velocity of the slab upon impact for SDOF analysis using equation (4.38). The velocities of the slab upon impact were lower compared to the striking velocities of the impactor due to the assumption that both the colliding bodies moved with the same velocity upon contact and the momentum was conserved. In the actual test, some external forces such as friction can be expected and affect the conservation laws. However the influence of the external forces was assumed to be negligible.

Table 6.4: Measured average velocities of the impactor and estimated velocities of the slab at the respective drop heights.

Drop Height (m)	v_i (m/s)	v_s (m/s)
2.8	7.32	5.62
2.3	6.61	5.08
1.5	5.32	4.09

The results from the SDOF simulation and the experimental data are shown in Figure 6.14. It can be seen that in most cases, the SDOF results are in good agreement with the experimental data. This finding is particularly true for the maximum deformation where the differences are calculated to be in the ranges of 0.2% to 11.3% and 2.1% to 11.3% for the undamaged and pre-damaged slabs, respectively. As for the permanent deformation, the differences are found to be higher, in the range of 37.0% to 49.5% and 5.0% to 31.6% for the undamaged and pre-damaged slabs, respectively. In most cases, the pattern of the results was similar where SDOF overestimates the experimental results and can be related to several factors, namely

i) The assumption of a perfectly plastic collision considers a zero coefficient of restitution where the whole slab and the impactor move together with the same velocity. In reality, the slab was restrained along all edges and the velocity of the panel varies across the profile. Based on the validation results, the velocity of the slab upon impact (v_s) was likely to be overestimated.

ii) The idealization of the permanent deformed shape based on elastic-plastic shape function has a direct influence on the participating mass of the actual slab. The standard values of the mass factor (K_M) are available for three strain-range conditions, elastic, elastic-plastic and plastic. In order to achieve a higher degree of accuracy, a more accurate mathematical expression needs to be computed to represent the actual deformed shape. However, such work is beyond the scope of this study.

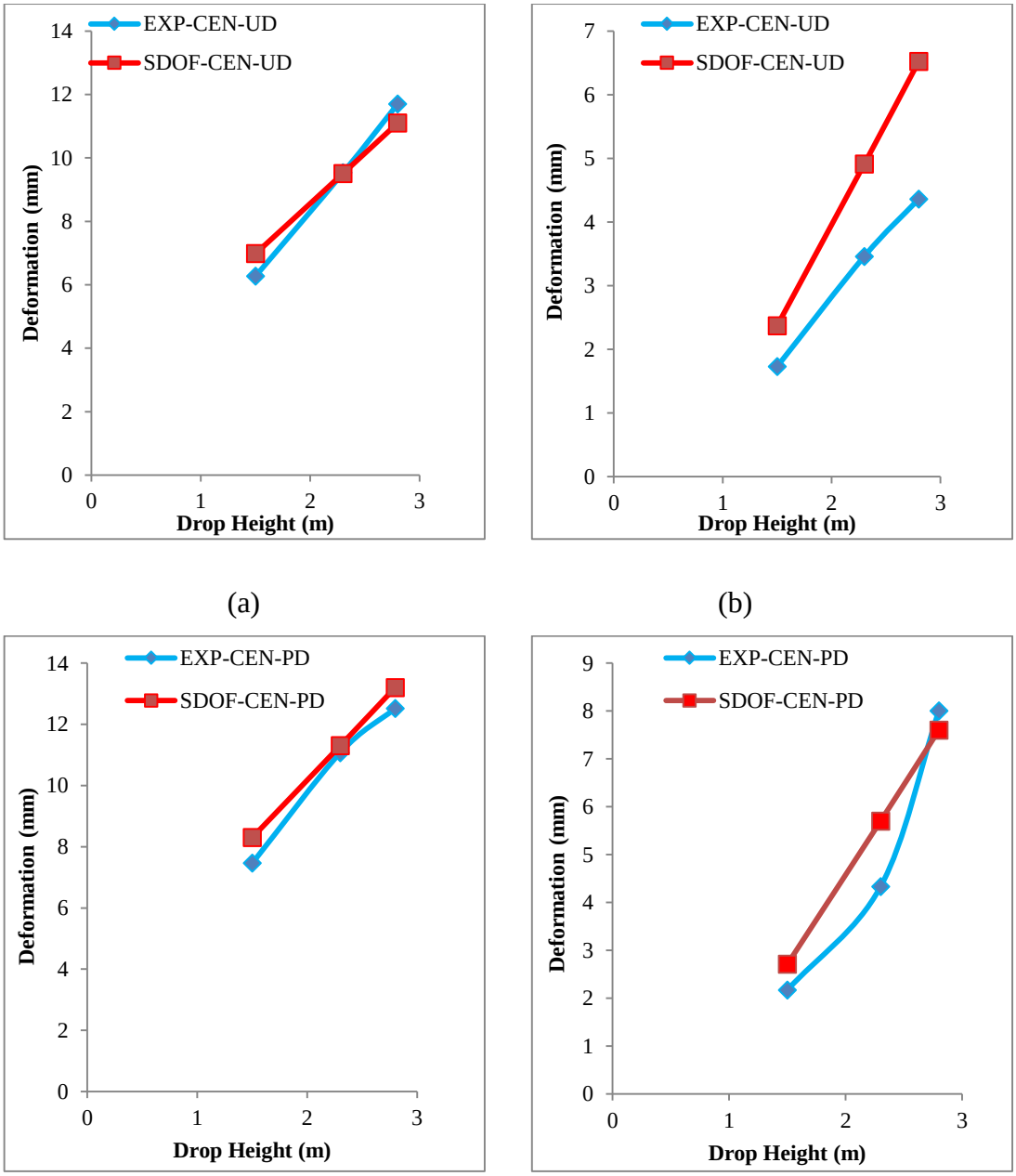

Figure 6.14: Comparison between the analytical SDOF predictions and experimental results for (a) maximum deformation of the undamaged slab; (b) permanent deformation of the undamaged slab; (c) maximum deformation of the pre-damaged slab, (d) permanent deformation of the pre-damaged slab.

6.5 Theoretical SDOF Input Parameters

The ultimate moment of resistance, M_{ult} was calculated to be 2,505 Nmm/mm based on equation (4.49). On the other hand, the maximum resistance, R_M was calculated using equation (4.48) and produced 40,080 N. In order to be consistent with the tri-linear resistance curve from the experimental work, the resistance force at the end of the elastic phase, R_1 were taken as 20,400 N, assumed to be half the value of R_M.

Finally, the stiffness for the elastic and elastic-plastic phases was obtained following equations (4.40) to (4.44). The shape function for the elastic strain range and elastic-plastic strain range were used following equations (4.28) and (4.29), respectively. Solving all the equations produced k_1 and k_2 to be 2.54×10^7 N/m and 1.44×10^7 N/m, respectively. The mathematical calculations for deriving k_1 (undamaged slab) is presented in Appendix D. Table 6.5 shows the overall resistance functions from the theoretical approach.

Table 6.5: Resistance functions derived theoretically.

Parameter	Unit	Undamaged Slab
R_1	N	20,400
R_M	N	40,080
k_1	N/m	2.54×10^7
k_2	N/m	1.44×10^7

The maximum and permanent deformations obtained from the theoretical SDOF parameters were validated with the average experimental results and shown in Figure 6.13. It can be seen that the theoretical approach underestimates the maximum deformation but overestimates the permanent deformation compared to the experimental data. The difference between the theoretical results and the experimental data is calculated to be 17.2% to 23.3% and 62.7% to 92.0% for the maximum and permanent deformation, respectively.

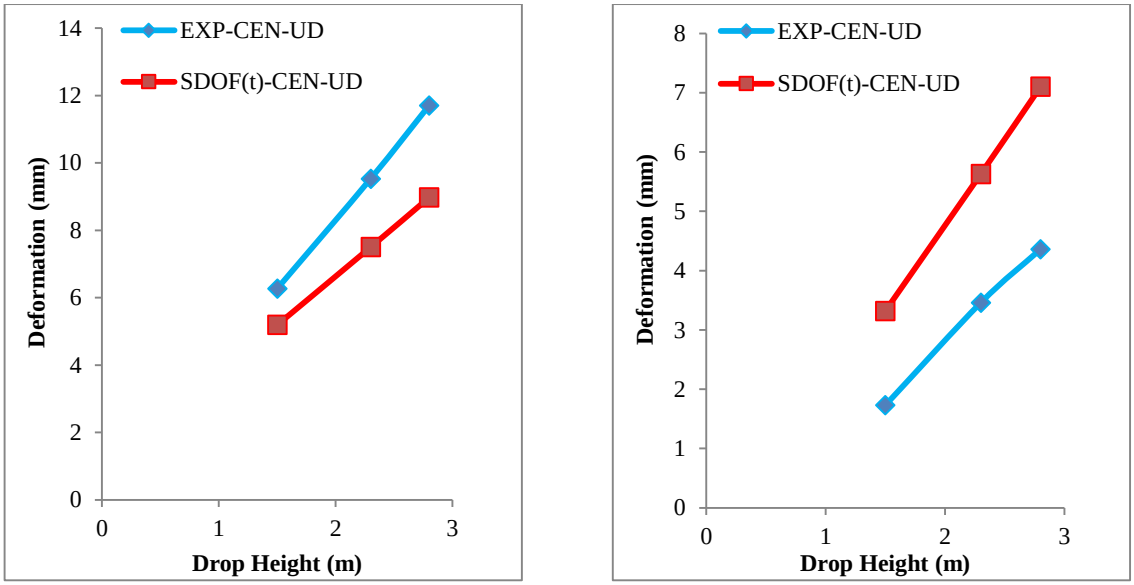

(a) (b)

Figure 6.15: Comparison between the theoretical SDOF predictions and experimental results for (a) maximum deformation; (b) permanent deformation.

The significant difference between the SDOF analysis (theoretical approach) and the experimental data, especially for the permanent deformation can be associated with the assumption made on the support condition of the slab. This assumption was reflected in the approach to determine R_M using yield-line theory where fully fixed edges were considered. As discussed earlier in section 4.4, this condition requires the slab to be monolithically cast with the support in order to activate the constraints effectively. As a result, the energy solution adopted for obtaining the stiffness showed higher theoretical values where the calculated k_1 and k_2 differ with the experimental data by 55.5% and 79.9%, respectively. The difference in the results was also contributed by the simplification made to derive the velocity of the slab, the shape function of the deformed slab and the omission of the softening branch in the resistance curve as mentioned earlier. However, it is worth mentioning that the high stiffness produced theoretically supports the assumption that the actual boundary condition along the edges of the slab in the experimental work was not ideally fixed.

On the other hand, the theoretical approach to estimate the ultimate moment of resistance (M_{ult}) using equation (4.33) gives a reliable maximum resistance force (R_M) where the difference between the experimental data and the theory was calculated to be 9.4%. Similarly, the assumption that the resistance force at the end of the elastic phase (R_1) was half the value of the maximum resistance (R_M) also gave a reasonably matched result with the experimental data with a difference of 11.3%.

Consequently, the SDOF modelling exercise demonstrates the ability of a simplified approach to predict a high energy dynamic event with acceptable limits provided due attention is given to the assumptions such as boundary conditions and mode shape. Such an approach can be confidently used as a preliminary analysis tool as the advantages are short run times and basic understanding of the underlying physics of the problem. Notwithstanding the above comments, care should be taken in using this approach beyond the range of validity.

6.6 Summary of Chapter 6

This chapter presented the results from the numerical analysis and discussion on validating the results with experimental data. ANSYS Explicit Dynamics Release 13.0 was used in the FE analysis to predict the deformations of the undamaged and pre-damaged slabs subjected to a single low velocity impact. Prior to the simulation exercise, sensitivity analyses on the mesh size, pressure loading condition, input parameter *B* for the RHT concrete model and support condition were performed.

The FE models predicted the maximum and permanent deformation of the undamaged slab with reasonably good agreement as demonstrated in some of the simulation results. On the other hand, the FE models for the pre-damaged slab offered a reasonably good agreement for predicting the maximum deformation at lower drop height. The rest of the simulations did not give as good predictions as the response of the UHPFRC slab. The evidence showed by the simulation results for the undamaged slabs suggests that the calibrated RHT concrete model can be used to represent the dynamic properties for the UHPFRC materials. However, a more realistic representation of the UHPFRC material and a refined simulation results can be expected by performing more characterization tests on UHPFRC materials.

On the other hand, the method of introducing high pressure loading with short rise time and extending over a longer simulation time were able to dampen the vibration of the UHPFRC slab. The pre-damaged slab model developed from this method showed promising results for predicting the maximum deformation of the actual slab especially at lower drop height.

SDOF models that incorporated a resistance curve developed from the static test data predicted the response of the undamaged slabs with reasonable accuracy in most of the simulations. The SDOF model for the pre-damaged slabs offered generally fair agreement with the experimental data. Finally the SDOF models that incorporated a resistance curve derived theoretically showed less degree of accuracy compared with the experimental data particularly for predicting the permanent deformation. It is considered that simplifications and assumptions made to the resistance function may have influenced the results.

6.7 References

[1] L. Agardh "FE-modeling of fibre reinforced concrete slabs subjected to blast load," *Journal de Physique IV*, vol. 7, pp. C3-723-C3728, 1997.

[2] S. Madjidi, W. S. Arnold and I. H. Marshall, "Damage tolerance of CSM laminates subject to low velocity oblique impacts," *Composite Structures*, vol. 34, no. 1, pp. 101-116, 1996.

[3] P. R. Hampson and M. Moatamedi, "A review of composite structures subjected to dynamic loading," *International Journal of Crashworthiness*, vol. 12, no. 4, pp. 411-428, 2007.

[4] T. Borvik, O. S. Hopperstad, T. Berstad and M. Langseth, "Perforation of 12mm thick steel plates by 20mm diameter projectiles with flat, hemispherical and conical noses: part II: numerical simulations," *International Journal of Impact Engineering*, vol. 27, no. 1, pp. 37-64, 2002.

[5] T. Belytschko, "On difficulty level in non linear finite element analysis of solids," *Bulletin for the International Association for Computational Mechanics*, vol. 2, pp. 6-8, 1996.

[6] T. Borvik, L. Olovsson, S. Dey and M. Langseth, "Normal and oblique impact of small arms bullets on AA6082-T4 aluminium protective plates," *International Journal of Impact Engineering*, vol. 38, no. 7, pp. 577-589, 2011.

[7] T. L. Teng, Y. A. Chu, F. A. Chang and H. S. Chin, "Simulation model of impact on reinforced concrete," *Cement and Concrete Research*, vol. *34, no.* 11, pp. 2067-2077, 2004.

[8] Y. Liu, A. Ma, and F. Huang, "Numerical simulations of oblique-angle penetration by deformable projectiles into concrete targets," *International Journal of Impact Engineering*, vol. 36, no. 3, pp. 438-446, 2009.

[9] O. S. Salawu, "Detection of structural damage through changes in frequency: a review," *Engineering Structures*, vol. 19, no. (9), pp. 718-723, 1997.

CHAPTER 7

CONCLUSIONS AND FUTURE RECOMMENDATIONS

7.1 Conclusions of the Research Work

This research was carried out with the aim to investigate the performance of pre-damaged UHPFRC slabs under dynamic loading conditions. The experimental work was performed to simulate the condition of a damaged UHPFRC floor, resulting from a blast load, being impacted by a failed column. The context of this research is the prevention of progressive collapse of building structure following extreme abnormal loading. A static pressure load was applied to create the initial damage (or pre-damage) representing the effects of blast loading on the slab while the low velocity impact loading represented the impact from a failed column. Numerical simulations were carried out using SDOF and FE models and validated with the experimental results. By referring to the objectives of this study (section 1.5), the following conclusions can be drawn:

i) To experimentally evaluate the impact resistance of the pre-damaged UHPFRC slabs subjected to various impact loading conditions.

- No investigations to date have been carried out to study the performance of UHPFRC slabs subjected to blast load followed by low velocity impact load. This research simplified the actual blast loading effect by pre-damaging the slabs using static pressure loading. A pressure loading device was used to produce the pre-damage on the slabs with good consistency throughout the pre-damage exercise.
- While the pre-damaged slabs carried initial deformation and cracks after being exposed to as much as 77% of the maximum static pressure capacity, the impact resistance of the pre-damaged slabs was substantially high. The experimental evidence showed that the maximum resistance was of the order of 50 - 85% that of the undamaged slab.
- The high residual strength of the pre-damaged slabs was also reflected in the pattern of the deformations and material degradation under multiple impact scenarios that was found to be relatively similar to the undamaged slabs. The strength contribution from the fibre bridging effect was not significantly reduced and the pre-damaged slabs were able to absorb high CIE. Their high strength reserve after initial damage make them appealing as a construction

material to withstand abnormal loading and mitigate progressive collapse of a structure.

- The minimum thickness of the pre-damaged slab to avoid perforation when subjected to a single strike at the centre of the slab can be conservatively estimated by modifying equation (2.1). This was carried out by incorporating a reduction factor based on the normalised CIE obtained from the experimental data. Equation (2.1) also has the potential to be used to estimate the minimum thickness of an undamaged slab subjected to the same impact condition.
- The acceptance criteria for the pre-damaged UHPFRC slab subjected to a low velocity impact is possible to be established by using the maximum deformation as the basis to calculate the support rotation. However, further investigation is required in order to establish the damage levels with respect to the magnitude of the support rotation.

ii) To develop an understanding on the sensitivity of the impact angle and impact location.

- In a realistic impact event, the impact location is variable. The impact resistance of a slab can be sensitive to the impact location and impact angle. No investigation has been carried out to date to investigate the impact resistance and the response of UHPFRC slabs subjected to asymmetrical impact.
- Slabs subjected to asymmetrical impact showed lower impact resistance compared to the usual concentric impact and this was particularly true as the impact location moves closer to the corner of the slab. Under the multiple impact scenarios, the experimental evidence showed that the slabs subjected to the asymmetrical impact required lesser number of strikes to perforate compared to the concentric impact. The internal damage that leads to the local material degradation and strength reduction was shown to have developed rapidly. As such, an asymmetrical impact condition resulting from a failed column onto a slab represents a higher risk towards initiating a failure that may lead to the progressive collapse of a building structure.

- On the contrary, tilting the slabs to 10° so as to represent an oblique impact condition and setting the impact location at the centre of the slab showed that the slabs exhibited higher impact resistance compared to the normal concentric impact case. Consequently, a slab subjected to an oblique impact represented lower risk of failure and progressive collapse of a building structure.
- The acceptance criteria for asymmetrical impact may not be possible to be established using the support rotation due to the possibility of developing different varying angles. Similarly, small support rotation angles may also be developed if the mode of failure is highly governed by shear punching.

iii) To develop finite element models and predict the mechanical response of the UHPFRC slabs subjected to low velocity impact and validate with the experimental results.

- FE analysis was performed using ANSYS Explicit Dynamics Release 13.0 software. A triangulated pressure loading with a peak pressure of 0.495 MPa and 0.04 s rise time showed similar response to the static test. An RHT concrete model was used to represent the dynamic material properties for UHPFRC. A number of the input parameters were calibrated based on the available experimental results and recommendations from other researchers.
- The perforation resistance of the undamaged and pre-damaged slabs was accurately modelled in all cases except for the undamaged slab subjected to the corner and oblique impact at 2.8 m drop height. The perforation of slab model subjected to the corner impact however was justified by the fact that one of the actual slabs also failed at the first strike. On the other hand, the perforation of the slab subjected to the oblique impact was not fully understood. However, the graphical impact sequence showed that the UHPFRC cylinder that formed part of the impactor model suffered severe damage and was not able to rebound. The condition of the cylinder in the FE simulation was not similar to the photographic evidence.

- The RHT concrete model embedded in the FE model predicted the maximum deformation with good accuracy in most of the simulations involving impact at 1.5 m and 2.3 m drop height. Similarly, the pre-damaged slab models predicted the maximum deformation with reasonable accuracy for impact simulation at 1.5 m and 2.3 m drop height. Numerical prediction for the permanent deformation showed less degree of accuracy. The evidence suggested that the calibrated RHT concrete model could be used to represent UHPFRC materials especially for impact simulation at lower drop height.

iv) To predict the mechanical response of the UHPFRC slabs subjected to central impact using single-degree-of-freedom (SDOF) model and validate with the experimental results.

- The analytical simulation results for the single impact scenario on undamaged and pre-damaged slabs based on SDOF idealisation were able to produce a reasonably good agreement with the experimental data. This is particularly true when the resistance functions were derived from the static test data.
- In another exercise where the resistance functions for the undamaged slab were derived theoretically, the SDOF model also showed reasonably good agreement when validating the maximum deformation results. However, larger differences were observed when comparing the results of the permanent deformation. Further investigation showed that the current formula based on a slab with fully fixed edges yielded significantly high stiffness values.
- The SDOF approach can be considered as a credible method in a preliminary design exercise to predict the deformation of UHPFRC slabs provided that the resistance functions are derived from actual static test results.

7.2 Recommendations for Future Work

It has been shown through this research that the UHPFRC slab has a notable potential to be used as a structural element able to resist abnormal loading. In order to fully appreciate the potential of UHPFRC slabs to mitigate progressive collapse due to abnormal loading, further studies are recommended in the following areas:

- More low velocity impact tests should be carried out to fully characterise the response of UHPFRC slabs. Focus should be given to other asymmetrical impact locations and tested under varying slab thickness. This work is necessary in order to correlate the impact resistance with the impact energy as well as the distance from the centroid of the slab. The results can lead to the development of equations that provide reliable estimation of the slab thickness to cater for the worst impact case scenarios.

- The work on pre-damaged UHPFRC slabs should be extended by varying the maximum capacity and the pre-damaged level of the slabs. This work should also include the point load static test to produce the respective resistance curves. With a broader spectrum of results, the correlation between the pre-damaged ratio and the resistance functions can be established in order to accurately validate the SDOF predictions.

- The impact resistance of the pre-damaged UHPFRC slabs subjected to a reversed bending impact should also be explored. This scenario represents the case of a pre-damaged floor by blast or otherwise arising from beneath the floor and subsequent impact from a failed column from above the floor.

- Additional characterization tests should be conducted in order to more accurately represent UHPFRC material using the RHT concrete model. Although the FE simulation in this study showed some accurate results for predicting the maximum deformation, the low residual strength of the FE model could be improved.

- Analytical work should also be developed to model the asymmetrical impact on UHPFRC slabs. This type of simulation is necessary as it can provide immediate results but with high accuracy. Parameters that are considered necessary to perform such analysis should also be identified. Eventually, an acceptance criteria for slabs subjected to asymmetrical impact can be established.

APPENDICES

APPENDIX A

UHPFRC CUBE STRENGTH TEST RESULTS

Casting Date	Density (kg/m^3)	7 Day Strength (MPa)	28 Day Strength (MPa)
01/03/2012	2442, 2445, 2443	151, 155, 156	161, 163, 164
05/03/2012	2423, 2424, 2420	156, 154, 155	162, 165, 164
22/03/2012	2454, 2444, 2435	154, 151, 149	164, 169, 166
03/05/2012	2442, 2431, 2440	156, 158, 156	160, 161, 162
08/05/2012	2435, 2450, 2441	159, 155, 158	162, 161, 163
10/05/2012	2443, 2451, 2459	155 ,156, 155	161, 164, 161
14/05/2012	2435, 2442, 2435	158, 155 ,157	164, 166, 167
17/05/2012	2445, 2437, 2450	161, 161, 162	166, 167, 168
20/05/2012	2450, 2442, 2438	163, 161, 160	170, 168, 169
24/09/2012	2442, 2441, 2438	154, 156, 157	162, 165, 166
23/10/2012	2443, 2447, 2442	158, 159,155	167, 166, 164
25/10/2012	2443, 2436, 2434	160, 158, 159	165, 169, 171
27/10/2012	2452, 2450, 2444	160, 158, 157	168, 167, 165
01/11/2012	2440, 2413, 2443	159, 155, 161	167, 166, 168
03/11/2012	2442, 2443, 2441	157, 159, 159	165, 168, 167
09/12/2012	2446, 2454, 2449	156, 161, 158	168, 172, 169
AVERAGE	2440.4	157.1	165.2
STD. DEV.	8.78	2.95	2.77

APPENDIX B1

MAXIMUM AND PERMANENT DEFORMATIONS: CENTRAL IMPACT

CEN-UD-1.5-P1			CEN-UD-1.5-P2		
Strike	Max. (mm)	Per. (mm)	Strike	Max. (mm)	Per. (mm)
1	6.53	2.02	1	5.91	1.44
3	8.99	2.91	3	9.65	2.99
5	11.25	4.67	5	12.65	4.15
7	12.88	6.01	7	14.66	5.65
9	15.34	7.43	9	16.02	7.03
11	16.87	9.02	11	17.77	8.44
13	18.96	10.46	13	19.40	9.98
15	21.15	12.02	15	21.73	11.58
17	24.42	14.35	17	24.86	13.81
19	27.96	16.94	19	28.2	16.62
21	FAIL	FAIL	21	32.69	21.54
22			22	FAIL	FAIL

CEN-PD-1.5-P1			CEN-PD-1.5-P2		
Strike	Max. (mm)	Per. (mm)	Strike	Max. (mm)	Per. (mm)
1	7.15	2.07	1	7.77	2.27
3	12.21	4.12	3	11.59	4.36
5	15.45	6.27	5	15.19	6.91
7	17.32	8.43	7	18.62	8.95
9	21.23	10.89	9	20.17	11.15
11	23.12	12.98	11	22.62	13.26
13	26.01	14.87	13	24.95	15.31
15	28.82	17.41	15	27.5	17.81
17	34.49	22.97	17	33.71	23.43
19	FAIL	FAIL	18	FAIL	FAIL

CEN-UD-2.3-P1			CEN-UD-2.3-P2		
Strike	Max. (mm)	Per. (mm)	Strike	Max. (mm)	Per. (mm)
1	9.67	3.24	1	9.39	3.68
2	14.41	6.12	2	13.45	6.6
3	19.45	10.16	3	18.89	10.94
4	24.79	15.24	4	24.25	16.24
5	28.94	20.55	5	FAIL	FAIL
6	FAIL	FAIL			

CEN-PD-2.3-P1			CEN-PD-2.3-P2		
Strike	Max. (mm)	Per. (mm)	Strike	Max. (mm)	Per. (mm)
1	11.67	4.43	1	10.47	4.23
2	17.66	8.52	2	16.00	8.96
3	24.29	15.12	3	FAIL	FAIL
4	FAIL	FAIL			

CEN-UD-2.8-P1			CEN-UD-2.8-P2			CEN-UD-2.8-P3		
Strike	Max. (mm)	Per. (mm)	Strike	Max. (mm)	Per. (mm)	Strike	Max. (mm)	Per. (mm)
1	11.33	4.56	1	12.07	4.09	1	12.29	4.43
2	17.54	9.25	2	17.95	10.07	2	19.14	10.62
3	26.62	19.23	3	FAIL	FAIL	3	FAIL	FAIL
4	FAIL	FAIL						

CEN-PD-2.8-P1			CEN-PD-2.8-P2			CEN-PD-2.8-P3		
Strike	Max. (mm)	Per. (mm)	Strike	Max. (mm)	Per. (mm)	Strike	Max. (mm)	Per. (mm)
1	13.1	8.14	1	12.47	8.00	1	11.9	7.87
2	FAIL	FAIL	2	FAIL	FAIL	2	FAIL	FAIL

APPENDIX B2

MAXIMUM AND PERMANENT DEFORMATIONS: EDGE IMPACT

EDG-UD-1.5-P1			EDG-UD-1.5-P2		
Strike	Max. (mm)	Per. (mm)	Strike	Max. (mm)	Per. (mm)
1	4.23	1.63	1	5.19	1.17
2	5.97	2.67	2	6.43	2.13
3	7.12	3.59	3	7.86	3.39
4	9.04	5.22	4	9.32	4.8
5	11.32	7.78	5	12.1	7.7
6	FAIL	FAIL	6		

EDG-PD-1.5-P1			EDG-PD-1.5-P2		
Strike	Max. (mm)	Per. (mm)	Strike	Max. (mm)	Per. (mm)
1	5.32	1.77	1	6.08	2.21
2	7.54	3.44	2	8.52	3.76
3	9.56	5.47	3	10.04	5.87
4	FAIL	FAIL	4	12.37	8.52
			5	FAIL	FAIL

EDG-UD-2.3-P1			EDG-UD-2.3-P2		
Strike	Max. (mm)	Per. (mm)	Strike	Max. (mm)	Per. (mm)
1	8.35	3.80	1	7.69	3.38
2	11.69	7.03	2	10.87	5.87
3	FAIL	FAIL	3	15.42	11.03
			4	FAIL	FAIL

EDG-PD-2.3-P1			EDG-PD-2.3-P2		
Strike	Max. (mm)	Per. (mm)	Strike	Max. (mm)	Per. (mm)
1	8.94	4.12	1	9.76	3.8
2	14.43	9.22	2	FAIL	FAIL
3	FAIL	FAIL			

EDG-UD-2.8-P1			EDG-UD-2.8-P2		
Strike	Max. (mm)	Per. (mm)	Strike	Max. (mm)	Per. (mm)
1	9.63	4.98	1	9.45	5.06
2	15.72	11.67	2	FAIL	FAIL
3	FAIL	FAIL			

EDG-PD-2.8-P1			EDG-PD-2.8-P2		
Strike	Max. (mm)	Per. (mm)	Strike	Max. (mm)	Per. (mm)
1	11.82	7.81	1	FAIL	FAIL
2	FAIL	FAIL			

APPENDIX B3

MAXIMUM AND PERMANENT DEFORMATIONS: CORNER IMPACT

COR-UD-1.5-P1			COR-UD-1.5-P2		
Strike	Max. (mm)	Per. (mm)	Strike	Max. (mm)	Per. (mm)
1	5.02	2.14	1	5.36	2.4
2	6.65	3.76	2	7.23	3.6
3	8.87	5.61	3	8.49	5.09
4	FAIL	FAIL	4	10.95	7.35
			5	FAIL	FAIL

COR-PD-1.5-P1			COR-PD-1.5-P2		
Strike	Max. (mm)	Per. (mm)	Strike	Max. (mm)	Per. (mm)
1	5.47	3.03	1	6.21	2.51
2	7.85	5.76	2	7.67	5.10
3	FAIL	FAIL	3	FAIL	FAIL

COR-UD-2.3-P1			COR-UD-2.3-P2		
Strike	Max. (mm)	Per. (mm)	Strike	Max. (mm)	Per. (mm)
1	9.66	6.83	1	9.04	6.69
2	FAIL	FAIL	2	FAIL	FAIL

COR-PD-2.3-P1			COR-PD-2.3-P2		
Strike	Max. (mm)	Per. (mm)	Strike	Max. (mm)	Per. (mm)
1	FAIL	FAIL	1	11.37	8.33
			2	FAIL	FAIL

COR-UD-2.8-P1			COR-UD-2.8-P2		
Strike	Max. (mm)	Per. (mm)	Strike	Max. (mm)	Per. (mm)
1	10.37	7.87	1	FAIL	FAIL
2	FAIL	FAIL			

COR-PD-2.8-P1			COR-PD-2.8-P2		
Strike	Max. (mm)	Per. (mm)	Strike	Max. (mm)	Per. (mm)
1	FAIL	FAIL	1	FAIL	FAIL

APPENDIX B4

(MAXIMUM AND PERMANENT DEFORMATIONS: OBLIQUE IMPACT)

OBL-UD-2.8-P1			OBL-UD-2.8-P2		
Strike	Max. (mm)	Per. (mm)	Strike	Max. (mm)	Per. (mm)
1	6.28	1.95	1	7.42	1.53
2	10.82	4.27	2	9.8	3.85
3	14.17	6.24	3	12.33	5.94
4	17.32	10.24	4	15.42	9.36
5	20.24	14.63	5	FAIL	FAIL
6	FAIL	FAIL			

OBL-PD-2.8-P1			OBL-PD-2.8-P2		
Strike	Max. (mm)	Per. (mm)	Strike	Max. (mm)	Per. (mm)
1	9.21	2.11	1	8.33	2.71
2	13.83	8.7	3	13.67	8.7
3	FAIL	FAIL	5	FAIL	FAIL

APPENDIX C

CALCULATION FOR DETERMINING THE MINIMUM THICKNESS OF UHPFRC SLABS AGAINST PERFORATION (FIRST STRIKE, CENTRAL IMPACT CASE)

i) Undamaged slab

$$e = \left(\frac{V_0}{v_i}\right)^{0.25} \left(\frac{m{v_i}^2}{df_c}\right)^{0.5} \left(1 + 5.39V_f\right)^{0.38}$$

where

V_0 = 60.96 m/s,

v_i = 7.32 m/s,

m = 15.672 kg,

d = 0.062 m,

f_c = 150 × 10^6 N/m^2 and

V_f = 0.02 %

Incorporating all the values in equation (2.1) yielded,

$e =$ 16.8 mm

ii) Pre-damaged slab

$E_{PD} = 0.6E_{UD}$

$\frac{1}{2} \times m_{PD} \times v_{PD} = 0.6 \times \frac{1}{2} \times m_{UD} \times v_{UD}$

$\therefore \frac{m_{PD} \times v_{PD}}{0.6} = m_{UD} \times v_{UD}$

Since the mass of the slab and velocity of the impactor is the same in both cases, rearranging equation (2.1) f and solving for the minimum thickness for the pre-damaged slab yielded,

$$e = \left(\frac{V_0}{v_i}\right)^{0.25} \left(\frac{m{v_i}^2}{0.6df_c}\right)^{0.5} \left(1 + 5.39V_f\right)^{0.38}$$

$e = 21.7$ mm

APPENDIX D

CALCULATION FOR DETERMINING THE THEORETICAL STIFFNESS

$$Strain\ Energy\ =\ 4\int_0^X\int_0^Y\int_{-z}^{z}\left(\frac{1}{2}E\ \in_{xx}^2+\ \frac{E}{2(1+\ \upsilon)}\in_{xy}^2+\ \frac{1}{2}E\ \in_{yy}^2\right)dx\,dy\,dz$$

$$\in_{xx}= z\left(\frac{\partial^2 w}{\partial x^2}\right)\qquad \in_{xy}= 2z\left(\frac{\partial^2 w}{\partial x\partial y}\right)\qquad \in_{yy}= z\left(\frac{\partial^2 w}{\partial y^2}\right)$$

In the elastic strain range;

$$w=\ \frac{\delta}{4}\left(1+cos\left(\frac{\pi x}{X}\right)\right)\left(1+cos\left(\frac{\pi y}{Y}\right)\right)$$

$$\frac{\partial w}{\partial x}=\ \frac{-\pi\delta}{4X}\ .\ sin\left(\frac{\pi x}{X}\right)\left(1+cos\left(\frac{\pi y}{Y}\right)\right)$$

$$\frac{\partial^2 w}{\partial x^2}=\ \frac{-\pi^2\delta}{4X^2}\ .cos\left(\frac{\pi x}{X}\right)\left(1+cos\left(\frac{\pi y}{Y}\right)\right)$$

$$\frac{\partial w}{\partial y}=\ \frac{\pi\delta}{4Y}\ .\ sin\left(\frac{\pi y}{Y}\right)\left(1+cos\left(\frac{\pi x}{X}\right)\right)$$

$$\frac{\partial^2 w}{\partial y^2}=\ \frac{\pi^2\delta}{4Y^2}\ .\ cos\left(\frac{\pi y}{Y}\right)\left(1+cos\left(\frac{\pi x}{X}\right)\right)$$

$$\frac{\partial^2 w}{\partial x\partial y}=\ \frac{\pi^2\delta}{4XY}\ .\ sin\left(\frac{\pi x}{X}\right)\ .\ sin\left(\frac{\pi y}{Y}\right)$$

$$\left(\frac{\partial^2 w}{\partial x^2}\right)^2=\ \frac{\pi^4\delta^2}{16X^4}\ .\ cos^2\left(\frac{\pi x}{X}\right)\left(1+cos^2\left(\frac{\pi y}{Y}\right)+2cos\left(\frac{\pi y}{Y}\right)\right)$$

$$\left(\frac{\partial^2 w}{\partial y^2}\right)^2=\ \frac{\pi^4\delta^2}{16Y^4}\ .\ cos^2\left(\frac{\pi y}{Y}\right)\left(1+cos^2\left(\frac{\pi x}{X}\right)+2cos\left(\frac{\pi x}{X}\right)\right)$$

$$\left(\frac{\partial^2 w}{\partial x\partial y}\right)^2=\ \frac{\pi^4\delta^2}{16X^2Y^2}\ .sin^2\left(\frac{\pi x}{X}\right)\ .\ sin^2\left(\frac{\pi y}{Y}\right)$$

$$Strain\ Energy=\ 4\int_0^X\int_0^Y\int_{\frac{-t}{2}}^{\frac{t}{2}}\left(\frac{Ez^2}{2}\left(\frac{\partial^2 w}{\partial x^2}\right)^2+\ \frac{4Ez^2}{2(1+\ \upsilon)}\left(\frac{\partial^2 w}{\partial x\partial y}\right)^2+\ \frac{Ez^2}{2}\left(\frac{\partial^2 w}{\partial y^2}\right)^2\right)dx\,dy\,dz$$

Integrate with respect to z for quarter slab only and $z=\ \frac{t}{2}$;

$$=\ \int_0^X\int_0^Y\left[\frac{Ez^3}{6}\left(\frac{\partial^2 w}{\partial x^2}\right)^2+\frac{2Ez^2}{3(1+\ \upsilon)}\left(\frac{\partial^2 w}{\partial x\partial y}\right)^2+\ \frac{Ez^3}{6}\left(\frac{\partial^2 w}{\partial y^2}\right)^2\right]_{-z}^{z}dx\,dy$$

$$\frac{Et^3}{12}\int_0^X\int_0^Y\left(\frac{1}{2}\left(\frac{\partial^2 w}{\partial x^2}\right)^2+\frac{2}{(1+\ \upsilon)}\left(\frac{\partial^2 w}{\partial x\partial y}\right)^2+\ \frac{1}{2}\left(\frac{\partial^2 w}{\partial y^2}\right)^2\right)dx\,dy$$

$$i)\ \int_0^X \int_0^Y \frac{1}{2}\left(\frac{\partial^2 w}{\partial x^2}\right)^2 dx\,dy$$

$$= \frac{1}{2}\int_0^X \int_0^Y \left(\frac{\pi^4\delta^2}{16X^4}.\ cos^2\left(\frac{\pi x}{X}\right)\left(1 + cos^2\left(\frac{\pi y}{Y}\right) + 2cos\left(\frac{\pi y}{Y}\right)\right)dxdy\right)$$

$$= \frac{1}{2}\int_0^X \frac{\pi^4\delta^2}{16X^4}.\ cos^2\left(\frac{\pi x}{X}\right)\left[\frac{y}{2} + sin\left(\frac{2\pi y}{Y}\right).\frac{Y}{4\pi} + 2sin\left(\frac{\pi y}{Y}\right).\frac{Y}{\pi}\right]_0^Y dx$$

$$= \frac{1}{2}\int_0^X \frac{\pi^4\delta^2}{16X^4}.\ cos^2\left(\frac{\pi x}{X}\right).\frac{3Y}{2}dx$$

$$= \frac{1}{2}.\frac{3Y}{2}.\frac{\pi^4\delta^2}{16X^4}\left[\frac{x}{2} + sin\left(\frac{2\pi x}{X}\right).\frac{X}{4\pi}\right]_0^X$$

$$= \frac{3\delta^2\pi^4 Y}{128X^3}$$

$$ii)\ \int_0^X \int_0^Y \frac{2}{(1+\upsilon)}\left(\frac{\partial^2 w}{\partial x\partial y}\right)^2 dx\,dy$$

$$= \frac{2}{(1+\upsilon)}\int_0^X \int_0^Y \frac{\pi^4\delta^2}{16X^2Y^2}.sin^2\left(\frac{\pi x}{X}\right).\ sin^2\left(\frac{\pi y}{Y}\right)dx\,dy$$

$$= \frac{2}{(1+\upsilon)}\int_0^X \frac{\pi^4\delta^2}{16X^2Y^2}.sin^2\left(\frac{\pi x}{X}\right)\left(\left[\frac{y}{2} - sin\left(\frac{2\pi y}{Y}\right).\frac{Y}{4\pi}\right]_0^Y\right)dx$$

$$= \frac{1}{(1+\upsilon)}.\frac{\pi^4\delta^2}{16X^2Y}\left[\frac{x}{2} - sin\left(\frac{2\pi x}{X}\right).\frac{X}{4\pi}\right]_0^X$$

$$= \frac{\pi^4\delta^2}{32(1+\upsilon)XY}$$

$$iii)\ \int_0^X \int_0^Y \frac{1}{2}\left(\frac{\partial^2 w}{\partial y^2}\right)^2 dx\,dy$$

$$= \frac{3\delta^2\pi^4 X}{128Y^3}$$

Combining i), ii) and iii) together with the constant;

$$Strain\ Energy\ (full\ slab) = \frac{Et^3}{12}\left(\frac{3\delta^2\pi^4 Y}{128X^3} + \frac{3\pi^4\delta^2}{96(1+\upsilon)XY} + \frac{3\delta^2\pi^4 X}{128Y^3}\right).4$$

$$= \frac{Et^3\delta^2}{16}\left(\frac{\pi^4 Y}{8X^3} + \frac{\pi^4}{6(1+\upsilon)XY} + \frac{\pi^4 X}{8Y^3}\right)$$

$For\ a\ square\ slab, X = Y;$

$$Strain\ Energy\ (full\ slab) = \frac{Et^3\pi^4\delta^2}{192L^2}\left(3\ +\ \frac{2}{(1+\upsilon)}\right)$$

$From\ the\ energy\ solution;$

$Potential\ Energy = Strain\ Energy - Work\ Done$

$U = Strain\ Energy - F.\delta$

$$U = \frac{Et^3\pi^4\delta^2}{192L^2}\left(3\ +\ \frac{2}{(1+\upsilon)}\right) - FC$$

$$At\ equilibrium\ \frac{dU}{d\delta} = 0$$

$$0 = \frac{Et^3\pi^4\delta}{96L^2}\left(3\ +\ \frac{2}{(1+\upsilon)}\right) - F$$

$$F = \frac{Et^3\pi^4\delta}{96L^2}\left(3\ +\ \frac{2}{(1+\upsilon)}\right)$$

$but\ F =\ k_1\delta\ , therefore$

$$k_1 = \frac{Et^3\pi^4}{96L^2}\left(3\ +\ \frac{2}{(1+\upsilon)}\right)$$

$$k_1 = \frac{21.51\ \times 10^3 \times 25^3 \times \pi^4}{96 \times 250^2}\left(3 +\ \frac{2}{(1+0.213)}\right) \times 1000$$

$$= 2.54\ \times 10^7\ N/m$$

By following the same steps, the stiffness of the slab in the elastic-plastic strain range where $w = \delta cos\ \left(\frac{\pi x}{2X}\right)\left(cos\frac{\pi y}{2Y}\right)$ yielded;

$$k_2 = \frac{Et^3\pi^4}{96L^2}\left(1\ +\ \frac{2}{(1+\upsilon)}\right)$$

$$k_2 = 1.44\ \times 10^7\ N/m.$$